THESIS FOR THE DEGREE OF DOCTOR OF PHILOSOPHY

Analysis of High-Frequency Electrical Transients in Offshore Wind Parks

TARIK ABDULAHOVIĆ

Department of Energy and Environment
Division of Electric Power Engineering
CHALMERS UNIVERSITY OF TECHNOLOGY
Göteborg, Sweden 2011

Analysis of High-Frequency Electrical Transients in Offshore Wind Parks
TARIK ABDULAHOVIC
ISBN 978-91-7385-598-3

Doktorsavhandlingar vid Chalmers tekniska högskola
Ny serie nr 3279
ISSN 0346-718X

Department of Energy and Environment
Division of Electric Power Engineering
SE-412 96 Göteborg
Sweden
Telephone +46(0)31-772 1000

Chalmers Bibliotek, Reproservice
Göteborg, Sweden 2011

Analysis of High-Frequency Electrical Transients in Offshore Wind Parks
TARIK ABDULAHOVIC
Department of Energy and Environment
Chalmers University of Technology

Abstract

In this thesis, a study of high frequency electromagnetic transient phenomena is performed. Models of various components needed for simulations of high frequency transients, such as for transformers, cables and breakers are developed. Measurements were performed in Chalmers research laboratory as well as at ABB Corporate Research in Västerås, Sweden for the purpose of parameter estimation of models and for verification of simulations. Critical cases where the voltage surges of the magnitude and/or rise time above basic lightning impulse voltage level appear, are identified. Also, some transient protection schemes are analyzed and the performance of different transient mitigation devices is studied. Furthermore, the voltage distribution along the winding during very fast transients is studied in order to estimate turn-to-turn voltages and the critical voltage envelope.

In the work it was found that simulations of the high frequency transients are in a very good agreement with the measurements obtained in the laboratory. Simulations predicted accurately critical surges with the highest magnitude and matched with good accuracy surge waveforms recorded during the measurements. The accuracy of the rise times is within 10%, while the magnitudes during the critical cases are within a 5% margin. During the testing and simulations, surges which exceed the basic lightning impulse voltage level of dry-type transformers specified by IEEE standards, both in magnitude and rise time are observed at the transformers even when surge arresters are used to protect the transformers. Furthermore, obtained voltage surges exceeded the proposed critical voltage envelope. It is shown that the most critical voltage strikes are obtained with dry-type transformers, where the rise time is five to ten times shorter compared to oil-insulated transformer with the same rating. It was confirmed both in simulations and measurements that the use of additional transient protections devices such as surge capacitors and RC protections, decreased the magnitude of surges to be below the critical level. The analysis of the voltage during very fast transients showed that the rise time of the transients directly influences the magnitude of the turn-to-turn voltages. Furthermore, during the breaker closing transient, turn-to-turn voltages, measured in delta connected dry-type transformers, were 2.5 times higher than the voltages obtained during the same transient with a wye connected dry-type transformer, or during the stress with a $4.4pu$ lightning impulse voltage.

Index Terms: very fast transient, breaker, surge, surge protection, transient overvoltage, prestrikes, restrikes, voltage escalation.

Acknowledgements

This work has been carried out at the Division of Electric Power Engineering, Department of Energy and Environment at Chalmers University of Technology, Göteborg, Sweden and ABB Corporate Research, Västerås, Sweden. The financial support provided by Vindforsk is gratefully acknowledged. In addition, I am also grateful for the in-house efforts by ABB, Vestas, Vattenfall and Gothia Power which made the project possible.

I would like to thank my supervisor and examiner Professor Torbjörn Thiringer and supervisor Professor Ola Carlson for their patience, encouraging, stimulating and critical comments regarding the work, and revising the thesis manuscript extensively to give it a better shape. In addition, I acknowledge support from my examiner Tore Undeland.

I express my sincere appreciation to Ambra Sannino and Lars Gertmar from ABB Corporate Research, Michael Lindgren, David Söderberg and Anders Holm from Vattenfall, Sture Lindahl and Andreas Petersson from Gothia Power, Professor Stanislaw Gubanski from Chalmers, Philip Kjaer and Babak Badrzadeh from Vestas for constructive discussions and suggestions during the reference group meetings.

I acknowledge the support from my dear colleagues at the division. I also acknowledge the support from Yuriy Serdyuk for Comsol simulations.

I would like to thank colleagues from ABB Corporate Research in Västerås, Lars Liljestrand, Henrik Breder, Dierk Bormann and especially Muhamad Reza for their support and very nice discussions.

Last, but certainly not least, heartfelt thanks go to my parents Agan and Zejna, my wife Esmeralda, daughter Merjem and brother Zijad, for their kindness, love, support and patience.

Tarik,
Göteborg,
December, 2011

Contents

Chapter 1

Introduction

1.1 Problem Overview

For many years, the lightning was the only phenomenon that could create pulses with very steep fronts in the order of micro seconds (μs). These wave pulses can be reflected off junctions in the system producing high overvoltages. High overvoltages produced by lightning are prevented from damaging insulation of the equipment by using surge arresters that are able to keep the voltage limited within the range that is not harmful to the protected equipment. This protection proved to be sufficient for the protection of the equipment and the failures were kept on an acceptable level.

Further research in this area was not needed until increased failures of the insulation of the equipment were detected again even on a low voltage level. These failures occurred more and more often with the development and improvements of electric power equipment, especially in motor drives. Two areas of the development are very important for this matter.

One of them is the development of semiconductors used in power electronics. The appearance of the fast switching insulated gate bipolar transistors (IGBT's) led to very short rise times of the pulses that were produced by IGBT's in pulse-width modulated (PWM) inverters that are often used with induction machines (IM) for variable speed drives. The rise time of the pulses could be as low as, or even below, 0.1 μs [1]. This is more than ten times quicker compared to the rise time of the lightning pulse. These fast switching IGBT's brought two major improvements to the inverters. At first, lower switching losses and secondly reducing the total harmonic distortion (THD) given a similar filter, due to the possibility of using a higher switching frequency.

Moreover, another important area is the development of the breakers used in the electric grid. Breakers used in grids can have a strong negative influence on insulation. The appearance of the vacuum circuit breaker (VCB) brought a switching device with excellent interruption and dielectric recovery characteristics [2]. Vacuum circuit breakers have low maintenance costs, good durability and provide the best breaker solution for medium voltage below 24 kV [3]. However, it was reported worldwide that many transformer insulation failures have occurred possibly by switching operations of VCBs, although those transformers have previously passed all the standard tests and complied to all quality requirements [4]-[8]. However, another study showed that it is not only the vacuum breaker that can create surges

potentially dangerous to the transformers, but also SF6 insulated breakers and disconnectors [9]. The breakdown in SF6 medium can have a typical rise time between $2 - 20ns$, and in addition, SF6 interrupters can generate re-strikes and pre-strikes during the operation [9]. A 10 years long study which included an investigation of failures of thousands of transformers conducted by Hartford Steam Boiler Earlier shows that the high frequency transients are the major cause of transformer failures [10]. The transformer failures caused by the high frequency transients reach a level of 33.9% according to this study and it was said to be the most likely cause of a transformer insulation failure [10]. Although, the direct proof of the negative impact of the high frequency transients on the transformer insulation is not yet found [9], some studies give description of the phenomenon that produces high overvoltages internaly in the transformer winding [4] potentially responsible for the transformer insulation failure during the high frequency transients. As some studies for induction motors showed, the appearance of repetitive strikes is dangerous for the induction motors [11],[12] and it is very likely that the same phenomenon is dangerous for the transformers insulation. A major problem of the transformer insulation failures occurred in the wind parks(WP) Middelgrunden and Hornsrev where almost all transformers had to be replaced with new ones due to the insulation failure [13], [14]. It is suspected that the fast switching breakers caused the insulation failures in these WP's.

During studies of insulation failures of motors caused by switching phenomenon, it is found that the surges generated during switching of the air magnetic circuit breakers are very similar to the vacuum devices [15]-[17]. According to one of these studies, surges generated by air magnetic circuit breakers generated surges of $4.4pu$ in magnitude with a rise times of $0.2\mu s$ where the vacuum breaker generated surges with $4.6pu$ magnitude but with longer rise times of $0.6\mu s$ [15]. An important finding of this study, is that although the vacuum breaker generates more surges, the magnitude and the rise time of the surges generated by these two types of breakers are very similar [15].

Another factor that contributed to the failures caused by the fast switching operations of the IGBT's and VCB's is the use of the cables both in low and medium voltage systems. The characteristic impedance of the cables is approximately ten times smaller than the characteristic impedance of a transmission line resulting in a ten times higher derivative of the transient overvoltage (TOV). The transient phenomenon is thus even more difficult to analyze since cables longer than approximately 50 m behave like transmission lines where the wave traveling phenomenon and the wave reflection phenomenon can be observed. This means that a proper high frequency transient analysis advanced cable model is required, which makes the transient phenomenon analysis fairly complicated. In order to perform calculations of the propagation of high frequency transients, an appropriate modeling and an appropriate software tool is needed

1.2 Purpose of the thesis and contributions

The aim of this thesis is to analyze generation, propagation and impact of high frequency transients in wind parks (WP's) and to present analysis as well as key results. In order to successfully achieve this goal, the modeling of important components as well as their implementation is to be investigated. The treated components will be breakers, cables and transformers. The general objectives of the work can be summarized as follows:

- Develop models for analysis of the electrical high frequency transients occurring in wind parks. The models need to be valid in a wide frequency range, between $50Hz$ and $10MHz$.
- Study the generation and propagation of high frequency transients in cable systems, i.e. offshore wind farms. The influence of the different topologies is to be investigated.
- To compare the influence of the high frequency transients generated during switching events and lightning impulses. Furthermore, to investigate if switching operations can lead to substantial overvoltages at the components.
- Analyze the impact of the high frequency phenomenon on the voltage distribution inside transformers in order to identify critical switching patterns and level of internal overvoltages.
- Compare turn-to-turn voltage stress obtained during very fast transients (VFT) with the turn-to-turn voltage stress measured during the basic lightning impulse level (BIL) in order to find if current transformer standards account for the voltage stress that appears during VFT.

The thesis covers a wide range of topics. The work is conducted at Chalmers University of Technology and some parts at ABB Corporate Research, Sweden, in a collaboration with Muhamad Reza. To the best knowledge of the author the contributions are summarized as follows:

- A new method to account for semiconducting layers in the cable models is proposed. The parameters of the cable model are adjusted to account for semiconducting layers at high frequency.
- A new, simplified model of the vacuum circuit breaker for the purpose of high frequency transient analysis is developed and verified successfully experimentally.
- Implementation of the vector fitting method in a black-box modeling of a reactor winding in order to study internal overvoltages. Moreover, a method for improvement of the measurement sets for the black-box modeling of a winding is developed.
- It is identified that connection transients, that do not generate overvoltages at transformer terminals, can generate excessive internal turn-to-turn overvoltages, that exceed the voltage level obtained during testing with a lightning pulse shaped voltage. It is experimentally shown that high internal overvoltages are obtained during VFT with very short rise times that stress dry-type transformers.
- The critical voltage envelope for surges with rise times between $50ns$ and $1.2\mu s$ is established using the maximum turn-to-turn voltage criteria.
- It is verified that standards for dry-type transformers do not account for the voltage stress that appears during VFT. Accordingly, based on the results, it is proposed that the BIL for dry-type transformers needs to be increased, or new tests need to be developed.

- It is shown theoretically as well as proven experimentally that the standard surge protection, that includes only surge arresters, provides insufficient protection, since the transients recorded during voltage restrikes exceeded the BIL level and/or critical voltage envelope.

1.3 Thesis structure

The structure of the thesis is the following:

Chapter 2 gives the background theory on surge propagation. This chapter gives insight on how it is possible to generate overvoltages during wave reflections, and which parameters of the network that are most dominant in shaping of transient overvoltages. Chapter 3 focuses on the modeling. In that chapter, the modeling of various components is presented. In some cases, guidelines are given on how to properly use existing models, and how to compensate for imperfections and shortcomings of existing models. Chapter 4 shows the voltage distribution along a winding during high frequency transients. This chapter shows the impact of VFT on turn-to-turn voltages, and compares these voltages against turn-to-turn voltages obtained during the stress with a lightning impulse shaped voltage wave. Chapter 5 shows a comparison of standards for critical voltages for distribution transformers and motors. Furthermore, a quantification method is presented. Chapter 6 shows analysis of the high frequency transients in the laboratory environment in ABB Corporate Research, Västerås, Sweden. Finally, some high frequency transient mitigation devices are tested and their level of protection is analyzed. Chapter 7 presents conclusions and future work.

1.4 List of publications

The following publications have been made during this project.

- Abdulahovic Tarik, Thiringer Torbjörn, Modeling of the energizing of a wind park radial, Nordic Wind Power Conference, Roskilde, Denmark, 2007.
- Muhamad Reza, Henrik Breder, Lars Liljestrand, Ambra Sannino, Tarik Abdulahovic, Torbjörn Thiringer, An experimental investigation of switching transients in a wind collection grid scale model in a cable system laboratory, CIRED, 20^{th} International Conference on Electricity Distribution, Prague, June 8-11 2009.
- Reza Muhamad, Srivastava Kailash, Abdulahovic Tarik, Thiringer Torbjörn, Combining MV laboratory and simulation resources to investigate Fast Transient Phenomena in Wind Cable Systems, European Offshore Wind, Stockholm, 2009.
- Abdulahovic Tarik, Thiringer Torbjörn, Comparison of switching surges and basic lightning impulse surges at transformer in MV cable grids, Nordic Wind Power Conference, Bornholm, Danmark, 2009.
- Abdulahovic Tarik, Teleke Sercan, Thiringer Torbjörn, Svensson Jan, Simulation accuracy of the built-in PSCAD and an owner-defined synchronous machine model, Compel-

the International Journal for Computation and Mathematics in Electrical and Electronic Engineering, 29 (3) pp. 840-855. 2010.

- Sonja Tidblad Lundmark, Tarik Abdulahovic, Saeid Haghbin, Learning improvements by students active preparations to Electric drives labs, Chalmers Conference on Teaching and Learning, KUL 2011, Göteborg, 2011.

Chapter 2

Background theory on surge propagation

The wave traveling phenomena on long transmission lines is known for a long time. The waves that travel over the conductor at the speed of light belong to the group of transverse waves, and the behavior of these waves is the same as the behavior of other transverse waves that propagate in other medium. The reflection of the waves we experience in everyday's life when we hear echo or look on the reflection in the mirrors or on a water surface. The same phenomena occurs at the end of cables and the transmission lines and can produce very high overvoltages in a transmission line or at cable ends in some cases.

2.1 Electromagnetic wave traveling and reflection

The first mathematical description of transverse electromagnetic waves is given by Maxwell in the 19^{th} century. These equations describe the dynamical properties of the electromagnetic field. They are based on experimental results and are written in the following form

$$\nabla \cdot \mathbf{E} = -\frac{\rho(t,x)}{\varepsilon} \tag{2.1}$$

$$\nabla \times \mathbf{E} = -\frac{\partial \mathbf{B}}{\partial t} \tag{2.2}$$

$$\nabla \cdot \mathbf{B} = 0 \tag{2.3}$$

$$\nabla \times \mathbf{B} = \mu \mathbf{j}(t,x) + \varepsilon\mu \frac{\partial \mathbf{E}}{\partial t} \tag{2.4}$$

where $\mathbf{E}$ is the vector of electric field, $\mathbf{B}$ is the magnetic flux density, $\rho(t,x)$ is the charge distribution, $\mathbf{j}(t,x)$ is the magnetic current density, μ is the permeability and ε permittivity of the material.

These four non-coupled partial differential equations, can be rewritten as two non-coupled second order partial equations for $\mathbf{E}$ and $\mathbf{D}$. These two equations are called the wave equations. Let us derive the wave equation for $\mathbf{E}$. Since the waves propagating in air or vacuum are considered, these equations are derived with electric and magnetic properties of the air, vacuum permeability and permittivity μ_0 and ε_0. In the beginning, let us take the curl of (2.2) and then insert (2.4) to obtain

$$\nabla \times (\nabla \times \mathbf{E}) = -\frac{\partial}{\partial t}(\nabla \times \mathbf{B}) = -\mu_0 \frac{\partial}{\partial t}(\mathbf{j}(t,x) + \varepsilon_0 \frac{\partial \mathbf{E}}{\partial t}). \tag{2.5}$$

In order to solve this, we are going to use the operator triple product "bac-cab" rule given by

$$\nabla \times (\nabla \times \mathbf{E}) = \nabla(\nabla \cdot \mathbf{E}) - (\nabla^2 \mathbf{E}). \tag{2.6}$$

Since the electrical charges are not present in the medium, $\rho(t,x) = 0$, a simplified form of (2.1) is obtained

$$\nabla \cdot \mathbf{E} = 0. \tag{2.7}$$

Considering (2.6) and (2.7), and taking into account Ohm's law given by

$$\mathbf{j}(t,x) = \sigma \mathbf{E} \tag{2.8}$$

(2.5) is rearranged and written in the form of

$$\nabla^2 \mathbf{E} - \mu_0 \frac{\partial}{\partial t}\left(\sigma \mathbf{E} + \varepsilon_0 \frac{\partial \mathbf{E}}{\partial t}\right) = 0. \tag{2.9}$$

Finally, considering

$$\varepsilon_0 \mu_0 = \frac{1}{c^2} \tag{2.10}$$

where c is the speed of light, the homogeneous wave equation for $\mathbf{E}$ is obtained

$$\nabla^2 \mathbf{E} - \mu_0 \sigma \frac{\partial \mathbf{E}}{\partial t} - \frac{1}{c^2}\frac{\partial^2 \mathbf{E}}{\partial t^2} = 0. \tag{2.11}$$

In a similar way, the homogeneous wave equation for $\mathbf{B}$ is derived. This equation is given by

$$\nabla^2 \mathbf{B} - \mu_0 \frac{\partial}{\partial t}\left(\sigma \mathbf{B} + \varepsilon_0 \frac{\partial \mathbf{B}}{\partial t}\right) = 0. \tag{2.12}$$

The homogeneous wave equation for $\mathbf{B}$ is obtained by inserting the relation for the speed of light into (2.12).

$$\nabla^2\mathbf{B} - \mu_0\sigma\frac{\partial\mathbf{B}}{\partial t} - \frac{1}{c^2}\frac{\partial^2\mathbf{B}}{\partial t^2} = 0. \tag{2.13}$$

For a plane wave where both electric and magnetic field depends on the distance x to a given plane, the wave equations for $\mathbf{E}$ and $\mathbf{B}$ are given by

$$\frac{\partial^2\mathbf{E}}{\partial^2 x} - \mu_0\sigma\frac{\partial\mathbf{E}}{\partial t} - \frac{1}{c^2}\frac{\partial^2\mathbf{E}}{\partial t^2} = 0 \tag{2.14}$$

$$\frac{\partial^2\mathbf{B}}{\partial^2 x} - \mu_0\sigma\frac{\partial\mathbf{B}}{\partial t} - \frac{1}{c^2}\frac{\partial^2\mathbf{B}}{\partial t^2} = 0. \tag{2.15}$$

These equations which describe the propagation of the plane waves in a conducting medium are called the telegrapher's equations or the telegraph equations. For insulators, where the conductivity is equal to zero ($\sigma = 0$), the telegrapher's equations become

$$\frac{\partial^2\mathbf{E}}{\partial^2 x} - \frac{1}{c^2}\frac{\partial^2\mathbf{E}}{\partial t^2} = 0 \tag{2.16}$$

$$\frac{\partial^2\mathbf{B}}{\partial^2 x} - \frac{1}{c^2}\frac{\partial^2\mathbf{B}}{\partial t^2} = 0. \tag{2.17}$$

A more convenient way to derive and write the telegrapher's equations is by using an equivalent scheme for two parallel conductors. Now, these equations are going to be written using voltages and currents, and inductances and capacitances instead of magnetic and electric field vectors. The equivalent scheme is defined for an infinitely small element of two conductors and it is presented in Fig.2.1.

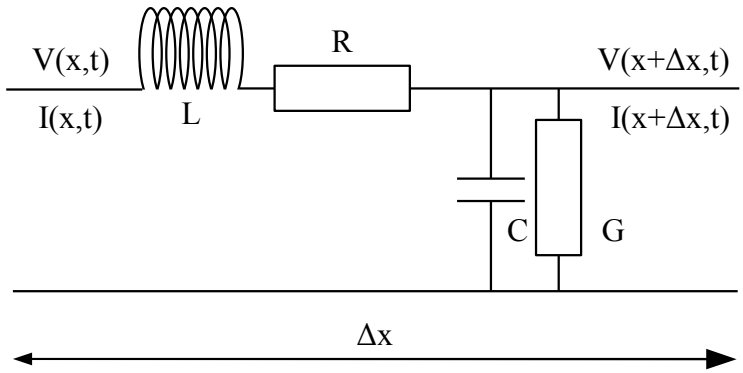

Figure 2.1: An infinitely small element of two parallel conductors.

For the sake of simplicity an equivalent scheme where the resistance of the conductor and the conductance between the two lines is neglected is presented in Fig.2.2.

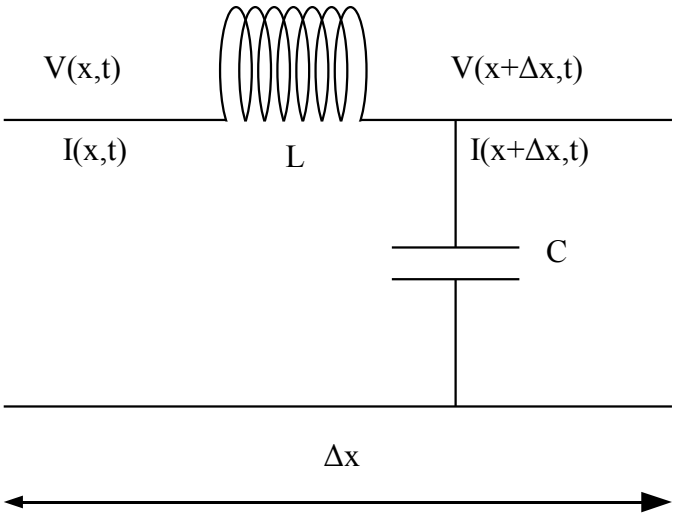

Figure 2.2: An infinitely small element of two parallel conductors.

It is quite easy to derive the telegraphers equations for this circuit using Kirchoff's Laws. Since the capacitance and the inductance presented in Figs. 2.1 and 2.2 are per unit length, values of the capacitance and inductance are obtained after multiplication by Δx. For the voltage and the current at length of $x + \Delta x$, two equations can be written as

$$V(x + \Delta x, t) = V(x, t) - C\Delta x \frac{\partial I(x, t)}{\partial t} \tag{2.18}$$

$$I(x + \Delta x, t) = I(x, t) - L\Delta x \frac{\partial V(x + \Delta x, t)}{\partial t}. \tag{2.19}$$

These two equations can be rewritten in the following way

$$\frac{V(x + \Delta x, t) - V(x, t)}{\Delta x} = -C \frac{\partial I(x, t)}{\partial t} \tag{2.20}$$

$$\frac{I(x + \Delta x, t) - I(x, t)}{\Delta x} = -L \frac{\partial V(x + \Delta x, t)}{\partial t}. \tag{2.21}$$

We take the limit as $\Delta x \to 0$ which yields $V(x + \Delta x, t) \to V(x, t)$ giving simplified telegrapher's equations for transmission lines

$$\frac{\partial V(x, t)}{\partial x} = -C \frac{\partial I(x, t)}{\partial t} \tag{2.22}$$

$$\frac{\partial I(x, t)}{\partial x} = -L \frac{\partial V(x, t)}{\partial t}. \tag{2.23}$$

These equations can be solved by taking the spatial derivative of one equation and substituting the other equation into it. Let us do it first by taking the spatial derivative of (2.22).

$$\frac{\partial^2 V(x,t)}{\partial x^2} = -C\frac{\partial^2 I(x,t)}{\partial t \partial x} \tag{2.24}$$

Substituting (2.23) into (2.24) the telegrapher equation for voltage is obtained.

$$\frac{\partial^2 V(x,t)}{\partial x^2} = LC\frac{\partial^2 V(x,t)}{\partial t^2} \tag{2.25}$$

In the same manner, the current equation is derived.

$$\frac{\partial^2 I(x,t)}{\partial x^2} = LC\frac{\partial^2 I(x,t)}{\partial t^2} \tag{2.26}$$

(2.25) and (2.26) represent (2.16) and (2.17) in a rewritten form. The voltage corresponds to the electric field and the current corresponds to the magnetic field. Now, let us solve the voltage equation. The other equations are solved in a similar way. At the start of the process we are going to make a guess and write solution as

$$V(x,t) = V_0 f(x - vt) \tag{2.27}$$

where V_0 is the amplitude of the wave and $f(x - vt)$ is a yet unidentified function which describes the behavior of the wave during the time t along the propagation axis x. The first time derivative of this function is

$$\frac{\partial}{\partial t} f(x - vt) = -(vf'). \tag{2.28}$$

The second time derivative and second space derivative are written as

$$\frac{\partial^2}{\partial t^2} f(x - vt) = v^2 f'' \tag{2.29}$$

$$\frac{\partial^2}{\partial x^2} f(x - vt) = f''. \tag{2.30}$$

Substituting (2.28), (2.29) and (2.30) into (2.25) we can write

$$V_0 f'' = LCV_0 v^2 f'' \tag{2.31}$$

which is true only as long as

$$v = \pm \frac{1}{\sqrt{LC}}. \tag{2.32}$$

So, it is defined for which value of parameter v this solution is valid, but still, the function $f(x-vt)$ remains unknown. Let us leave this aside at the moment and observe this function at two time instants t_1 and t_2 and two positions along the axis x. At the position x_1 and time instant t_1, the voltage will have a value of $V_1 = V_0 f(x_1 - vt_1)$. The position x_2 is reached after the time Δt. Since a lossless propagation is observed, the value of the voltage $V_2 = V_0 f(x_2 - vt_2)$ is equal to the voltage in the initial point $V_2 = V_1$. This means that the arguments are the same

$$x_1 - vt_1 = x_2 - vt_2. \tag{2.33}$$

From (2.33) we find that v represents the speed of propagating waves by solving (2.33) for v

$$\frac{x_2 - x_1}{t_2 - t_1} = \frac{\Delta x}{\Delta t} = v = \frac{1}{\sqrt{LC}}. \tag{2.34}$$

Since the solution for the telegrapher's equations is valid for two opposite values of the speed according to (2.32), two waves propagating in opposite direction exists and are given by

$$V_{pos} = V^+ f\left(x - \frac{1}{\sqrt{LC}}t\right). \tag{2.35}$$

$$V_{neg} = V^- f\left(x + \frac{1}{\sqrt{LC}}t\right). \tag{2.36}$$

2.2 Surge propagation

The surge characteristics is mainly determined by the characteristic or the surge impedance of the transmission line or cable,

$$Z_0 = \sqrt{\frac{L}{C}}. \tag{2.37}$$

Due to the differences in the geometry of the cables and the transmission lines, the capacitance and the inductance of the cable and the transmission line differ a lot. The value of the characteristic impedance for transmission lines is about Z_0=400 Ω. For the cables this value is about ten times smaller and has the value of about Z_0=40 Ω.

The differences in geometries lead to a difference in the wave velocities that the wave propagates with through the transmission line and through the cable.

$$v_0 = \frac{1}{\sqrt{LC}} \tag{2.38}$$

The other important characteristic of the cable is that the velocity of the wave that propagates through the cable is approximately one half to two thirds of the propagation velocity of the wave that propagates through the transmission line and varies from $v_0 = 1.5 \times 10^8\ km/s$ to $v_0 = 2 \times 10^8\ km/s$.

The surge that appears in the cable systems is strongly influenced by these characteristics. If the system consisting of a cable and a transformer is studied, a good approximation of the system for the prediction of high frequency transients needs to have stray capacitances added to the the transformer. An example of such a system is presented in Fig. 2.3

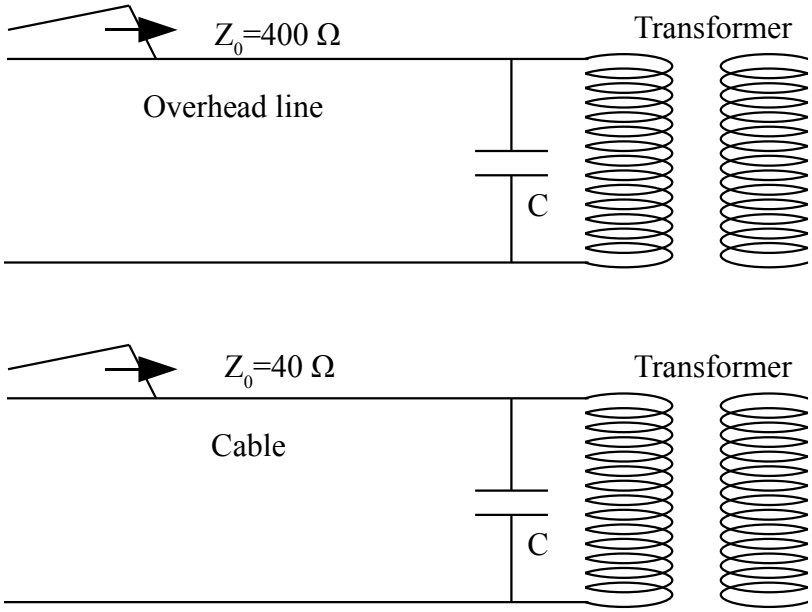

Figure 2.3: Simple system consisting of one cable and one transformer.

This system can be represented as a first order system neglecting the inductance of the transformer which is very large, meaning that its time constant is a couple of orders of magnitude slower than the time constant of the cable and the stray capacitance.

The time constant of the approximated first order system can be determined as

$$\tau = \sqrt{\frac{L}{C}} C_{stray} = Z_0 C_{stray}. \tag{2.39}$$

Taking into account the fact that the surge impedance of the cable Z_0 is ten times smaller than the surge impedance of an OH line, leads to the consequence that the time constant of the cable is also ten times quicker. This means that the surge created in the system will have ten times steeper front in systems with cables.

Chapter 3

Modeling in PSCAD/EMTDC

3.1 Vacuum circuit breaker

Vacuum and SF6(sulfur-hexafluoride) are the most modern breaking techniques used in the circuit breakers for medium and high voltage applications. The first appearance of the vacuum and SF6 circuit breakers was in the 1960's followed by fast development during the 1970's. The vacuum interrupters are primarily targeted for the medium voltages while the SF6 interrupters are produced both for medium and high voltage [3].

The vacuum circuit breakers (VCB) have a long list of advantages over other breaking techniques such as:

1. it is completely self-contained, does not need any supply of gases or liquids, and emits no flame or smoke,
2. does not need maintenance, and in most applications its life time will be as long as the life-time of the other breakers,
3. it may be used in any orientation,
4. it is not flammable,
5. it has very high interrupting ability and does not need low ohmic resistors or capacitors to interrupt short-circuit currents,
6. it requires small mechanical energy for operation,
7. it is silent in operation.

These advantages of the vacuum breaking technique have been the main driving force of the VCB development. One of the early main disadvantages of the VCB was it's price. However, already in 1970's the price was in the VCB favor comparing the price of the conventional and the VCB [18].

Nowadays, with the environmental issues getting more in focus, the vacuum breaking technique brings another advantage. Studies show that the VCBs offer the lowest environmental impact of all medium voltage switching technologies over the entire product life cycle. The materials used in the VCBs are safe to handle during periodic out-of-service maintenance and at end-of-life disposal. It's main competitor in the medium voltage level, the SF6 technology is an extremely potent greenhouse gas. In addition, SF6 arc by-products are harmful and possess significant health concerns for handling and disposal. Environmental concerns have led to an increase of the total cost of ownership (TCO) of the SF6 breakers increasing its cost for purchasing, usage and disposal [19].

Constant development of the vacuum technology, vacuum processing, contact materials and evolution of the VCB design led to a significant decrease in size of the VCB over past years [20].

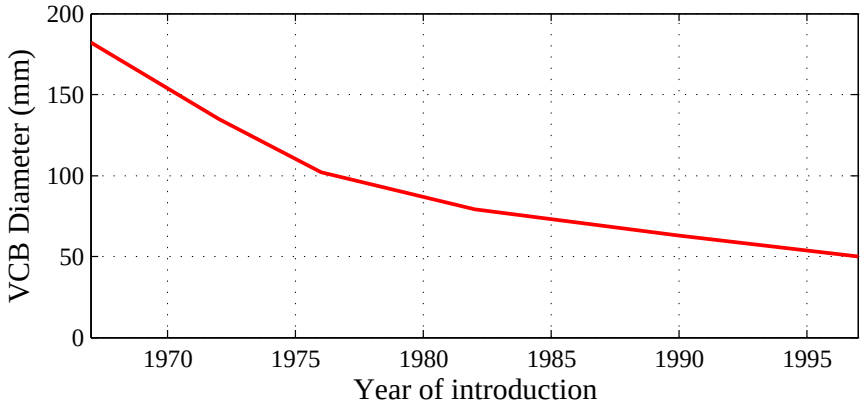

Figure 3.1: Size reduction of the 15(kV) 12(kA) vacuum interrupter 1967-1997.

The vacuum breaking technique provides a very high interrupting ability and other favorable features that made it the number one choice for the medium voltage level switching apparatus. With the respect to the transient analysis in the system where the VCBs are used, it is of a substantial importance to understand the phenomenon of the arc breaking in the vacuum. In this thesis, only the phenomenon that can be "seen" from the outer system is going to be described, treating the VCB as a "black box". However, the phenomenon that leads to such a behavior of a VCB will be described in detail since the VCB itself is not in the main focus of this research. The main phenomenon in VCBs discussed in this thesis are:

- the current chopping,
- high-frequency current quenching,
- restrikes and the voltage escalation,
- prestrikes.

3.1.1 Vacuum breaker modeling

In this work, a simplified deterministic VCB model that neglects the stochastic behavior of the arc interruption is modeled. When it comes to identifying the case which generates the

most severe overvoltages, the stochastic nature of the VCB model may not be as suitable as the deterministic model since a number of simulations with the same parameters are required to be conducted in order to identify if such a case is potentially dangerous. The deterministic model lacks the ability to provide the accuracy of the stochastic model for the risk assessment of the transient overvoltage generation in a specific grid setup. However, it may still provide a descent tool for a rough risk assessment since the arcing time (AT) or arcing angle (AA) as a stochastic parameter, natively present in both models, is the most important for appearance of voltage restrikes and voltage escalation. Other parameters and phenomenon such as the rate of rise of the dielectric strength (RRDS), the current chopping and the high frequency current quenching capability are very important and have a significant role in shaping the envelope of transient overvoltages. For that reason, modeling of these phenomena and accurate calculation of its parameters is conducted in such a way so the transient overvoltage behavior in simulations matches the measurements.

Current chopping

To explain the process during the opening of the contacts more detailed, some parameters of the VCB have to be introduced first. The transient voltage that appears over the VCB during an interruption is called the transient recovery voltage (TRV). The TRV is of high importance for the dielectric breakdown. The TRV is superimposed to the steady-state power frequency voltage. Its peak value is related to the chopping current which is a parameter to the VCB's first reignition. The dielectric recovery of the VCB is another parameter of the VCB. This parameter depends on the velocity of the contact separation. When the contacts of the VCB are opening and the TRV starts to rise due to the current chopping, the TRV and the dielectric withstand of the VCB start to chase with each other. If the TRV reaches the value of the dielectric withstand of the gap between the contacts, the arc will be established again and the VCB will conduct the current. This underlines the importance of how fast the VCB recovers its dielectric withstand. The time interval between the time instant of the contact opening and the power frequency current zero is called the arcing time (AT) or the arcing angle (AA) and is of substantial importance for the transient behavior of the VCB. When the arcing time is short, the dielectric withstand of the VCB is still very small when the current reaches the zero crossing. This means that the TRV will reach the dielectric withstand of the VCB very quickly after the initial current interruption, and the VCB will start leading current again.

The current chopping is a phenomenon that can lead to severe overvoltages and occurs when small inductive and capacitive currents are switched. These overvoltages are produced in the case when the current is interrupted before the power frequency current reaches zero. When conducting a small current, the arc in the vacuum is very unstable. This means that the arc will disappear before the current reaches its zero value. This has been considered as the major disadvantage of the vacuum breaking technique over the other breaking techniques. The current value when this happens is called the chopping current and the point when this happens is called the chopping level.

Fig. 3.2 presents parameters of the vacuum breaker. The current declines with a very high di/dt when it is chopped. This means that a very high di/dt will produce very high overvoltage over an inductive load. The value of the di/dt and the overvoltage itself is in direct proportion to the chopping current. During the very high load current (high RMS)

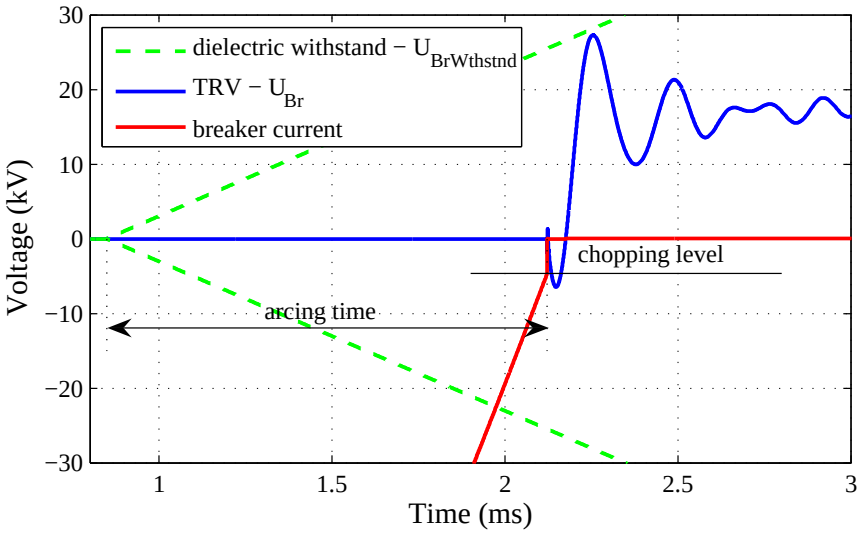

Figure 3.2: TRV, dielectric withstand, arcing time.

this phenomenon does not exist. The reason for this is that due to the high current, the arc is not unstable any longer. The chopping level depends mainly on the choice of the contact materials and there has been a lot of researchers effort dedicated to reduce the chopping level by using proper materials for the contacts in VCB [21]. The chopping current is lower if the contacts open close to zero current [22]. The current chopping level is dependent on the load type and the surge impedance of the load that is switched.

In order to obtain a mathematical description of the chopping current phenomenon, two different approaches can be taken. One of them is proposed by Reininghaus U. [23],

$$i_{ch} = a - b\hat{I} - clogZ_N \tag{3.1}$$

where a, b and c are constants depending on the type of the material used for the contacts in the VCB and Z_N is the surge impedance of the circuit that is switched and $\hat{I}$ is the magnitude of the load current that is switched.

The other method for current chopping level calculation is proposed by Smeets [24]. This method uses the formula

$$i_{ch} = (2\pi f \hat{I} \alpha \beta)^q \tag{3.2}$$

where f is the grid frequency, $\hat{I}$ is the magnitude of the load current that is switched and α, β and q are the constants dependent on the contact materials. These constants which are available for the commercially available vacuum switchgear [25]:

$$\alpha = 6.2 \times 10^{-16}(s), \quad \beta = 14.2,$$

$$q = -0.07512, \qquad q = (1-\beta)^{-1}.$$

The current chopping level given by (3.2) varies between $3A$ and $8A$. However, if the current at the power frequency is lower than the chopping level, the current is chopped

immediately. Both approaches give the mean value of the chopping current which varies with the higher standard deviation compared to the breakers utilizing other breaking techniques.

Breaker dielectric withstand

The dielectric withstand of the breaker is a very important parameter for the analysis of switching transients. During the operation of the breaker, when pre-strikes and re-strikes occur, it is of the highest importance to properly model the dielectric withstand capability of the breaker. During the initial separation of contacts, the dielectric withstand starts increasing from an initial dielectric withstand with value varying from $0.69kV$ to $3.4kV$ [26] depending on the breaker. In most of the published literature, the RRDS of the breaker is constant [25] but it may be represented with the first order polynomial that shows a constant increase of RRDS. However, the voltage plots obtained during the measurements show that the speed of the contacts in the breaker increases during the operation and cannot thus be modeled using a straight line with the slope that represents the speed of the contact separation.

To model the dielectric withstand characteristics of the breaker, a simplified mechanical model of the breaker is analyzed. A representation of this system is shown in Fig. 3.3.

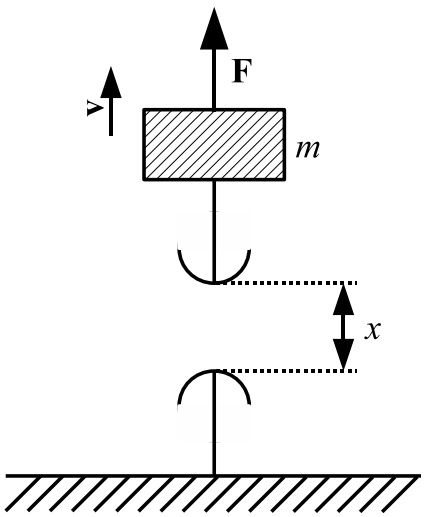

Figure 3.3: Representation of the breakers mechanical system.

For this analysis, the force that separate the breaker contacts is assumed to be constant. This gives that the breaker contacts are constantly accelerated yielding that the speed of the contact separation is linearly increasing and not remaining constant as stated in the literature. This gives that the speed of the constant separation $\mathbf{v}$ and the distance between contacts $\mathbf{x}$ are

$$\begin{aligned} \mathbf{v} &= \mathbf{v}_0 + at = \mathbf{v}_0 + \frac{\mathbf{F}}{m}t \\ x &= vt = v_0 t + \frac{F}{m}t^2. \end{aligned} \tag{3.3}$$

Since the initial speed of the breaker contacts is equal to zero, the final expression for the distance between contacts is

$$x = \frac{F}{m}t^2. \tag{3.4}$$

By assuming that the dielectric withstand between the contacts is proportional to the distance (this is true for small distances), we can write

$$V_{br} = Cx + V_0 = C\frac{F}{m}t^2 + V_0. \tag{3.5}$$

Since the constants C, F and m are unknown and it is difficult to obtain them, this analysis is used just to describe the behavior of the dielectric withstand of the breaker during the breaker operation. To obtain the accurate dielectric withstand curve of the breaker, the dielectric withstand is analyzed during the opening and the closing of the breaker. The opening of the breaker is presented in Fig. 3.4.

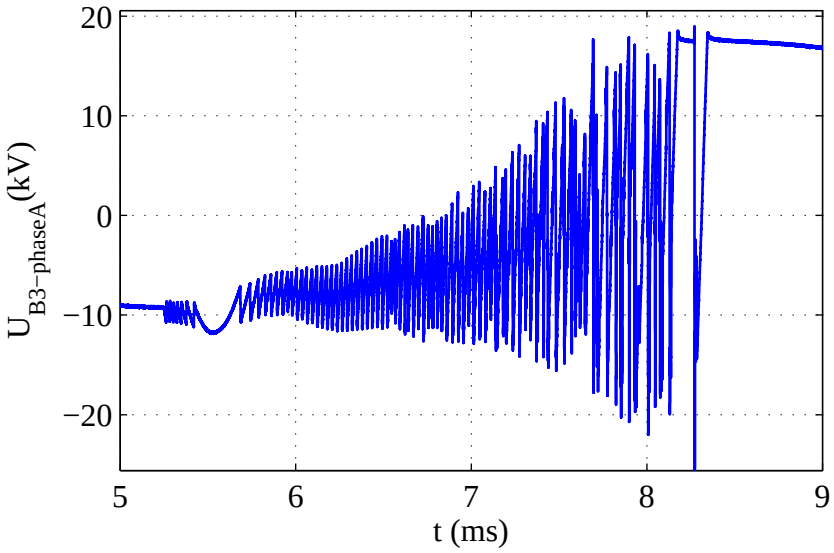

Figure 3.4: Voltage at breaker during opening - inductive load.

In Fig. 3.4 it can be noted that the dielectric withstand of the breaker is not linear, and for that reason, it is going to be approximated using the second order polynomial. In order to define the dielectric withstand curve by the second order polynomial

$$V_{br} = at^2 + bt + c, \tag{3.6}$$

parameters a, b and c have to be calculated. In order to do that, the rate of rise of the dielectric withstand is calculated from the plot obtained by measurements in the beginning of the opening operation and approximately $2ms$ after. The value of the c parameter is equal to the dielectric withstand in the very beginning of the opening operation.

This is shown in Figs. 3.5 and 3.6.

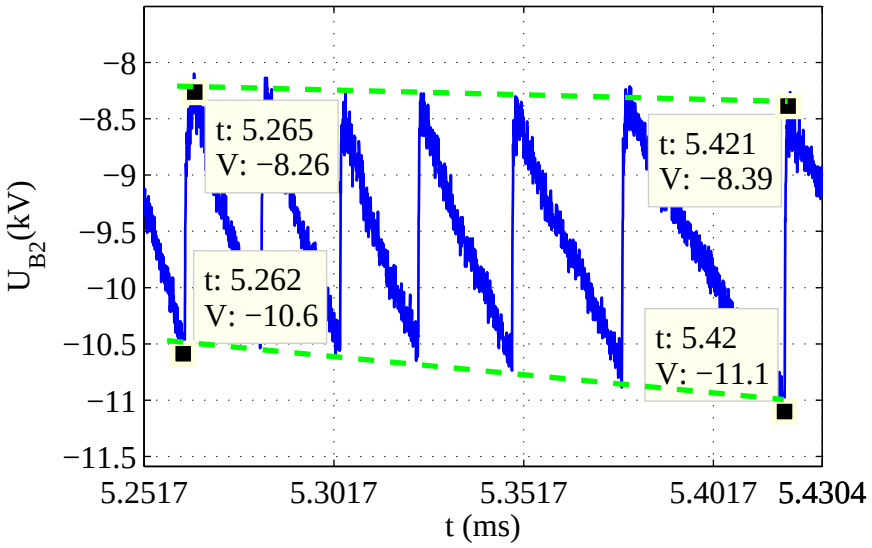

Figure 3.5: Calculation of c parameter and rate of rise of V_{br} at beginning of opening.

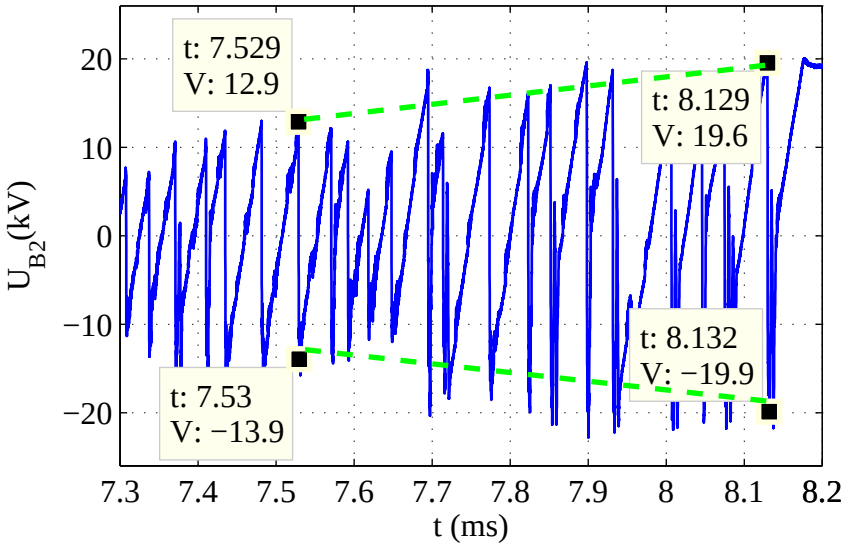

Figure 3.6: Rate of rise of V_{br} $2.2ms$ after beginning of opening.

In the breaker model, the stochastic nature of the breaker is neglected and the calculated dielectric withstand of the breaker represents its mean value. Whenever the voltage over the breaker is equal or greater than the dielectric withstand, the breakdown occurs and the breaker conducts the current. Using the measurement data obtained at the breaker opening event, the mean value of the breaker dielectric withstand is

$$V_{br} = 5.25 \cdot 10^9 t^2 + 4.15 \cdot 10^6 t + 1200. \tag{3.7}$$

During the closing operation, the breaker contacts reach very high speed, and the acceleration of the contacts cannot be observed. To model the dielectric withstand curve of the breaker during the closing operation, it is more convenient to use the constant speed ap-

proach. In Fig. 3.7 it can be observed that the speed of contacts is very high and therefore it can be considered as linear.

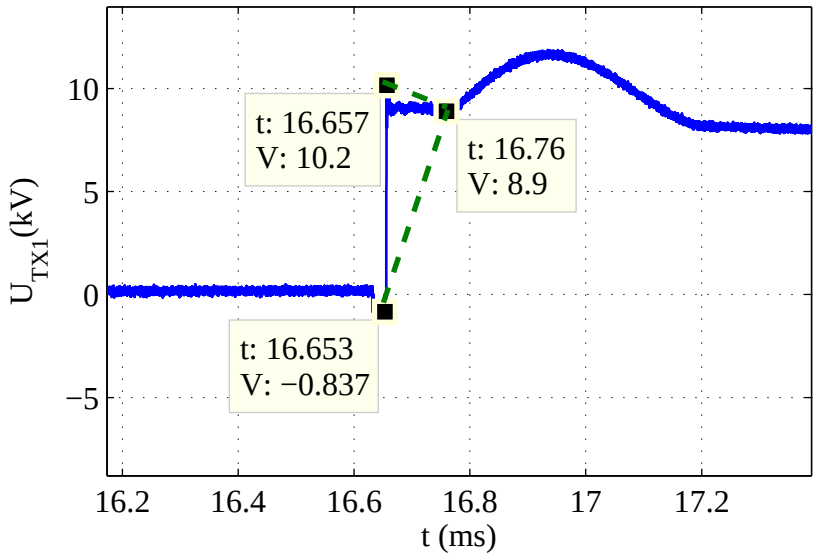

Figure 3.7: Breaker dielectric withstand at closing.

At the time instant of $t = 16.653ms$ a pre-strike occurs. When this happens, the cable is charged and the current is interrupted immediately after. For that reason, the voltage remains constant until the time instant of $t = 16.76ms$ when the contacts are finally closed. The closing speed of the contacts vary between $45kV/ms$ and $65kV/ms$, and in this case, a speed of $50kV/ms$ is recorded.

Interruption of the high frequency current

The frequency of the HF current is mainly determined by the stray parameters of the VCB and it does not change during the conducting state of the VCB. For this breaker, stray capacitance is $0.2nF$, stray inductance is $50nH$ and stray resistance is 50Ω. These stray elements connected in series are added in parallel to the switch that represents an ideal vacuum interrupter. The HF current that appears during the switching is superimposed to the power frequency current. The HF current is damped quite quickly. The VCB is not capable of breaking HF currents at the zero crossing if the di/dt value of the HF current is too high. However, as the magnitude of the HF current declines, the value of di/dt decreases too. After a certain number of current zero crossings the value of the di/dt is small enough so the VCB can break the current. That critical value of di/dt represents the quenching capability of the HF current. One of the methods for determination of the quenching capability of a VCB is given by M. Glinkowski [26]. This method proposes a linear equation for definition of the quenching capability

$$\overline{di/dt} = C_C(t - t_0) + D_D. \tag{3.8}$$

This equation gives the mean value of the quenching capability which has a normal distribution with the same standard deviation as the dielectric withstand. In this work,

only the mean value of the HF current quenching capability is taken into account since the developed model is deterministic. In Table 3.1 the values of the constants used in (3.8) are given [26].

Table 3.1: HF current quenching capability constants

DW type	$C_C(\mathrm{A}/\mu\mathrm{s}^2)$	$D_D(\mathrm{A}/\mu\mathrm{s})$
High	-0.034	255
Medium	0.31	155
Low	1	190

Some other authors suggest that the HF current quenching capability characteristics $\overline{di/dt}$ is constant [27]. The suggested values of the critical current derivative vary between 100 $A/\mu s$ and 600 $A/\mu s$. This assumption significantly simplify the calculation of the derivative of the high frequency current di/dt at which the breaker is not capable to interrupt the high frequency current when crossing the zero value.

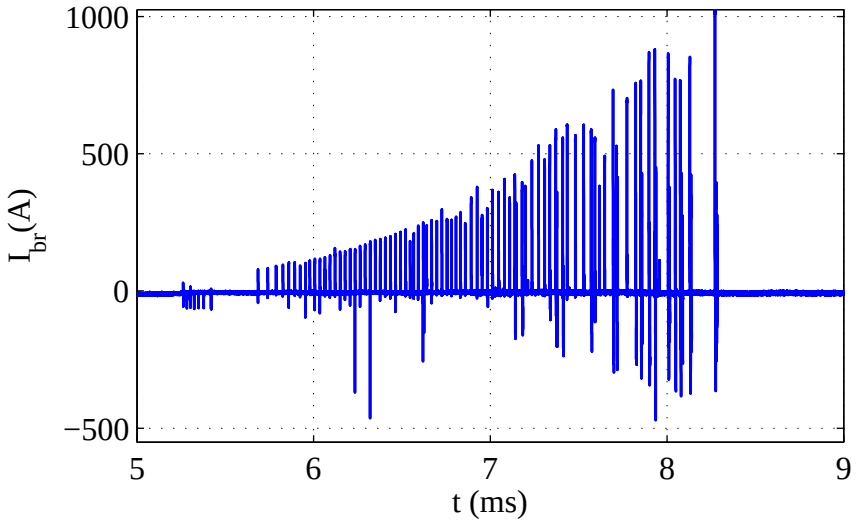

Figure 3.8: Current through breaker at opening.

Fig. 3.8 shows the current through the breaker during voltage restrikes. It can be observed that while the peak of the high frequency current and its derivative, which is directly proportional to it, are low, the breaker is capable of breaking the high frequency current almost at every zero crossing. This justifies the use of the simplified model for the HF current quenching capability proposed in [27].

To obtain the value of di/dt at which the breaker is not able to interrupt the high frequency current at the zero crossing, the current graph presented in Fig. 3.8 is zoomed to show show the current plot in details.

The current at the time interval between $7.85ms$ and $7.866ms$ is presented in Fig. 3.9. In this figure it can be observed that the breaker did not manage to interrupt the high frequency current with $di/dt = 350A/\mu s$. The high frequency current is interrupted only when the value of di/dt is equal or lower to $250A/\mu s$. For the model of this breaker, the value of di/dt parameter of $350A/\mu s$ is chosen as the critical value.

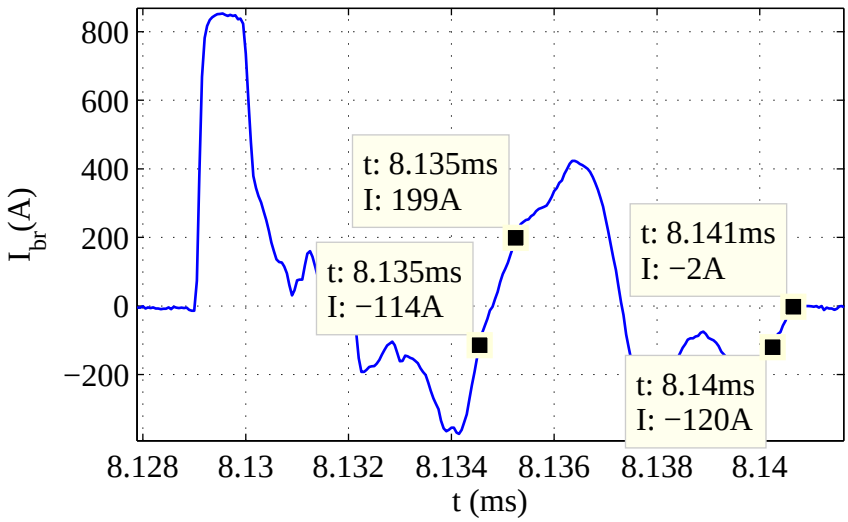

Figure 3.9: Interruption of high frequency current at zero crossing.

3.1.2 Model verification

Model verification is performed for both opening and closing operations of the breaker, in order to identify all the parameters of the breaker. In order to model and verify the dielectric withstand of the breaker, an inductive load is used in order to provoke voltage restrikes.

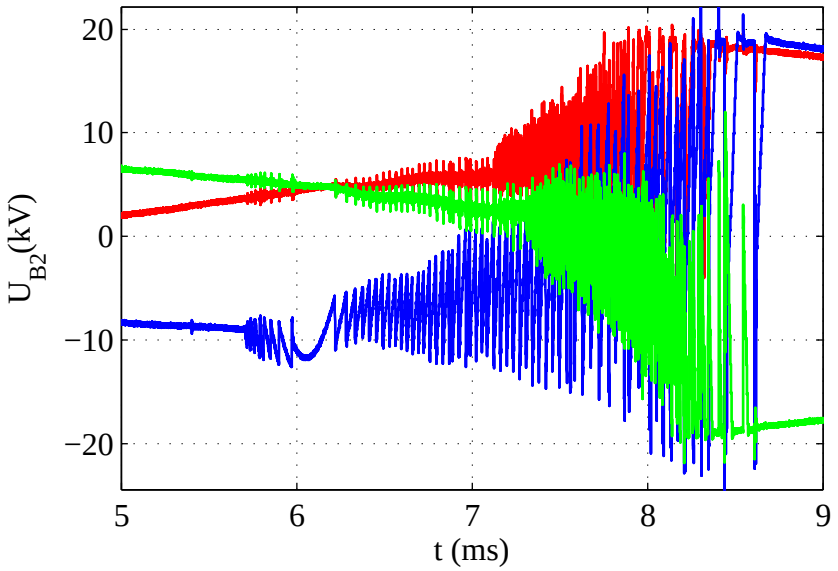

Figure 3.10: Transient voltage at TX1 during opening - inductive load - measurement.

Fig. 6.14 presents voltages recorded at the transformer TX1 during voltage restrikes. The measurement from phase A, plotted by the blue line, is used to define the parameters for the dielectric withstand of the breaker. During this measurement, the phase A pole of the breaker opened approximately $1.5ms$ before the other two poles.

Fig. 6.15 presents voltages obtained during simulation at the transformer TX1 during

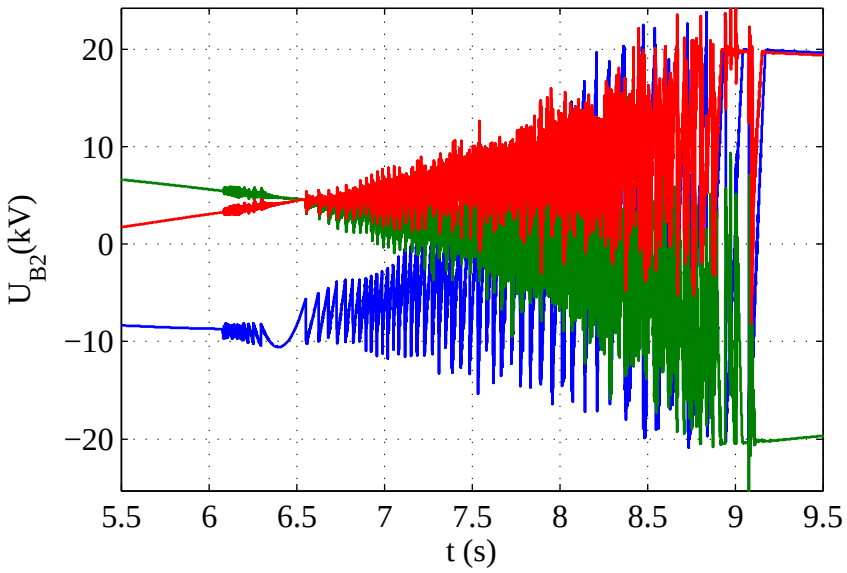

Figure 3.11: Transient voltage at TX1 during opening - inductive load - simulation.

voltage restrikes, where the developed breaker model is used. One can note a good matching between the dielectric withstands of the breaker for the phase A, plotted using the blue line. This is the phase where the voltage restrikes started. The voltage restrikes observed in other two phases are initiated by the capacitive coupling between the phases. Since the capacitive coupling between the phases seems to be much stronger in the simulation, the other two phases show higher voltages compared to the measurements. The reason for a stronger capacitive coupling in simulations is mainly due to a simplified transformer model, where stray capacitances are simply added to the standard transformer model. No additional damping is added to the model, so the high frequency oscillations are poorly damped.

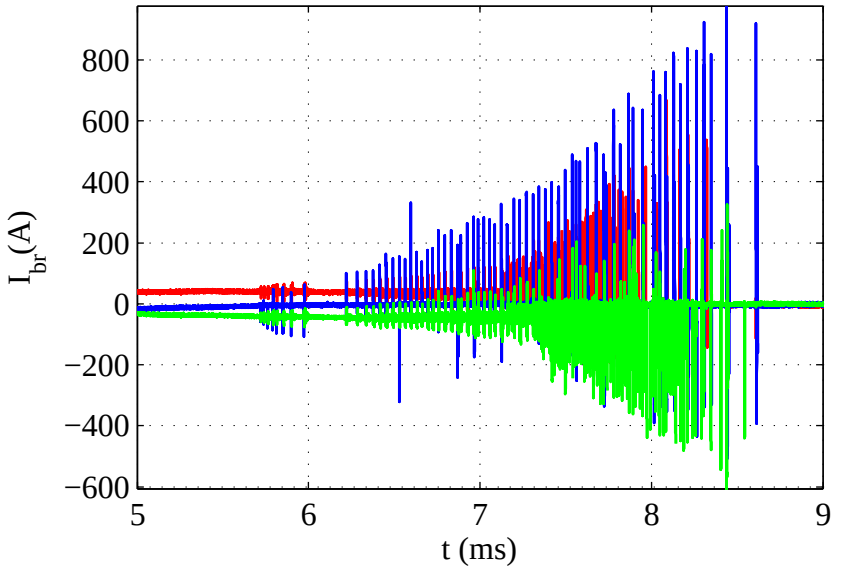

Figure 3.12: Current through breaker during opening - inductive load - measurement.

Fig. 3.12 presents currents through breaker recorded during voltage restrikes. The measurement from phase A, plotted by the blue line, is used to define the parameters for the

quenching capability of the HF current.

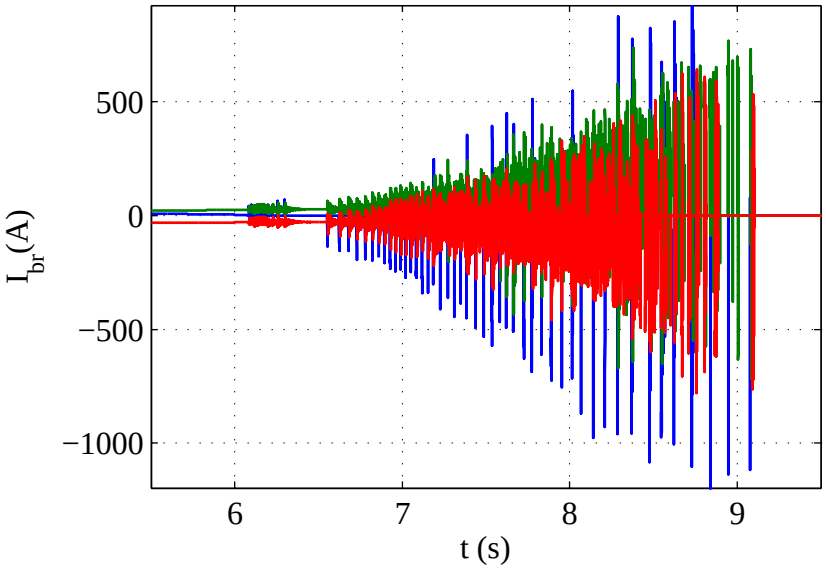

Figure 3.13: Current through breaker during opening - inductive load - simulation.

Fig. 3.13 shows the breaker current obtained during the simulation for the same switching scenario. A somewhat higher currents are recorded comparing to the measurements. This is due to circuit parameters and not due to the breaker model. The magnitude of the HF current depends on the voltage magnitude at the voltage breakdown and the circuit parameters. From the statistical point of view, the breaker model interrupts the HF current at the zero crossing if the di/dt of the HF current is below $350A/\mu s$. This is in accordance with the measurements.

3.2 Modeling of underground cables

The reflection phenomenon at the cable ends occurs when the rise time of the transient is shorter than the wave traveling time across the cable. The velocity of the wave that travels across the cable is given by (2.38). For transmission lines, the velocity of the propagating wave is the same as the speed of light in vacuum, which is $300m/\mu s$. Due to different electric and magnetic properties of cables, the wave propagation velocity in cables is lower, reaching $200m/\mu s$.

When the transformer is connected to the cable, then the rise time of the voltage surge is given by (2.39). The stray capacitance of the transformers with oil impregnated paper insulation is in order of nF [28] and that of the dry-type transformers is approximately ten times smaller [29]. Therefore, the rise time of the voltage surge is less than $100ns$ given that the surge impedance of the cable is in the order of a couple of tens of Ohms. This means that even very short cables with a length of tens of meters is long enough to establish observable wave propagation and reflection phenomenon. For that reason, the lumped cable model should be avoided and will not be treated in this thesis. Instead the focus is on the distributed parameter cable models, that allow for such a phenomenon to be studied.

To obtain a detailed model of the cable suitable for time domain simulations and studies of the high frequency phenomena, a distributed parameter model is to be developed. To develop equations using this theory, an infinitely small piece of a single conductor line buried into the ground presented in Fig. 3.14 is observed.

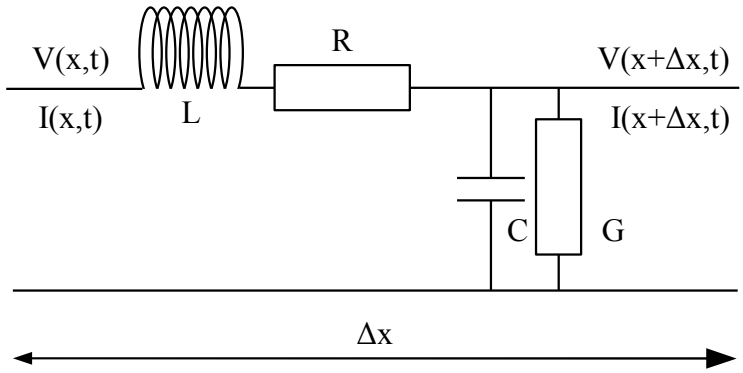

Figure 3.14: An infinitely small element of cable.

The time domain equations of a single conductor-line presented in Fig. 3.14 can be expressed as follows,

$$-\frac{\partial v(x,t)}{\partial x} = Ri(x,t) + L\frac{\partial i(x,t)}{\partial t} \tag{3.9}$$

$$-\frac{\partial i(x,t)}{\partial x} = Gv(x,t) + C\frac{\partial v(x,t)}{\partial t}, \tag{3.10}$$

where $v(x,t)$ is the voltage of the line, $i(x,t)$ is the current of the line, while G, C, R and L are lumped parameters of the line that represent conductance, capacitance, resistance and inductance expressed in per-unit length. In a real cable, all these parameters are not constant, but frequency dependent. This means that the solution for these equations, even for the high frequency transients is performed in the frequency domain [30]. The set of frequency domain equations written for the same conductor can be written as

$$-\frac{d\mathbf{V}_x(\omega)}{dx} = \mathbf{Z}(\omega)\mathbf{I}_x(\omega) \tag{3.11}$$

$$-\frac{d\mathbf{I}_x(\omega)}{dx} = \mathbf{Y}(\omega)\mathbf{V}_x(\omega) \tag{3.12}$$

where $Z(\omega)$ and $Y(\omega)$ are the series impedance and the shunt admittance matrices of the cable per-unit length respectively. Analytical expressions and finite element method calculations can be used to determine the frequency dependent admittance and impedance matrix.

In order to solve system of equations given by (3.11) and (3.12), at first (3.12) is differentiated with respect to x and substituted into (3.11). A solution can now be found for the current, while a solution for the voltage vector needs some further deductions.

$$\frac{d^2\mathbf{I}_x(\omega)}{dx^2} = \mathbf{Y}(\omega)\mathbf{Z}(\omega)\mathbf{I}_x(\omega). \tag{3.13}$$

The solution for (3.13) is given in the form of a sum of two traveling current waves propagating in forward and backward direction

$$\mathbf{I}_x = e^{-\mathbf{\Gamma}x}\mathbf{I}_f + e^{\mathbf{\Gamma}x}\mathbf{I}_b, \tag{3.14}$$

where $\mathbf{I}_f$ and $\mathbf{I}_b$ are the forward and backward traveling waves of current and $\mathbf{\Gamma}$ is equal to $\mathbf{YZ}$. The voltage vector can be found from (3.12) and (3.14) as follows

$$\mathbf{V}_x = -\mathbf{Y}^{-1}\frac{d\mathbf{I}_x}{dx} = \mathbf{Y}^{-1}\sqrt{\mathbf{YZ}}(e^{-\mathbf{\Gamma}x}\mathbf{I}_f - e^{\mathbf{\Gamma}x}\mathbf{I}_b) = \mathbf{Y}_c^{-1}(e^{-\mathbf{\Gamma}x}\mathbf{I}_f - e^{\mathbf{\Gamma}x}\mathbf{I}_b), \tag{3.15}$$

where $\mathbf{Y}_c$ is the characteristic admittance matrix which is given by (3.16).

$$\mathbf{Y}_c = \sqrt{(\mathbf{YZ})^{-1}}\mathbf{Y} \tag{3.16}$$

In the next step, (3.15) is multiplied with $\mathbf{Y}_c$ and added to (3.14) which yields

$$\mathbf{Y}_c\mathbf{V}_x + \mathbf{I}_x = 2e^{-\mathbf{\Gamma}x}\mathbf{I}_f. \tag{3.17}$$

Applying boundary conditions for (3.17) at both ends of the cable, where for node 1, the cable length $x = 0$ and for node 2, the cable length $x = l$, (3.18) and (3.19) are obtained respectively.

$$\mathbf{Y}_c\mathbf{V}_1 + \mathbf{I}_1 = 2\mathbf{I}_f \tag{3.18}$$

$$\mathbf{Y}_c\mathbf{V}_2 + \mathbf{I}_2 = 2e^{-\mathbf{\Gamma}l}\mathbf{I}_f = 2\mathbf{H}\mathbf{I}_f \tag{3.19}$$

The matrix $\mathbf{H}$ is the wave propagation matrix. Substituting (3.18) into (3.19), the expression for the current in node 2 is obtained.

$$\mathbf{Y}_c\mathbf{V}_2 + \mathbf{I}_2 = \mathbf{H}(\mathbf{Y}_c\mathbf{V}_1 + \mathbf{I}_1) \tag{3.20}$$

In (3.20) the direction of current $\mathbf{I}_2$ is from the node like the direction of current $\mathbf{I}_1$ which is according to Fig. 3.14. When the direction of current $\mathbf{I}_2$ is into the node , (3.20) can be rewritten as

$$\mathbf{I}_2 = \mathbf{Y}_c\mathbf{V}_2 - \mathbf{H}(\mathbf{Y}_c\mathbf{V}_1 + \mathbf{I}_1). \tag{3.21}$$

In a similar way, the equation for current $\mathbf{I}_1$ can be obtained.

$$\mathbf{I}_1 = \mathbf{Y}_c\mathbf{V}_1 - \mathbf{H}(\mathbf{Y}_c\mathbf{V}_2 + \mathbf{I}_2) \tag{3.22}$$

(3.21) and (3.22) represent n coupled scalar equations but can be decoupled using modal decomposition. The modal decomposition matrices for the voltage and current vectors are obtained by

$$\mathbf{T}_I^{-1}\mathbf{YZT}_I = \lambda, \tag{3.23}$$

where $\mathbf{T}_I$ is the current transformation matrix and λ is the diagonal eigenvalue matrix. According to the eigenvalue theory [31], the voltage and current vectors and matrices of $\mathbf{Y}_c$ and $\mathbf{H}$ can be transformed using the following equation

$$\begin{aligned} \mathbf{I} &= \mathbf{T}_I\mathbf{I}^m \\ \mathbf{V} &= \mathbf{T}_v\mathbf{V}^m \\ \mathbf{Y}_c &= \mathbf{T}_I\mathbf{Y}_c^m\mathbf{T}_I^T \\ \mathbf{H} &= \mathbf{T}_I\mathbf{H}^m\mathbf{T}_I^{-1}, \end{aligned} \tag{3.24}$$

where $\mathbf{I}^m$, $\mathbf{V}^m$, $\mathbf{Y}_c^m$ and $\mathbf{H}^m$ are the modal voltage vector, current vector, characteristic admittance matrix and wave propagation matrix. It should be noted that

$$\mathbf{T}_V = \mathbf{T}_I^{-T}, \tag{3.25}$$

where $\mathbf{T}_I^{-T}$ is the transpose of $\mathbf{T}_I^{-1}$. Now (3.21) and (3.22) can be rewritten in the form of n decoupled equations after modal decomposition.

$$\mathbf{I}_1^m = \mathbf{Y}_c^m\mathbf{V}_1^m - \mathbf{H}^m(\mathbf{Y}_c^m\mathbf{V}_2^m + \mathbf{I}_2^m) \tag{3.26}$$

$$\mathbf{I}_2^m = \mathbf{Y}_c^m\mathbf{V}_2^m - \mathbf{H}^m(\mathbf{Y}_c^m\mathbf{V}_1^m + \mathbf{I}_1^m) \tag{3.27}$$

In earlier studies [32], the frequency independent modal decomposition is performed. However, when the frequency dependent modal decomposition is performed, the model decomposition matrices have to be calculated for each frequency. This model does not require as much computations as a full frequency dependent modal domain models but has a good accuracy both in the steady-state and transient conditions [33]. When transformed to the time-domain, (3.26) and (3.27) become

$$i_1(t) = y_c(t) * v_1(t) + h(t) * (y_c(t) * v_2(t) + i_2(t)) \tag{3.28}$$

$$i_2(t) = y_c(t) * v_2(t) + h(t) * (y_c(t) * v_1(t) + i_1(t)), \tag{3.29}$$

where symbol '$*$' denotes matrix-vector convolutions. When functions of $\mathbf{Y}_c$ and $\mathbf{H}$ are fitted with rational functions [33], then the time-domain functions can be obtained using recursive convolutions [34]. When the recursive convolutions are used, the expression for nodal currents at both cable ends can be written using a history current term, node voltage and equivalent admittance.

$$i_1(t) = y_{eq}(t)v_1(t) + i_{hist-1}(t) \tag{3.30}$$

$$i_2(t) = y_{eq}(t)v_2(t) + i_{hist-2}(t) \tag{3.31}$$

This can be presented in the circuit with an ideal current source and an equivalent admittance which is shown in Fig. 3.15.

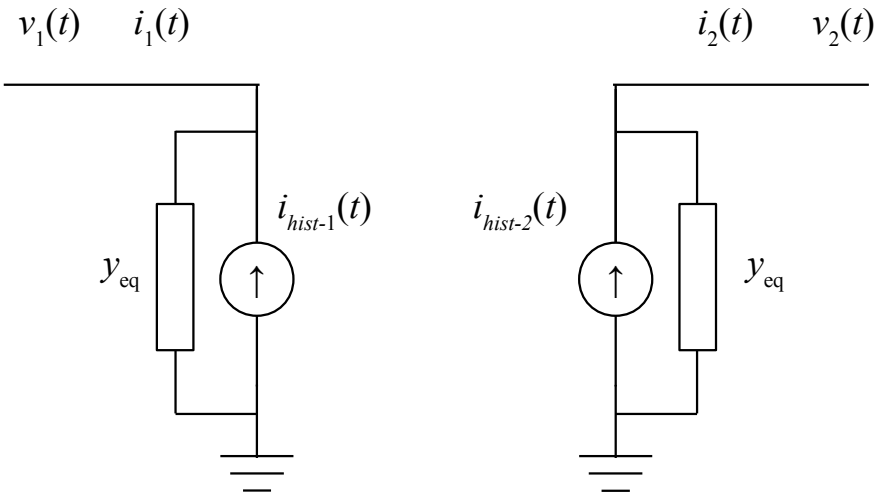

Figure 3.15: Network interface of the cable model.

3.2.1 Cable modeling in PSCAD/EMTDC

Cable and transmission line models

The cable models and the transmission line models in PSCAD/EMTDC are distributed parameter models where the parameters of the cable are frequency dependent. However, the main differences between the three available models are if the model includes lossless or lossy representation of the line equations and if the transformation matrices for the modal-decomposition are constant or frequency dependent and latter fitted in the phase domain using rational functions and later integrated using recursive convolutions.

The Bergeron cable model is the least accurate cable model for the high frequency transient analysis. This model is a lossless model, but still the cable reflections can be studied since the mathematical description uses the same approach as given in Section 3.2. It should be noted that the $\mathbf{Y}_c$ matrix for a lossless line contains only real numbers and is presented with $\mathbf{G}_c$ matrix. That is why the network interface of the model uses ideal current sources representing the history current and equivalent conductance.

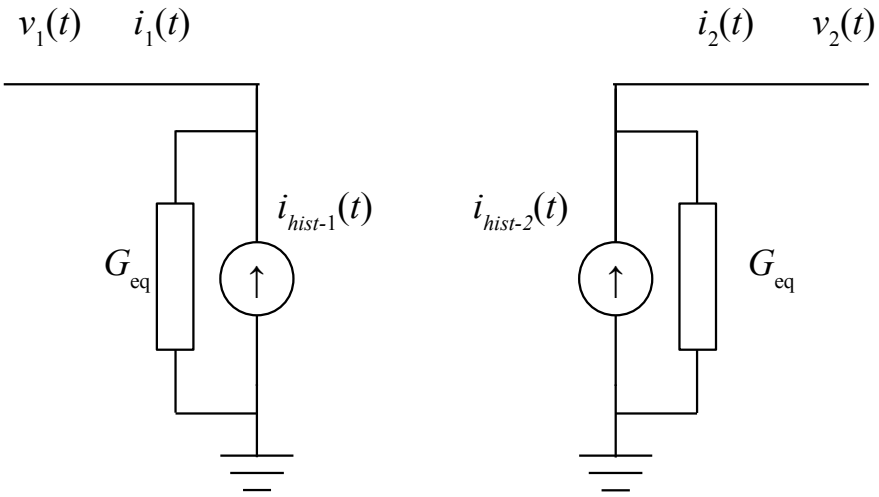

Figure 3.16: Network interface of Bergeron model.

The accuracy of the Bergeron model for transient time-domain simulations is not satisfactory for a wide band of frequencies. It is accurate only for the power frequency [35]. Observing Fig. 3.17 it is easy to note the difference between the frequency dependent cable model and the Bergeron model when the cable model is used for high frequency transient studies.

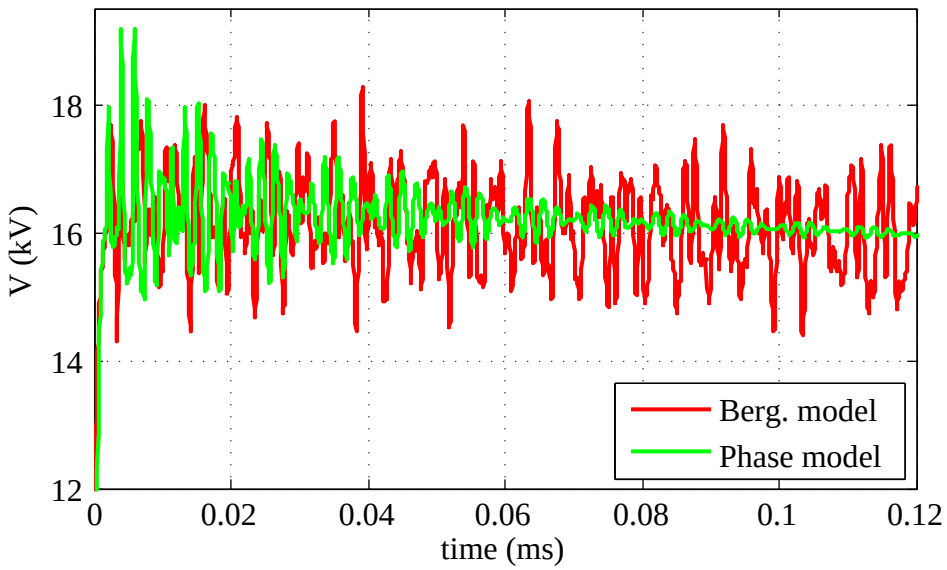

Figure 3.17: Voltage surge measured at cable end.

It can be noted that the damping of the Bergeron model is very weak since the cable is treated as lossless.

For better accuracy, PSCAD/EMTDC offers two different lossy cable models for transient analysis. The first is called the Frequency Dependent (Mode) model, representing a model with constant modal decomposition matrices [32]. The more advanced Frequency dependent(Phase) model use rational approximation of $\mathbf{Y}_c^m$ and $\mathbf{H}^m$ matrices as explained in Section 3.2 allowing recursive convolution calculations. This method is based on a novel rational function fitting technique called the vector fitting (VFT) [36]. Accuracy and computation efficiency is improved compared to the frequency dependent(mode) model [37] providing very accurate time-domain simulations for the high frequency transients and for the steady-state operation.

Cable geometry definition in PSCAD/EMTDC

PSCAD/EMTDC provides an interface for the definition of physical properties of cables and transmission lines. For the transmission lines, the user can define different types and sizes of towers. A detailed information about the number of sub-conductors in a bundle is to be defined for certain types of towers. Definition of multi-pipe cables is provided where user can specify the position and dimension of each cable. A configuration of the three phase cable is shown in Fig. 3.18

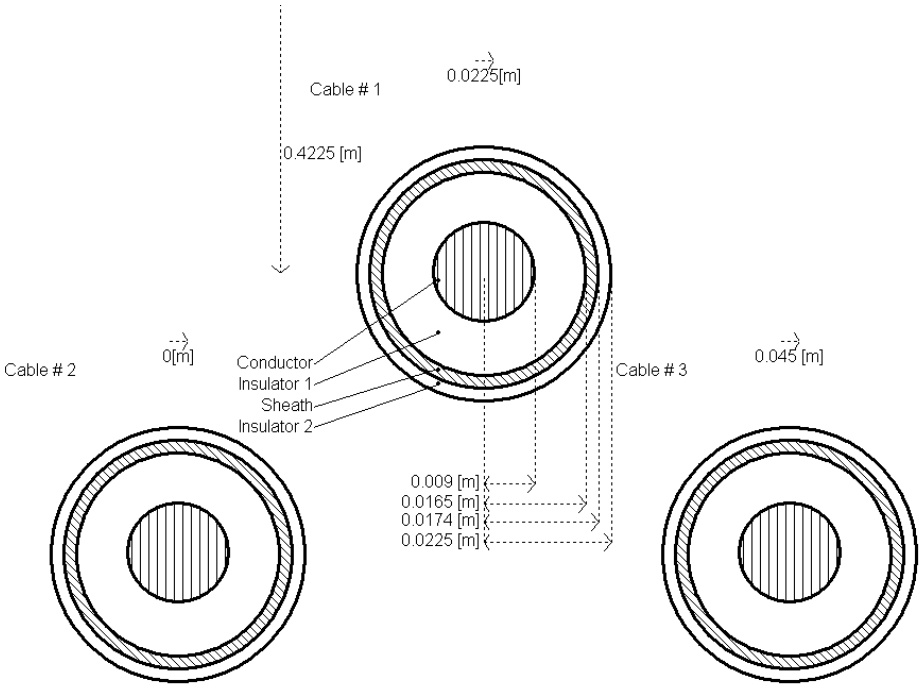

Figure 3.18: Geometry definition of three phase cable in PSCAD/EMTDC.

Although a multi-pipe geometry can be entered in the PSCAD/EMTDC interface, the PSCAD/EMTDC model treats the multi-pipe model as a model with separated three single phase cables. The capacitances of the multi-pipe cable are calculated only for one phase and mutual capacitances between cables are neglected. The capacitances between conductors in one cable are calculated using the formula that neglects semiconductor layers assuming constant relative permittivity over the insulator in between. This gives

$$C = \frac{2\pi\varepsilon_r\varepsilon_0}{\ln\left(\frac{D}{d}\right)}, \tag{3.32}$$

where, ε_r and ε_0 are relative permittivity and the permittivity of the vacuum respectively and D and d are diameters of the outer and inner conductor.

To take the capacitive coupling between phases into account in a multi-pipe cable as well as the influence of the semi-conducting layers, a cable model is developed in a FEM software. For this purpose, the COMSOL software is used which enables the definition of the cable material parameters more in detail than it is possible in PSCAD/EMTDC.

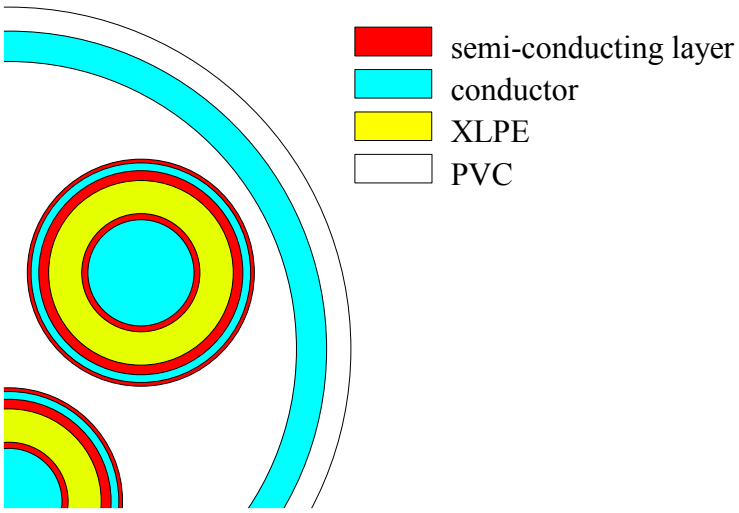

Figure 3.19: Detailed cable model.

As can be observed in Fig. 3.19, a more complex model is designed compared to the PSCAD/EMTDC model. For the COMSOL model, the relative permittivity of the insulating and semi-conducting layers is set to the constant value of $\varepsilon_{XLPE} = 2.3$ and $\varepsilon_{semi\_cond} = 12.1$ respectively. The conductivity of the semi-conducting layers is set to $\sigma_{semi\_cond} = 1.6e-3\,S/m$ while the conductivity of the XLPE insulation is negligible. To study the conductor-shield capacitance, an analytical expression that neglects the conductance of the insulating layers and the COMSOL calculated capacitance are compared. To obtain the capacitances between the conductors in the cable, the in-plane electric and induction currents and potentials model is used. The boundary settings of the conducting layers are set to *port* with input property *forced voltage*. The model is solved using a parametric solver where the frequency is set to vary between $50Hz$ and $10MHz$. In this application mode, the admittance matrix $\mathbf{Y}$of the cable is obtained. The capacitance matrix $\mathbf{C}$ of the cable is calculated by

$$\mathbf{C} = \frac{imag\{\mathbf{Y}\}}{2\pi f} \tag{3.33}$$

where f is the frequency. When there are multiple insulating layers with different relative permittivity placed between the conductor and the shield cylindrical conducting layers as it is the case in the XLPE cable, an analytical expression for the capacitance between the conductor and the shield C_{CS} is given by

$$C_{CS} = \frac{2\pi\varepsilon_0}{\frac{\ln\left(\frac{r_2 r_4}{r_1 r_3}\right)}{\varepsilon_{semi\_cond}} + \frac{\ln\left(\frac{r_3}{r_2}\right)}{\varepsilon_{XLPE}}} \tag{3.34}$$

where r_1 and r_4 are the outer radius of the conductor and inner radius of the shield respectively, r_2 and r_3 are the outer radius and the inner radius of the of the semi-conducting layer respectively. The calculation of the conductor-shield capacitance using the analytical expression and COMSOL is presented in Fig. 3.20.

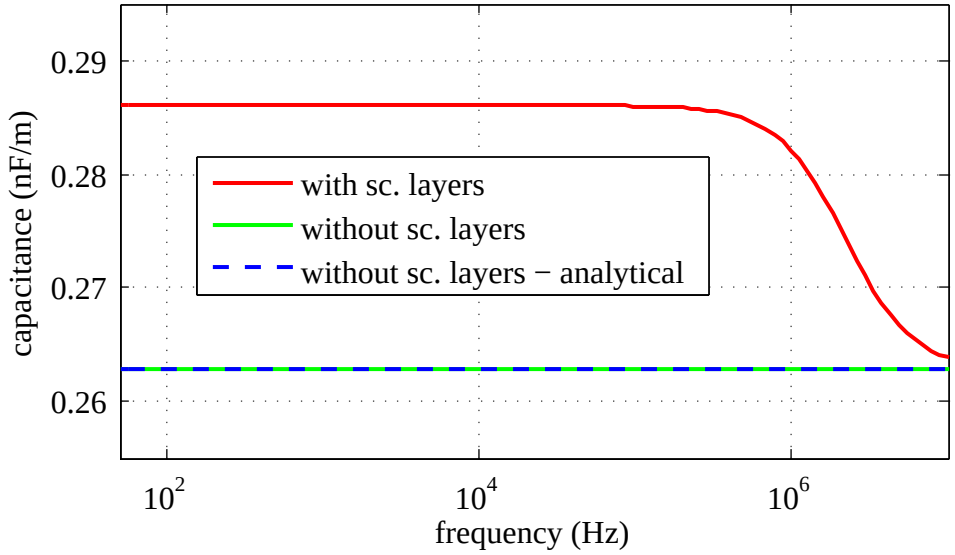

Figure 3.20: Capacitance comparison.

It can be noted in Fig. 3.20 that there is a significant influence of the semi-conducting layers on the cable capacitance. Due to different time constants (ε_r/σ) of different insulation levels, the capacitance is varying with frequency and will approach the capacitance of the simplified cable model only at frequencies higher than $10MHz$. The difference between the capacitances for models with and without semi-conducting layers for a frequency range from $50 - 10^6 Hz$ is 8.8%. This is a quite significant margin and will influence even the steady state values for $50Hz$ signals. This means that the capacitance should be adjusted in such a way so it takes the influence of the different (ε_r/σ) properties of the semi-conducting layers and the XLPE insulation into account.

Since the cable model interface in PSCAD/EMTDC allows the definition of insulators and conductors only, the semi-conducting layers and the XLPE layer between the conductor and the shield are replaced by a single insulator. These layers with different electric properties are to be represented by only one layer with the ε_{res} and σ_{res} values that will match the capacitance of the full cable model

$$C_{CS} = \frac{2\pi\varepsilon_0}{\frac{\ln\left(\frac{r_2 r_4}{r_1 r_3}\right)}{\varepsilon_{semi\_cond}} + \frac{\ln\left(\frac{r_3}{r_2}\right)}{\varepsilon_{XLPE}}} k_{cap} = \frac{2\pi\varepsilon_{res}\varepsilon_0}{\ln\left(\frac{r_4}{r_1}\right)} \tag{3.35}$$

where ε_{res} is the resulting permittivity of the insulation layer in PSCAD/EMTDC and

k_{cap} is the coefficient that takes into account different (ε_r/σ) properties of the semi-conducting layers and the XLPE insulation and in the case of this cable its value is $k_{cap} = 8.8\%$. Now the value of ε_{res} can be calculated using the following expression.

$$\varepsilon_{res} = k_{cap} \frac{\ln\left(\frac{r_4}{r_1}\right)}{\frac{\ln\left(\frac{r_2 r_4}{r_1 r_3}\right)}{\varepsilon_{semi\_cond}} + \frac{\ln\left(\frac{r_3}{r_2}\right)}{\varepsilon_{XLPE}}} \tag{3.36}$$

3.3 Transformer modeling

The transformer model suitable for the transient analysis differs significantly from the model used for power system analysis. As it could be seen in the previous figures, in cases where the VCB is switching, very high frequency transients are generated and an adequate transformer model is needed for accurate time-domain simulations. An ideal transformer model would include the non-linearities of the core magnetization and frequency dependent parameters for good response at a wide range of frequencies. However, obtaining such a model is very difficult and usually the transformer model is designed depending on the frequency of the signal applied to the transformer terminals and depending on the analyzed phenomena.

When it comes to the transformer modeling, in general, two different modeling approaches can be used to design the model for the transient studies. If the impact of the transients on the transformer itself is the subject of the study, then a detailed modeling is the preferred choice. In that case, the construction details such as the winding type, electrical properties of the insulating materials and dimensions of the transformer elements are taken into account [38]-[42]. In such studies, inter-turn and inter-coil voltages can be studied since each turn or coil can be represented using an equivalent circuit [38]-[41]. This approach is introduced in 1950 [38] and many authors found it to give accurate results [38].

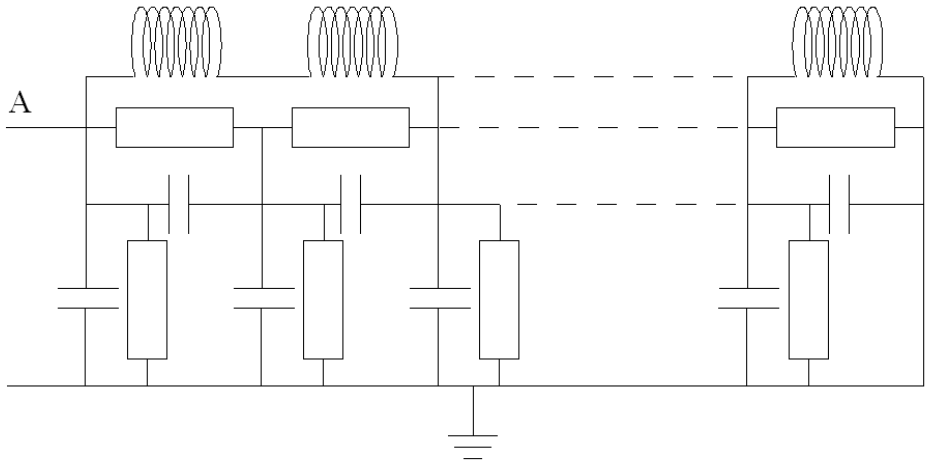

Figure 3.21: Equivalent network of one phase of the transformer.

The advantage of these models is that they are very accurate for a wide band of frequencies. One important disadvantage is that this model is linear and does not consider the non-linearities of the core when the transformer is saturating. However, when the fast

transients are studied, the transformer can be considered linear if one of the windings is loaded [43]. If the transformer is unloaded it is considered linear only for the transients with frequencies higher than $100kHz$ [43]. The most important problem for those who want to develop such a model is that the internal structure of the power transformer is not available even to the transformer owner. If needed, even the owner of the transformer can not develop detailed transformer model for transient analysis unless the transformer is opened and it's structure analyzed.

Another, more practical method is to design a black-box model of the transformer. The first developed black-box transformer models were based on modal analysis [44] previously used in mechanics to describe the dynamic behavior of elastic structures [44]. To develop a black-box model, measurements are carried out to determine the admittance matrix. Numerous scientific articles are written on this topic [44]-[48]. Once the admittance matrix is measured for the wide band of frequencies, the admittance or impedance vector between each terminal is fitted with a rational form given in the frequency domain as

$$Y(s) = Z(s)^{-1} = \frac{a_0 s^m + a_1 s^{m-1} + \ldots + a_{m-1} s + a_m}{b_0 s^n + b_1 s^{n-1} + \ldots + b_{n-1} s + b_n}. \tag{3.37}$$

The function presented in (3.37) can be presented as a sum of partial functions as shown in (3.38), and the vector fitting method for the complex curve may be used [36], [47] to obtain parameters r_m,a_m,d and e.

$$Y(s) = \sum_{m=1}^{N} \frac{r_m}{s - a_m} + d + se \tag{3.38}$$

For a three phase transformer, there are 36 admittance vectors and each one of them has to be fitted. However, the problem can be simplified since it has been shown that the admittance vectors have a common set of poles [49].

For the time-domain simulations it is necessary either to develop the equivalent network [44], [46], [50] or to use recursive convolutions [34]. The method of recursive convolutions is used to obtain the time-domain simulations for the frequency dependent cable models.

For the transients with the frequencies reaching up to $3kHz$, the core nonlinearities are important and for the proper transient studies they have to be implemented in the transformer model [51]. This is the case even when the transient frequency reaches $20kHz$ if the transient energizing and the load rejection with high voltage increase are studied [51].

The PSCAD/EMTDC software includes different transformer models that include the model of the core nonlinearities. The transformer models are based on scheme presented in Fig. 3.22.

The parameters of the transformer L_1, L_2, R_1, R_1 and R_m are kept constant. Core nonlinearities are modeled so the parameter of the mutual inductance L_m is modeled according to the saturation curve defined in the properties of the model. PSCAD/EMTDC offers two different transformer models when it comes to the saturation modeling. The first model does not take into account the magnetic coupling between different phases, so from the magnetic aspect, the three phase transformer is treated as three single phase transformers [35]. The

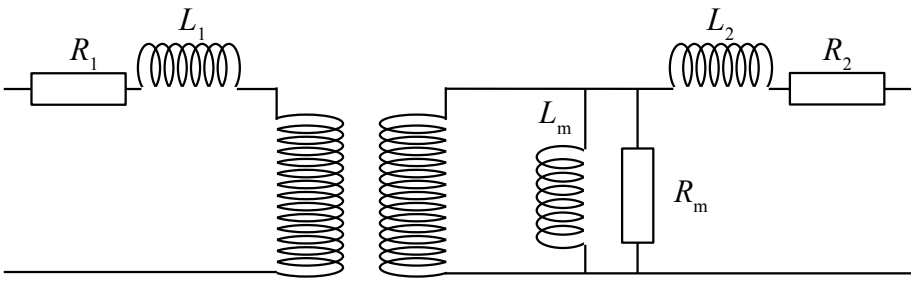

Figure 3.22: Transformer model implemented in PSCAD.

magnetic coupling between phases does not exist and if one phase is saturated, the others are not affected. In order to improve the transformer model, an effort is made for more detailed modeling of the three phase transformer saturation [52]-[53]. For the transformer model based on the Unified Magnetic Equivalent Circuit (UMEC) algorithm, phases are magnetically coupled as shown in Fig. 3.23.

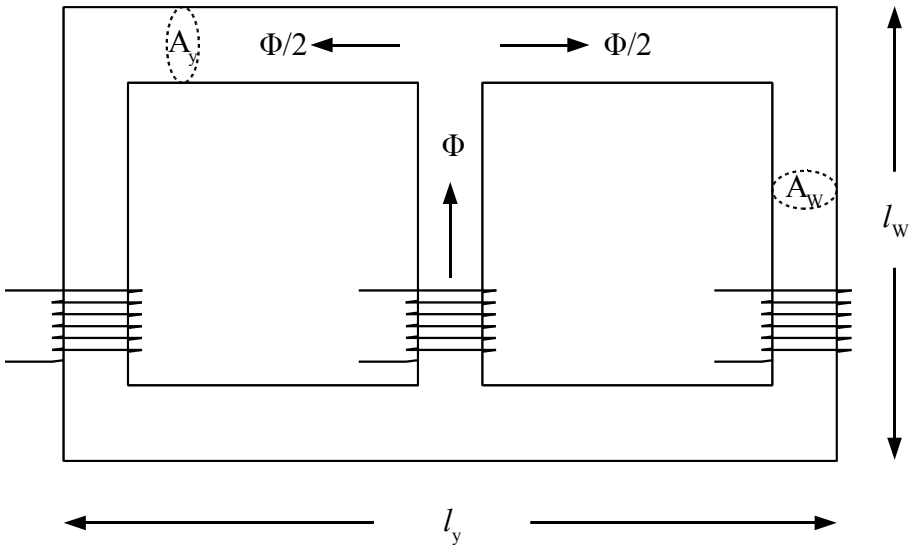

Figure 3.23: Core model used in UMEC algorithm.

However, since the resistance parameters of the transformer model which represent losses in the transformer windings, and the losses in the core are constant, the skin effect, the proximity effect and the core losses which are frequency dependent are not accounted for correctly. To analyze the impact of the skin effect on the transformer winding resistance, the COMSOL software is used. The resistance of the transformer conductor changes significantly if the frequency increases from $50Hz$ to $1kHz$. The current density figures at $50Hz$ and $1kHz$ is shown in Fig. 3.24

For the $1kHz$ signal, the current is pushed towards the surface of the conductor thus increasing the resistance of the conductor.

The resistance of the transformer windings as the function of frequency is plotted in Fig. 3.25

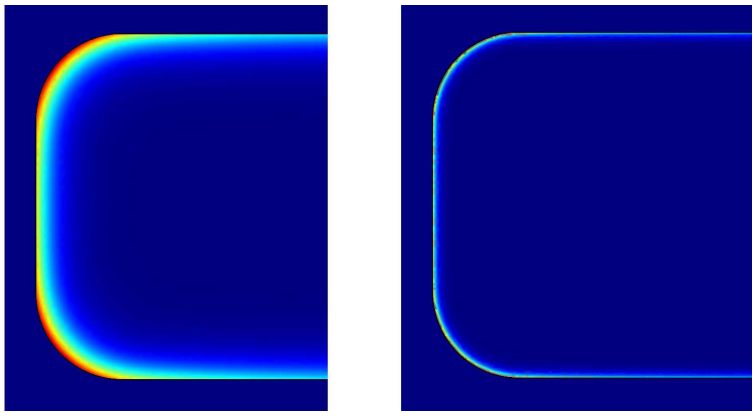

Figure 3.24: Current density in transformer conductor at $50Hz$ and $1kHz$.

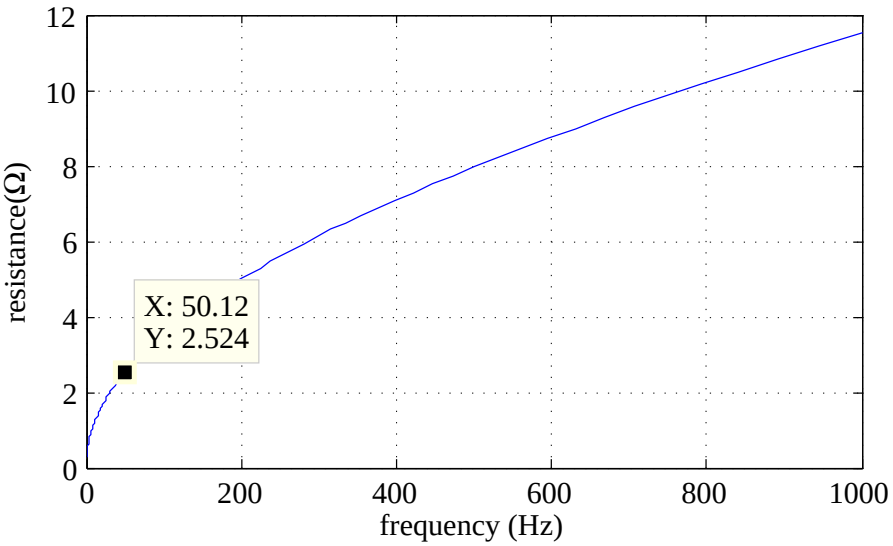

Figure 3.25: Resistance of the transformer windings as the function of frequency.

To account for the frequency dependent resistance of the transformer conductors, the standard PSCAD/EMTDC model is extended using the Foster equivalent circuit. The parameters of the Foster circuit are calculated using the vector fitting algorithm [36]. In order to account properly for the skin effect in the transformer windings, the leakage reactance and the frequency dependent resistance of the windings are fitted using the vector fitting algorithm [36],[50] and added to the existing UMEC model. The winding resistance and the leakage reactance of the model in PSCAD/EMTDC is adjusted accordingly, giving that at the $50Hz$ frequency, the Foster equivalent network connected in series with the UMEC transformer model will give a correct value of the leakage reactance and the winding resistance.

In the upper part of Fig. 3.26, an equivalent Foster circuit with parameters fitted to match the transformer impedance up to $1kHz$ is presented. When the Foster equivalent circuit is added to the PSCAD/EMTD transformer model based on the UMEC algorithm, than R_0 and L_0 are added to the leakage reactance and the winding resistance parameters which are entered directly into the model parameters. The equivalent network consisting of the Foster equivalent network and the UMEC transformer model is shown in the lower part of Fig. 3.26

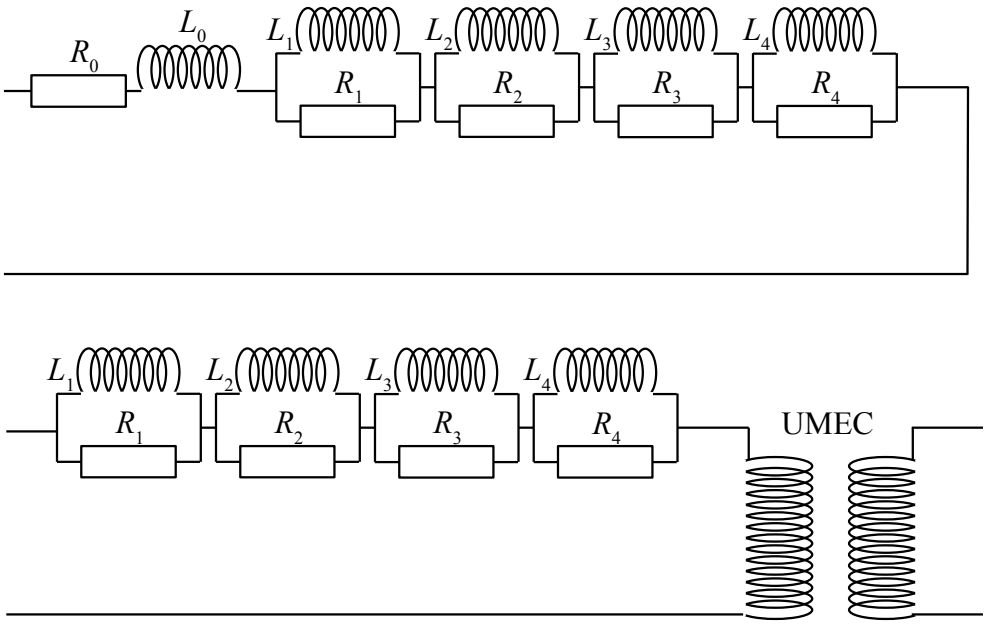

Figure 3.26: Transformer model that takes into account skin effect in transformer windings.

3.3.1 Transformer modelling for high frequency transient analysis

When the analysis of the high frequency transients is required, a suitable transformer model is needed to give a proper response to the high frequency transients generated mainly during the operation of the switching apparatus. The model described in the previous section, with modeled skin effect of the windings is suitable for the low frequency transients. For the low frequency transient, the leakage reactance is the dominant component of the transformer impedance and in power system analysis, the transformer is usually represented with an ideal transformer and the transformers corresponding leakage reactance. However, when the frequency moves to the other side of the frequency spectrum approaching infinity, it has been observed on various types of rotating machines and transformers that the impedance is approaching zero [43].

$$\lim_{\omega \to \infty} \{|Z(j\omega)|\} = 0 \tag{3.39}$$

The phase angle of the transformer impedance for the low frequency disturbances as mentioned before is approximately 90° degrees or $\frac{\pi}{2}$ radians. However, when the frequency approaches infinity, the argument of the impedance approaches $-90°$ degrees or $-\frac{\pi}{2}$ radians. So, for the high frequencies, the transformer stray capacitances dominate in the transformer response.

$$\lim_{\omega \to \infty} \{Arg[Z(j\omega)]\} = -\frac{\pi}{2} \tag{3.40}$$

Therefore, a very simple but reasonably accurate model of the transformer for very high frequency transient analysis can be made using only a capacitor connected in parallel to the standard model. This approach was used in many studies [28], [54]-[57] and proved to

give satisfactory results for the high frequency transient analysis. Usually for the transient studies, only the stray capacitance of the transformer side exposed to the transient is to be added to the standard transformer model. This is good for the specific type of studies when a VCB, cable and loaded/unloaded transformer system is observed for the switching transient studies. This is the case of transients in collection grids in wind parks [54] and is used in this study. If the surges through transformers are the subject of study, then the stray capacitance between primary and secondary side and the stray capacitance between the secondary side and the ground are important [28].

For the values of the stray capacitances, the manufacturer of the transformer should be contacted. However, the value of these capacitances are within certain limits for a specific rated power of the transformer and can be taken approximately [28],[58] and [59]. For the core-form transformers, typical values of stray capacitances are given in Table 3.2 [28]. For the dry-type transformers, the value of the stray capacitances are in order of hundreds of pico Farads [29] or approximately ten times smaller compared to the core-form transformer transformers.

Table 3.2: Typical stray capacitances of HV and LV to ground and between HV and LV sides (nF)

Transformer rating (MVA)	HV-ground cap.	LV-ground cap.	HV-LV capacitance
1	1.2-14	3.1-16	1.2-17
2	1.2-16	3-16	1-18
5	1.2-14	5.5-17	1.1-20
10	4-7	8-18	4-11
25	2.8-4.2	5.2-20	2.5-18
50	4-6.8	3-24	3.4-11
75	3.5-7	2.8-13	5.5-13

3.4 Black-box modeling of reactor winding

When the internal voltage distribution and the impact of the transients on the transformer is studied, a black box model can be used if the transformer is available. If the transformer is on the design stage, a physical model is needed to find the equivalent circuit elements. The black-box modeling has been used quite a lot in studies of high frequency transients [44]-[48]. However, for internal models of the transformer or reactor windings, this method is rarely used.

In order to make a black-box model, a set of measurements needs to be performed. For transformers, it is needed to measure the admittance matrix and the voltage ratios of the transformer at the transformer terminals [47]-[48]. Essentially, a set of open circuit and short circuit tests is toe be performed in a wide frequency range. Once the model is obtained, voltage and currents at the terminals of the transformers can be simulated, while the internal voltage distribution remains unknown. If the internal voltage distribution is the subject of study, the admittance matrix of the transformer can be measured at the points of interest and not only at the transformer terminals. The highest stress during very fast transients is usually at the beginning of the winding, therefore some points close to the terminals of the transformer should be chosen.

However, in order to make measurements at selected measurement points, the insulation of the transformer needs to be removed. This makes this method very impractical for oil-insulated transformers and sealed dry-type transformers. Basically, the windings of the transformer need to be open and accessible for the measurements, making this method practically performable for research projects only. The advantage of this method is that it provides good models with very high accuracy.

3.4.1 Measurement of admittance matrix

This method is going to be presented using a winding of a reactor. As such, the ends of the winding present two outer terminals of the reactor. However, one can choose other points along the winding as additional terminals of the reactor. These terminals or points are chosen freely, but the selection of these additional terminals is going to provide us the points of interest where a high voltage stress can be expected.

The test reactor is a single phase reactor that is usually connected with one end to the ground. For this study however, this winding is considered to be connected in a line-to-line arrangement where none of the terminals is ground connected. In order to obtain an admittance matrix, all terminals of the winding except the one at which the voltage source is connected are short circuited. A sketch of the arrangement is presented in Fig. 3.27.

The measurement of the admittance matrix is performed using an Anritsu Network Analyzer MS4630B. To measure a total admittance in a terminal, the voltage and the injected current are measured at that node. By this, the diagonal elements $\mathbf{y}_{ii}$ of the admittance matrix Y are obtained. In order to obtain non diagonal elements of the matrix $\mathbf{y}_{ij}$, the voltage at the voltage source at node i and the current injected into the node j are measured.

Since this model is always going to be used in an open circuit configuration, it is essential

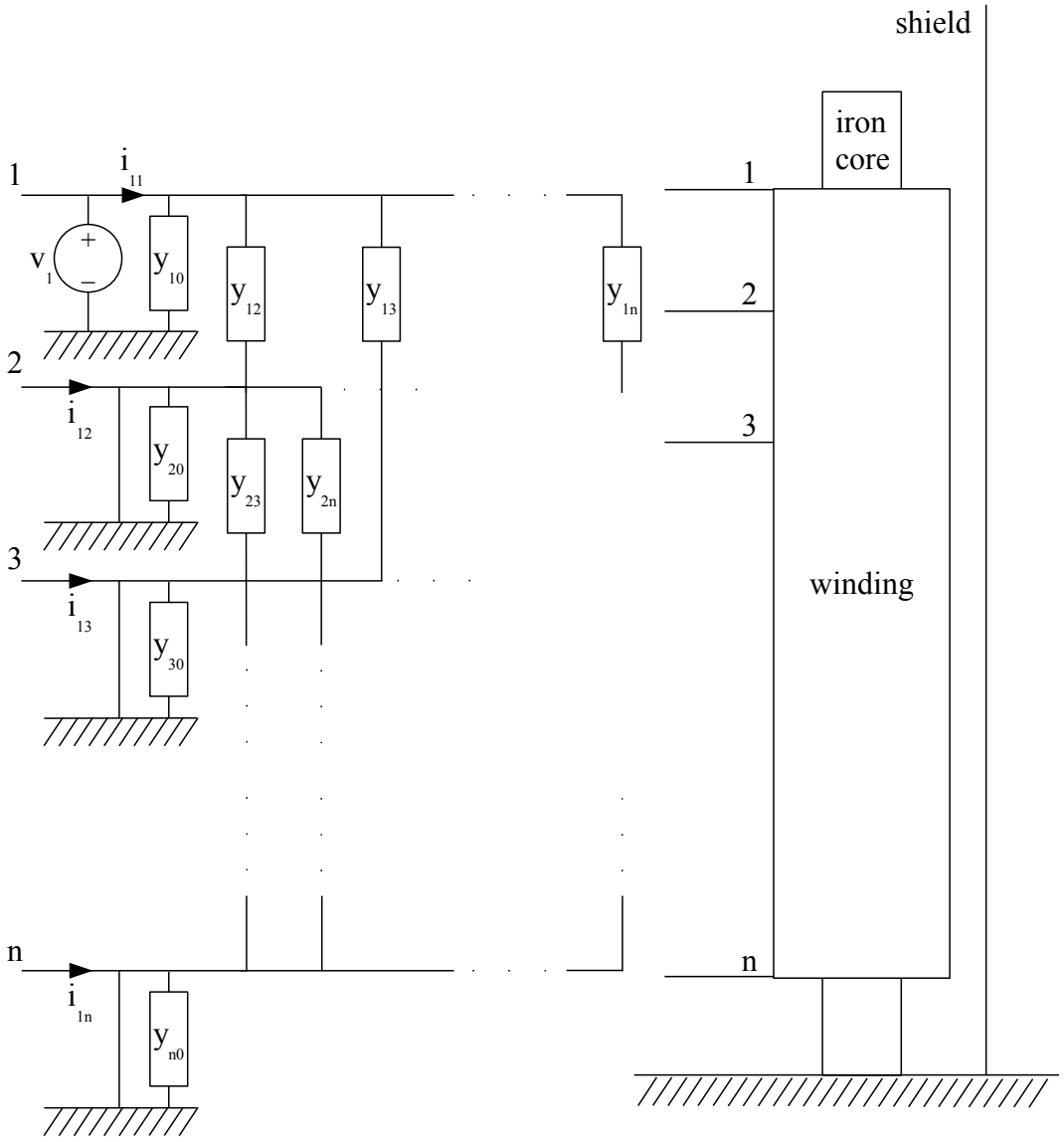

Figure 3.27: Measurement of admittance matrix.

that the model response is good for a wide range of frequencies. Since the admittance matrix is obtained using short circuit tests, the admittance matrix obtained in such a way is not good for the prediction of the response at the low frequency end [47]-[48]. Furthermore, since the admittance matrix is going to be implemented in PSCAD, it is needed to calculate the admittance to ground $\mathbf{y}_{i0}$ at each point of the transformer,

$$\mathbf{y}_{i0} = \mathbf{y}_{ii} - \sum_{j=1,n;j\neq i} \mathbf{y}_{ij}. \tag{3.41}$$

The admittance vectors $\mathbf{y}_{i0}$ obtained in such a way, have a large error at frequencies below $10kHz$ for this particular winding.

In order to improve the measurement set, the voltage ratio between selected nodes $\mathbf{V}_{ij}$ needs to be measured [47]-[48]. In the voltage ratio measurement, the measurement of the

voltage ratio vector between nodes i and j is performed while all other measurement points are connected to the ground, or $\mathbf{V}_k = 0$ where $k \neq i, j$. By this method $n(n-1)$ voltage ratio vectors $\mathbf{V}_{ij}$ are obtained. Measurement of the voltage ratio vector $\mathbf{V}_{ij}$ between nodes i and j is presented in Fig. 3.28.

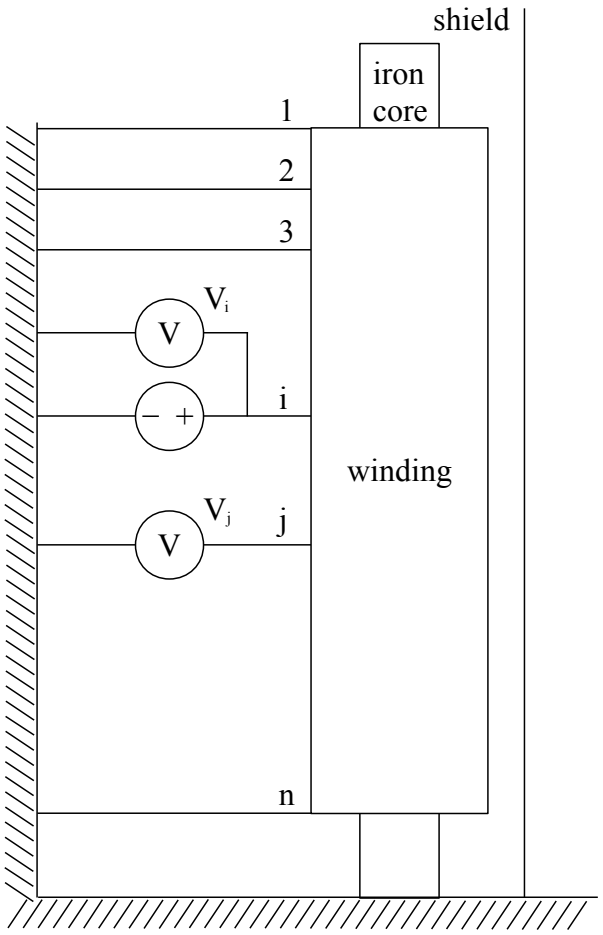

Figure 3.28: Measurement of voltage ratio vectors.

Once these vectors are obtained, the voltage ratio vectors are used to calculate $\mathbf{y}_{i0}$ admittance vectors with more accuracy at the low frequency end. These admittance vectors $\mathbf{y}_{i0}$ are calculated by voltage ratios $\mathbf{V}_{ij}$ and admittance vectors $\mathbf{y}_{ij}$, where $i \neq j$. In order to calculate admittance vectors $\mathbf{y}_{i0}$, the equation of currents injected into the node i is utilized, where $\sum_{j=0,n} I_{ij} = 0,\ (j \neq i)$. For node i this equation becomes

$$\mathbf{V}_i \mathbf{y}_{i0} - \sum_{\substack{j=1 \\ j \neq i}}^{n} (\mathbf{V}_j - \mathbf{V}_i)\mathbf{y}_{ji} = 0. \tag{3.42}$$

Since the voltage ratios are measured, and not the node voltages, (3.42) needs to be expressed using the voltage ratio vectors $\mathbf{V}_{ij}$. Note that the reference voltage at node i, $\mathbf{V}_i$, is equal to 1 and the voltages at the other nodes $\mathbf{V}_k$, where $k \neq i$, $k \neq j$ are equal to 0.

$$\mathbf{V}_i = \mathbf{V}_{ii} = 1 \Rightarrow \mathbf{V}_j = \mathbf{V}_{ij} \Rightarrow \mathbf{V}_k = \mathbf{V}_{ik} = 0 \tag{3.43}$$

In this case, the most simple solution for (3.42) is when the node at which we are calculating $\mathbf{y}_{i0}$ is the voltage reference mode. Then, the solution for (3.42) is given by

$$\mathbf{y}_{i0} = -\sum_{\substack{k=1 \\ k\neq i; k\neq j}}^{n} \mathbf{y}_{ki} + (\mathbf{V}_{ij} - 1)\mathbf{y}_{ji}. \tag{3.44}$$

However, this simple solution does not have any physical meaning and yields completely wrong result. The reason for this is that the voltage at node i at which the admittance vector $\mathbf{y}_{i0}$ is calculated is kept constant because at that node the voltage source is applied. Thus, the voltage vector at the node i, $\mathbf{V}_i$, is constant during the measurement. What is essentially wrong with this procedure is that the voltage variations of the voltage vector $\mathbf{V}_i$, which contain valuable information for the calculation of the $\mathbf{y}_{i0}$ admittance vector, do not exist in this measurement set. Instead, such information can be found for node j since the $\mathbf{V}_{ij}$ voltage ratio vector is measured. Therefore, it is very important to measure the voltage ratio vector $\mathbf{V}_{mi}$, where the node at which this vector is measured is actually the node at which the admittance vector $\mathbf{y}_{i0}$ needs to be calculated.

Furthermore, the selection of node m, which is taken as the reference is also very important. This is due to the nature of the object that is measured. Since the winding at low frequency can be observed as a set of resistances and inductances connected in series, it is obvious that the admittance between neighboring nodes is larger than the admittance between two non-neighboring nodes due to the conductor length,

$$\mathbf{y}_{i(i\pm1)} > \mathbf{y}_{i(i\pm j)}; j > 2. \tag{3.45}$$

What is also important to stress is that the voltage ratio vectors $\mathbf{V}_{ij}$ obtained for non-neighboring nodes, where $|i - j| > 1$, are very small values that are difficult to measure accurately. This narrows down the selection of the nodes at which the voltage ratio vector $\mathbf{V}_{mi}$ is measured down to two nodes $m_{1,2} = i \pm 1$. This means that for the voltage ratio measurement, only these two nodes $i \pm 1$ can be selected as reference nodes. Consequently, (3.42) for this system becomes

$$\mathbf{V}_{(i\pm1)i}\mathbf{y}_{i0} - \sum_{\substack{j=1 \\ j\neq i}}^{n} (\mathbf{V}_{(i\pm1)j} - \mathbf{V}_{(i\pm1)i})\mathbf{y}_{ji} = 0. \tag{3.46}$$

Let us first separate the terms from the sum in (3.46) where $j = i \pm 1$. Since $i\pm$ is the reference node, $\mathbf{V}_{(i\pm1)(i\pm1)} = 1$, the following relation can be found,

$$\mathbf{V}_{(i\pm1)i}\mathbf{y}_{i0} - (1 - \mathbf{V}_{(i\pm1)i})\mathbf{y}_{(i\pm1)i} - \sum_{\substack{j=1 \\ j\neq i; j\neq i\pm1}}^{n} (\mathbf{V}_{(i\pm1)j} - \mathbf{V}_{(i\pm1)i})\mathbf{y}_{ji} = 0. \tag{3.47}$$

Considering that all voltage ratio vectors $\mathbf{V}_{(i\pm1)j}$ from the sum in (3.47) are equal to 0 and dividing (3.47) by $\mathbf{V}_{(i\pm1)i}$, the expression

$$\mathbf{y}_{i0} = \left(\frac{1}{\mathbf{V}_{(i\pm1)i}} - 1\right)\mathbf{y}_{(i\pm1)i} - \sum_{\substack{j=1 \\ j\neq i; j\neq i\pm1,}}^{n} \mathbf{y}_{ji} \tag{3.48}$$

is obtained. Note that the term $\frac{1}{\mathbf{V}_{(i\pm1)i}}$ is obtained by element wise operation, where teh elements of the obtained vector are inverse of the elements of $\mathbf{V}_{(i\pm1)i}$ vector.

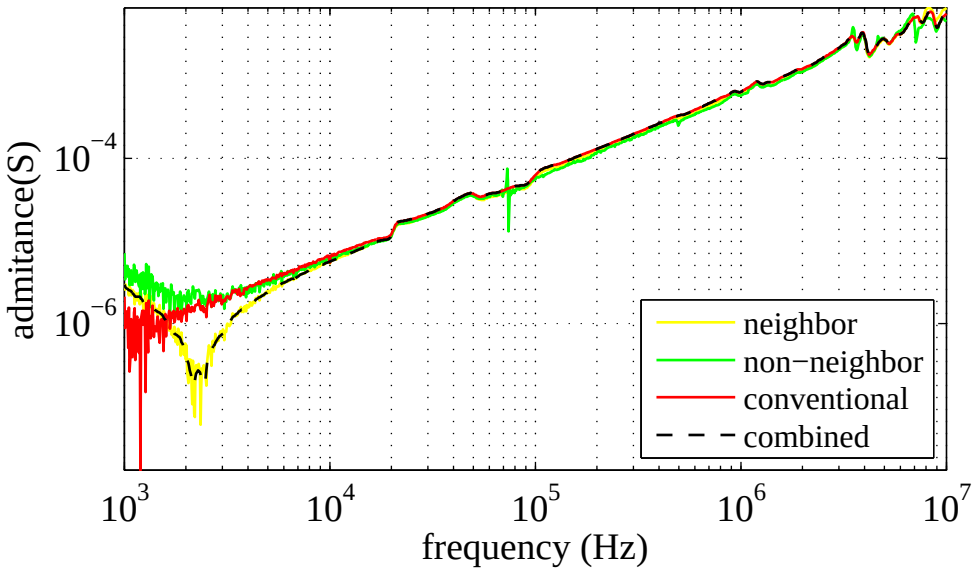

Figure 3.29: Comparison of admittance measurements at the last node.

Fig. 3.29 shows the comparison of admittances obtained using different previously described methods at the end terminal of reactors winding. The difference between different methods is substantial at low frequencies between $1kHz$ and $10kHz$. Furthermore, the admittance obtained by direct measurement of admittances shows quite a substantial noise at that frequency range. It can be noted that the admittance obtained using voltage ratio measurement with a reference node neighboring the node at which the admittance is calculated, reveals the first anti-resonance at a frequency of about $2kHz$. Moreover, by this method, the obtained admittance is much smoother compared to the admittance obtained by other methods.

In the region between $20kHz$ and $70kHz$, all methods yield almost identical results. However, after this frequency range, the discrepancies start to be visible again. The admittance obtained using voltage ratios where non-neighboring nodes are taken as the reference shows a substantial error at a frequency of $73kHz$. The voltage ratio at this frequency is extremely low and the captured values are not accurately measured. Furthermore, it can be noted that the admittance obtained by this method differs slightly across the whole frequency range. Moreover, a slight difference between the other two accurate methods exists at the range of high frequencies, above $100kHz$. Since the direct measurement method provides accurate results at high frequencies, this measurement is considered to be more accurate.

Finally, the admittance vector at this node is obtained by combining measurements of the standard method where only admittances are measured and the method that combines

the voltage ratio and the admittance measurement. An intersection point is found where these two methods start to produce almost identical results. This point is usually found in the frequency range between $20kHz$ and $70kHz$.

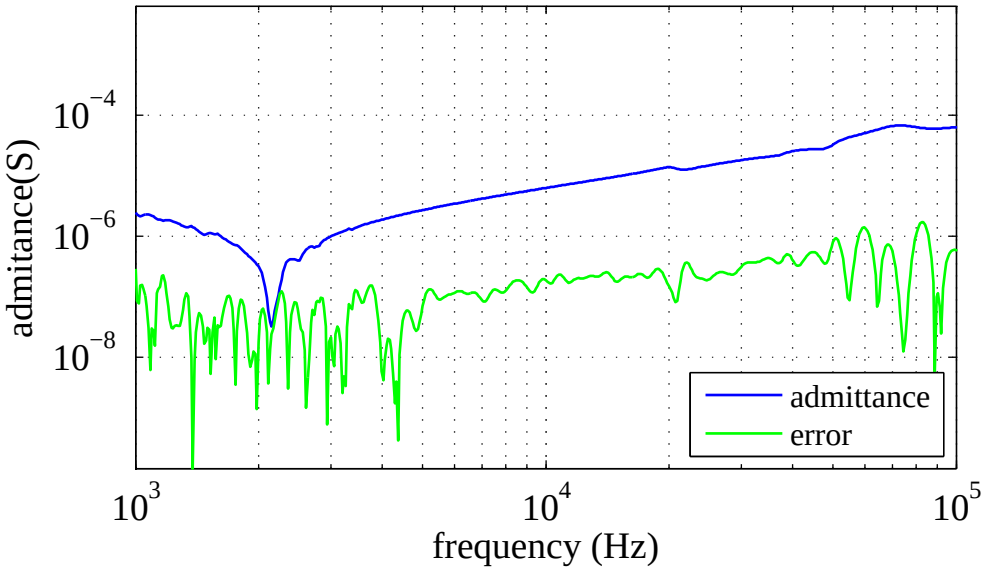

Figure 3.30: Fitting error of admittance between first node and ground.

The accuracy achieved during the fitting is very high. The only exception was the fitting of the diagonal elements in the low frequency region. This is presented in Fig. 3.30. However, since the obtained admittance is extremely low and that the measurement was not as smooth as it is at frequencies above $5kHz$, this error is expected. However, this error does not significantly influence the results obtained in time simulations where this model is used.

The admittance vectors measured at the test object are presented in Fig. 3.31.

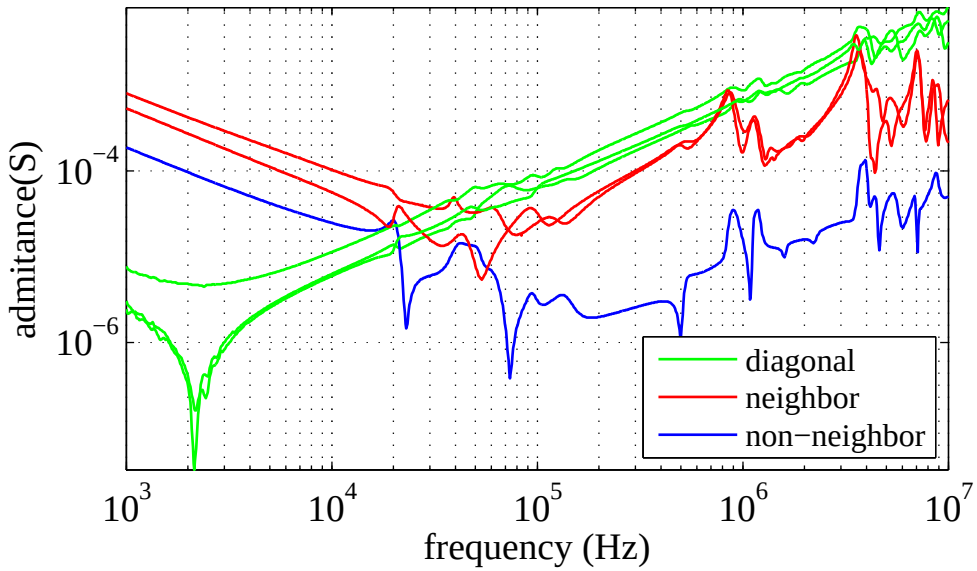

Figure 3.31: Admittance vectors of test object.

As expected, the non-neighboring admittance is very low. Actually, it is much lower than

the neighboring admittances in the whole frequency range. At high frequencies, where the reactor winding response is capacitive, the diagonal elements have much higher admittance. This means that the parallel stray capacitances are much larger than the series capacitances. Furthermore, the diagonal elements are dominantly capacitive since the nodes are not connected to the ground, where mainly a capacitive current flows from the nodes to the ground. Since this capacitance is very small, with values that vary about $0.1 - 0.15nF$ between different nodes, it is expected that the diagonal admittances at low frequencies are very small. Therefore, the voltage ratio at low frequencies is very much dependent on the value of diagonal admittances. For that reason, measurement of the voltage ratios is used to determine the diagonal admittances at frequencies below $50kHz$.

3.4.2 PSCAD interface

To obtain time domain simulations, the state-space model obtained with the vector fitting method is implemented in PSCAD. Implementation of such a state-space model in PSCAD is not straight forward and different methods can be utilized [60], [61].

Interfacing with the electrical network of PSCAD is done by using a branch interface. During the development of the model it was found that the node interface can become unstable if the model is connected using a high impedance to the PSCAD network or if simulated with open nodes. Since the model is intended to be used for analysis of the voltage distribution when the nodes are not connected to any point except with each other, the node interface was abandoned and the branch interface is used instead. The branch interface is made by using ideal current source I_{his} and a conductor with conductance G. This is shown in Fig. 3.32.

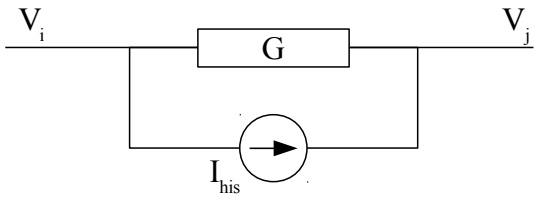

Figure 3.32: PSCAD branch interface.

PSCAD allows a more advanced branch interfacing using an ideal voltage source in addition. In this model, that feature is not used. Furthermore, PSCAD allows a user definition of passive elements such as resistors, capacitors and inductors through a user defined code with minimum code required.

The model that is needed to be interfaced in PSCAD is given in the state-space form by

$$\begin{aligned} \frac{d\mathbf{x}}{dt} &= \mathbf{A}\mathbf{x} + \mathbf{B}\mathbf{u} \\ \mathbf{y} &= \mathbf{C}\mathbf{x} + \mathbf{D}\mathbf{u} + \mathbf{E}\frac{d\mathbf{u}}{dt}. \end{aligned} \tag{3.49}$$

For this state-space form, the branch voltage vectors are identified as inputs $\mathbf{U} = \mathbf{u}$ while the current vectors represent the outputs of the state-space $\mathbf{I} = \mathbf{y}$. The model PSCAD

interfacing is going to be shown on a single branch example, where the voltage and the current vectors become scalars U and I.

In order to determine a suitable form for model interface, (3.49) is rewritten into

$$\begin{aligned} \mathbf{x} &= \mathbf{A}\int \mathbf{x}dt + \mathbf{B}U \\ I &= \mathbf{C}\mathbf{x} + DU + E\frac{dU}{dt}. \end{aligned} \tag{3.50}$$

The equation for current I in (3.50) shows that the resulting current I can be calculated as a sum of three currents. The first current is the current calculated by integration of the state-space variables $\mathbf{x}$. The second current is a current that flows through a conductor with a conductance D, while the third current is a capacitive current that flows through a capacitor with capacitance E. For the last two parts of the current equation, a simple interfacing in the form of capacitor and a resistor is used. However, for the first part, a more advanced method that integrates state variables needs to be used. This method requires calculation of the current at each time step. This equation in the form of the PSCAD interface is presented in Fig. 3.33, where the input voltage is presented by the branch voltage $U = V_i - Vj$.

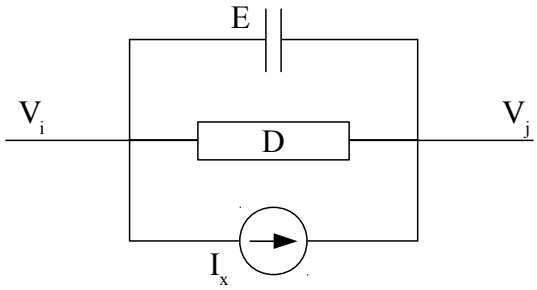

Figure 3.33: PSCAD branch interface for state-space model.

I_x current is obtained by

$$I_x = \mathbf{C}\left(\mathbf{A}\int \mathbf{x}dt + \mathbf{B}U\right). \tag{3.51}$$

The integration of the state variables $\mathbf{x}$ is performed using the fifth order Runge-Kutta solver. This improves significantly the stability and the accuracy of the model, compared to using forward Euler or second order integration methods. However, the input voltage U is measured with one step delay. Due to a very short time step, this delay does not contribute to any noticable simulation errors.

3.4.3 Modeling and simulation

In this thesis a single winding reactor is modeled using a black-box modeling method. In order to observe internal voltages, an internal point of the winding is selected. The admittance matrix is measured for the system with three nodes, where the first and the last node

represent the end nodes of the winding, and the middle node represents the middle point of the winding. This is presented in Fig 3.34.

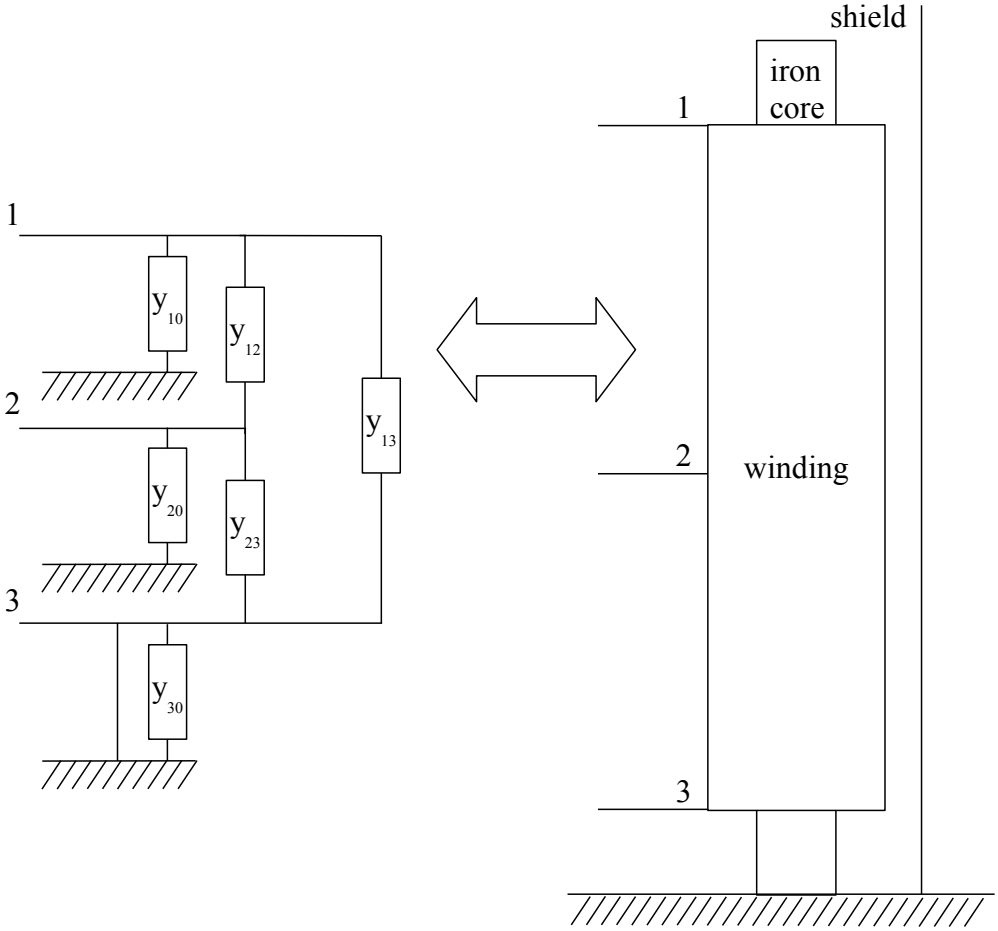

Figure 3.34: Selected measurement points.

In order to demonstrate and compare results obtained by different methods, the admittance matrix is obtained by the standard method of direct measurement of admittances and by the combined method, where the admittance measurement is combined with the measurement of the voltage ratios. The vector fitting method is used to obtain state-space matrices from the admittance matrix [36], [50], [62]-[64].

The voltage source in the PSCAD model of the system that includes the voltage generator, the cable and the reactor is a controlled voltage source with the magnitude defined by the imported voltage signal measured at the first node of the reactor. This means that the reactor and its model are excited by almost identical voltage. For that reason, the voltage source and the cable do not need to be modeled. Furthermore, the accuracy of the reactor winding model can be better evaluated.

Fig. 3.35 compares results obtained by the direct measurement and two different models of the reactor winding. Both models give very good results in the high frequency range which is observed during the first $10\mu s$ of the simulation after the excitation. Right before the voltages reach their peaks, the difference between simulations and the measurement starts to be visible. This is especially the case for the voltage obtained with the conventional

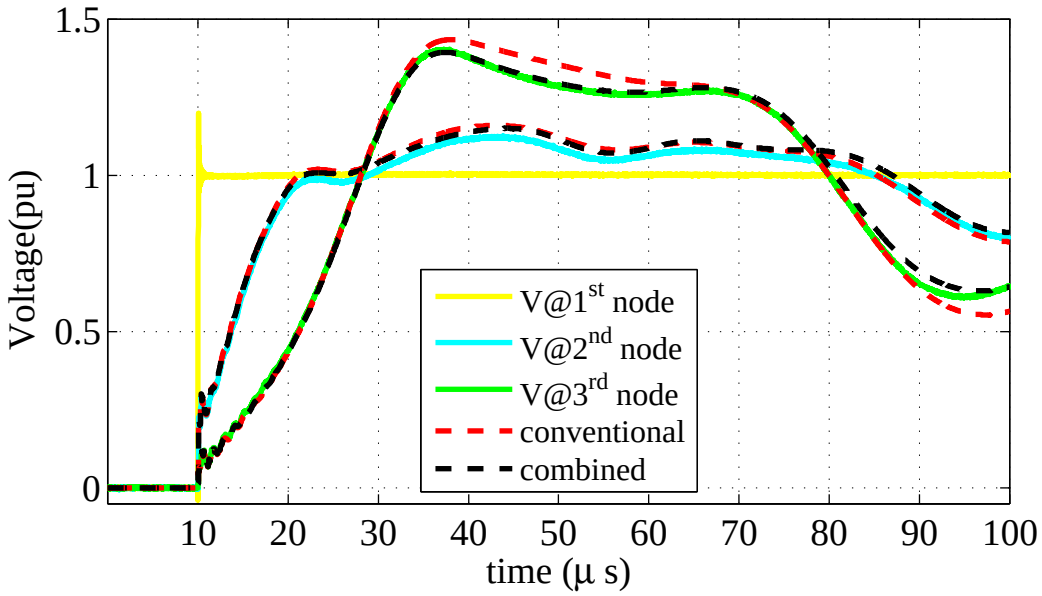

Figure 3.35: Simulation comparison of different models.

model at the third node. However, the combined model provides very accurate simulation of the voltage at the third node across the whole simulation time. This shows an improved accuracy of the combined model at low frequency. The root mean square (RMS) error of the simulated voltages at the third node are 3.4% and 1.7% for the conventional and the combined model respectively. The combined method yielded two time less error in this case.

However, the difference in the results obtained by the two models at the second node is not that large. The combined method gives a marginally better result, where the RMS errors for the conventional and the combined models are 2.5% and 2.3% respectively.

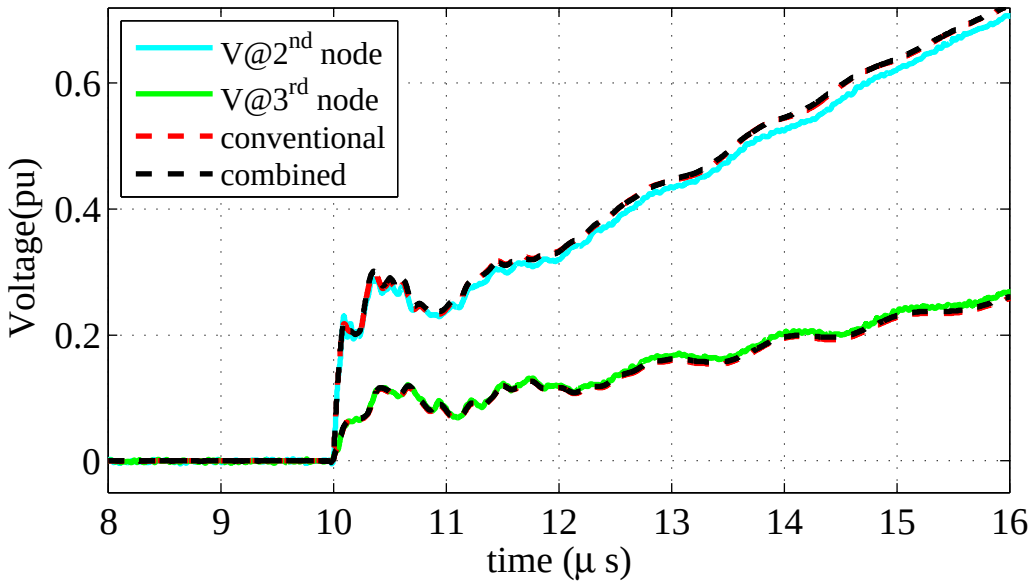

Figure 3.36: Simulation comparison of different models - zoom.

Fig. 3.36 shows the response of the two models during the first $6\mu s$ of the transient. As expected, simulations gave almost identical waveforms as the measured ones for the first $2\mu s$

of the transient. The response of both models is identical since the combined method uses the admittance matrix obtained by the conventional method at frequencies beyond $70kHz$.

Chapter 4

Transient voltage distribution along reactor winding

As it is presented in the introduction of this thesis, it was reported worldwide that many transformer insulation failures have occurred possibly by switching operations of vacuum circuit breakers (VCBs), although the transformers have previously passed all the standard tests and complied to all quality requirements [4]-[8]. Furthermore, a 10 years long study that included investigation of failures of thousands of transformers conducted by Hartford Steam Boiler Earlier concludes that the high frequency transients are the main cause of transformer insulation failures [10]. In this chapter, the goal is to determine the effect of different switching scenarios, different rise times of the surges and voltage derivatives on internal voltage distribution and turn-to-turn voltages. Furthermore, the aim is to determine the worst case scenarios and their possible negative impact on insulation lifetime. Results are compared with the turn-to-turn voltages obtained during the BIL test that are used as a reference.

4.1 Connection transients

In this work, only transients generated by closing operations of breakers are considered. Although the magnitudes of the voltages at the terminals of the transformer produced by the closing of the breaker are well within the limits and do not exceed the magnitude of the peak grid voltage, some transformer failures are reported during such transients [4]-[7].

The transformer energizing transients differ significantly depending on the connection of the high voltage side windings. In this article, only energizing of stray capacitances and leakage inductances is considered. Core energizing and inrush currents are not in the scope of this analysis since the observed time window is very short. For a wye connection, one end of the windings is connected to the common neutral point which is never excited by a voltage step. In the case of ungrounded transformers, the neutral may have a voltage, but it is never exposed directly to a voltage step. For a grounded transformer, the neutral point is always at zero voltage if the grounding is done properly where the grounding path is short thus minimizing grounding inductance L_g. During an energizing transient, the maximum terminal voltage to which a transformer winding is exposed, is the peak phase to ground

voltage. This is presented in Fig. 4.1.

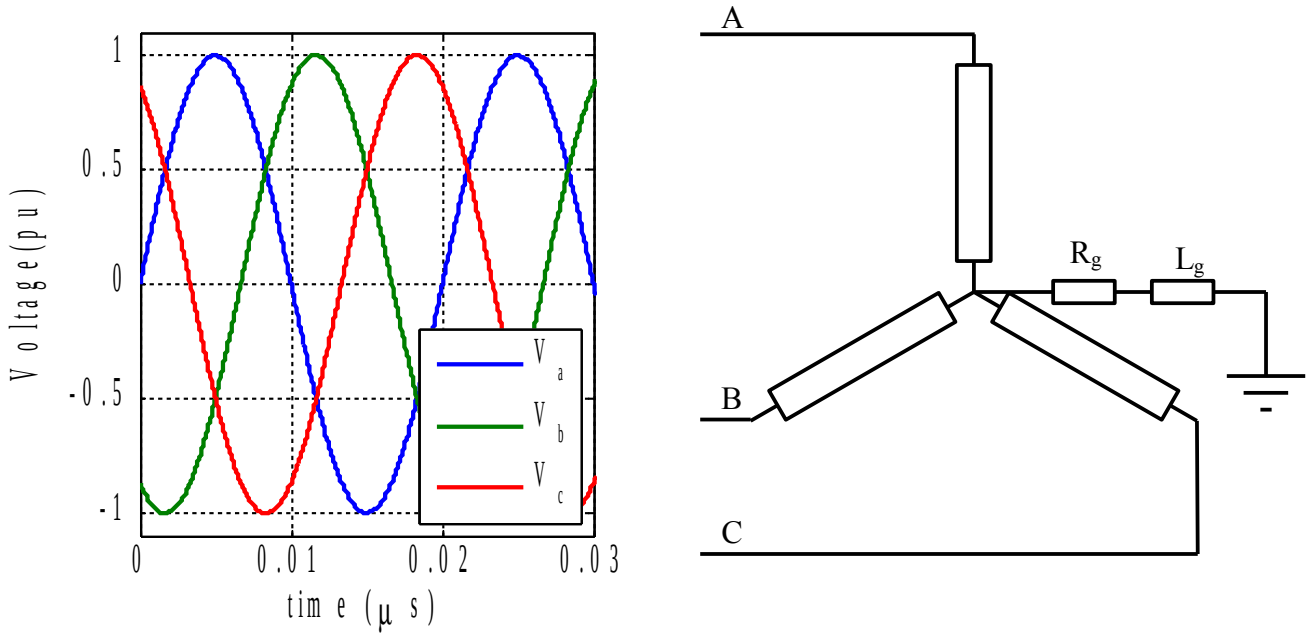

Figure 4.1: Star connected transformer.

In medium voltage cable grids, with voltage levels up to $30kV$, the high voltage transformer side is almost always delta connected. This is always the case in wind farms, where the grounding is done either at the platform transformer or at an auxiliary transformer that is used to supply apparatus at the substation. For a delta connected transformer, a simple energizing transient can give a very complex response due to a wave traveling phenomenon. Consequently, it can produce much higher internal voltages in a transformer. In a delta connected winding, the end of one winding is connected to the beginning of the other winding. This means that a winding of a transformer can be excited from both sides. A winding of a delta connected transformer is excited by line-to-line voltage. The maximum of the line-to-line voltage is achieved when one phase reaches $0.86pu$ and another -0.86 of its value. In this case scenario, the voltage by which the winding is excited exceeds $\sqrt{3}$ times the voltage to which a wye connected transformers winding is exposed. However, it can be shown how a transformer winding can be exposed even to a higher voltage. This scenario is possible when there is a certain delay between energizing at two ends of a winding. Let us observe closely such a scenario by looking to an energizing transient of an ungrounded winding. This transient can be seen in Fig. 4.2.

As can be observed in Fig. 4.2, the initial voltage distribution along the winding is determined by parallel stray capacitances of the winding. As the time progresses, the voltage along the winding rises as the voltage wave propagates through the winding. The voltage at the end of the winding oscillates with the highest magnitude at the resonance frequency of the winding. This resonant frequency depends directly on series stray capacitances, leakage inductance and the length of the winding. Ideally, the voltage magnitude at the end of the winding could reach $2pu$ magnitude due to wave reflections, while in reality it reaches about $1.8pu$. For this particular winding, this voltage level is reached after approximately $50\mu s$ or $0.05ms$. Let us consider a very possible scenario in which the negative voltage step is applied at the end of the winding when the positive voltage reaches its maximum of $1.8pu$.

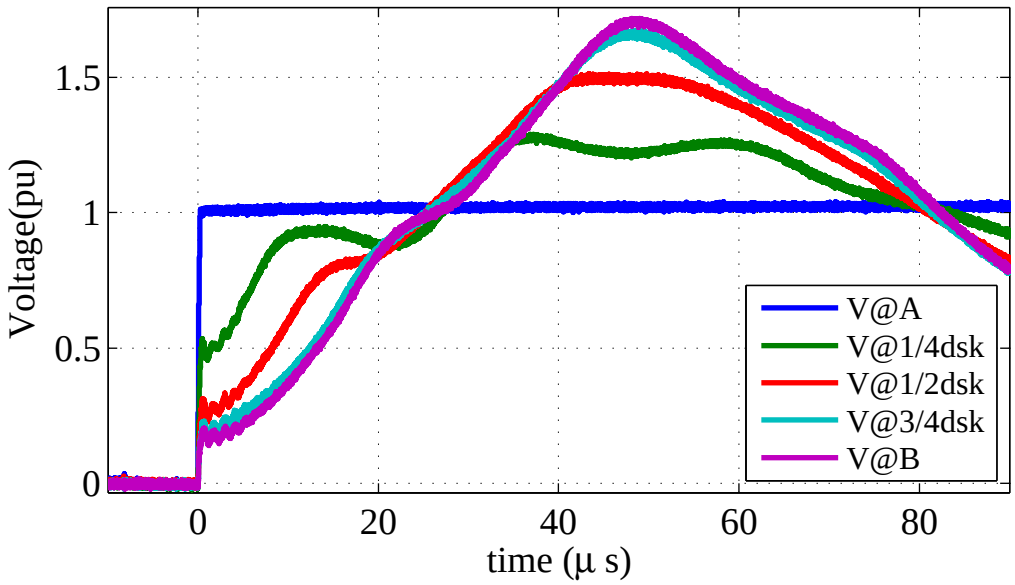

Figure 4.2: Energizing of a winding.

If the magnitude of the negative voltage step is $1pu$, then the resulting voltage step is the difference between the positive and the negative step, which results in a $2.8pu$ voltage step. This is the worst case scenario. Such a case scenario is presented in Fig. 4.3.

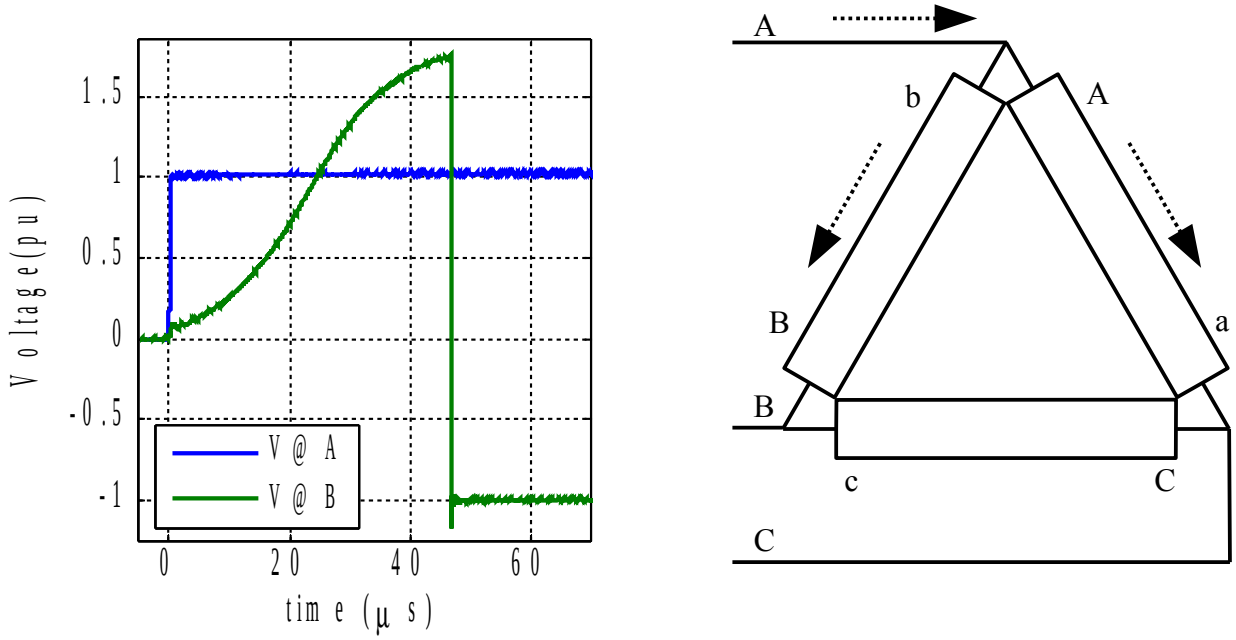

Figure 4.3: Delta connected transformer.

In Fig. 4.3 it can be seen that the voltage wave propagates along two windings connected to terminal A. At about $t = 45\mu s$, the wave will reach its maximum at terminals B and C. If any of these two terminals are excited by a negative voltage step at time instant, the resulting voltage step will reach a magnitude of $2.8pu$.

4.1.1 Test setup

The experimental setup used consists of a reactor, pulse generator and measurement equipment. The reactor is rated at $10kV$, $200kVA$, and consists of two windings. An aluminum shield is built around the reactor in order to give a more realistic distribution of stray capacitances, while holes in the front cover are left open in order to enable access to measurement points.

The voltage step generators were made to produce custom voltage steps. The principle of operation is a MOSFET controlled discharge of a charged capacitor over the reactor winding. The resistance between the pulse generator and reactor terminals is negligible. The rise time is tuned by a variable resistor in the gate circuit of a MOSFET that operates as a switch. The minimum recorded rise time of the voltage step is $35ns$ which is limited by the electrical properties of the reactor winding. The minimum rise time of the voltage step when the voltage step generator is connected directly to an oscilloscope is $20ns$ which is limited by the MOSFET's electrical properties. The MOSFETs used in the circuit have a very low output capacitance of $37pF$ which ensures that the MOSFETs do not impact the circuit parameters to a significant extent.

During the tests, two different pulse generators were used. Since the subject of this study are high frequency transients, the voltage level of the pulse generators is between $6V$ and $9V$, depending on the generator. One generator can only make single pulses. By adjusting the resistor in the pulse generator, the rise time and the tail time can be adjusted. Therefore, this pulse generator is used to generate lightning impulse shaped voltages and to simulate the energizing of a transformer with a wye connected high voltage side. A simplified scheme is given in Fig. 4.4.

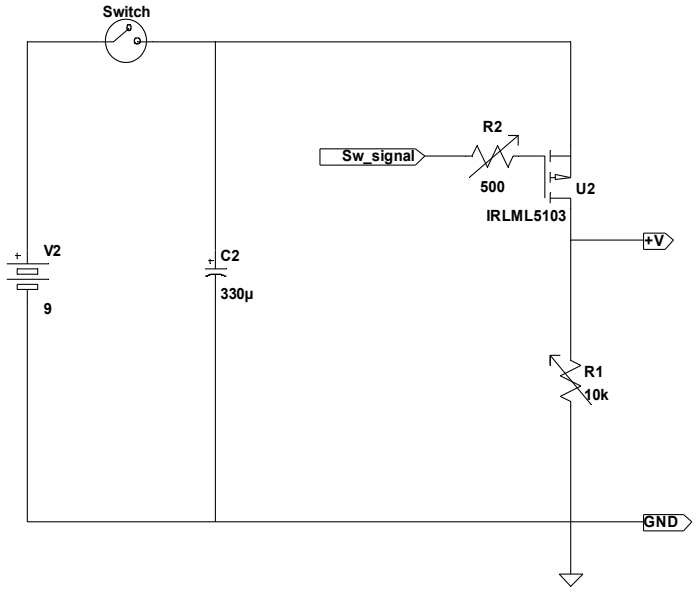

Figure 4.4: Pulse generator simplified scheme.

Another generator is used to generate both positive and negative pulses. This pulse generator is used to emulate a case scenario when a delta connected transformer is energized. In this case, a winding of the delta connected transformer is excited from both ends, where

one end of the winding is energized by a positive pulse, while the other end is excited by a negative pulse. This is a very common scenario during a connection of a transformer with a delta connected high voltage side. The time delay between the positive and a negative pulse can be adjusted by a variable resistor. Furthermore, in order to estimate the impact of the rise time of a voltage step, the rise time of both the positive and negative step can be tuned by additional variable resistors.

For the measurement of the transients, two oscilloscopes were used simultaneously. The same pulse was used for triggering at both oscilloscopes and it was possible to measure up to eight channels at the same time. The bandwidth of the oscilloscopes is $200MHz$ and $1.5GHz$ while the probes used have a bandwidth of $500MHz$. The sampling speed of the oscilloscopes is $20MS/s$ and $20GS/s$. The resolution of the two oscilloscopes is $8bits$. In the data analysis, the signals were filtered using a $25MHz$ digital low pass filter without a delay by using the $filtfilt$ Matlab function. Furthermore, both oscilloscopes were calibrated, and during the measurements one of the signals is measured by both oscilloscopes in order to fine tune the triggering and to check if there are any discrepancies in the measurement between the two oscilloscopes. The measurement setup is presented in Fig. 4.5.

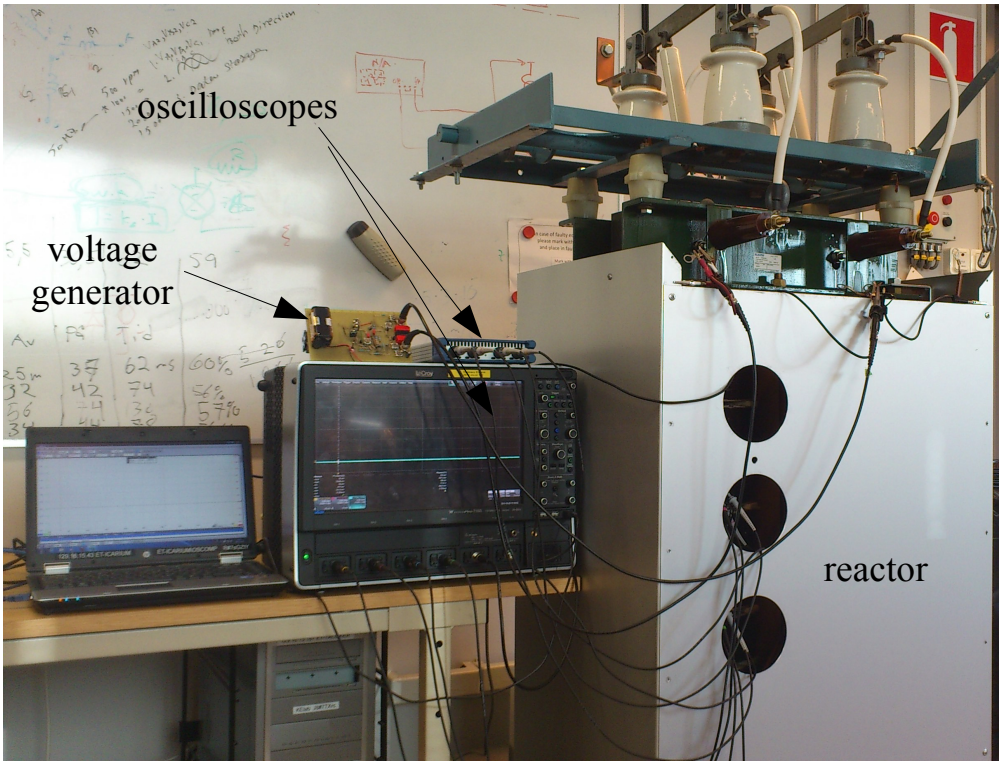

Figure 4.5: Measurement setup.

4.1.2 Test reactor

In this work, a single phase $10kV$ reactor rated at $200kVA$ with two windings is used as a a test object. Ideally, a three phase delta connected transformer would be used, but this reactor is suitable to perform all the important switching tests one could perform an a three phase delta connected transformer. This reactor is built in such a way so the measurement points

between the disks are easily accessible. The reactor is enclosed in an aluminum enclosure in order to give a more realistic distribution of the stray capacitances, while the front panel is made with holes in order to comfortably reach the measurement points. The reactor is presented in Fig. 4.6.

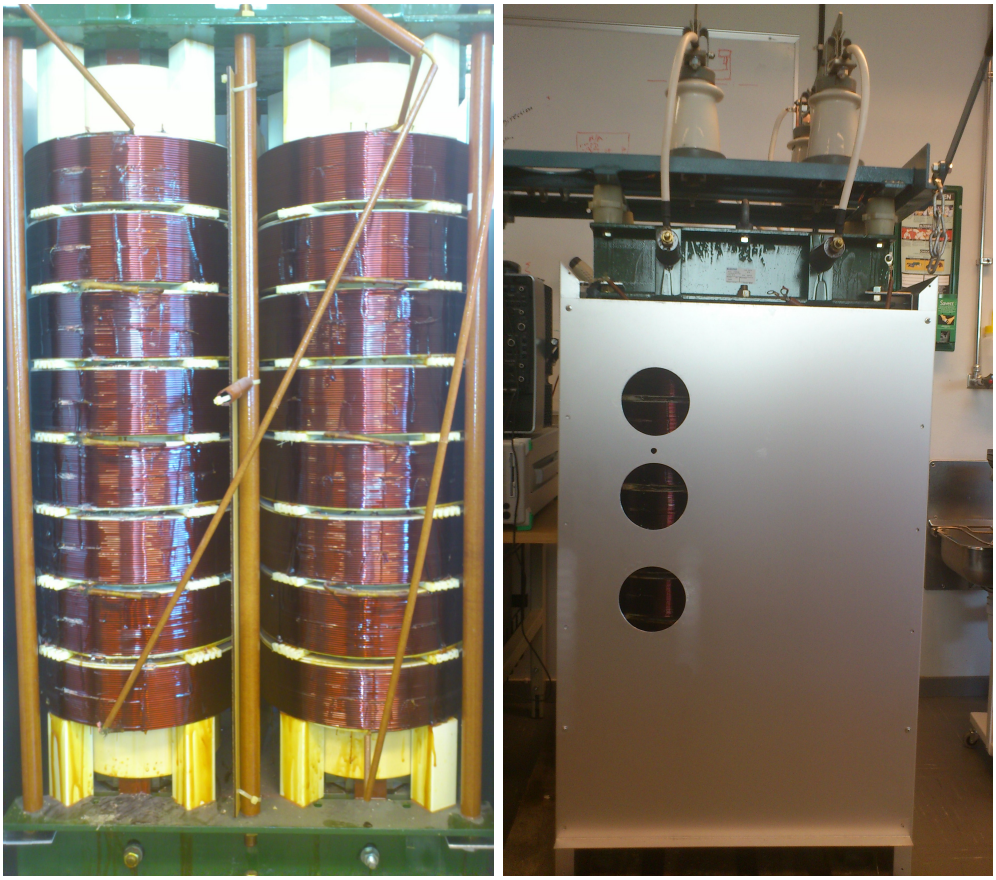

Figure 4.6: Reactor winding, enclosure with holes.

Each winding of the reactor consists of 8 disks. Each disk is wound in the same way, where odd disks are wound starting from the outer layers while even disks are wound starting from the inner layers. Each layer consists of 30 conductors, while each disk consists of 9 layers. The structure of the reactor winding is presented in Fig. 4.7.

Terminals T1 and T2 mark the end terminals of the winding. Disks 4,5 and 6 are not presented in Fig. 4.7 in order to decrease the size of the figure.

Since the focus of this work not only to measure voltages at disks interconnections but inside the disks too, additional measurement points are made by pealing off the insulation from the top conductors. Measurement points for the first reactor are presented in Fig. 4.8.

It can be noted that the voltage step propagates following the maximum admittance path, which means the conductor. That means that the disk energizing is made by first energizing the outer layer from the top to bottom, then the next layer from the bottom to top, and so on. By this, the highest turn-to-turn voltage is obtained at the beginning of the layers where the beginning of one layer meets the end of another layer, like conductors 1 and 60 for example. In that case, the initial voltage distribution at the top of the disk is determined by the distribution of the parallel stray capacitances between the top conductors. During the

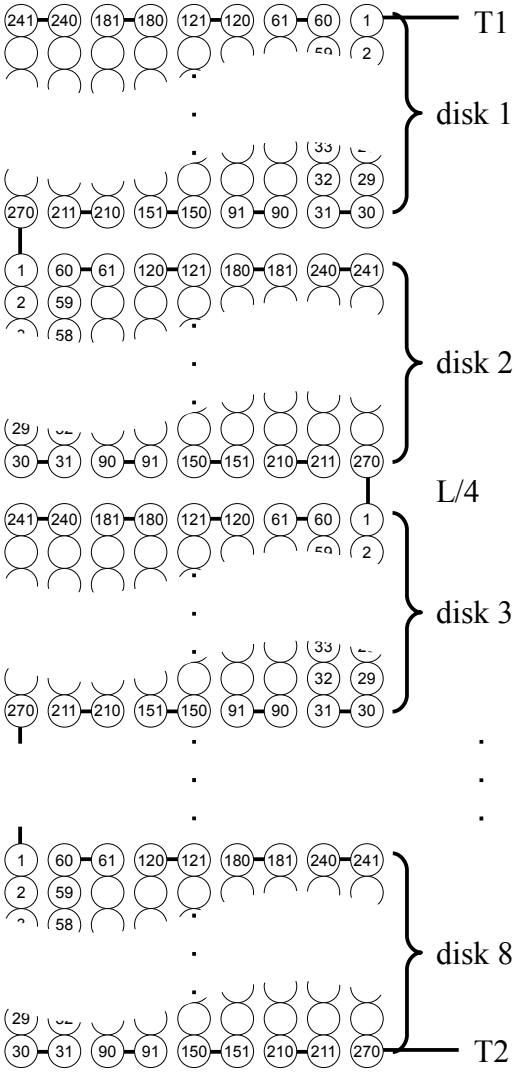

Figure 4.7: Reactor winding scheme.

time in which the voltage step arrives from conductor 1 to conductor 60, a substantial turn-to-turn voltage is developed. Of course, this is not the case for the two adjacent conductors such as 60 and 61 where they are almost at identical potential, even during the very fast transients. Such a choice of the measurement points ensures that the highest turn-to-turn voltages are recorded.

4.2 Measurements and data Analysis

The goal of this work is to study the voltage distribution along the winding during transients such as the lightning impulse or switching events. In our laboratory environment, these tests were performed using voltage generators that produce voltages of about $10V$. Using these voltage generators, both lightning impulses and switching events are generated. Since the high frequency transients above $10kHz$ are not affected by the core saturation [65] due to a high reluctance of the iron core during very fast transients [66], it is realistic to perform these tests with the scaled down equipment.

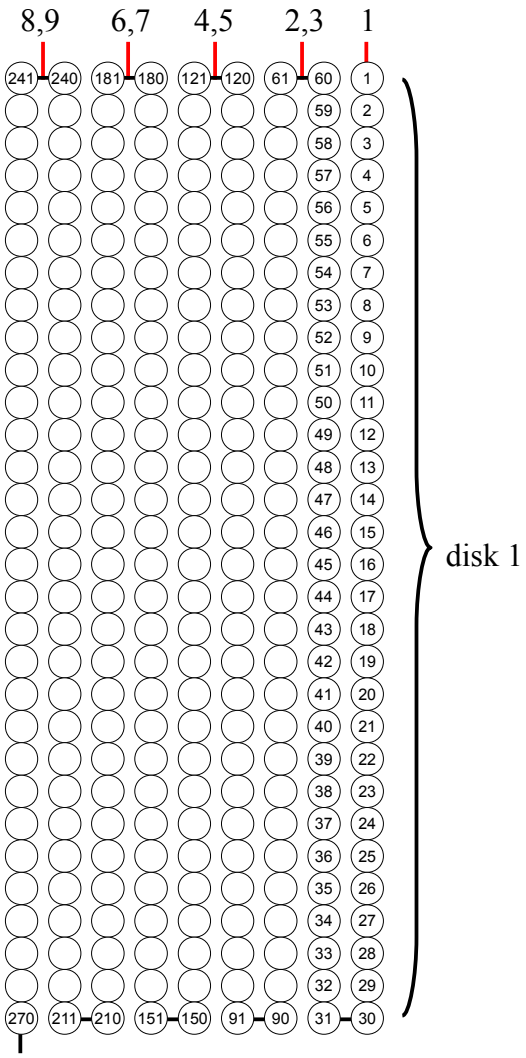

Figure 4.8: The 1^{st} disk winding scheme.

The results obtained in this work are compared to standard values of the basic lightning impulse voltage level (BIL). The standards for both dry-type and oil filled transformers define for each voltage level the BIL at which the transformer will not show any signs of insulation damages. These voltage impulse tests are considered as the strongest stress that can occur to the insulation of a transformer and therefore, if the transformer is able to withstand this voltage without any damages, its insulation should survive other high frequency transients. For this reason, the turn-to-turn voltage obtained during the lightning impulse shaped voltage stress are considered as the reference

The BIL defined by standards for dry-type and oil-impregnated transformers is given in Table 4.1.

In Table 4.1, "S" stands for the standard value, "1" is an optional higher level where the transformer is exposed to high overvoltages, and "2" is the case where surge arresters are used and found to provide appropriate surge protection.

This data is used for comparison with voltage stress during very fast transients. Since the voltage generators used in these tests produce low voltage impulses, the data is presented in per unit (pu). However, the BIL for each voltage level has a different value when expressed

Table 4.1: Nominal System Voltage and Basic Lightning Impulse Insulation Levels (BIL) for Dry-type Transformers [67]

	BIL (kV)	45	60	75	95	110	125	150	200
U_{nom}									
8.7		S	1		1				
15			S		1	1			
24					2	S	1	1	
34.5							2	S	1

in *pu* making the direct comparison meaningless. The *pu* values are calculated as the ratio of the BIL and the peak phase voltage. For example, for the $8.7kV$ level, the basic lightning insulation level is $6.33pu$, while for the $34.5kV$ level the BIL value is $4.44pu$ with a surge arrester protection and $5.33pu$ as a standard BIL. As a reference, the $4.44pu$ BIL level is chosen since it has the lowest magnitude in *pu*. Another reason for taking this level as a reference is that the $34.5kV$ voltage level is used in large offshore wind farms where transformers are usually protected by surge arresters.

4.2.1 Turn-to-turn voltages in the 1^{st} disk

The focus of this study are the top disks of the winding. The reason for this is that the voltage derivative and the rise time of the voltage step applied to the terminal of the winding decreases significantly along the winding as the wave travels from one terminal to another. Since the speed of the wave propagation in the winding is constant, due to a lower voltage derivative and the rise time of the wave front, the voltage change, and therefore the turn-to-turn voltage decreases along the winding. Furthermore, it is very difficult to draw any conclusions by looking at disk-to-disk voltages due to large distances in between, and for that reason, the disk-to-disk voltage is not discussed in this work. Furthermore, there haven't been any reports on the insulation failures between disks indicating that the transformer insulation can withstand disk-to-disk overvoltages without any problems.

Turn-to-turn voltages in the 1^{st} disk during the BIL test

Let us observe the turn-to-turn voltages in the first disk. Since the rise time and the derivative of the voltage step are as highest close to the terminal, transformer manufacturers usually apply special winding techniques in order to decrease the turn-to-turn voltage in the top disk. However, such a technique is not used in the reactor winding used for the tests.

The voltage is measured at the top of the disk. This gives the possibility to measure the turn-to-turn voltage between the turns where it reaches the maximum. As it can be seen in Fig. 4.9, these turns are 1, 61, 121, 181 and 241 respectively.

Initially, a low voltage $1.2/50\mu s$ impulse is used for the tests. The magnitude of the voltage is presented in *pu*, where as the reference a $4.44pu$ value is chosen which corresponds to the maximum BIL of a surge arrester protected dry-type transformer at a $34.5kV$ voltage level. The difference between this test and a real lightning impulse test is that the other end of the winding is not grounded. From the perspective of the voltage stress on the top

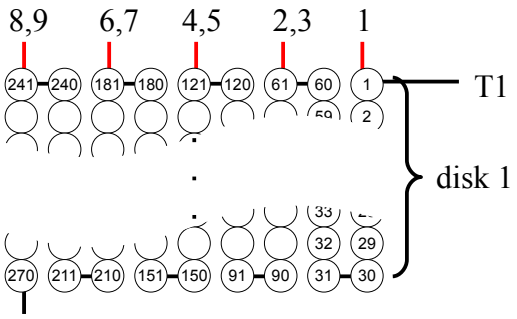

Figure 4.9: The 1^{st} disk measurement points.

disk, this does not make too much of a difference since the highest turn-to-turn voltage is recorded during the rise time of the lightning pulse, during which the voltage at the end disk is almost zero.

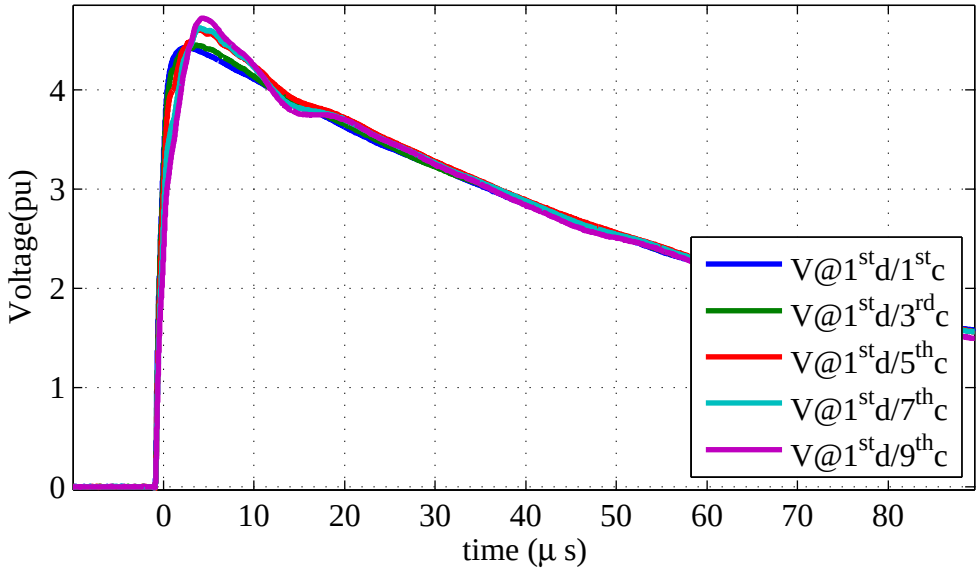

Figure 4.10: BIL at 1^{st} disk.

Fig. 4.10 shows the voltages measured at top turns of layers 1, 3, 5, 7 and 9 respectively. By observing Fig. 4.9, the measurement points are at turns 1, 61, 121, 181 and 241 respectively. In Fig. 4.10 it can be observed that the rise time of the propagating voltage pulse decreases as the pulse progresses through the disk. By looking at the impulse at this scale, it can be noticed that the wave corresponds to a $1.2/50\mu s$ lightning impulse.

By closely studying the voltages in Fig. 4.11, it can be noticed that the magnitude of the voltage increases and reaches a level of $4.72pu$.

The plot with turn-to-turn voltages is presented in Fig. 4.12. It can be noticed that the highest turn-to-turn voltage is not developed at the first turns. Instead, the highest voltage of $0.4pu$ is obtained towards the end of the disk. The lightning impulse excites the internal resonant frequency of the disk at about $170kHz$. As a result, the highest voltages are recorded at the end of the disk. When Figs. 4.11 and 4.12 are compared, it can be seen that the first half-period of the turn-to-turn voltage oscillations occurs during the front of

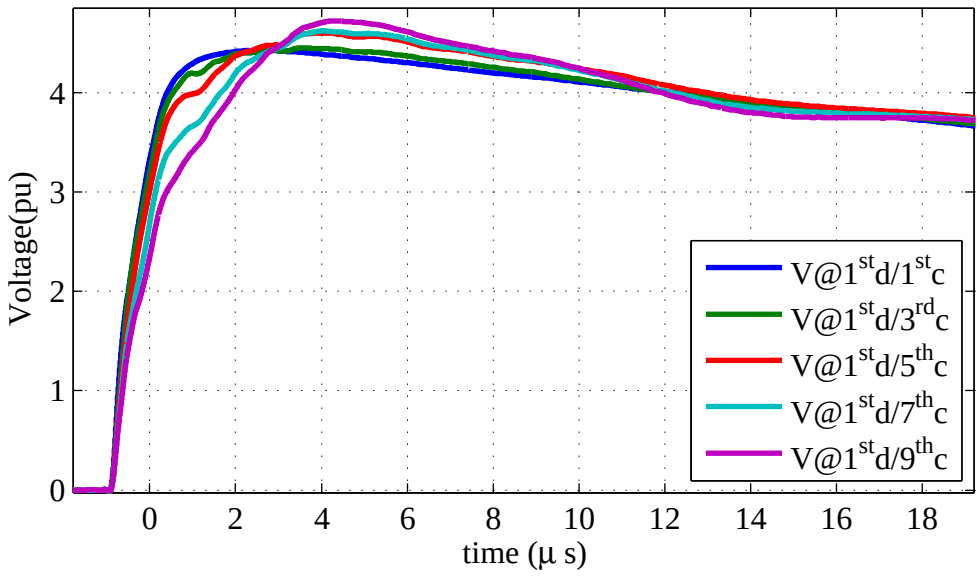

Figure 4.11: BIL at 1^{st} disk - zoom.

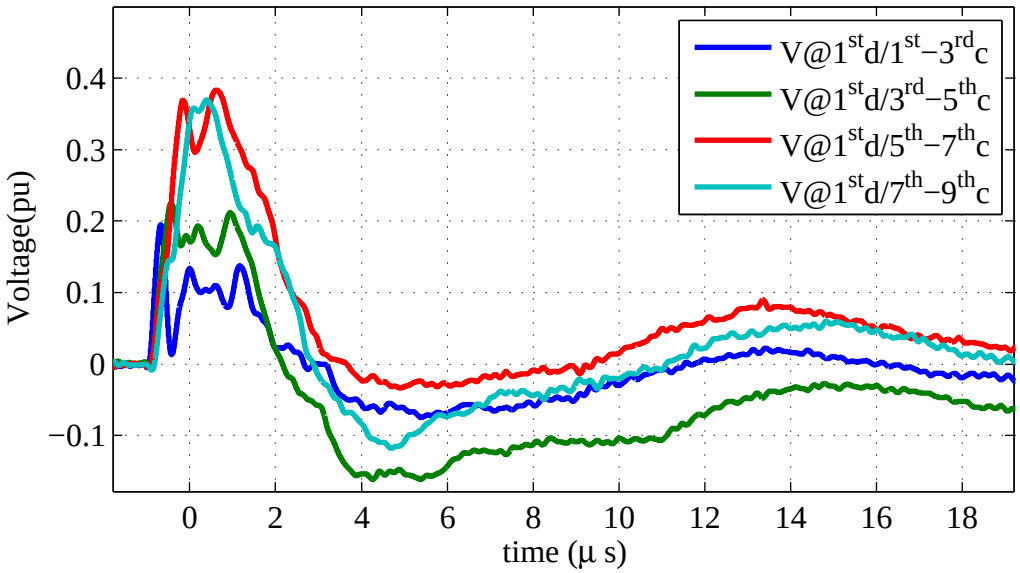

Figure 4.12: Turn-to-turn voltages at 1^{st} disk during BIL.

the voltage impulses.

When the voltage derivative $\frac{dV}{dt}$ is observed, the highest value is recorded at the first conductor, $7.2pu/\mu s$. It's value drops towards the last layer where $4.5pu/\mu s$ is observed.

Turn-to-turn voltages in the 1^{st} disk during connection of a wye connected Transformer

In order to observe turn-to-turn voltages during the connection of a wye connected transformer, a single voltage step is applied to the reactor. The magnitude of the voltage step is

set to $1pu$, which corresponds to the peak phase-to-ground voltage. This is the worst case scenario, which is selected to perform this study.

This test is performed with different rise times of the voltage step. This is done in order to study the turn-to-turn voltage for different types of insulation. It is known that different insulation types contribute to different stray capacitances of transformers, and therefore, the voltage step rise times [28], [56]. Because of that, the rise time is varied between the minimum of $35ns$ to approximately $500ns$.

Due to a much shorter rise time compared to the BIL, it is expected that the turn-to-turn voltages are significantly higher at the first turns. Fig. 4.13 shows the turn voltages at the first disk. Due to the very short rise time of $35ns$, the internal interlayer resonances are excited. Because of that, a voltage ringing is observed at the first conductor, yielding a $1.2pu$ voltage magnitude at the first layer.

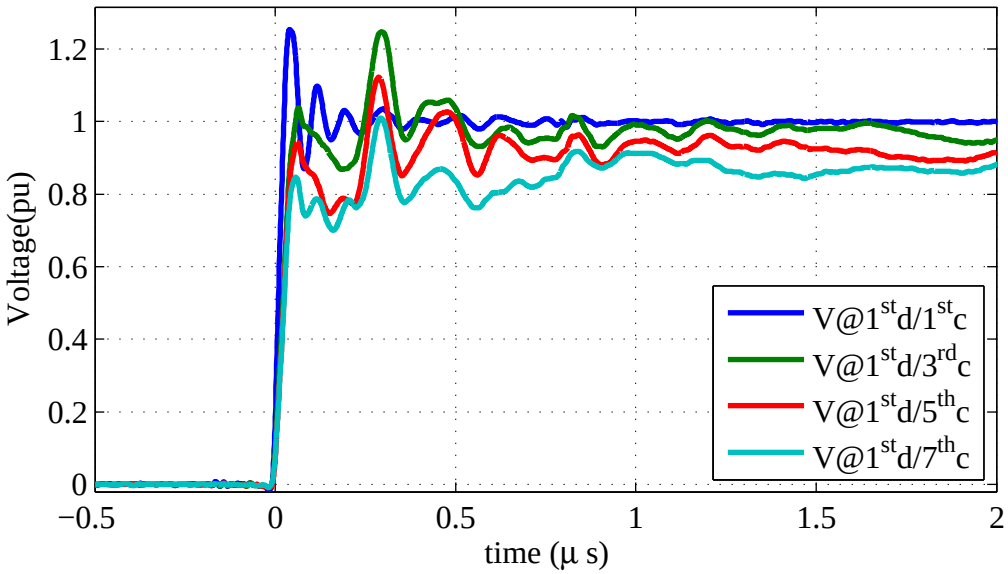

Figure 4.13: Turn voltages at 1^{st} disk during $35ns$ t_{rise} voltage step.

The initial frequency recorded at the top conductors at each coil varies between $13.7MHz$ at the first turn of the outer layer, down to $11.5MHz$ measured at the top conductors of the internal layers. The discrepancy in frequencies is due to differences in structure, where internal layers are surrounded by neighboring layers, while the outer layer has air as a boundary on one side. This impacts the rise time significantly, where the rise time of the first conductor of the outer layer is two times shorter compared to the rise time recorded for the internal layers, that have almost the same rise time. Consequently, the turn-to-turn voltage between the outer and the first internal layer is much higher compared to the other turn-to-turn voltages, reaching the value of $0.49pu$. This is presented in Fig. 4.14.

As Fig. 4.14 shows, the turn-to-turn voltage recorded during the energizing of a wye-connected transformer exceeds the turn-to-turn voltages during the BIL impulse test. The significant difference is that the peak voltage is recorded at the beginning of the disk, while during the BIL test, the highest recorded turn-to-turn voltage is recorded at the end of the disk. The reason for such a high turn-to-turn voltage during the BIL test is the resonance frequency of the disk, while for the energizing test, the main reason for the high turn-to-turn

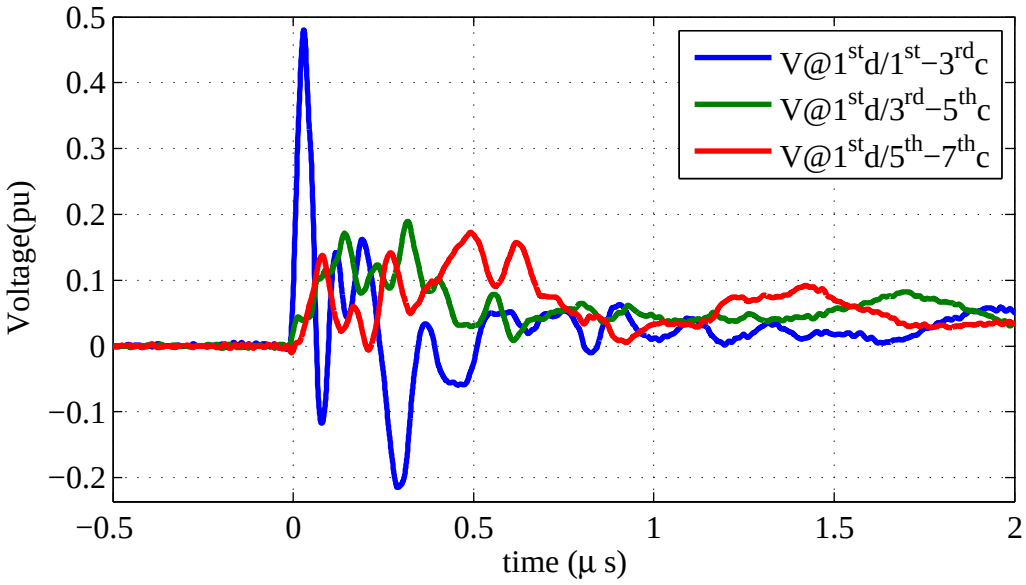

Figure 4.14: Turn-to-turn voltages at 1^{st} disk during $35ns$ t_{rise} voltage step.

voltage is a very short rise time of the voltage step that excites the internal layer-to-layer resonances.

Consequently, by increasing the rise time, the turn-to-turn voltage at the beginning of the disk will be reduced. To simulate a response of an oil-insulated transformer, a very long $500ns$ rise time during the energizing of a wye connected transformer is selected. This rise time corresponds to approximately to the rise time of the voltage during the energizing of an oil insulated transformer in a cable grid. Fig. 4.15 shows the turn-to-turn voltages during a $500ns$ rise time voltage step.

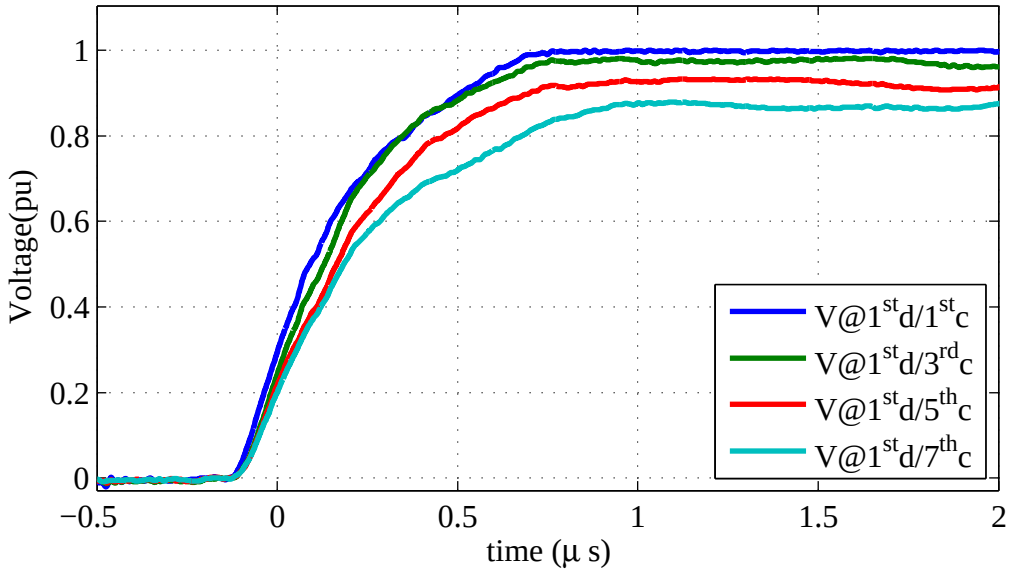

Figure 4.15: Turn voltages at 1^{st} disk during $500ns$ t_{rise} voltage step.

As can be seen from Fig. 4.15, a much slower $500ns$ rise time voltage step does not excite the internal inter layer resonances. There is no overshoot in the voltage step, and the

response is much more similar to the BIL excited reactor. The voltages at the first two layers are very similar, while some more notable voltage differences are recorded at the internal layers. This becomes more obvious when Fig. 4.16 is observed.

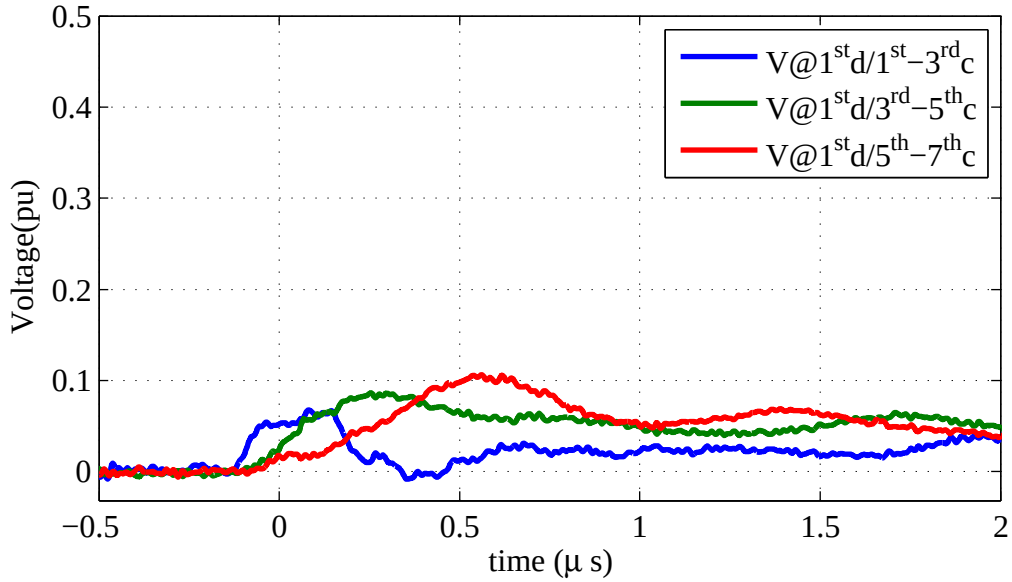

Figure 4.16: Turn-to-turn voltages at 1^{st} disk during $500ns$ t_{rise} voltage step.

Fig. 4.16 shows turn-to-turn voltages recorded at the first disk. As noted before, the turn-to-turn voltage between the first two layers is very low compared to the other turn-to-turn voltages. The highest turn-to-turn voltage is recorded at the end of the disk and reaches a magnitude of $0.1pu$.

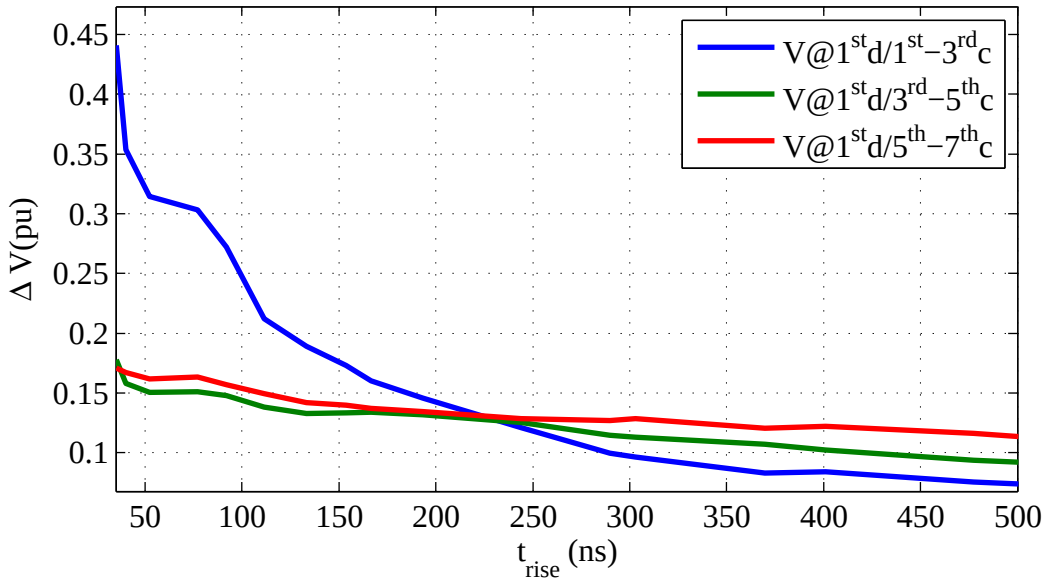

Figure 4.17: Turn-to-turn voltages at 1^{st} disk for different rise times t_{rise}.

The tests are performed by incrementally increasing the rise time. The results are shown in Fig. 4.17 that shows the turn-to-turn voltage as function of the rise time. As it is observed earlier, the highest turn-to-turn voltage is obtained for short rise times for the outer conductors.

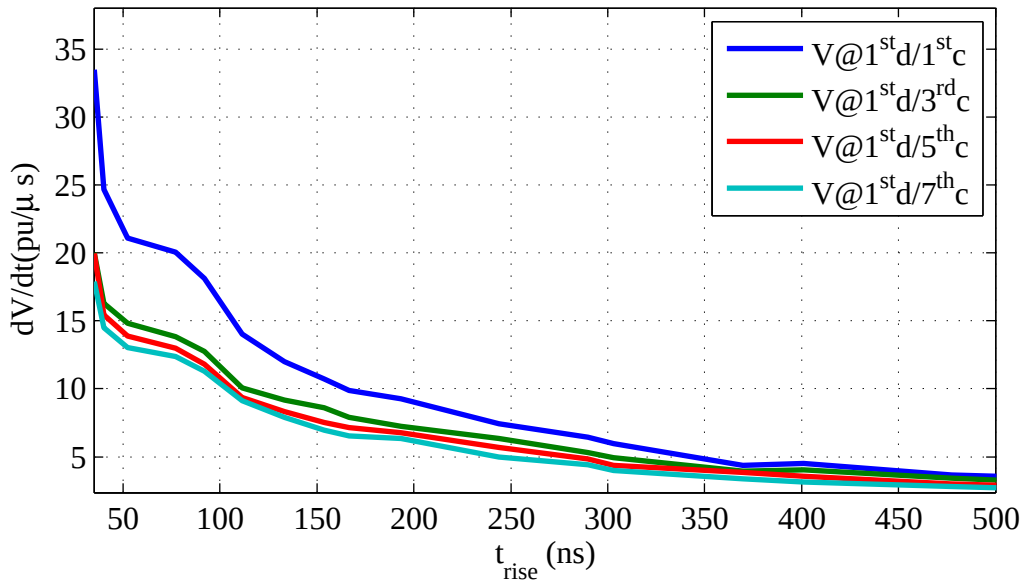

Figure 4.18: Voltage derivative $\frac{dV}{dt}$ at 1^{st} disk for different rise times t_{rise}.

A similar observation can be made for the voltage derivatives in Fig. 4.18 that shows the voltage derivative $\frac{dV}{dt}$ as a function of the rise time t_{rise}. The highest voltage derivative is obtained at the first conductor for the shortest rise time. When compared to the voltage derivative values recorded during the BIL test, the maximum voltage derivative recorded during this test exceeds almost 5 times the value of $7.2pu/\mu s$ recorded during the BIL test.

Turn-to-turn voltages in the 1^{st} disk during connection of a delta connected transformer

In order to observe turn-to-turn voltages during the connection of a delta connected transformer, two voltage steps are applied simultaneously to the reactor winding terminals. The magnitude of the voltage steps is set to $\pm 0.86pu$, which corresponds to a peak line-to-line voltage of $2 \cdot 0.86 = 1.72pu$. This is the worst case scenario, which is selected to perform this study. However, in order to obtain high internal overvoltages it is needed to apply these voltage steps with a certain time delay as shown in Section 4.1.

The positive and the negative voltage step are applied at two ends of the winding where the reference one is taken as the beginning and the other one as the end of the winding. A positive voltage step of $0.86pu$ is applied first at the end of the winding. Consequently, the voltage at the beginning of the winding is rising slowly and reaches its maximum value after some tens of micro seconds. This is presented in Figs. 4.2, 4.3 and 4.19. This is exactly the same scenario that may occur during the connection of a delta connected transformer.

This test is performed with different rise times of the negative voltage steps. With this method, it is possible to study and compare the turn-to-turn voltages for different types of insulation. As for the previous tests, a $35ns$ rise time is referred to as the minimum rise time, while a $500ns$ rise time t_{rise} is set as the maximum, due to that the maximum rise time set by oil insulation.

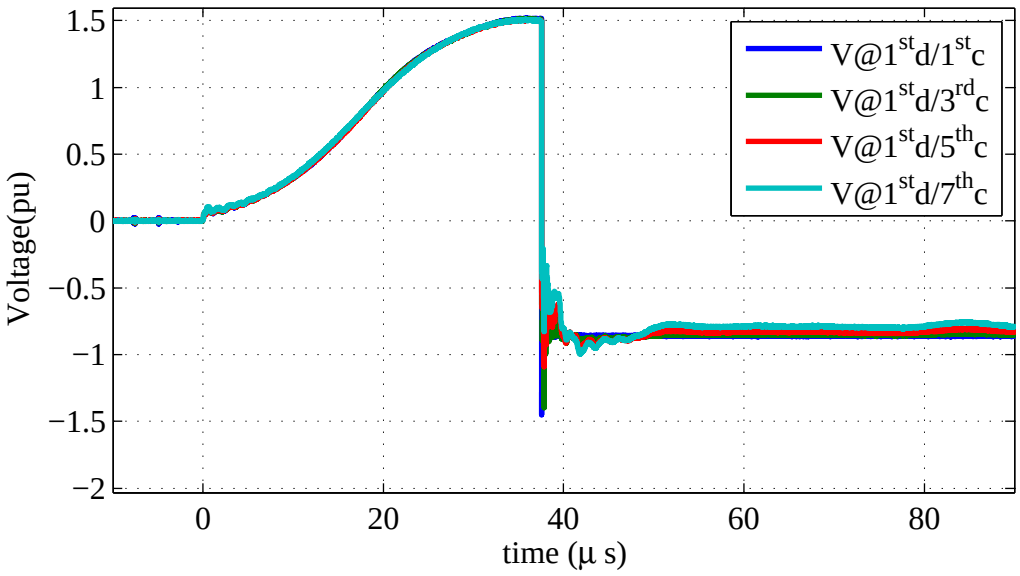

Figure 4.19: Turn voltages at 1^{st} disk during $35ns$ t_{rise} positive and negative voltage step.

When compared to the previous cases, the connection of a delta connected transformer generates voltage steps of a very short rise time as observed with the connection of a wye connected transformer. This rise time is much shorter when compared to the BIL. Furthermore, a much higher magnitude of the voltage step is obtained when compared to the voltage step obtained for the connection of a wye connected transformer.

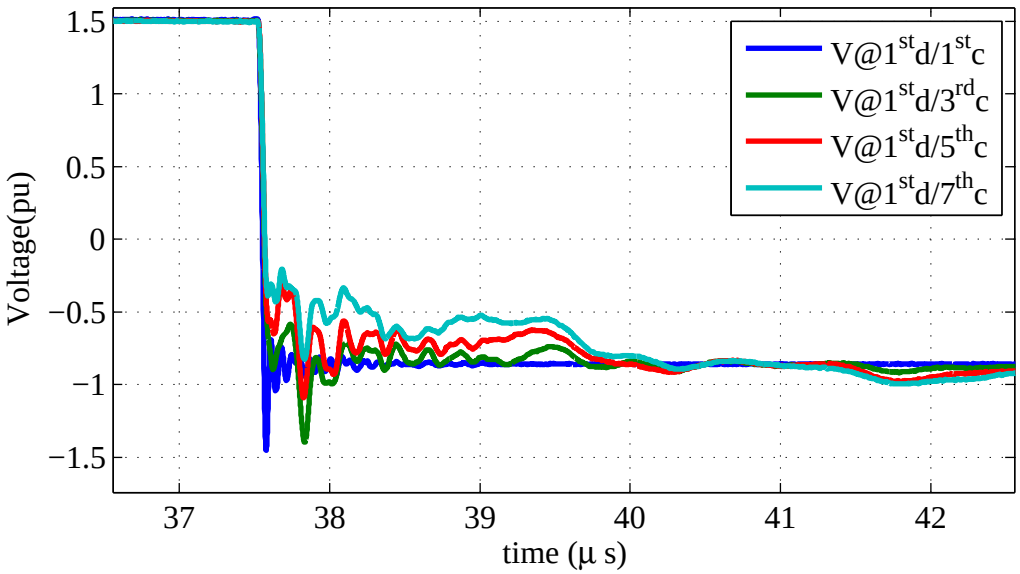

Figure 4.20: Turn voltages at 1^{st} disk during $35ns$ t_{rise} voltage step.

Fig. 4.20 shows zoomed switching transient presented in Fig. 4.19. A voltage step with a very short rise time of $35ns$ excited internal interlayer resonances, where strong oscillations are noted right after the step is applied. Consequently, a 50% overshoot of the voltage is observed at the first conductor.

Fig. 4.21 presents the turn-to-turn voltages recorded at the first disk. As observed with

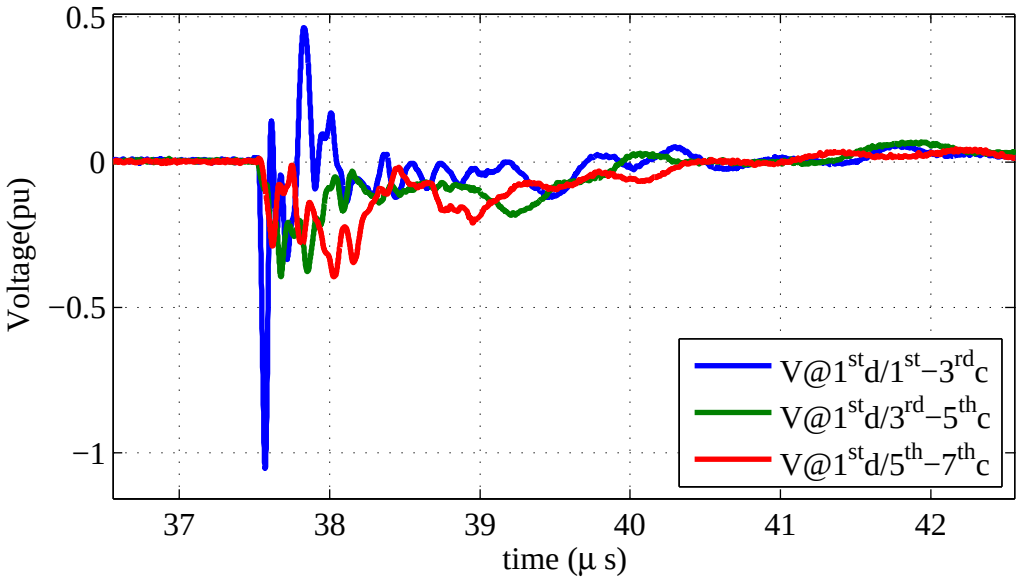

Figure 4.21: Turn-to-turn voltages at 1^{st} disk during $35ns$ t_{rise} voltage step.

the wye connected transformer, the frequency recorded at the top conductors at each coil varies between $13.7MHz$ at the first turn of the outer layer, down to $11.5MHz$ measured at the top conductors of the internal layers. The difference in the physical properties of the outer and the internal layers, where the outer layer has air as a boundary on one side, results in different resonant frequencies of the outer and the internal layers. As a consequence, the turn-to-turn voltage between the outer and the first internal layer is much higher compared to other turn-to-turn voltages, reaching the value of $1.05pu$ in the case of a connection of a delta transformer.

As presented in Fig. 4.21, the turn-to-turn voltage recorded during the energizing of a delta connected transformer exceeds the turn-to-turn voltages during the BIL impulse test and the energizing of a wye connected transformer. Furthermore, the turn-to-turn voltage recorded during this test is about 2.5 times higher than the turn-to-turn voltage recorded during the BIL test. The significant difference to the BIL test is that the peak voltage is recorded at the beginning, between the outer layer and the first internal layer, while during the BIL test, the highest recorded turn-to-turn voltage is recorded towards the end of the disk. The reason for the very high turn-to-turn voltage is the very short rise time of the voltage step that excites the internal layer-to-layer resonances.

As expected, with the increase of the rise time, the turn-to-turn voltage at the beginning of the disk is reduced. To record the behavior of an oil-insulated transformer, the winding is energized with a voltage step having a $500ns$ rise time. This rise time is typically recorded when oil type transformers are energized from a cable grid. Fig. 4.22 presents the turn-to-turn voltages during a $500ns$ rise time voltage step.

As it can be noted in Fig. 4.22, the internal inter layer resonances are not excited by a slower $500ns$ rise time voltage step. The overshoot in the voltage step does not exist any longer, and the response is very similar to the one recorded during the BIL test. The voltages at the first two layers are very similar, while some more notable voltage differences are recorded at the internal layers.

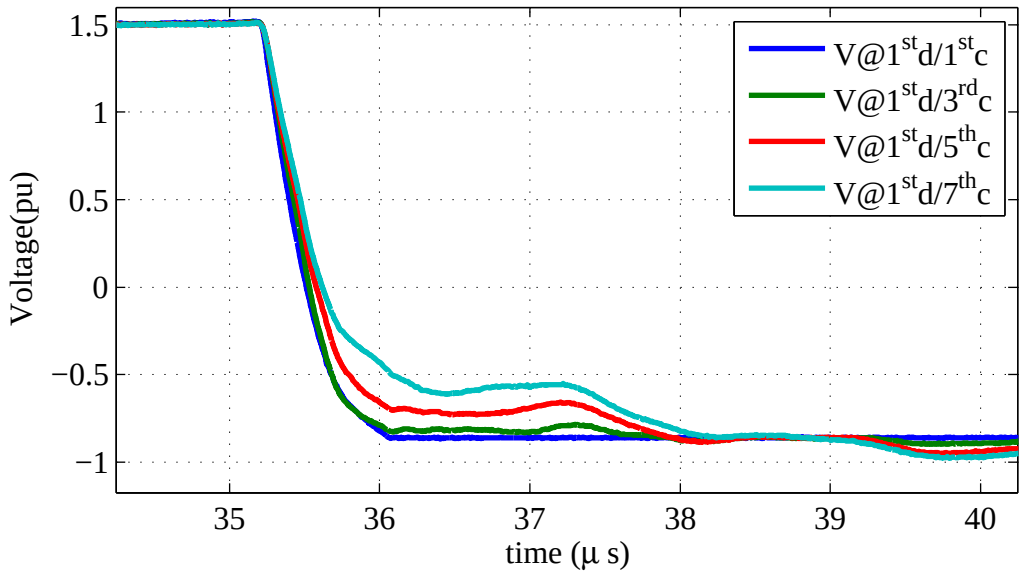

Figure 4.22: Turn voltages at 1^{st} disk during $500ns$ t_{rise} voltage step.

The turn-to-turn voltages recorded at the first disk are presented in Fig. 4.23.

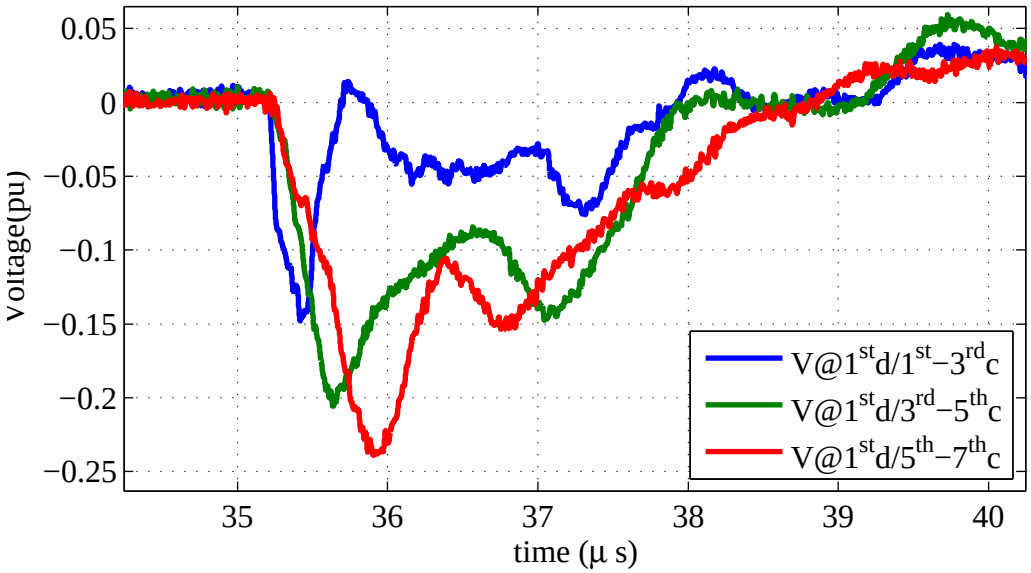

Figure 4.23: Turn-to-turn voltages at 1^{st} disk during $500ns$ t_{rise} voltage step.

For a slow rising voltage step, higher turn-to-turn voltages are recorded towards the end of the winding. The highest turn-to-turn voltage is recorded at the end of the disk and reaches a magnitude of $0.24pu$. This is because the slow rising pulse excites the resonant frequency of the disk where the highest oscillations are recorded at the end of the disk.

More than 10 tests are performed by incrementally increasing the rise time. As a result, a plot that shows the turn-to-turn voltage as a function of the rise time is obtained.

Fig. 4.24 shows how the turn-to-turn voltage decreases with increasing rise time of the voltage step. The highest turn-to-turn voltage is obtained for short rise times of the conduc-

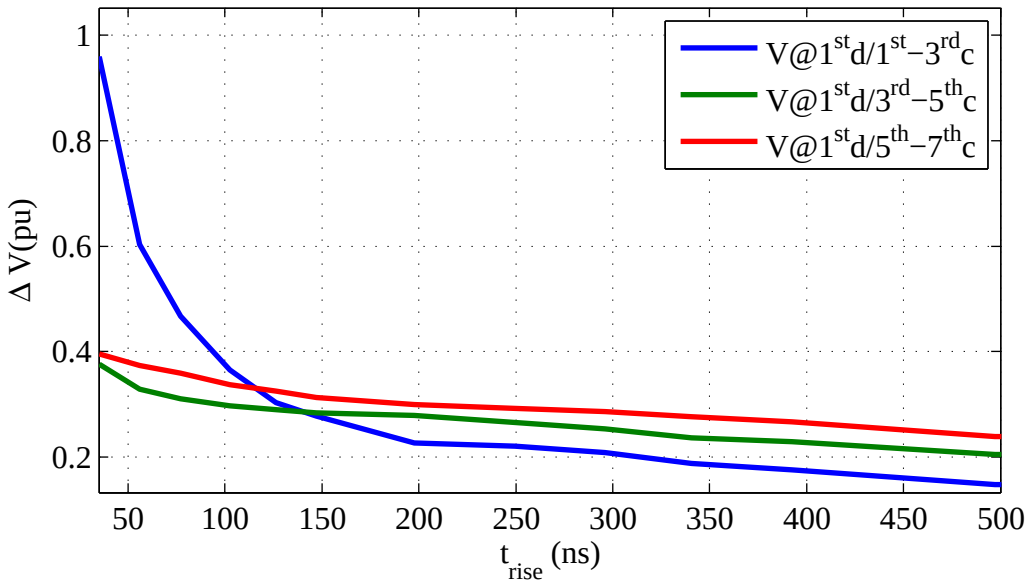

Figure 4.24: Turn-to-turn voltages at 1^{st} disk for different rise times t_{rise}.

tors, where for this case of the energizing of a delta connected transformer, the turn-to-turn voltage exceeds 2.5 times the voltage recorded during the BIL test.

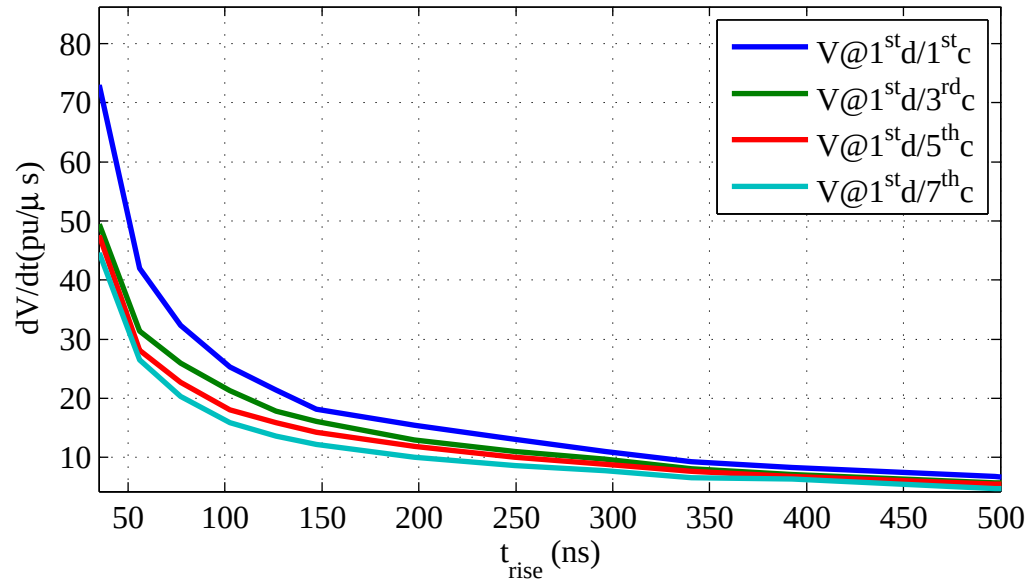

Figure 4.25: Voltage derivative $\frac{dV}{dt}$ at 1^{st} disk for different rise times t_{rise}.

Fig. 4.25 shows the voltage derivative as a function of the rise time. The maximum is obtained at the first conductor for the minimum rise time t_{rise}. This is expected, and the same behavior is observed in the previous two cases. However, the magnitude of the voltage derivative recorded in this case is very high. It exceeds about 10 times the maximum value recorded at the BIL test and 2 times the value obtained at the connection of a wye connected transformer test.

Measurements of the transient turn-to-turn voltages recorded at the first disk showed

clearly that a simple connection of a delta connected dry-type transformer in a cable grid results in a voltage with a very high magnitude. As the measurements show, the highest stress is in the beginning of the winding. This finding can explain failures of transformers reported in [6] and [7], where insulation failure and flashovers are noted at the beginning of the winding.

4.2.2 Turn-to-turn voltages in the 2^{nd} disk

After examining the voltage distribution and the turn-to-turn voltage stress in the 1^{st} disk, the 2^{nd} disk is analyzed. The voltage derivative and the rise time of the voltage step applied to the terminal of the winding decrease significantly as the wave propagates through the winding. Due to a constant speed of the wave propagation in the winding, it is expected that the turn-to-turn voltages are decreased significantly compared to the case of the 1^{st} disk. Since the obtained turn-to-turn voltages during the connection of a delta connected transformer reached values twice as high compared to the BIL test, it is very important to investigate if such high overvoltages can be created in the second disk during the switching transients.

Turn-to-turn voltages in the 2^{nd} disk during the BIL test

Let us first study the turn-to-turn voltages during the BIL test. As the rise time and the derivative of the voltage step are decreased significantly as the wave reaches the second disk, it is consequently expected that the turn-to-turn voltages decrease as well.

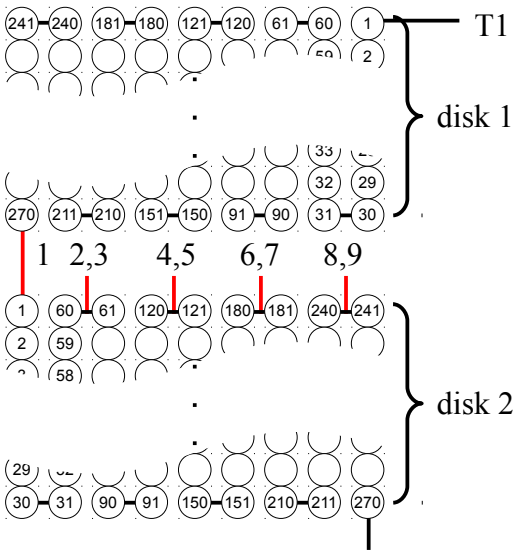

Figure 4.26: Measurement points at the 2^{nd} disk.

Fig. 4.26 shows the structure of the second disk and the measurement points at which the voltage probes are connected. Similarly to the the first disk, the voltage is measured at the top of the disk. This selection of measurement points gives us ability to measure the turn-to-turn voltage between the turns where it reaches the maximum. As it can be seen in the Fig. 4.26, these turns are 1, 61, 121, 181 and 241 respectively.

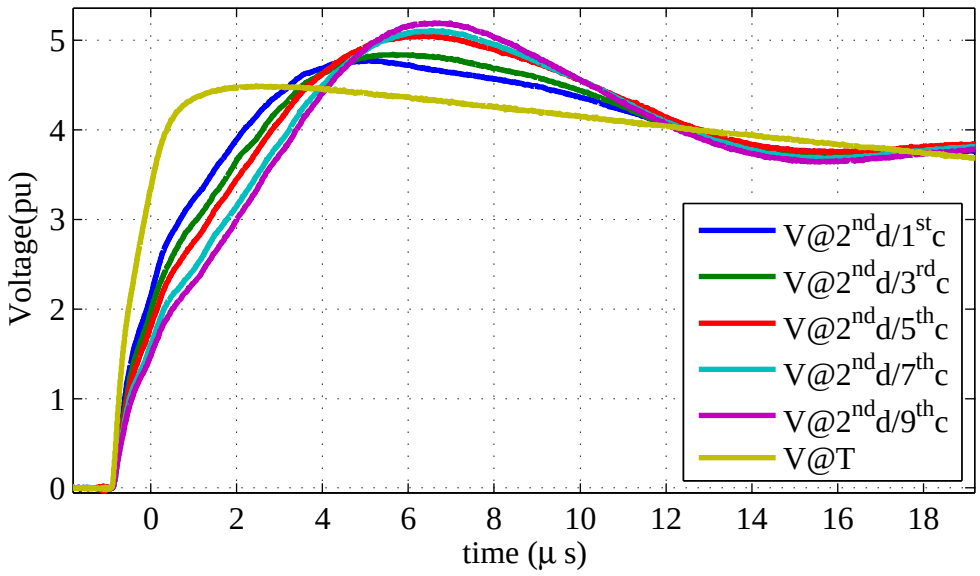

Figure 4.27: BIL at 2^{nd} disk - zoom.

Fig. 4.27 shows turn voltages recorded at the aforementioned measurement points. One can notice that the magnitude of oscillations increase as the measurement points move further down the winding. Added stray series capacitances and stray inductances decrease the frequency of the oscillations inversely proportional to the wire length, while the voltage magnitude increases to about $5.2pu$, which is an 18% increase over the magnitude of the voltage step applied to terminal T1.

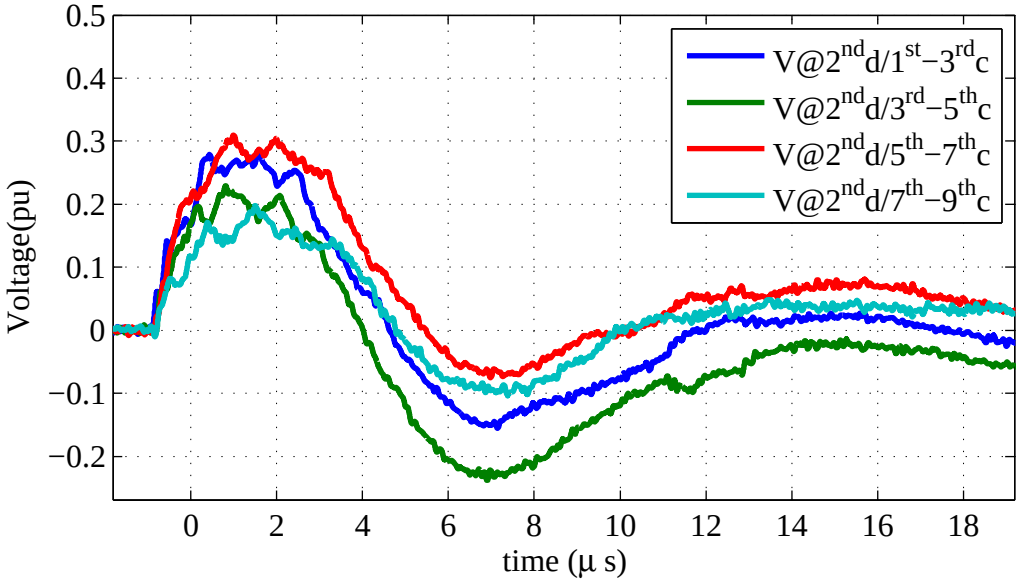

Figure 4.28: Turn-to-turn voltages at 2^{nd} disk during BIL.

The plot with the turn-to-turn voltages is presented in Fig. 4.28. Similarly to the 1^{st} disk, it can be noticed that the highest turn-to-turn voltage is not developed at the first turns. Instead, the highest voltage of about $0.3pu$ is obtained towards the end of the disk. The lightning impulse excites the internal resonant frequency measured at the 2^{nd} disk having a frequency of about $80kHz$, which is about half of the resonant frequency measured at the

end of the 1^{st} disk. This is quite expected since the length of the wire in the two disks is twice as long as the wire length in one disk alone. The highest turn-to-turn voltages are recorded towards the end of the disk. When the results presented in Fig. 4.27 and Fig. 4.28 are compared, it can be seen that the highest turn-to-turn voltage appears during the rise time of the voltage pulses.

The highest voltage derivative $\frac{dV}{dt}$ is recorded at the first layer with the value of $3.4pu/\mu s$, and the lowest is obtained at the last layer with the value of $2.4pu/\mu s$. This is much slower compared to $7.2pu/\mu s$ and $4.5pu/\mu s$ recorded at the first disk.

Turn-to-turn voltages in the 2^{nd} disk during connection of a wye connected transformer

In this test, a single voltage step is applied to the reactor. Using a voltage step, the connection of a wye connected transformer is simulated. The magnitude of the voltage step is set to a peak phase-to-ground voltage of $1pu$. This represents the worst case scenario, but due to a three phase system, it is very likely that the voltage during switching in reality usually is about this value. To take into account a wide variety of transformer sizes and insulation types, the rise time is varied between a minimum of $35ns$ to approximately $500ns$.

Fig. 4.29 shows the turn voltages recorded at the measurement points at the second disk. As a reference, the voltage step at terminal T1 is also shown in Fig 4.29. Due to a very short voltage step rise time of about $35ns$, parallel disk-to-disk and disk-to-ground stray capacitances, shape the voltage response at the second disk in the beginning of the transient. One can observe that the voltage at the beginning of the second disk is a little bit over half of the magnitude of the step recorded at terminal T1. During a fast rising voltage step, parallel stray capacitances determine the voltage distribution and the winding acts as a capacitive voltage divider. This behavior could not have been noted during the BIL test due to the slow rising voltage step shaped by the series stray capacitances and stray inductances. After the initial transient and oscillations are finished, after about $0.6\mu s$, the voltage response is determined by the series stray capacitances and stray inductances and continue to rise slowly.

The parallel stray capacitances reduce the fast rising voltage step magnitude at the second disk voltage step down to $0.6pu$ while the series stray capacitances and stray inductances increase the voltage magnitude to $5.2pu$. The rise time of the fast rising voltage step is increased to about $44ns$, which is still much shorter than $3.2\mu s$ recorded at the measurement point 1, or $4.5\mu s$ recorded at the measurement point 9.

The turn-to-turn voltages are presented in Fig. 4.30. As a consequence of a reduced voltage step magnitude recorded at the second disk, the turn-to-turn voltages are significantly lower compared to the turn-to-turn voltages recorded at the first disk during the same test. Since the turn-to-turn voltages remained quite high at $0.3pu$ during the BIL test, the voltage stress during the connection of the wye connected transformer reached only to about half of that magnitude. It can be noticed that the maximum turn-to-turn voltage produced by the difference in rise times reaches it's maximum of $0.1pu$ in the very beginning of the transient. The maximum of $0.15pu$ is reached after $300ns$ as a consequence of inter-layer oscillations. Since the inter-layer oscillations are excited by the fast rising voltage step, one can say

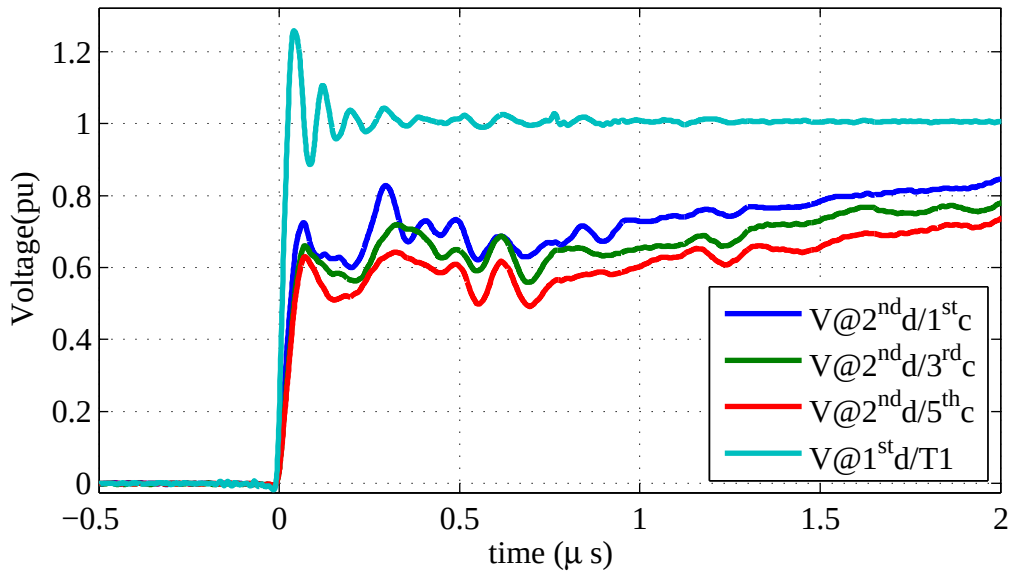

Figure 4.29: Turn voltages at 2^{nd} disk and at terminal T1 during $35ns$ t_{rise} voltage step.

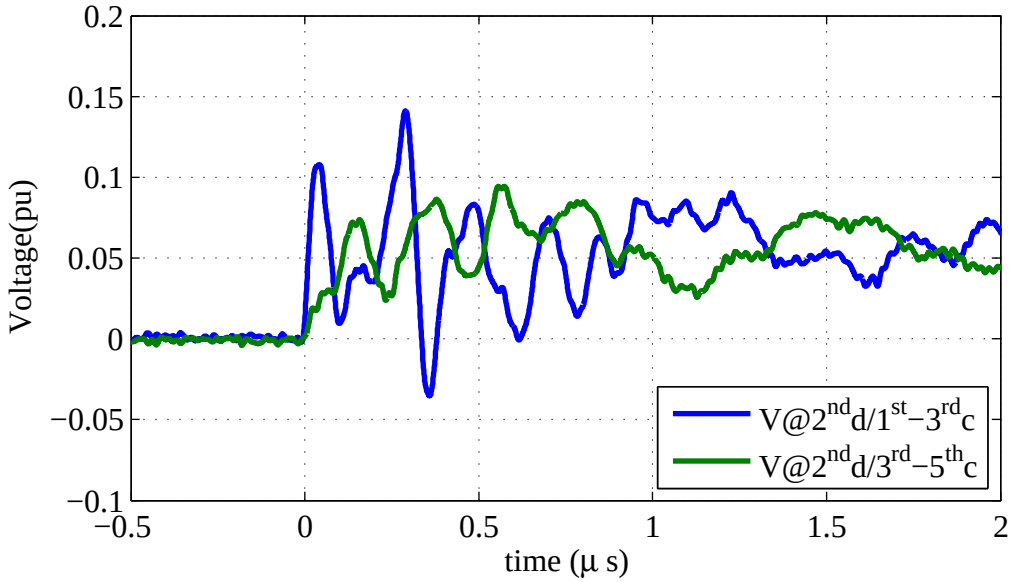

Figure 4.30: Turn-to-turn voltages at 2^{nd} disk during $35ns$ t_{rise} voltage step.

that the rise time of the voltage step directly impacts the magnitude of the turn-to-turn overvoltages.

The frequency at which the turn-to-turn voltage oscillates during the very fast transient is in the order of $10MHz$, which is about 100 times higher than the frequency of oscillations recorded during the BIL test. Furthermore, the highest turn-to-turn voltage obtained in the BIL test appears at the end of the disk, while for the very fast transient it is the opposite. The short rise time of the turn voltages during the very fast transient directly affect this.

When the rise time of the very fast transient decreases in order to simulate the switching of bigger transformers and/or transformers with oil insulation, the recorded response is very similar to the response recorded during the BIL test. Due to a much lower magnitude

compared to the BIL, the turn-to-turn voltages reached only $0.06pu$. The frequency content of the recorded turn-to-turn voltages is also similar to the ones obtained during the BIL test, where oscillations at about $80kHz$ and $1MHz$ are noted.

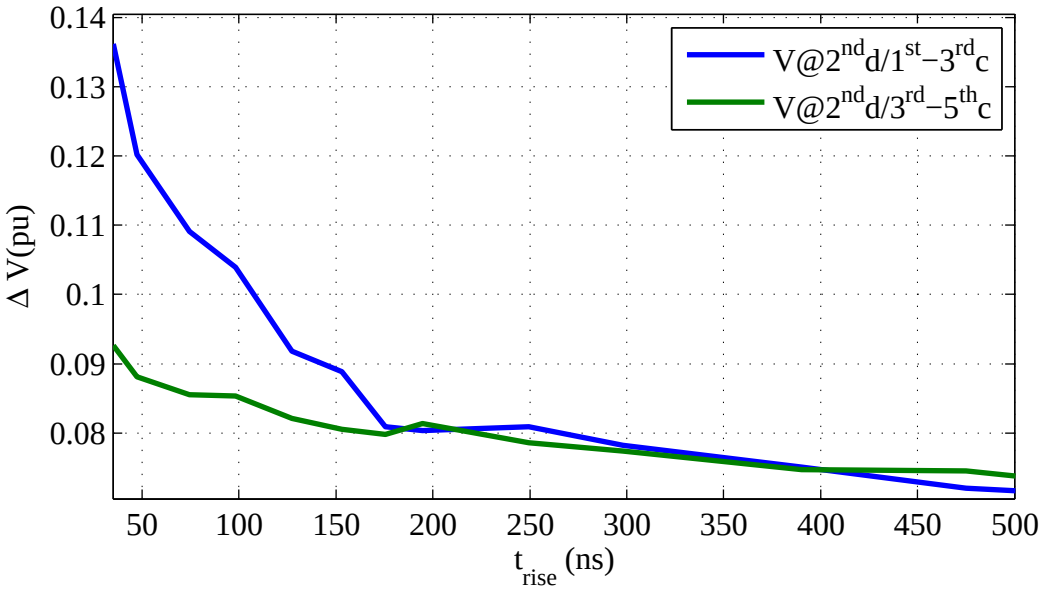

Figure 4.31: Turn-to-turn voltages at 2^{nd} disk for different rise times t_{rise}.

Fig. 4.31 presents the turn-to-turn voltages as a function of the rise time t_{rise}. As noted earlier, the highest turn-to-turn voltage is obtained for short rise times and in the first conductors. Once the rise time of the voltage step increases above $180ns$, the turn-to-turn voltages become almost identical across the whole disk, while the magnitude becomes very low, below $0.08pu$. Furthermore, Fig. 4.31 shows that only voltage steps with a rise time shorter than $180ns$ possess a rise time short enough to generate higher turn-to-turn voltages between the first layers. Consequently, these very fast transients excite high frequency oscillations between turns, which is noted in the plots.

Fig. 4.32 presents the voltage derivative $\frac{dV}{dt}$ as a function of the rise time t_{rise}. The highest voltage derivative is measured at the first conductor for the shortest rise time. The voltage derivative values recorded during this test are substantially higher than during the BIL test. The maximum voltage derivative recorded exceeds 2.5 times the value of $7.2pu/\mu s$ recorded at the first disk during the BIL test and 5.5 times the value of $3.3pu/\mu s$ obtained at the second disk during the BIL test.

Turn-to-turn voltages in the 2^{nd} disk during connection of a delta connected transformer

This test is performed by applying two voltage steps simultaneously to the reactor winding terminals. The magnitude of the voltage steps is set to $\pm 0.86pu$. This difference is the magnitude of the peak line-to-line voltage ($0.86 - (-0.86) = 1.72pu$). This is considered as the worst case scenario since the magnitude of the resulting voltage step is as highest then. The time delay between the positive and the negative step is set to 1/4 of the wave length of the resonant frequency of the winding, so the negative step is applied when the positive step

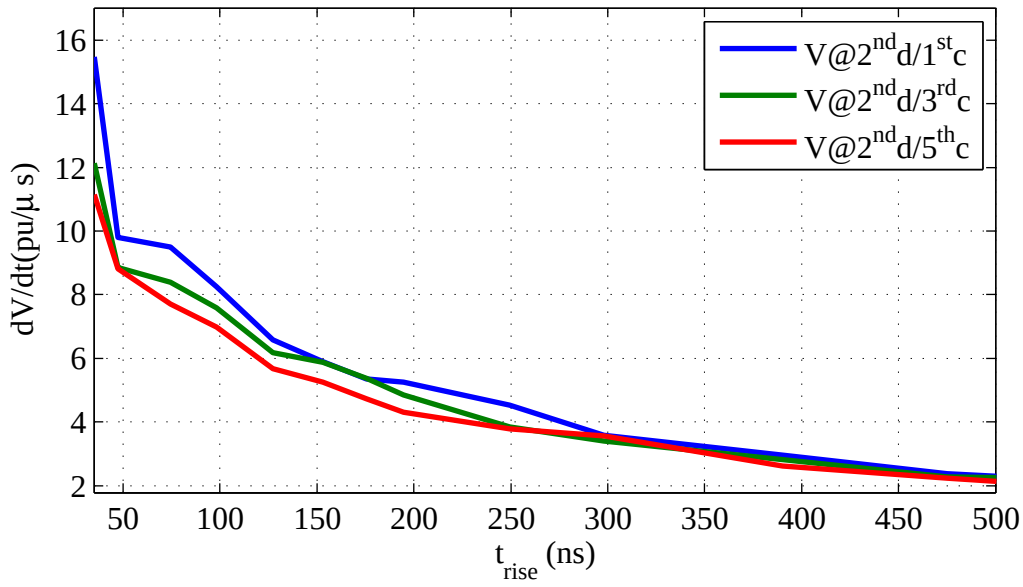

Figure 4.32: Voltage derivative $\frac{dV}{dt}$ at 2^{nd} disk for different rise times t_{rise}.

is at its maximum. By varying the rise time of the negative voltage step, the turn-to-turn voltages for different types of insulation and transformer sizes are studied. For very fast transient tests, a $35ns$ rise time is taken as the minimum rise time, where a $500ns$ rise time t_{rise} is set as the maximum, since this is the maximum rise time observed in oil-insulated transformers connected in cable systems.

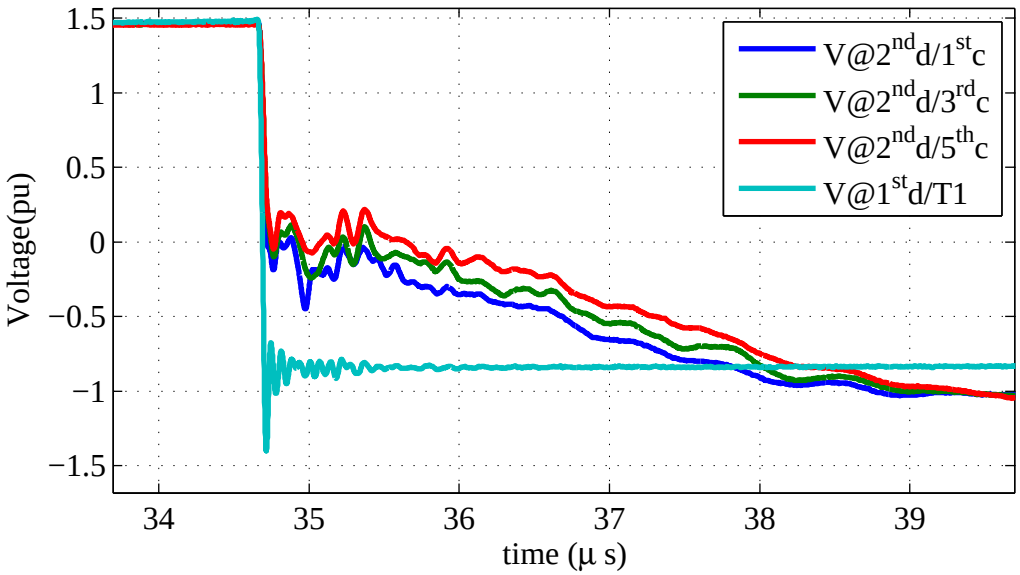

Figure 4.33: Turn voltages at 2^{nd} disk and at terminal T1 during $35ns$ t_{rise} voltage step.

Fig. 4.33 shows turn voltages recorded at the second disk and the voltage measured at the beginning of the winding at terminal T1. It can be noted that the magnitude of the voltage recorded at the second disk is reduced due to the parallel stray capacitances. As mentioned before, during very fast transients, the parallel stray capacitances shape the voltage magnitude during the beginning of the transient, where the winding acts as a capacitive

voltage divider. As a result, the magnitude of the voltage step is reduced to about 2/3 of the magnitude measured at the beginning of the winding.

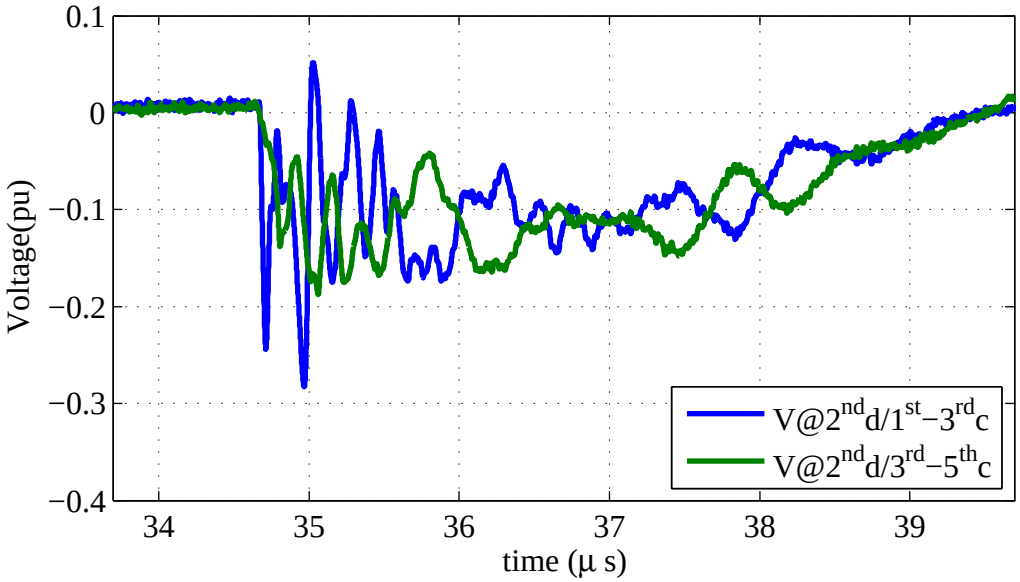

Figure 4.34: Turn-to-turn voltages at 2^{nd} disk during $35ns$ t_{rise} voltage step.

Fig. 4.34 shows the turn-to-turn voltages measured at the second disk. The internal interlayer resonances are excited by the voltage step with a very short rise time of $35ns$, where voltage oscillations of a high magnitude are noted right after the step is applied. As observed in the previous cases, the initial frequency recorded at the top conductors at each layer of the second disk varies between about $13MHz$ at the first turn of the inner layer, down to about $11MHz$ measured at the top conductors of the internal layers. The inner and the outer layers are bounded by air at one side which makes them different from the internal layers. Therefore, a discrepancy in frequencies of about $2MHz$ is measured in the disk.

The magnitude of the observed turn-to-turn voltages is much higher compared to the case of connecting a wye connected transient. It can be observed that the maximum turn-to-turn voltage produced by the front of the very fast transient reaches it's maximum of $0.23pu$ in the very beginning of the transient. A maximum of $0.28pu$ is reached after approximately $300ns$ as a consequence of inter-layer oscillations.

As shown in Fig. 4.34, the turn-to-turn voltage recorded during the connection of a delta connected transformer is slightly below the magnitude of the turn-to-turn voltages measured during the BIL impulse test. Moreover, although the magnitude of the voltage step is larger than during the connection of a wye connected transformer, due to a longer rise time of the voltage step, the measured turn-to-turn voltages at the second disk are lower than the turn-to-turn voltages recorded at the first disk during the connection of a wye connected transformer shown in Fig. 4.14. However, the recorded magnitude of the turn-to-turn voltage at the second disk is certainly not negligible and certainly makes a stronger insulation stress than the BIL voltage step due to a more than 100 times higher frequency of the transient and more than 100 times shorter rise time of the voltage step front.

For a transient with a slow rise time of about $500ns$, which simulates the switching of transformers with oil insulation, the recorded response is very similar to the response

recorded at the 2^{nd} disk during the BIL test. The magnitude of the recorded turn-to-turn voltages reached only $0.12pu$. The frequency content of the turn-to-turn voltages is also similar to the ones obtained during the BIL test, where oscillations at about $80kHz$ and $1MHz$ are noted.

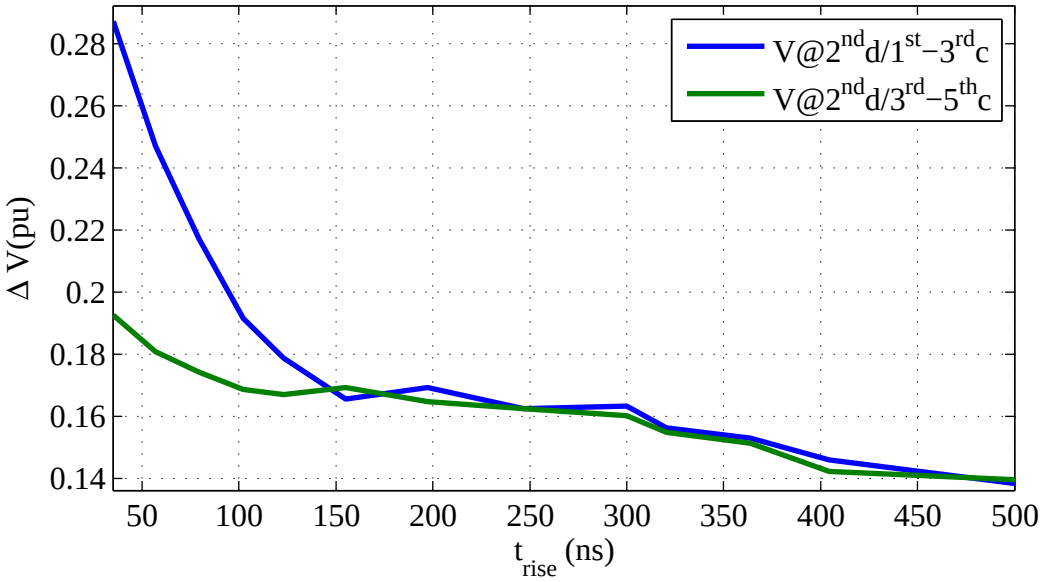

Figure 4.35: Turn-to-turn voltages at 2^{nd} disk for different rise times t_{rise}.

In order to obtain the turn-to-turn voltage as a function of the rise time of the voltage step, more than 10 tests are performed by incrementally increasing the rise time. Fig. 4.35 shows how the turn-to-turn voltage decreases with the increasing rise time of the voltage step. The highest turn-to-turn voltage is obtained for short rise times and for thefirst conductors. For this case i.e. the energizing of a delta connected transformer, the magnitude of the turn-to-turn voltages is just slightly lower than the magnitude obtained during the BIL test. However, the frequency and the rise time of the turn-to-turn voltage measured during very fast transients, exceeds the frequency and the rise time recorded during the BIL test more than 100 times.

The rise time affects the magnitude of the turn-to-turn voltages only if it is shorter than $150ns$. Once the rise time passes that value, the turn-to-turn voltages are almost identical across the critical points of the second disk.

The voltage derivative as a function of the rise time is presented in Fig. 4.36. The maximum value is obtained at the first conductor for the minimum rise time t_{rise}, while at the other conductors inside the disk, the magnitude of the voltage derivative is just a fraction lower. This plot confirms that the stress on insulation of the second disk during the very fast transient generated during the connection of a delta-connected transformer in a cable grid, significantly exceeds the stress produced during a BIL test. The voltage derivative recorded is more than 5 times the voltage derivative recorded at the first disk during the BIL test, and more than 11 times the voltage derivative of $3.3pu/\mu s$ recorded at the second disk. The insulation stress on the second disk during the connection of a delta-connected transformer is similar to the stress on the first disk during the connection of a wye-connected transformer in terms of the turn-to-turn voltage rise time and the time derivative. Only the magnitude of the turn-to-turn voltage is a fraction lower.

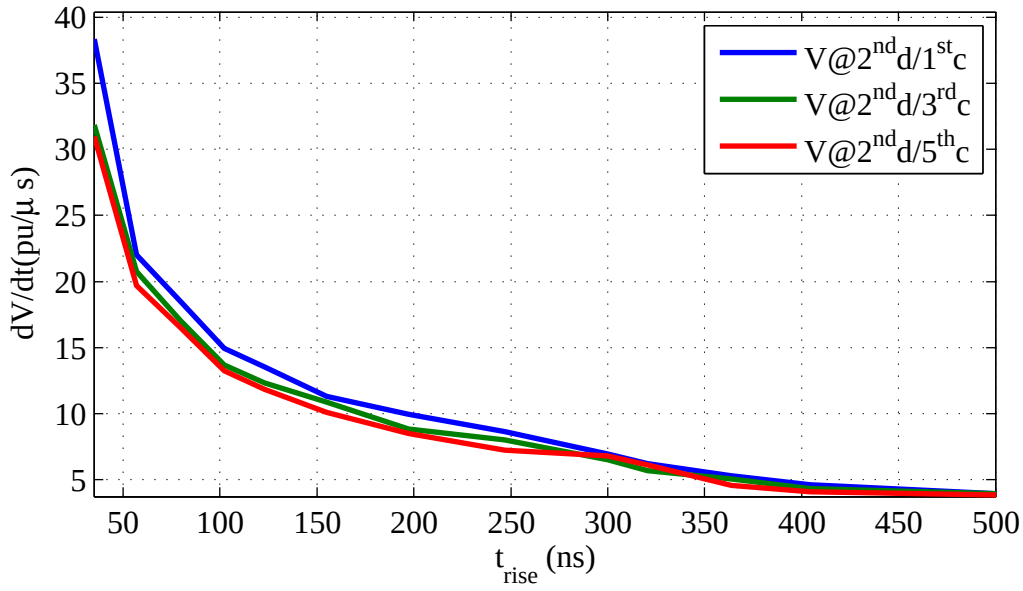

Figure 4.36: Voltage derivative $\frac{dV}{dt}$ at 2^{nd} disk for different rise times t_{rise}.

4.2.3 Turn-to-turn voltages in the 3^{rd} disk

The next disk that is going to be examined is the third disk. The voltage stress in terms of the turn-to-turn voltage magnitude, the rise time and the derivative of the voltage is decreasing along the winding. Already at the second disk, the magnitude of the turn-to-turn voltage recorded during fast transients dropped below the highest level recorded during the BIL test. However, the turn-to-turn voltages during the connection of a delta-connected transformer were quite high, almost on the level of the turn-to-turn voltages at the second disk produced by the BIL. Therefore, it is very important to investigate voltages even at the third disk.

Turn-to-turn voltages in the 3^{rd} disk during the BIL test

The results of the BIL test are always taken as the reference in this study, and for that reason, the turn-to-turn voltages are measured and studied first. As we have seen during the previous tests, the rise time and the derivative of the voltage step are decreased gradually as the point of observation is moving further from the terminal to which the voltage excitation is applied. Therefore, initially the voltages excited by the BIL are measured at the third disk.

Fig. 4.37 shows the structure of the third disk and the measurement points at which the voltages are studied. Similarly to the first two disks, the voltage is measured at the top of the third disk. Like in the first disk, the outer layer is the first layer of the disk. This measurement points are selected since the highest turn-to-turn voltages obtained there. They are shown in Fig. 4.37, and these turns are 1, 61, 121, 181 and 241.

Fig. 4.38 presents turn voltages recorded at measurement points 1, 3 and 5. It can be noticed that the magnitude of oscillations is almost identical on the measurement points

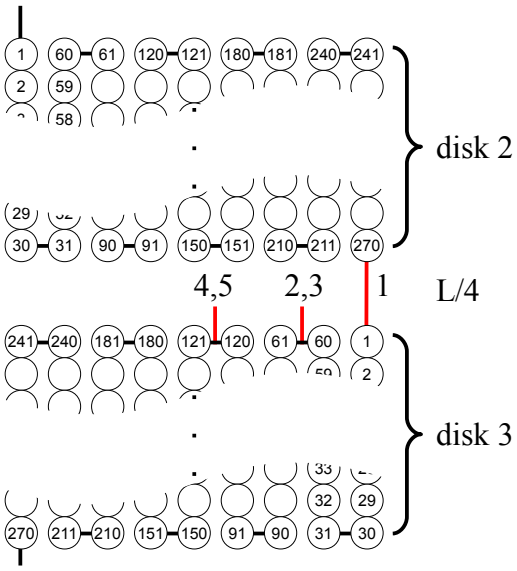

Figure 4.37: Measurement points at the 3^{rd} disk.

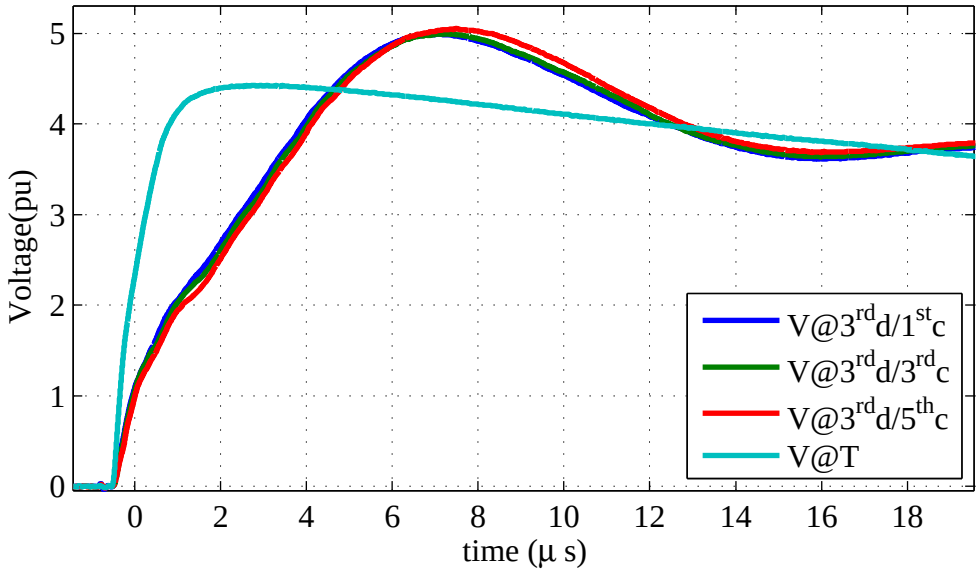

Figure 4.38: BIL at 3^{rd} disk - zoom.

at the third disk. The frequency of the oscillations recorded at the winding is inversely proportional to the wire length due to added stray series capacitances and stray inductances. The magnitude of the voltage increases to about $5.1pu$, which represents a 16% increase in the magnitude of the voltage step applied to the terminal T1.

The turn-to-turn voltages during the BIL test are presented in Fig. 4.39. Due to expected low values of the turn-to-turn voltages, the measurements were performed only on the first half of the disk, where the last measurement point is point 5. The highest voltage of about $0.12pu$ is obtained between layers 3 and 5 and is just slightly higher than the turn-to-turn voltage recorded between the outer and the first internal layer. It can be noted that with three times longer wires, the resonant frequency is about one third of the resonant frequency recorded at the first disk during the BIL test. The resonant frequency measured at the 3^{rd}

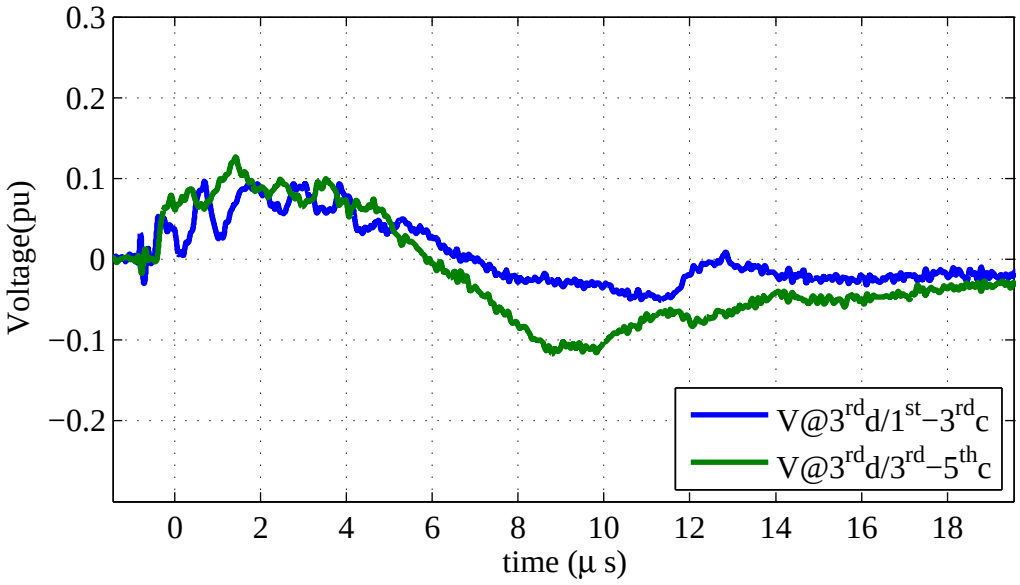

Figure 4.39: Turn-to-turn voltages at 3^{rd} disk during BIL.

disk is at about $50kHz$, which is about one third of the resonant frequency measured at the end of the 1^{st} disk. When the turn-to-turn voltages in the beginning of disks 2 and 3 are observed in Figs. 4.28 and 4.39 respectively, one can note that the first zero crossing of the turn-to-turn voltage appears in about $4\mu s$ at the second disk and about $6\mu s$ in the third disk.

The highest voltage derivative $\frac{dV}{dt}$ is recorded at the first layer with the value of $2.8pu/\mu s$, and the lowest is obtained at the last layer with the value of $2.4pu/\mu s$. This differs significantly from the values of $7.2pu/\mu s$ and $3.4pu/\mu s$ recorded at the beginning of the first and the second disk respectively.

Turn-to-turn voltages in the 3^{rd} disk during connection of a wye connected transformer

A single voltage step is applied to the reactor during the test of the connection of a wye-connected transformer in a cable grid. The connection of a wye-connected transformer is simulated by energizing the winding by a single voltage step. The magnitude of the voltage step is set to the peak phase-to-ground voltage of $1pu$ which represents the worst case scenario. The rise time of the voltage step is varied between the minimum of a $35ns$ to approximately $500ns$ to account for energizing transients of transformers with different insulation types.

Fig. 4.40 presents the turn voltages obtained at the measurement points 1,3 and 5 at the third disk and at terminal T1 which is shown as a reference. Because of a very fast rising time of the voltage step, parallel disk-to-disk and disk-to-ground stray capacitances are dominant during the initial transient and shape the voltage response at the third disk in the beginning of the transient. It can be noted that the magnitude of the voltage step recorded at the beginning of the third disk is decreased significantly when compared to the voltage magnitude on the terminal T1, and even on the beginning of the second disk.

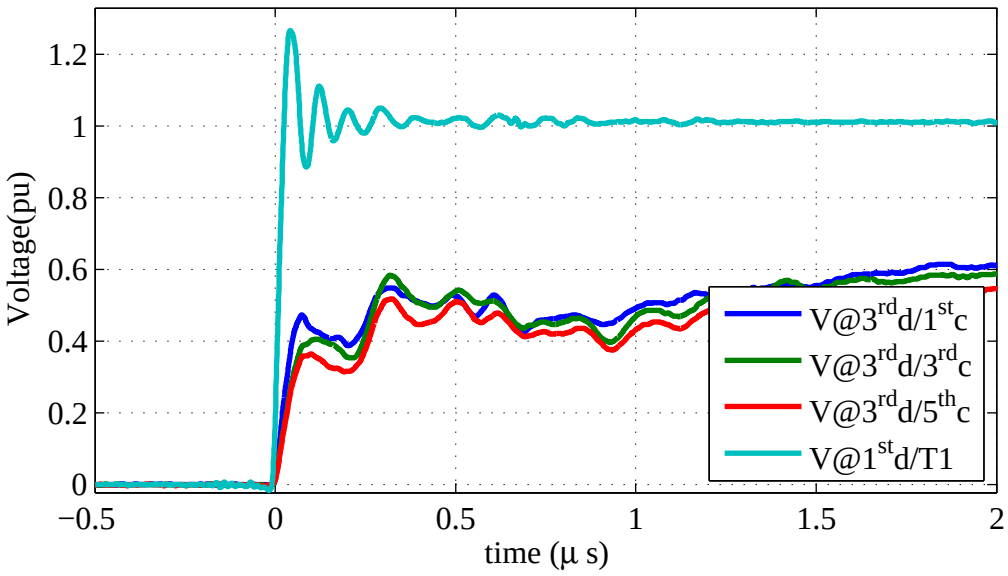

Figure 4.40: Turn voltages at 3^{rd} disk and at terminal T1 during $35ns$ t_{rise} voltage step.

This behavior is not observed during the BIL test due to a slowly rising voltage step that is determined by the series stray capacitances and stray inductances. After the initial transient and oscillations are completed after about $0.6\mu s$, the voltage continues to rise slowly since it is, after the initial transient, shaped by the series stray capacitances and stray inductances.

The magnitude of the voltage step recorded at the beginning of the third disk during this test is about 2/3 of the magnitude recorded at the beginning of the second disk and about 44% of the magnitude of the voltage recorded at the beginning of the disk during the same test. The magnitude of the voltage step is limited by parallel stray capacitances and it is significantly lower than $5.1pu$ recorded at the third disk during the BIL test. The rise time of the voltage step is about $48ns$, which is still much shorter than the $4.5\mu s$ recorded during the BIL test.

Fig. 4.41 shows the turn-to-turn voltages recorded at the third disk during the connection of a dry-type wye-connected transformer in a cable grid. As a direct consequence of a reduced voltage step magnitude, the turn-to-turn voltages are substantially lower when compared to the turn-to-turn voltages recorded at the first and the second disk during the same test. The magnitude of the maximum recorded turn-to-turn voltage is almost identical to the maximum magnitude recorded during the BIL test. In both cases, the highest voltage stress is between the first measurement points.

Due to the same structure of each disk, interlayer resonant frequencies are identical at each disk. As it was recorded in the first and the second disk, the frequency recorded during the beginning of the transient, at the top conductors at each coil of the third disk varies between $11MHz$ and $13MHz$, between the internal layers and the outer layer respectively. Similarly to the second disk, the rise time recorded at the first layer is not much shorter compared to the rise times measured at the internal conductors.

The frequency at which the turn-to-turn voltage oscillates during the very fast transient is in order of $10MHz$, while the high frequency oscillations during the BIL test are about $60kHz$, which is about 200 times lower. Moreover, the highest turn-to-turn voltage obtained

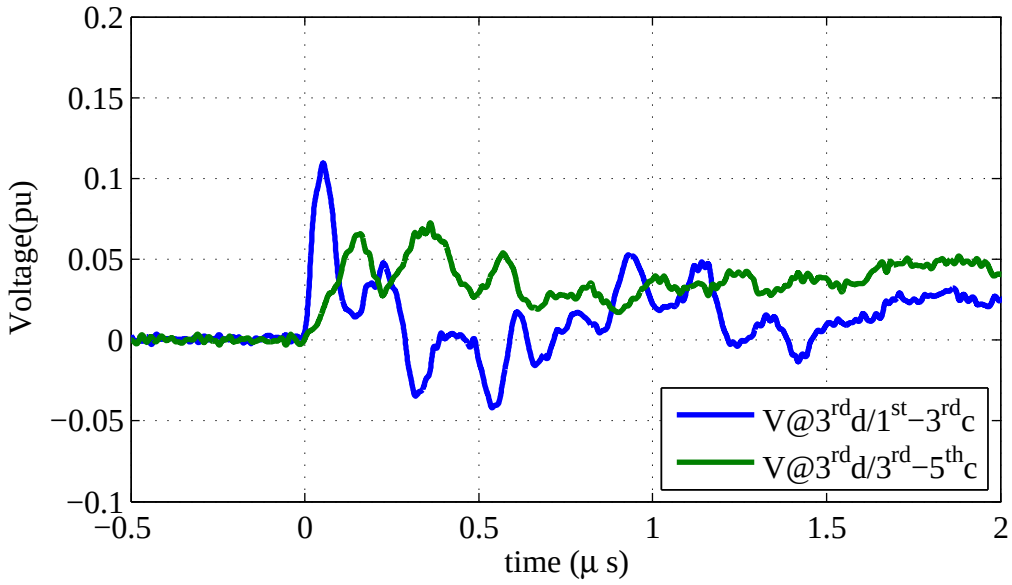

Figure 4.41: Turn-to-turn voltages at 3^{rd} disk during $35ns$ t_{rise} voltage step.

during the very fast transient appears on the outer layers and in the beginning of the disk, while during the BIL test it appears at the end of the disk. This is directly influenced by the short rise time of the turn voltages.

During the test with a $500ns$ rise time voltage step, the recorded response is very similar to the response recorded during the BIL test. Due to a much lower magnitude compared to the BIL, the turn-to-turn voltages is below $0.05pu$. The frequency content of the recorded turn-to-turn voltages is also similar to the ones obtained during the BIL test, where oscillations at about $80kHz$ and $1MHz$ are noted.

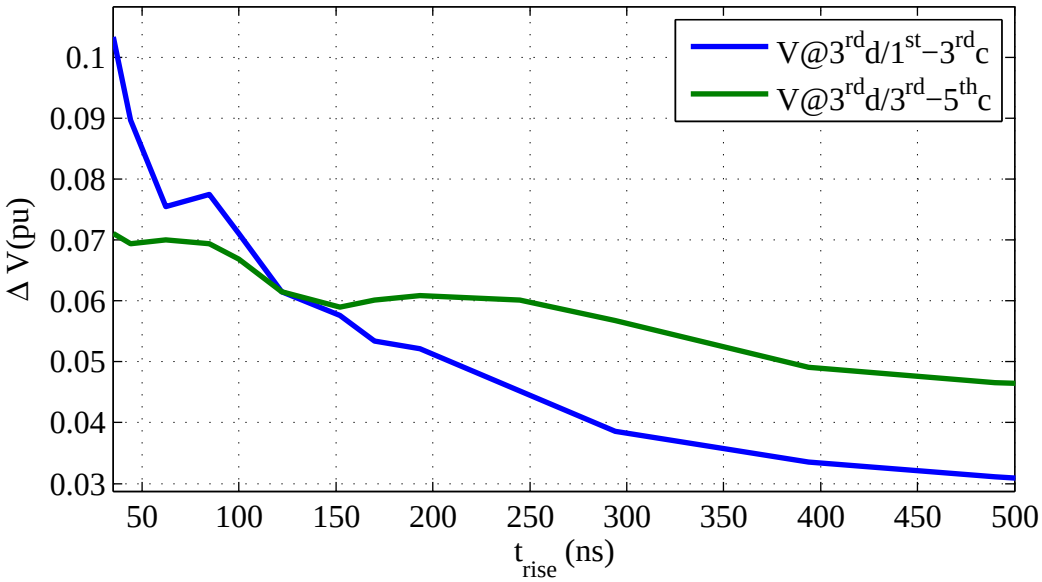

Figure 4.42: Turn-to-turn voltages at 3^{rd} disk for different rise times t_{rise}.

Fig. 4.42 presents the turn-to-turn voltages as a function of the rise time t_{rise}. The highest turn-to-turn voltage is obtained at the first conductors and during short rise times. Once

the rise time of the voltage step increases above $150ns$, the turn-to-turn voltage between internal layers becomes larger than the turn-to-turn voltage recorded at the first layers. Moreover, Fig. 4.42 shows that only voltage steps with a rise time shorter than $150ns$ can generate higher turn-to-turn voltages between the first layers and excite oscillations of very high frequency noted only at the plots where the winding is excited by very fast voltage transients. The same observation is made for the first two disks.

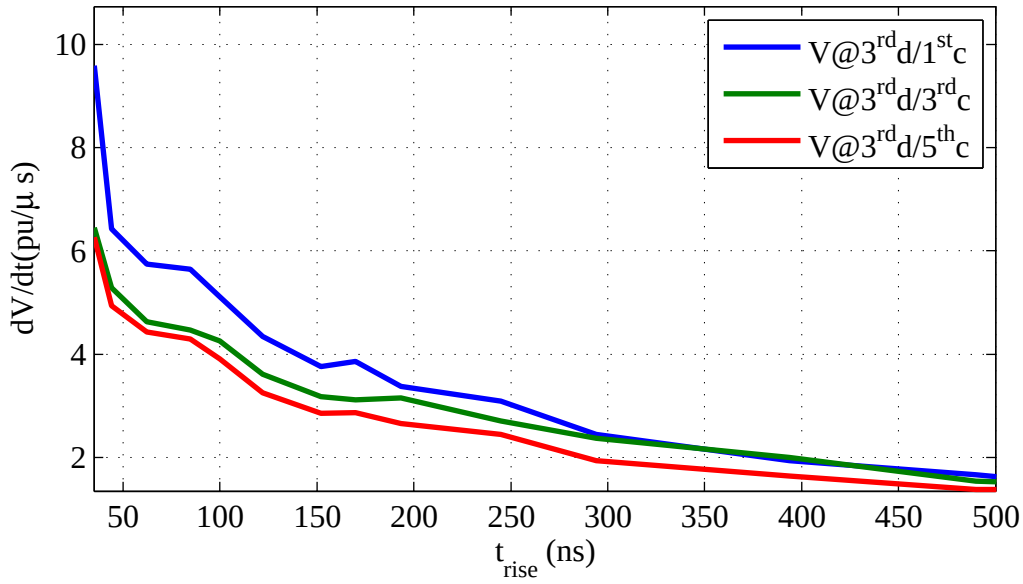

Figure 4.43: Voltage derivative $\frac{dV}{dt}$ at 3^{rd} disk for different rise times t_{rise}.

Fig. 4.43 shows the voltage derivative $\frac{dV}{dt}$ as a function of the rise time t_{rise}. The highest voltage derivative is observed between the first layers for the shortest rise time. The voltage derivatives recorded during this test are substantially higher than during the BIL test. The maximum voltage derivative recorded during this test is $10pu$ compared to the value of $7.2pu/\mu s$ recorded at the first disk during the BIL test and it is about 3.5 times larger than the maximum voltage derivative obtained at the third disk during the BIL test.

Turn-to-turn voltages in the 3^{rd} disk during connection of a delta connected transformer

The test that simulates the connection of a delta-connected transformer is performed by applying two voltage steps with a short time delay to the reactor winding terminals. As mentioned before, the magnitude of the voltage steps is set to $\pm 0.86pu$, so a peak line-to-line voltage is achieved. Identically to the same test applied to the first two disks, a time delay of about 1/4 of the wave length is set between the positive and the negative voltage step. This test is performed with different rise times of the negative voltage step. As the shortest rise time, a value of $35ns$ is taken. A $500ns$ rise time t_{rise} is set as the maximum since this is the maximum rise time observed in oil-insulated transformers connected in a cable system.

Fig. 4.44 presents turn voltages recorded at the third disk and the voltage measured at the beginning of the winding at terminal T1. The magnitude of the voltage obtained at the third disk is reduced substantially due to parallel stray capacitances. During very fast

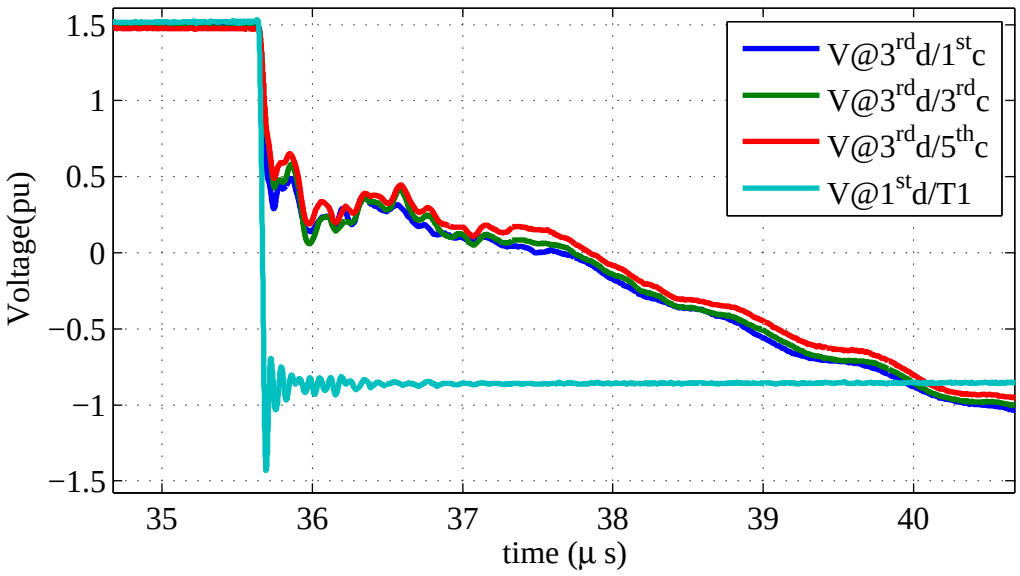

Figure 4.44: Turn voltages at 3^{rd} disk and at terminal T1 during $35ns$ t_{rise} voltage step.

transients it is the parallel stray capacitances that directly determine the voltage magnitude during the beginning of the transient. When compared to the voltage magnitude obtained at terminal T1 and at the first conductor of the second disk, the magnitude of the voltage step is reduced to about 2/3 of the magnitude measured at the beginning of the previous disk. This same behavior is noted during the connection of a wye-connected transformer.

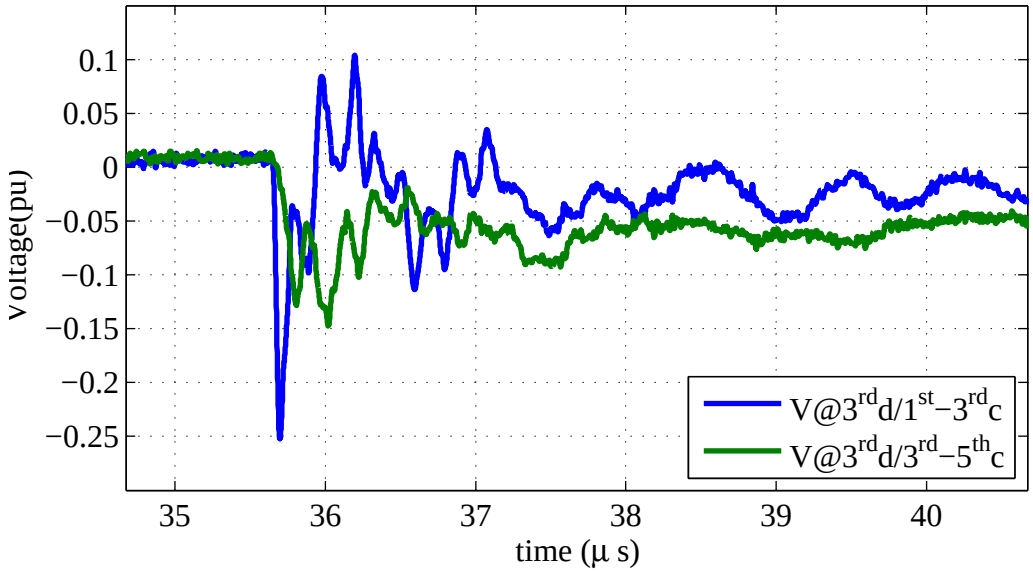

Figure 4.45: Turn-to-turn voltages at 3^{rd} disk during $35ns$ t_{rise} voltage step.

Fig. 4.45 presents the turn-to-turn voltages measured at the third disk during the very fast transients. The voltage step with a rise time of $35ns$ excites internal interlayer resonances, with substantial voltage oscillations of a high magnitude noted in the first $1\mu s$ of the transient. Similarly to the previous cases, the frequency of the oscillations recorded at the top conductors at each layer of the third disk varies between about $13MHz$ at the first turn of first layer, down to about $11MHz$ measured at the top conductors of the internal layers.

Since each disk is constructed equally, such a result is expected where the same resonant frequencies are excited in all observed disks.

The magnitude of the observed turn-to-turn voltages is much higher compared to the case of connecting a wye connected transient and the BIL test. It can be observed that the maximum turn-to-turn voltage produced by the front of the very fast transient reaches it's maximum of $0.25pu$ in the very beginning of the transient. This is a very high magnitude and is comparable to magnitudes obtained at first two disks during the BIL test. Furthermore, it is 2.5 times larger than the turn-to-turn voltage recorded at the third disk during the BIL test. This means that substantially larger insulation stress is applied to the third disk during a simple connection than during a BIL test.

The frequency and the rise time of the turn-to-turn voltage recorded during this test is about 200 times higher than the frequency of the turn-to-turn voltage recorded during the BIL test. Furthermore, the rise time is about 100 times shorter than the rise time during a BIL test. This additionally increases the insulation stress on the third disk.

Since the rise time of the voltage step is responsible for high turn-to-turn voltages, it is expected that voltage steps with a longer rise time will produce lower turn-to-turn voltages at the third disk. A $500ns$ rise time voltage step produces similar turn-to-turn voltages as recorded during the BIL test. The maximum turn-to-turn voltage during energizing with a $500ns$ voltage step is about $0.08pu$.

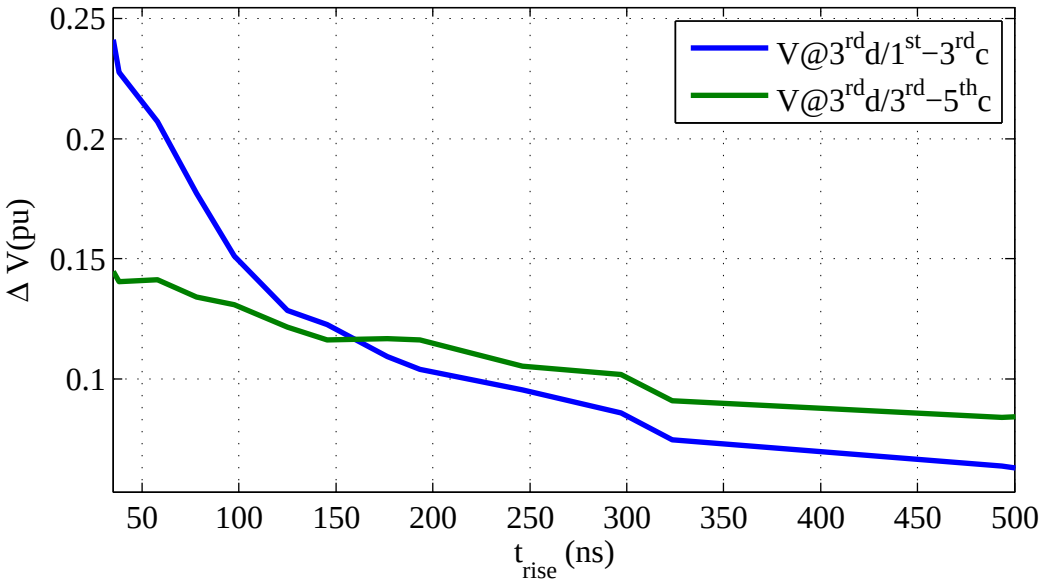

Figure 4.46: Turn-to-turn voltages at 3^{rd} disk for different rise times t_{rise}.

Fig. 4.46 presents the turn-to-turn voltages as a function of rise time of the voltage step. More than 10 tests are performed where the rise time of the voltage step is increased incrementally from $35ns$ to about $500ns$. The highest turn-to-turn voltage is measured during the test with a short rise times and at first conductors. The magnitude of the turn-to-turn voltages recorded during the energizing of a delta connected transformer is slightly lower than the magnitude obtained during the BIL test. However, the rise time of the turn-to-turn voltage and the frequency measured during very fast transients, exceeds the rise time and the frequency recorded during the BIL test more than 100 times.

The rise time affects the magnitude of the turn-to-turn voltages only if it is shorter than $160ns$. Very similar and almost identical behavior is noted at the first two disk. Once the rise time increases over that value, the turn-to-turn voltage at the first disk becomes lower than the voltage recorded at the internal layers.

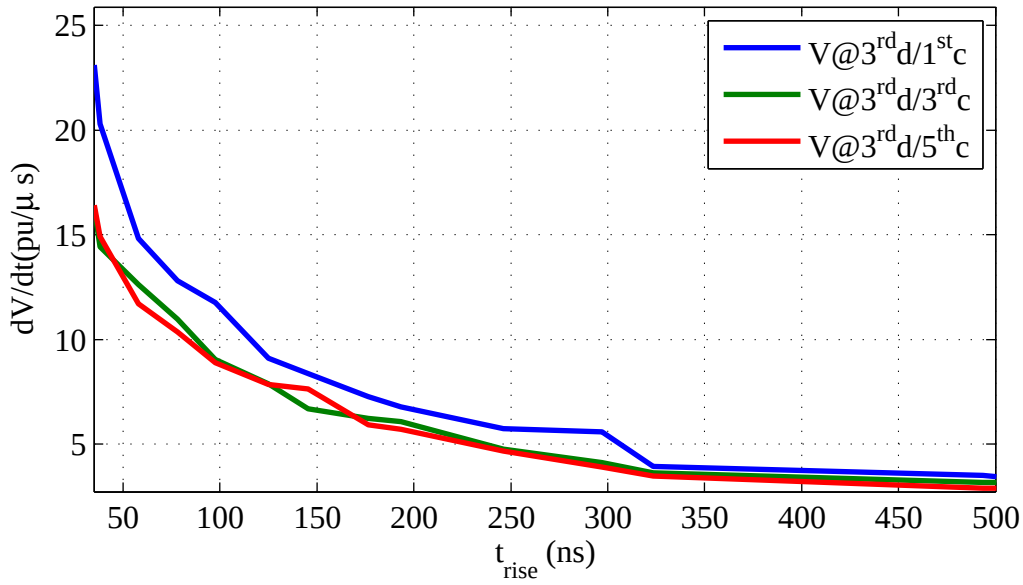

Figure 4.47: Voltage derivative $\frac{dV}{dt}$ at 3^{rd} disk for different rise times t_{rise}.

Fig. 4.47 shows the voltage derivative as a function of the rise time. The maximum value of the voltage derivative is obtained at the first conductor for the minimum rise time t_{rise}. The magnitude of the voltage derivative measured at the other conductors inside the disk is slightly lower. The stress on the insulation of the third disk during the very fast transient generated by the connection of a delta-connected transformer in a cable grid in terms of the voltage derivative, significantly exceeds the stress generated during the BIL test. The voltage derivative obtained is more than 3.5 times the voltage derivative measured at the first disk during the BIL test, and more than 9 times the voltage derivative of $2.8pu/\mu s$ recorded at the third disk. The insulation stress in terms of the turn-to-turn voltage rise time and the time derivative measured on the third disk during the connection of a delta-connected transformer is similar to the stress on the second disk, and on the first disk during the connection of a wye-connected transformer. Only the magnitude of the turn-to-turn voltage is slightly lower. Furthermore, the highest stress is recorded at the first conductor. This finding can explain some of the failures of transformers reported in [5] and [7], where the insulation failure and flashovers are recorded at the outer layers of the winding.

4.3 Critical voltage

The analysis conducted in this chapter showed that the rise time of the voltage steps significantly influences the turn-to-turn voltages. Consequently, voltage steps with rise times shorter than the rise time of the lightning impulse increase the voltage stress between the turns of a winding for the same magnitude of the voltage steps. Furthermore, the highest stress is recorded on the top disk, which is the first one exposed to the voltage step.

Plots shown in this Chapter, show how the turn-to-turn voltages increase with the rise time of the voltage steps. The highest voltage stress that transformers are able to withstand without damaging its insulation, is defined by the lightning impulse. In this case, a $4.4pu$ lightning pulse produced the highest turn-to-turn voltage of $0.38pu$ at the top disk. However, it is important to show how the magnitude of the critical voltage steps decreases with decreasing rise times. Critical voltage steps are those that produce a magnitude of $0.38pu$ of turn-to-turn voltage at the top disk. It is assumed that the insulation breakdown appears at the same voltage level for different rise times. This assumption is not entirely accurate, but it is expected that breakdown voltages decreases with rise times due to a higher voltage derivative.

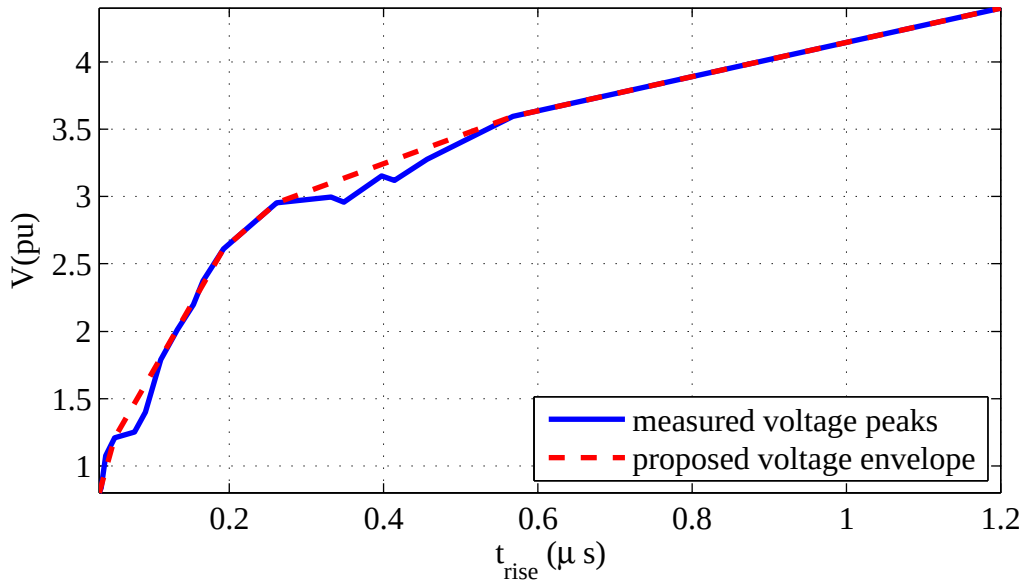

Figure 4.48: Voltage envelope - critical voltage as function of rise time.

Fig. 4.48 shows the critical voltage as a function of the rise time. It shows that the magnitude of the critical voltage reduces significantly with the rise time. For rise times shorter than $200ns$ the critical voltage drops to about 60% of the BIL. With the decrease of the rise time further on, the critical voltage drops linearly, and reaches about 25% of the BIL for a voltage step with a $50ns$ rise time.

Chapter 5

Standards for distribution transformers and inverter-fed motors

5.1 Comparison of standards

The results obtained in this work are compared to standard values of the basic lightning impulse voltage level (BIL). The standards for both dry-type and oil filled transformers define for each voltage level the BIL at which the transformer will not show any signs of insulation damages. These voltage impulse tests are considered as the strongest stress that can occur to the insulation of a transformer and therefore, if the transformer is able to withstand this voltage without any damages, its insulation will most probably survive other high frequency transients.

The BIL defined by standards for dry-type and oil-impregnated transformers is given in Table 5.1.

Table 5.1: Nominal System Voltage and Basic Lightning Impulse Insulation Levels (BIL) for Dry-type and Oil-filled Transformers [67],[68].

	BIL (kV)	45	60	75	95	110	125	150	200
U_{nom}									
8.7 (DT)		S	1		1				
15 (DT)			S		1	1			
24 (DT)					2	S	1	1	
34.5 (DT)							2	S	1
8.7			S						
15				S					
24								S	
34.5									S

In Table 5.1 "S" is referred as the standard value, "1" as an optional higher level where the transformer is exposed to high overvoltages, "2" is the case where surge arresters are used and found to provide appropriate surge protection and DT is dry-type transformers.

Standards [67],[68] do not specify any additional test that may produce voltage waveforms

with a very short rise time, such as the chopped-wave test used for power transformers at higher voltage levels. As it is shown in Chapter 4, distribution transformers can be exposed to transients with very short rise times. Consequently, these transients produce critical turn-to-turn voltages even when the magnitude of the voltage steps is reduced significantly. However, when it comes to standards for distribution transformers, nothing is defined yet.

NEMA, IEC and IEEE standards for motors consider maximum voltage withstand for transients with rise times shorter than $1.2\mu s$ [69]-[71]. The IEC standard for large motors includes surges with a rise time as short as $0.5\mu s$, NEMA standard accounts for surges with up to a $0.1\mu s$ rise time, while the IEEE standard includes even an ideal voltage step with zero rise time in it's voltage withstand envelope.

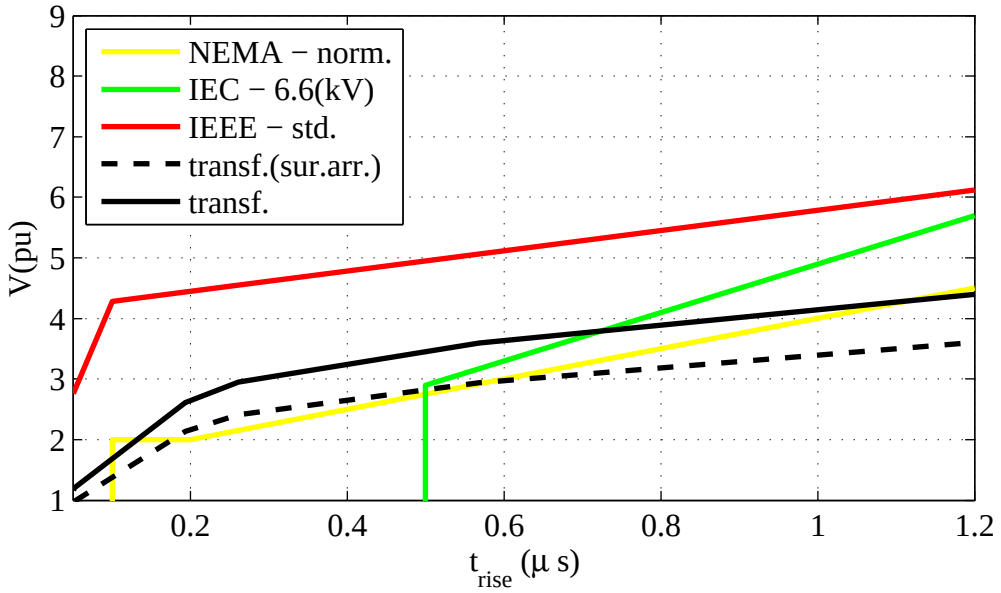

Figure 5.1: Standards for motors and transformers measured critical voltage.

Fig. 5.1 shows critical voltages for motors given by NEMA, IEC and IEEE standards, and measured critical voltages for transformers measured and presented in Section 4.3. The only difference comparing to the critical surge presented in Fig. 4.48 in Section 4.3 is that the measured critical voltages now are calculated in per unit with respect to the rms value of the line-to-line voltage both for a standard level and a decreased level when surge arresters are used. This corresponds to a BIL level of $150kV$ and $125kV$ for a $34.5kV$ dry-type transformer, or in per unit, $4.35pu$ and $3.6pu$. NEMA, IEC and IEEE standards for motors each give at least two critical voltage envelopes, and in Fig. 5.1, only the one with the lowest voltage level is presented. However, it can be noted that the trend of the measured critical voltage of the transformer shows a similar pattern compared these standards, i.e. the magnitude of the measured critical voltage reduces proportionally to the standards.

The main reason that standards for motors include voltage surges of short rise times, is that the insulation of inverter-fed motors failed very quickly when the first inverter-fed motors were used with a long cable connecting motors and inverters. Transformers are not that often exposed to such high frequency transients. In fact, only during switching of transformers in cable systems there is a risk for such transients. However, as it is shown in Section 4.3, critical voltages measured during such transients correspond to standard critical voltages for motors.

As shown in Chapter 4, the lightning impulse does not produce the highest voltage stress on turn-to-turn insulation. It is VFT with a very short rise time that produce the highest voltage stress. Therefore, it is needed to extend the standards for transformers in order to account for VFT. By doing that, transformers insulation will be designed accounting for the voltage stress caused by VFT too.

5.2 Data characterization

As it is seen in Chapter 4, turn-to-turn voltages during the switching transients depend strongly on the magnitude and the rise time of the voltage step. Therefore, in order to study high frequency switching transients, it is need to characterize voltage signals and detect possible dangerous voltage surges.

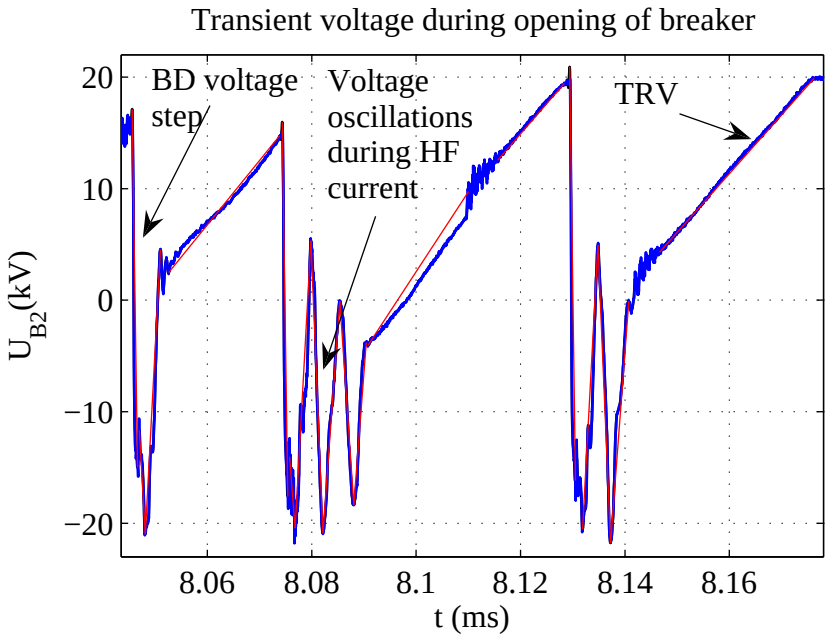

Figure 5.2: Characteristic voltage steps during transient.

Therefore, a signal characterization method is utilized to obtain the magnitude of strikes and its rise times as its important characteristics [72]. In the scatter plots, these transient voltage characteristics are compared to the BIL voltage which serves as a reference. Consequently, the inspection of the transient voltages is simplified and it is easy to notice if the strikes during the transient voltage exceed the rise time and/or the magnitude of BIL. A plot showing the transient overvoltage and the detection of strikes is presented in Fig. 5.2.

As it can be noted, voltage steps of different slopes are generated during the transient. The steepest voltage slope is generated right after the voltage breakdown in the vacuum. The steepness of this voltage is determined by the surge impedance of the cable and the stray capacitance of the transformer, yielding a very steep voltage front with the rise time t_{rise} in the order of $0.5\mu s$. Observing Fig. 5.3 it can be seen that these voltage steps belong to the first group of the fastest transients.

Right after the breakdown, the high frequency current generates voltage fronts with rise times t_{rise} in order of $2\mu s$ giving the oscillation frequency of $500kHz$ approximately. These

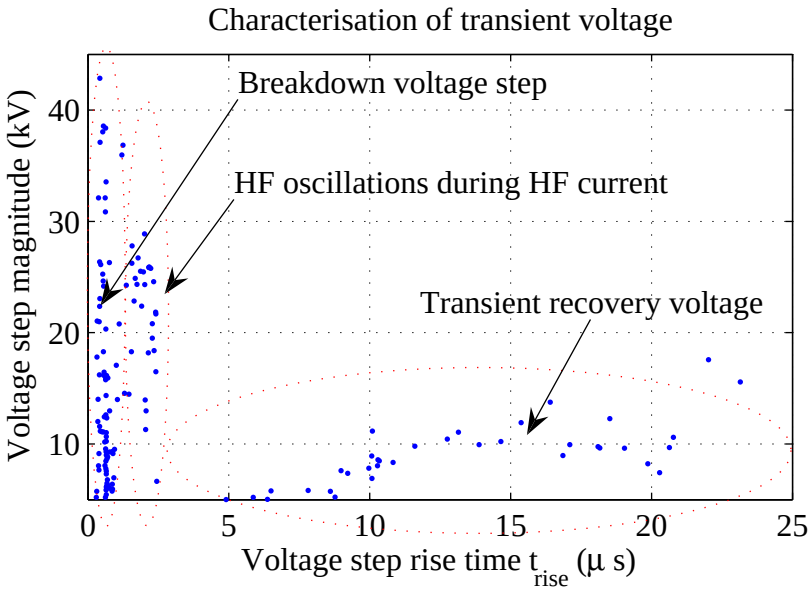

Figure 5.3: Characterization of transient voltage - scatter plot.

voltage steps are placed in the second group of voltage steps and can be easily separated by visual inspection in Fig. 5.3.

The voltage steps with the highest rise time represent the transient recovery voltage which occurs during the period of time when the arc is interrupted. Since the rate of rise of the transient voltage is almost constant, it can be observed that the longer the rise time, the higher the magnitude of the voltage step.

Figs. 5.2 and 5.3 give a simple and clear insight how the characterization data can be observed and interpreted. Scatter plots, as one shown Fig. 5.3, will be used to present results and to compare the simulation and the measurement data to BIL.

Chapter 6

The Cable Lab

A cable lab for the transient analysis studies is built in the facilities of ABB Corporate Research in Västerås, Sweden. The cable lab is built in order to replicate a feeder/turbine system found in the wind farms for the fast transient studies. The benefits of the lab measurements compared to the measurements in the field are many. The lab is built in a way so it enables reconfiguration of the test setup so it can replicate various wind turbine and feeder connection arrangements. Furthermore, various protection measures can be tested and compared in an environment that provides a good platform for the comparison of the protective devices.

6.1 Layout of the Three Phase Test Setup

The cable lab is a three phase setup where full scale tests are performed for the purpose of high frequency transient studies. The setup of the cable lab consists of $550m$ long $20kV$ XLPE three core cable with $240mm^2$ cross section of conductor, $52m$ long $20kV$ XLPE single core cable with the same conductor cross section and two transformers, where transformer TX1 represents the transformer placed in the wind turbine while transformer TX2 represents the platform transformer. Two different transformers are used as transformer TX1, where one is an oil-insulated and the other one is a dry-type transformer. As a switching device, a vacuum circuit breaker is used. The full test setup is presented in Fig. 6.1

The setup is built so it may provide different connection arrangements found in real wind parks. Cables marked as SC1 and SC5 with $72m$ of length, represent the cable in the wind turbine which is placed between the wind turbine transformer (TX1) and the breaker (BRK). Cable SC5 is terminated at the other end, and in the test setup represents a disconnected wind turbine. This is very suitable for the analysis of the wave reflection and its impact on the high frequency transients. The SC2 cable is a cable which connects two turbines. The length of the cable is a bit too short compared to the cable between two wind turbines in a real wind park collection grid, but still, its length is sufficient for the high frequency transient analysis. Cables SC3 and SC4 represent two feeders of the WP collection grid with the length of $162m$. Feeder 2 or SC4 cable is terminated at the end, and represents a feeder with all wind turbines disconnected. The setup allows to have this feeder both connected or disconnected. When connected, Feeder 2 adds additional capacitance to the system and

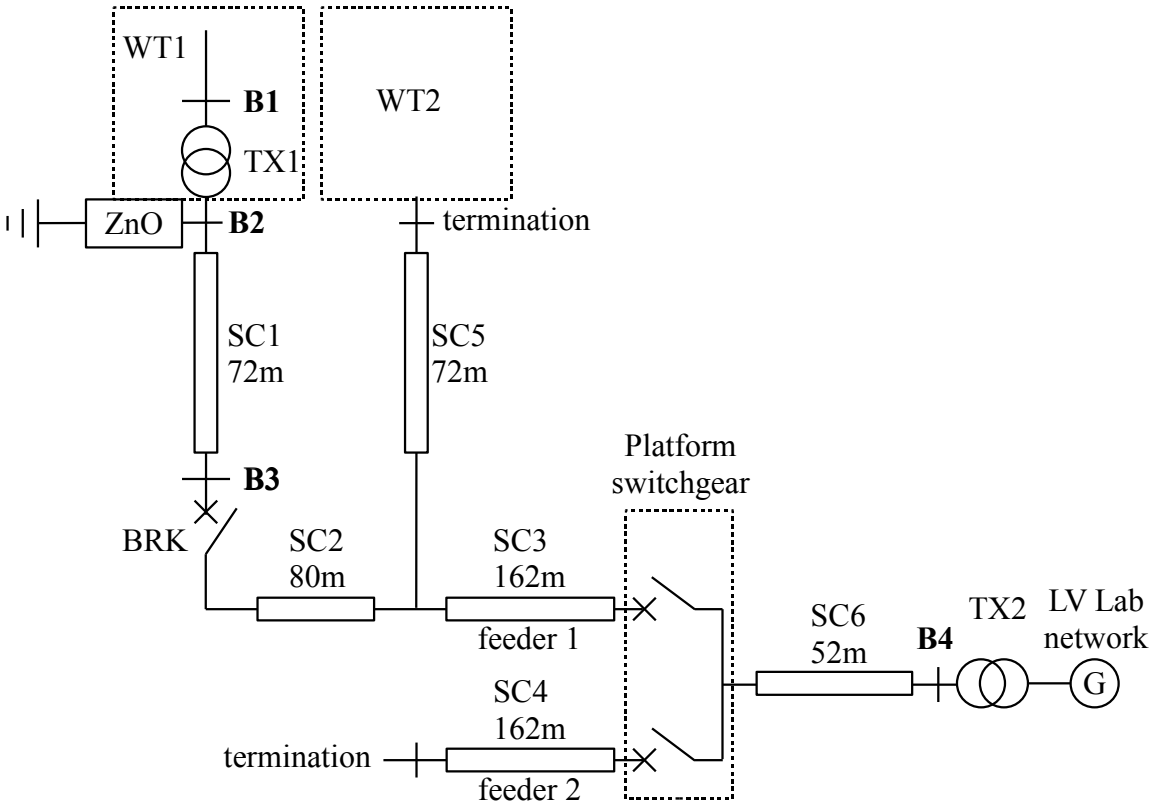

Figure 6.1: The cable lab setup layout.

reflection point at its end where is terminated. The switchgear platform is connected to the platform using a single phase $52m$ long $20kV$ XLPE cable. On the platform, TX2 transformer is placed and it is connected to the grid from the low voltage (LV) lab network. Since both TX1 and TX2 transformers are connected in delta arrangement on the high voltage side, an artificial neutral point is provided using three $24kV$ rated voltage transformers connected with their primary windings connected in wye. During the inductive load test, an inductor with a $0.318mH$ inductance is placed at bus **B1** for test with the oil-insulated transformer, while a $17mH$ inductor is used with the dry-type transformer.

In tests with the oil-insulated transformer, transformer TX1 is protected with a surge arrester consisting of two ZnO blocks connected in series in order to prevent overvoltages of very high magnitude that can damage the transformer. Furthermore, in tests with the oil-insulated transformer, the low voltage level supplied from the lab network is set to give $12kV$ voltage level on the high voltage side of the transformer TX2. The voltage is set to $12kV$ since the voltage rating of the vacuum circuit breaker used in the testing with the oil-insulated transformer is also $12kV$.

The tests with dry-type transformer are performed at the rated voltage level of $20kV$. Due to an increased voltage level, three or four ZnO blocks are used for prevention of high overvoltages. Furthermore, a $20kV$ ring main unit (RMU) with a VCB as a switch is used instead of the $10kV$ VCB used in the tests with the oil-insulated transformer.

The rating of the equipment installed in the cable lab is as follows:

- $550m$ of $20kV$ XLPE three core cable with $240mm^2$ cross section of conductor;
- $52m$ of $20kV$ XLPE single core cable with the same conductor cross section;
- Transformer TX1(oil-insulated), $20.5/0.41kV/kV$, $1.25MVA$, Dyn11 $Z_k = 5.4\%$;
- Transformer TX1(dry-type), $20/0.69kV/kV$, $0.9MVA$, Dyn11 $Z_k = 6\%$;
- Transformer TX2, $20/0.69kV/kV$, $1MVA$, Dyn11 $Z_k = 5.1\%$;
- Breaker rated at $12kV$, $3.15kA$;
- RMU rated at $20kV$, $200A$.

In the lab, various different protection devices are tested. As mentioned before, during the tests, transformer TX1 is always protected using the ZnO surge arrester in order to prevent damage to the transformers. For the transient studies, an RC protection and a surge capacitor protection with different connection arrangements is tested. During the tests, the following surge protection is used:

- Two,three or four blocks of ZnO connected in series with continuous operating voltage $COV = 14.3kV$, with characteristic points of $1mA$@$17.2kV$ and $10kA$@$28.5kV$;
- Surge capacitors with $83nF$ and $130nF$ capacitance;
- Resistors with 20Ω and 30Ω resistance.

During the tests, different protection schemes are tested. In some cases, different protection devices were placed at two buses at the same time in order to find the best solution.

6.2 Measurement Setup

In Fig. 6.2 the measurement setup is presented. Measurements are performed at buses **B2** and **B3**, where **B2** is the bus where the high voltage side of transformer TX1 is connected. The breaker is placed at bus **B3** where cable SC1, which represents the wind turbine cable, is connected.

On bus **B2**, only the voltage is measured. It is of the highest importance to measure this voltage with good accuracy since the voltage measured at this bus is the voltage that stresses the insulation of transformer TX1. On bus **B3** both currents and voltages are measured. Since this is a bus where a breaker is connected, the measured current represents the current through the breaker which is important to study the breaker phenomena. By measurement of voltages at these two buses it is possible to observe the wave traveling and reflection phenomenon which creates high frequency transient overvoltages.

Since a high frequency phenomenon is measured, measurement equipment with high bandwidth is used. For measurement of the voltages at bus **B2**, Northstar voltage dividers Type VD-100 are used. The accuracy of these voltage dividers is 1% in frequency range

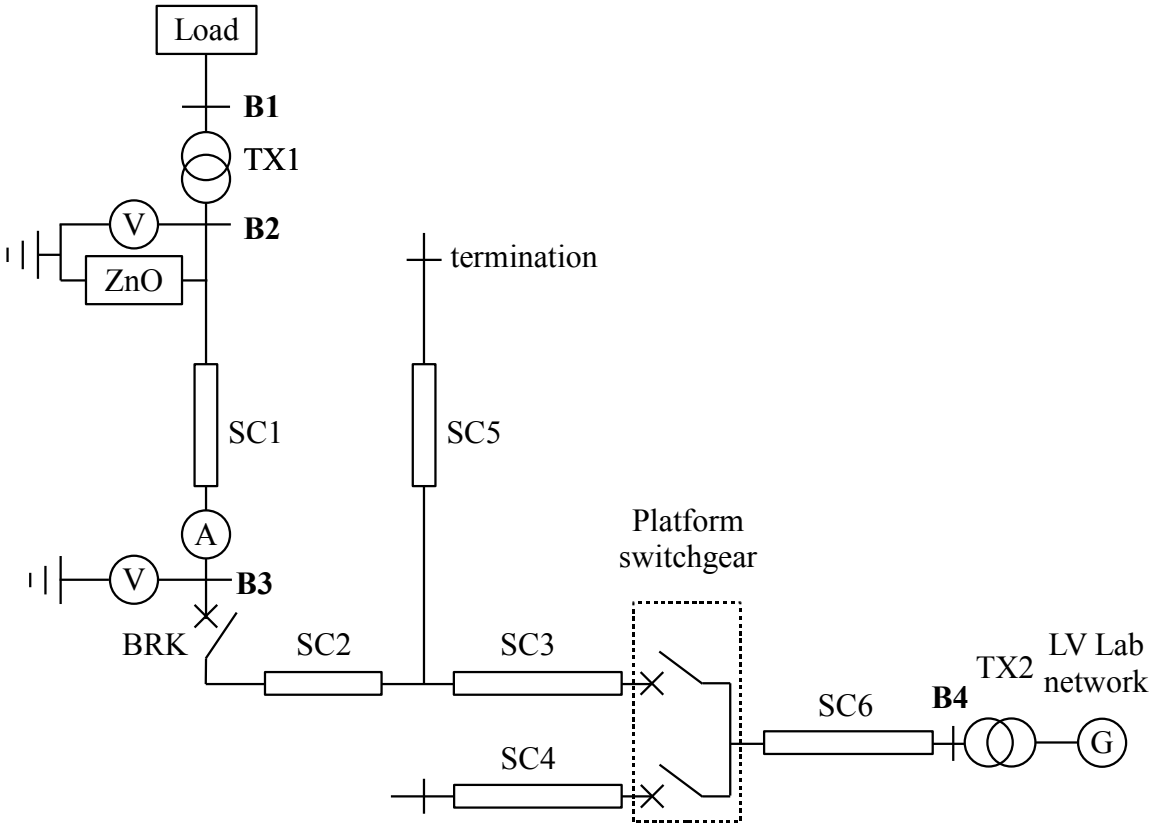

Figure 6.2: The cable lab measurement setup layout.

between $10Hz - 1MHz$ while at frequency range between $1MHz - 20MHz$ it is 3%. The divider ratio is 10000 : 1. At bus **B3** HILO Type HVT40RCR voltage dividers are used. The bandwidth of these dividers is $10MHz$ while the ratio is 2500 : 1. For the current measurement at bus **B3**, Pearson current monitor type D101 is installed. The bandwidth of this current probe is $4MHz$ with maximum peak current of $50kA$.

The Signals from voltage dividers and current probes are lead by optical link to two transient recorders type TRA 800s. By using optical links it is ensured that the measured signal is not disturbed. Nine channels in total are recorded at a sampling rate of $25MS/s$ with a 12 bit resolution.

6.3 Measurement Results and Analysis

In this section, the results obtained during the measurements and the simulation results, are compared and analyzed. The purpose of the analysis is to verify the model developed for simulation of the high frequency transients, to study generation and propagation of the high frequency transients, and to analyze the impact of different mitigation methods.

The system model is built using the component models developed as described in Chapter 3. The parameter estimation of the components is based on the measurements for the base

case. The base case is the case with only surge arresters connected to the system. The results obtained using the transient mitigation equipment are compared to the base case and the influence of the different mitigation devices is studied.

Since the results depend on many parameters, the worst case scenario is chosen when possible. This report does not estimate the risk of obtaining the worst case, but considering the projected life time of the transformers and the number of the breaker operation during such a period, the worst case scenario will most likely occur during transformers life time.

When it comes to the worst case scenario, it is important to note that the characteristics of a high-frequency transient such as the magnitude of the voltage surge and the number of strikes depend on the arcing time (arcing angle) of the breaker, or the time that passes from the start of the contact separation until the power frequency current zero crossing. The arcing time is essential for the appearance of the reignitions in the system. If the reignitions are to be avoided, the point-on-wave control can control the breaker in such a way so the high frequency transients are avoided completely. On the other hand, to make sure that the worst case scenario is investigated during the test and the simulation, the arcing time of the breaker for all cases of the breaker opening operation is chosen so the breaker starts the separation of the contacts at the very instant when the current in one of the phases just passes the current chopping level. This gives that the dielectric withstand of the breaker is at its minimum when the breaker interrupts the current, thus producing reignitions very shortly after the current interruption. This case produces voltage escalations with the maximum voltage level and therefore this is the worst case scenario for the breaker opening operation. The exception is the no-load case when the current never reaches the chopping level. In this case, the contacts of the breaker start separating when the current is at its maximum. This gives the fastest rate of rise of the transient recovery voltage since it is directly proportional to the level of the chopped current.

For the closing operation of the breaker, the worst case scenario for a wye connected transformer that produces the highest magnitude of the surge voltage is when the dielectric withstand of the gap reaches the phase voltage when it is at its maximum. For a delta connected transformer the worst case scenario is to close a breaker when the maximum line-to-line voltage is achieved. In this case, the voltage surges of the highest magnitude over transformers winding are generated.

Since the voltage breakdown, the current chopping and the high frequency current interruption are the stochastic phenomena and very much determine the results presented in the time-domain, the exact replication of the measurement results using simulations is not possible. This is especially the case for the opening of the breaker, where larger number of the stochastic strikes appears. Therefore, the verification of the simulation models is performed by verifying the following characteristics of the high frequency transient:

- The appearance of repetitive strikes;
- The highest magnitude of the surge voltage;
- The rise time of the surge created during the strike.

Furthermore, the obtained results are compared to standard values of the basic lightning impulse voltage level (BIL) extended using the critical voltage curve obtained in Section 4.3

and withstand voltages for motor standards given in Chapter 5. The results obtained in this section for the oil-insulated transformer are measured at a non-standard voltage level which is set below the rated voltage of the transformers, cables and other equipment. This is performed in order to avoid damages on the equipment used for testing since the simulations showed that transient overvoltages of very high magnitudes are expected during some tests.

The standards for both dry-type and oil filled transformers define for each voltage level the BIL at which the transformer will not show any signs of insulation damages. These voltage impulse tests are considered as the highest stress that can happen to insulation of a transformer and therefore, if the transformer is able to withstand this voltage without any problems, its insulation will most probably survive other high frequency transients. Since these standards are not defined for very fast transients, the maximum allowed voltage stress in the region of transients between $50ns$ and $1.2\mu s$ is defined by the critical voltage obtained in Section 4.3 and withstand voltages for motor standards given in Chapter 5.

For the presentation of the voltage strikes in the scatter plots, the magnitudes of the voltage strikes are shown in per unit, where $1pu$ presents the nominal voltage of the transformer. This is done because, the maximum magnitudes of the voltage strikes obtained at any voltage level with properly calculated surge arresters is the same when presented in per unit. However, the BIL for each voltage level has a different value when expressed in pu making a comparison difficult. For example, for the $8.7kV$ level, the basic lightning insulation level is $5.2pu$ for dry-type transformers and $8.6pu$ for oil insulated transformers while for the $34.5kV$ level the BIL values are $3.6pu$ (with surge arrester used) and $4.35pu$ respectively. For this reason, the minimum value in per unit is used as the reference value for the dry-type and the oil insulated transformers. The comparison is done for both standards since the magnitude of the voltage strikes is the same for both dry-type and oil insulated transformers and the difference is only in the rise time of the surge. Furthermore, as the standards do not define critical voltages for surges with rise times shorter than 1.2 μs, characteristics measured in Section 4.3 is used to extend the area of critical voltages.

6.3.1 Base Case Results

As mentioned before, the case with only surge arresters connected to the transformer terminals is taken as the base case. The reason for having surge arresters connected all the time is just a precaution in order to avoid any damage to the transformers during testing. However, a simulation case without any surge protection devices is presented to illustrate the magnitude of the generated surges. This case is simulated only for the opening operation of the breaker since the highest magnitudes of surges are obtained during reignitions due to the voltage escalation.

No-load case

The no-load case is performed for both closing and opening operation of the breaker with the surge arrester connected to the transformer terminals. This case is presented only for the oil-insulated transformer. The scheme that presents this case is shown in Fig. 6.3.

During the closing operation of the breaker, the prestrikes are expected to occur. The

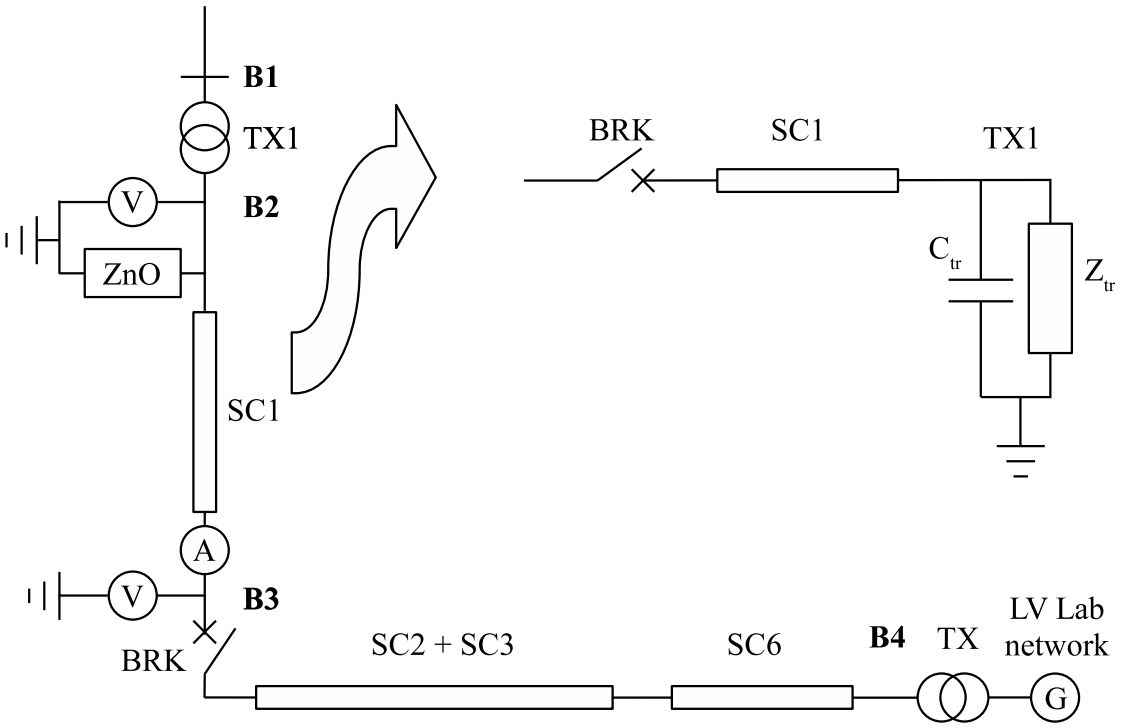

Figure 6.3: No-load case with surge arrester at TX1.

prestrikes are generated at time instants when the dielectric withstand of the gap between the breaker contacts is lower than the voltage over the gap. Therefore, the time instant to close the contacts is chosen so the dielectric withstand of the breaker reaches the voltage over the gap when its level is at the maximum.

As it can be noted in Fig. 6.4, the switching of the breaker does not occur exactly at the maximum voltage, but at a point very close to it. The reason for that is that during the experiment this margin was treated as sufficiently good, and therefore, the simulations are set for a similar switching time instant.

During closing operations of a breaker, voltage prestrikes occur in the system. The critical point for the verification of the model is to compare the rise time t_{rise} calculated analytically to the measurement and to the simulation. During the prestrike, the voltage surge is determined by the voltage level at which the voltage breakdown appears, and the time constant of the system. The time constant of the system is determined by the surge impedance of the cable Z_{cab} and the stray capacitance of the transformer C_{tr} and is given by

$$\begin{aligned} \tau &= Z_{cab} C_{tr} \\ t_{rise} &= 2.2\tau. \end{aligned} \tag{6.1}$$

During the measurement of the stray capacitances of the transformer, a stray capacitance of $8.5\mu F$ is measured. A transformer model consisting only of the stray capacitance and the surge impedance is presented in Fig. 6.5. The surge impedance of the cable is calculated to

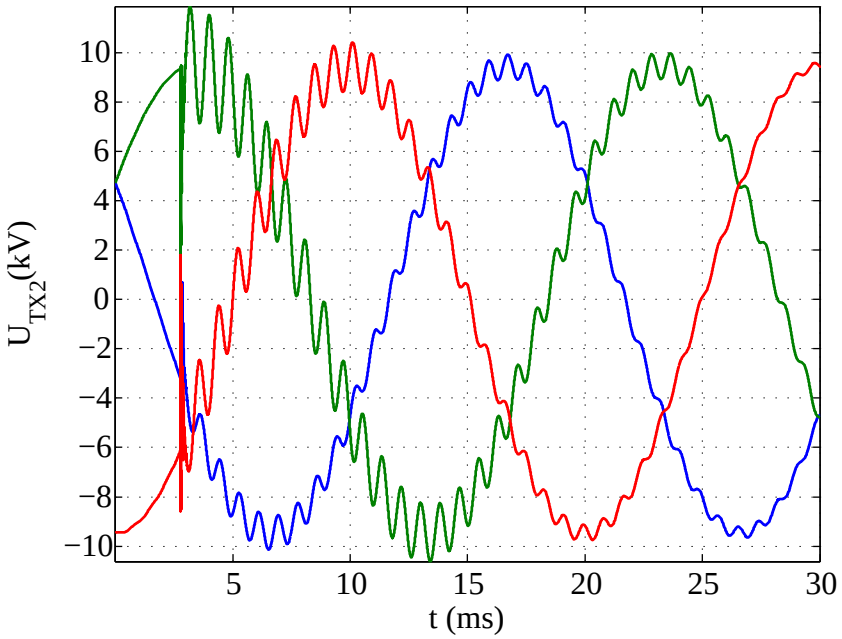

Figure 6.4: Voltage at TX2 during closing of breaker - simulation.

be 24.8Ω giving the analytically calculated $t_{rise} = 0.462\ \mu s$.

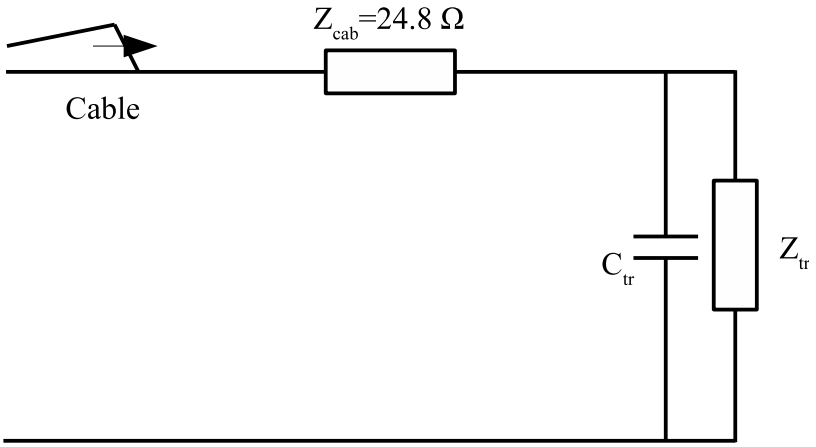

Figure 6.5: Cable/Transformer model for HF transient.

When this result is compared to the measurement and the simulation, a very good agreement is observed. Due to different voltage levels at the occurrence of the prestrike, the steady-state voltage levels in the plot are not identical. The ideal case is approximated using expression

$$V = V_0 \left(1 - e^{\frac{-t}{\tau}}\right) \tag{6.2}$$

where V_0 is the steady-state voltage level, and τ is the time constant given by (6.1). For the simulation case, this voltage is set at $9.3kV$, while it is set to $10.1kV$ for the simulation.

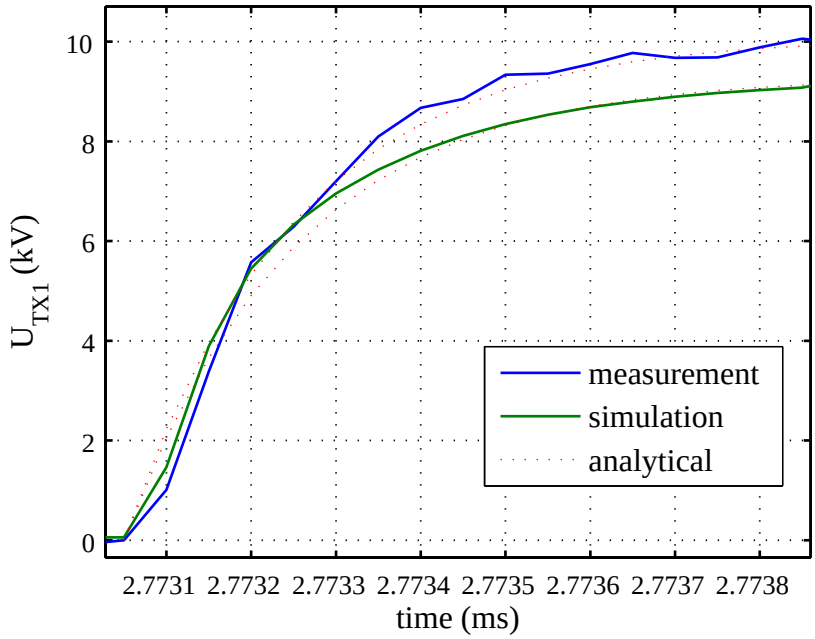

Figure 6.6: Voltage surge rise time.

In Fig. 6.6 it can be seen that the simulation result matches the measurement and the analytically calculated value. It shows that the transformer model gives good response for high frequency transients.

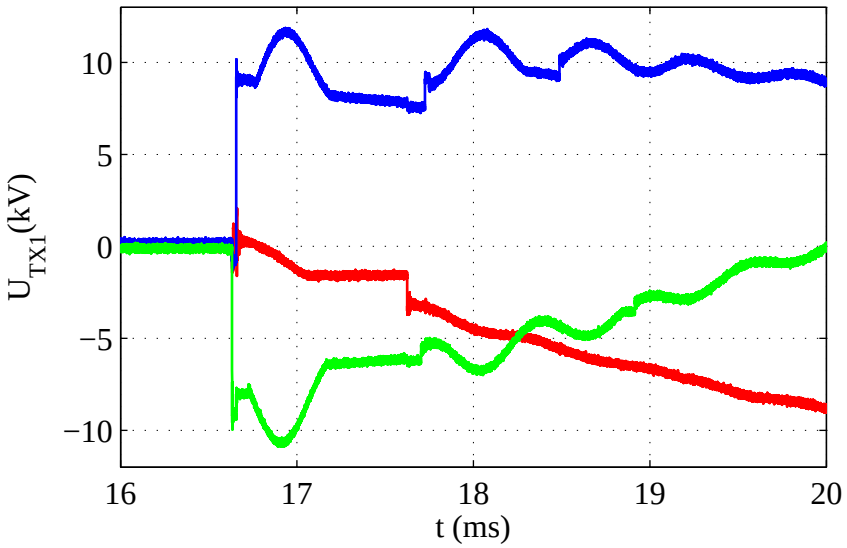

Figure 6.7: Transient voltage at TX1 during closing - no load - measurement.

To observe the response of the whole system, and the generation of the high frequency transients during a closing operation of a breaker, the whole time span which shows the closing cycle including the transient voltage from the very first prestrike until the contacts are closed is observed. This transient can be seen in Figs. 6.7 and 6.8.

As the contacts of the real breaker close at slightly different time instants compared to

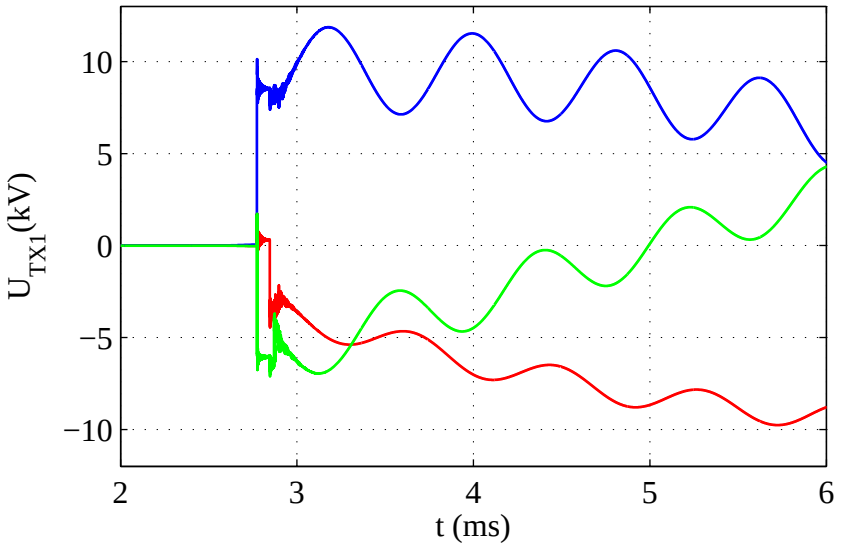

Figure 6.8: Transient voltage at TX1 during closing - no load - simulation.

the simulation, the phase to phase comparison of the voltages in the time domain, obtained by the simulation and measurement is almost impossible. The simulation shows only one prestrike in each phase, while in the measurement it can be observed that another prestrike appears approximately $1ms$ after the first one. This happens due to the bouncing of the contacts of the breaker and it will be shown later more in detail. This phenomenon is not modeled since it does not play a significant role in generation of high magnitude surges.

Furthermore, the $900Hz$ oscillations that appear in the transient voltage are much better damped in the real system. This is expected since the transformer model and the grid model does not include modeling of the skin-effect phenomenon.

When the characterization algorithm presented in Section 5.2 is applied, the magnitude and the rise time of the strikes are calculated. The magnitude of the transient and its rise time obtained by simulation are in good agreement with the measurement. It is important to note that the magnitudes of surges are below $1pu$ and much below the BIL of the dry-type and oil insulated transformers. However, the rise time of these strikes is shorter than the BIL rise time of 1.2 μs. In the case of dry-type transformers, the rise time of the surge is approximately 10 times shorter than the rise time of the surge when the oil insulated transformer is used. This is due to a 10 times smaller stray capacitance of the dry-type transformers.

It is expected to record a higher number of repetitive strikes during an opening transient. At the time instant of the contact separation, the transformer magnetizing current is chopped and generates fast rising transient recovery voltage. As the contacts are separated with rate of rise of the dielectric withstand which is much slower than the rate of rise of the transient recovery voltage, a reignition occurs shortly after the separation of the contacts. This is shown in Fig. 6.9 that shows the measured voltages at a time instant of $t = 10.6ms$, and in Fig. 6.10 which shows simulated voltages at a time instant of $t = 4ms$.

Furthermore, it is observed that the contacts start to open in phase A (blue curve) approximately $1.5ms$ before in the other two phases. This time delay is stochastic and in the

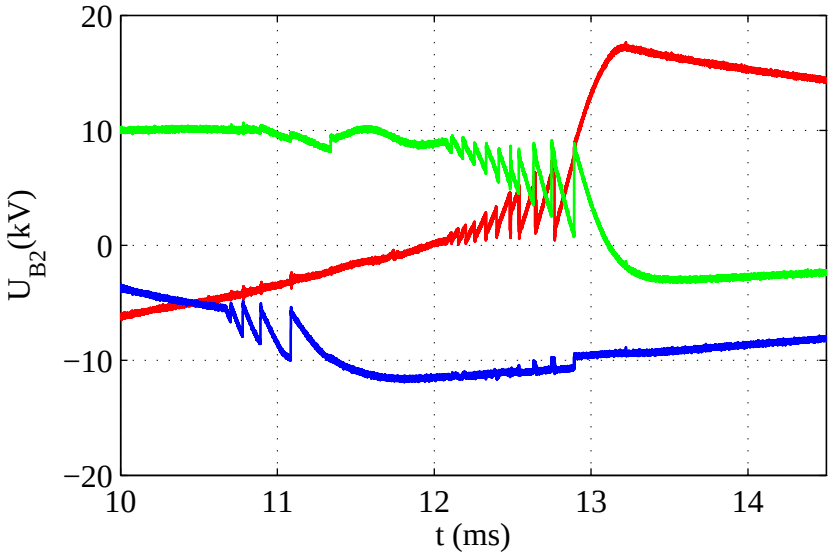

Figure 6.9: Transient voltage at TX1 during opening - no load - measurement.

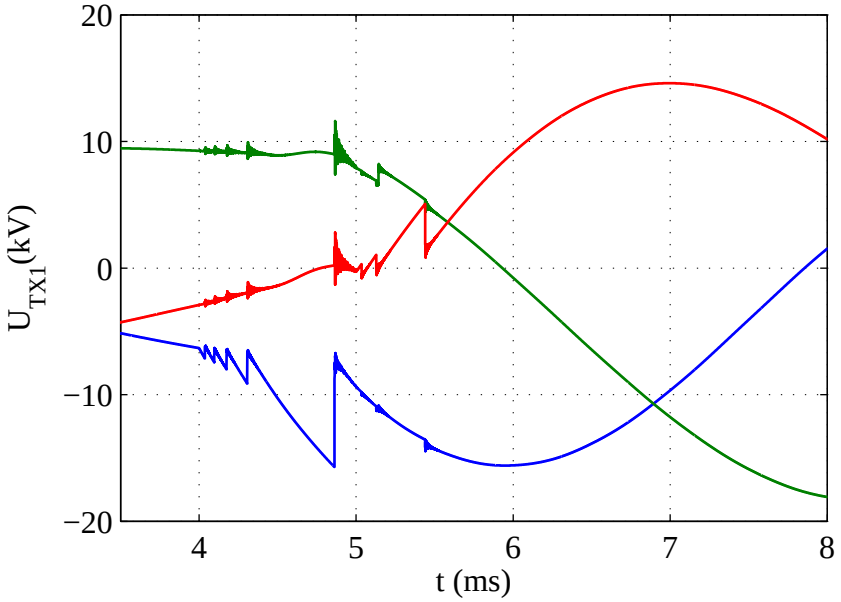

Figure 6.10: Transient voltage at TX1 during opening - no load - simulation.

simulations it is set to $1ms$. The timing of the contact separation is critical to obtain a good agreement since the rate of rise of the recovery voltage very soon after the contact separation becomes slower than the rate of rise of the dielectric strength. Although the difference in the number of reignitions exists when the simulation is compared to the measurement, the repetitiveness of the strikes is confirmed both in the simulation and the measurements. The magnitude and the rise time of the highest strike obtained in the simulation is in agreement with the measurements which shows a good accuracy of the model.

The magnitude of the strikes is well below $1pu$ with the rise times about 1 μs. The reason for such a voltage level of the surges is that the chopped current is very small which makes the rate of rise of the dielectric strength of the breaker becoming quicker than the transient

recovery voltage very soon after the contacts separate. For that reason, the reignitions occur only for a very short period of time right after the separation of the contacts.

Inductive load case - oil insulated transformer

The case with a switching of an inductive load is chosen since it represents one of the worst case scenarios for generation of transient voltages. When the current reaches the chopping level, the voltage in that phase is very close to its maximum because of the 90° phase shift. If the breaker contacts are opened at that time instant, the transient voltage is superimposed to the power frequency voltage when it is at its maximum. This produces transient overvoltages with the highest magnitude.

It is important to stress that an interruption of an inductive current is an extreme case conducted to obtain the worst case scenario. However, it does not represent a normal operation in a wind park where it should not be normal practice to open the breakers and switches when the transformer is fully loaded. This case could still happen accidentally, due to malfunction or other reasons. Furthermore, even if such an accident happens, the risk of generation of multiple reignitions and the voltage escalation is quite low since this phenomenon can appear only if the contacts open during a very narrow time window when the current is below the current chopping level.

If a voltage escalation incident occurs in a setup where surge arresters are not installed, the transient voltage can easily breach BIL and damage the transformer. This case is not performed during the measurement for the sake of the tested transformer. Simulations show that in this case, a very high overvoltage is generated. This case simulated with the oil-insulated transformer is presented in Fig. 6.11.

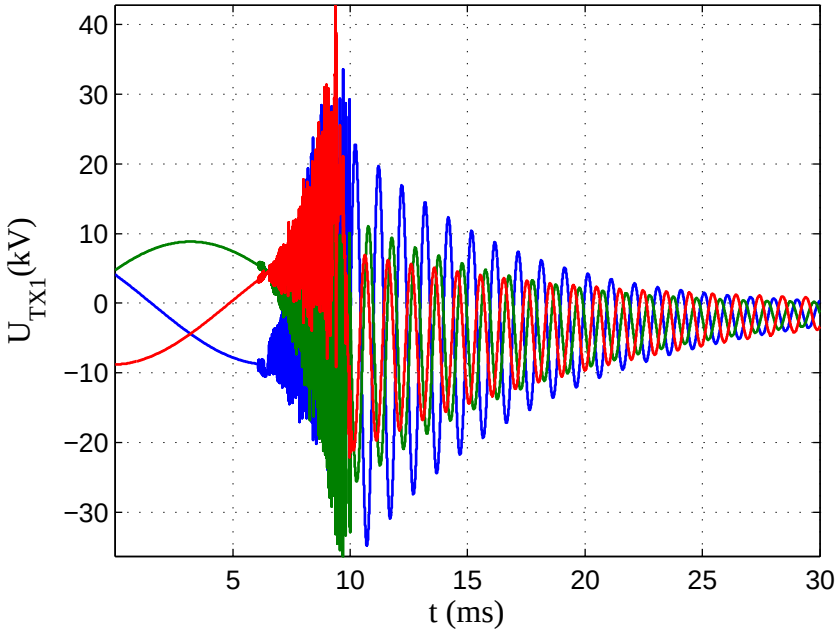

Figure 6.11: Strikes recorded during opening transient at no load without surge arrester - simulation.

During a closing operation, it is expected that the transient voltage does not differ much from the no-load case. The reason for this is that the response of the system during the time between the first prestrike and the touching of the breaker contacts is determined by the same parameters as in the no-load case, the stray capacitance of the transformer C_{tr} and the surge impedance of the cable Z_{cab}. However, due to bouncing of the contacts, measurement show low magnitude reignitions at the time instant $0.6ms$ after the first prestrike. This behavior of the breaker will generate larger number of strikes when compared to the simulation. This is shown in Figs. 6.12 and 6.13.

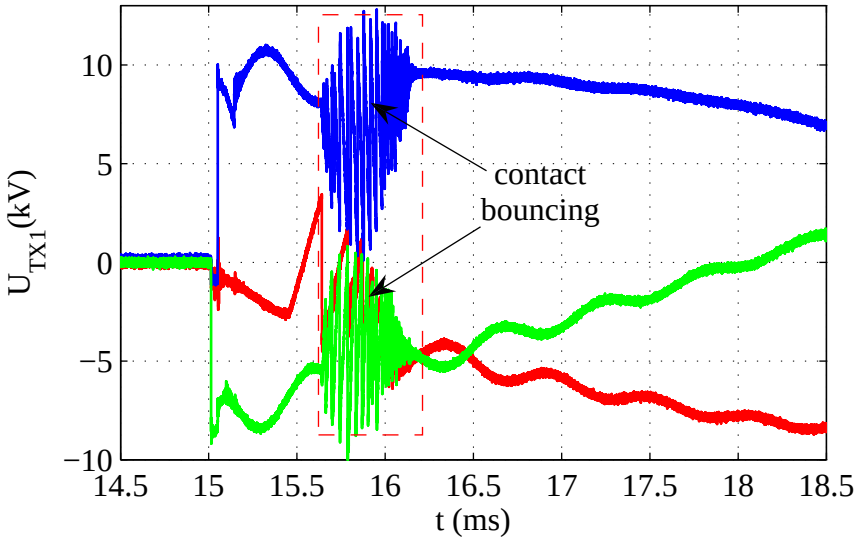

Figure 6.12: Transient voltage at TX1 during closing - inductive load - measurement.

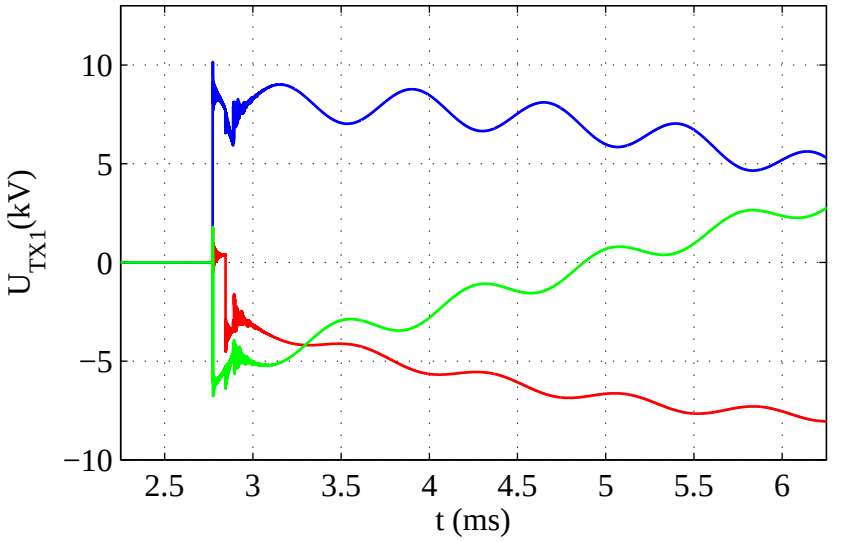

Figure 6.13: Transient voltage at TX1 during closing - inductive load - simulation.

A somewhat larger number of strikes are observed during the measurement. The magnitudes of the voltage strikes are well below BIL levels specified for the dry-type and oil insulated transformers, but have a shorter rise times which is the same as in the no-load case.

During an opening operation of the breaker, a high number of reignitions with the transient voltages reaching the level of the surge protection is expected. As it was mentioned before, the rate of rise of the transient recovery voltage is much quicker than the rate of rise of the breakers dielectric withstand due to the current chopping. The current chopping level is found to be between $2.5 - 5A$ which is much higher current level compared to the no-load case. This results in a very large number of reignitions. To obtain a good agreement between the measurements and the simulations, a good breaker model is needed. This is especially the case for the modeling of the dielectric withstand and the high frequency current quenching capability of the breaker. Observing Figs. 6.14 and 6.15 it can be seen that the dielectric withstand of the breaker is accurately modeled and calculated using the algorithm described in Section 3.1.1.

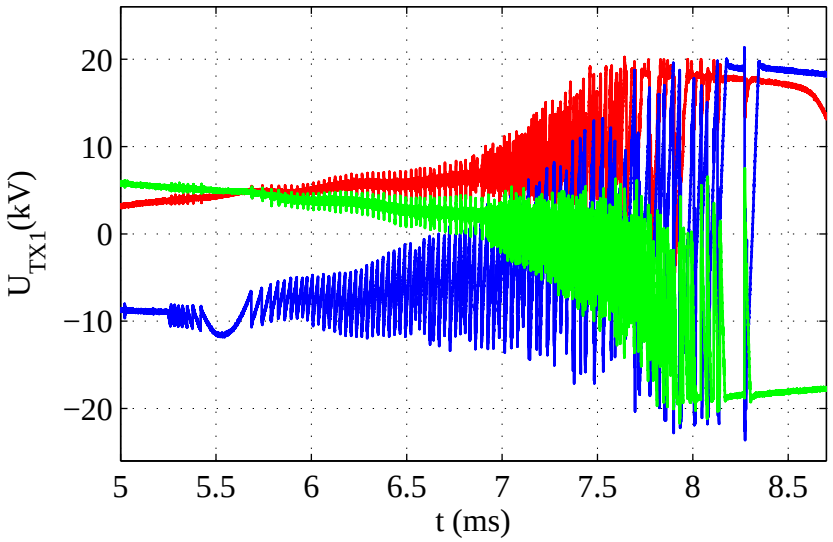

Figure 6.14: Transient voltage at TX1 during opening - inductive load - measurement.

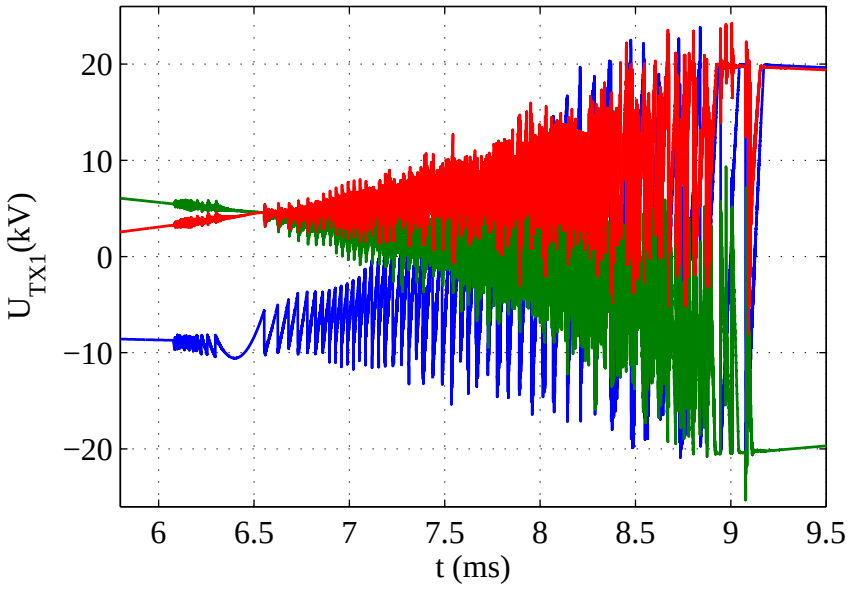

Figure 6.15: Transient voltage at TX1 during opening - inductive load - simulation.

The high frequency oscillations caused by the high frequency current are simulated with a good accuracy. That can be seen in Fig. 6.16 during the time period between the start of the voltage surge and $0.02ms$ after. Observing the low magnitude high frequency oscillations induced by surges in the other two phases due to the capacitive coupling, it can be seen that these oscillations are damped very poorly in the simulation. This is because of a simplified transformer model with added stray capacitances. This can be improved by adding some resistance to the transformers stray capacitances. These oscillations are observed between $8.5ms$ and $8.54ms$ in the simulation plot shown in Fig. 6.17 and between $8.11ms$ and $8.12ms$ in the measurement plot presented in Fig. 6.16.

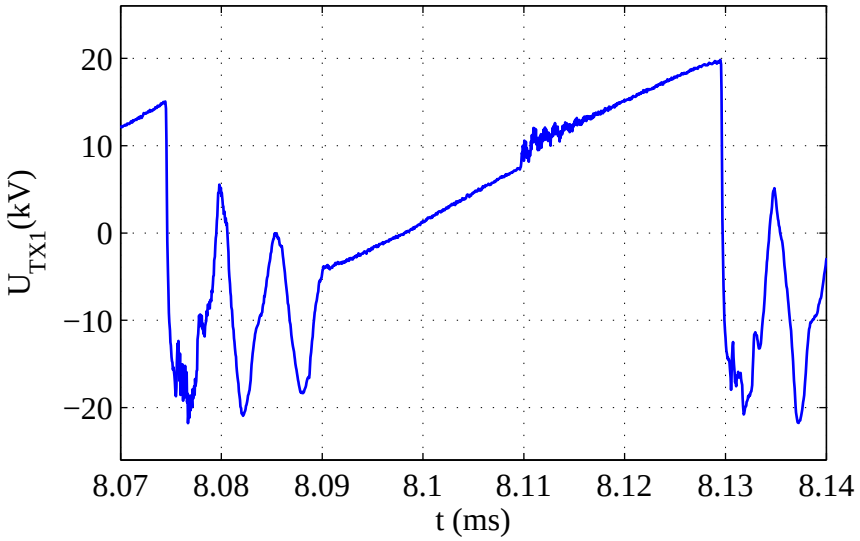

Figure 6.16: Transient voltage HF oscillations - inductive load - measurement.

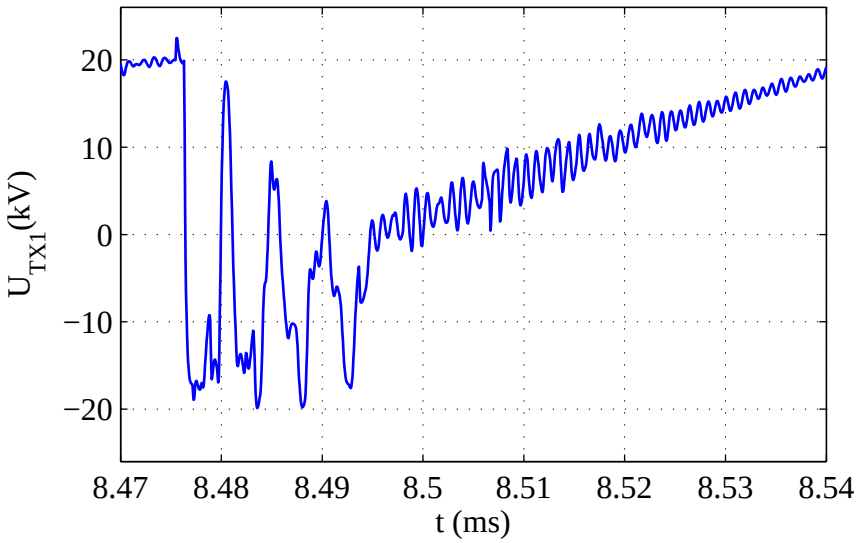

Figure 6.17: Transient voltage HF oscillations - inductive load - simulation.

The steepness of the voltage slope and its rise time match very well when the simulation results are compared with the measurements. This result is already shown for the closing

operation, and for the opening operation it is presented in Fig. 6.18. In this direct comparison of the measured and the simulated voltage surge, a very good agreement in the voltage slope is obtained. However, the magnitude of the voltage transient obtained by the simulation is reduced due to stronger oscillations caused by a low damped capacitive coupling of the transformer. Furthermore, the high magnitude oscillations that appear at the time instant $t = 8.7315ms$ present the voltage wave reflected from transformer TX2. It can be noticed that the wave propagates at a slightly higher speed in the simulations. This is because the cable model is made using three single-core cables instead of a three-core cable due to the limitations of the PSCAD/EMTDC cable model.

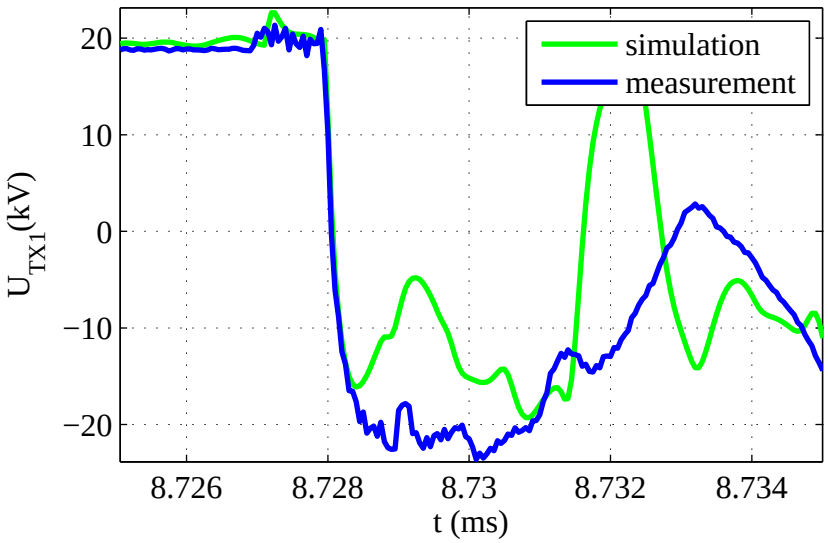

Figure 6.18: Voltage slope - comparison.

The voltage strikes obtained by characterization of the line-to-line transient votlages are presented in Figs. 6.19 and 6.20. This case present a critical case where the transients with the highest magnitude are developed. The simulation predicts the highest stress voltage stress with a 5% error, while the rise time prediction is within a 10% margin. The fastest voltage surges have a rise time of 0.5 μs. This group represents the voltage surges formed during the breakdown of the dielectric in the breaker.

Surges obtained during simulations and measurements are compared with the standard BIL level for oil-insulated transformers (BIL-OI) and lower BIL level for dry-type transformers protected by surge arresters (BIL-DT). Furthermore, these BIL curves are extended into a region below 1.2 μs rise time using the proposed critical voltage envelope obtained in Section 4.3 and adjusted NEMA, IEC and IEEE critical voltages for large motors. The withstand voltage envelopes for large motors given by NEMA, IEC and IEEE standards are adjusted so the critical voltage with a 1.2 μs rise time corresponds to the BIL of dry-type transformers protected with surge arresters. Surges recorded both in simulations and measurements show that the magnitude and the rise time of the surge exceeds the limits defined by the BIL. This occurs even with a surge arrester installed at the terminals of the transformer, proving that the surge arrester protection can not provide sufficient protection without the use of additional protective devices. Moreover, the voltage strikes with a 0.5 μs rise time have a magnitude that is higher than the critical voltages defined by NEMA, IEC and IEEE standards, as well as the proposed critical voltages presented in Section 4.3.

When simulations are compared to the measurements, good agreement is observed in the rise time and in the magnitude of the surges. However, a larger number of voltage surges are observed in the simulations. This result is influenced mostly by the lightly damped capacitive coupling of the transformer, since the most important difference is in the other two phases (B and C) where the breaker poles start to separate approximately $1 - 1.5$ ms later. This difference is also observed in Fig. 6.14.

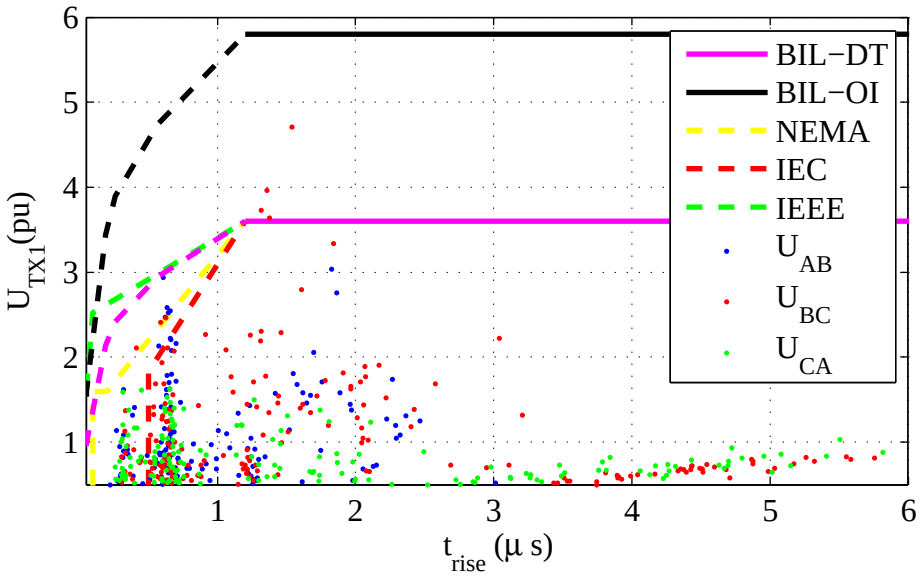

Figure 6.19: Strikes at TX1 during opening - inductive load - measurement.

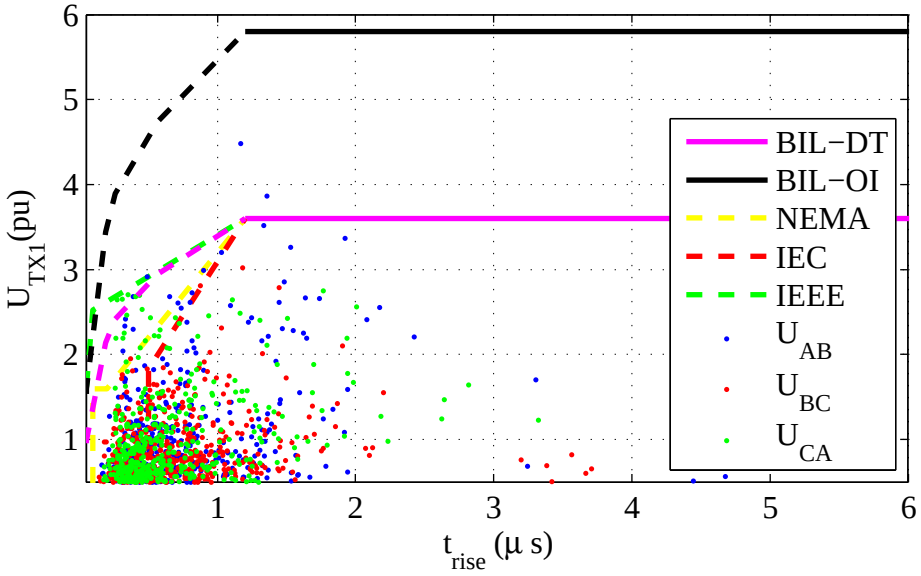

Figure 6.20: Strikes at TX1 during opening - inductive load - simulation.

The group of the voltage strikes with rise times of $2 - 2.5$ ms, represent high frequency oscillations caused by a high frequency current that appears right after the voltage breakdown as shown in Figs 6.16 and 6.17 at time intervals between $8.075 - 8.09$ μs and $8.475 - 8.495$ μs respectively. Both the magnitude and the rise time show a good agreement between the measurements and simulations.

The slowest group of strikes which represent the transient recovery voltage is completely missing in the simulation scatter plots. The reason for this is that the characterization algorithm did not recognize the transient recovery voltage as single voltage steps due to the presence of the high frequency oscillations shown in Fig. 6.17.

Inductive load case - dry-type transformer

The dry-type transformer tests are performed at a rated voltage of $20kV$. Consequently, the number the ZnO blocks is increased to four, where the voltage is clamped at approximately $40kV$. Four blocks are used in order to make it possible to make a direct comparison with the results obtained at a $12kV$ level using the oil-insulated transformer. Furthermore, this test is performed with both TC1 and TC2 connected.

The RMU unit with a VCB is used in this setup. The rate of rise of dielectric strength (RRDS) of the VCB in the RMU is about four times quicker compared to the RRDS of the VCB used with the oil-insulated transformer. This is presented in Fig. 6.21.

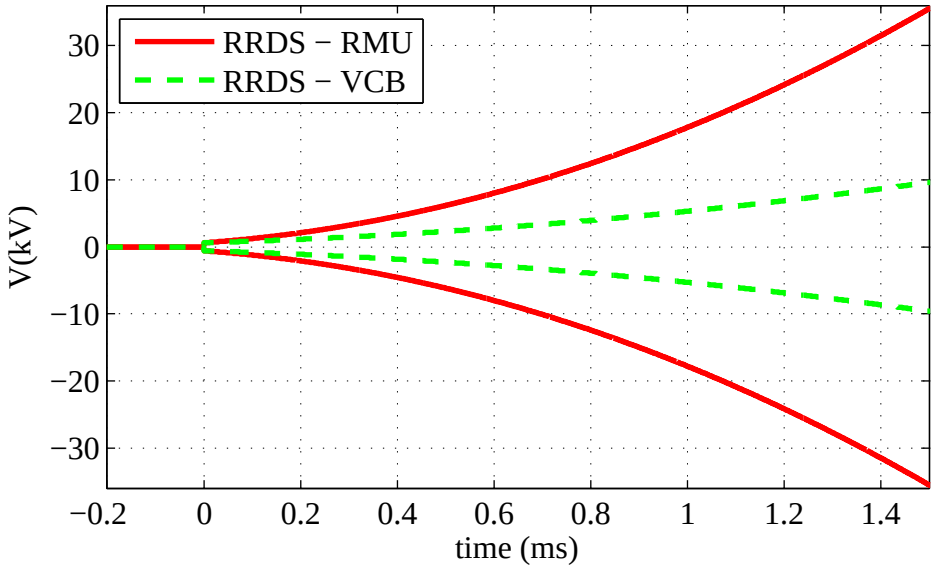

Figure 6.21: Comparison of VCB's and RMU's RRDS.

Due to a lower current level in this setup, it was not possible to generate the worst case scenario like it is performed with the oil-insulated transformer. The peak current is about $3.6A$, which corresponds to the chopping current. This means that very low current is interrupted when the voltage is at it's peak. A low di/dt gives a lower voltage rise and fewer number of restrikes due to a slower TRV. However, for the sake of better comparison, the inductive load test with the dry-type transformer is simulated both with a $17mH$ load and a $0.94mH$ in order to get the same current level through the breaker.

Fig. 6.22 shows measurements of voltage restrikes at the dry-type transformer TX1. It can be noted that the voltage restrikes do not begin at the maximum voltage since the breaker interrupts the current as soon as the contacts start to separate.

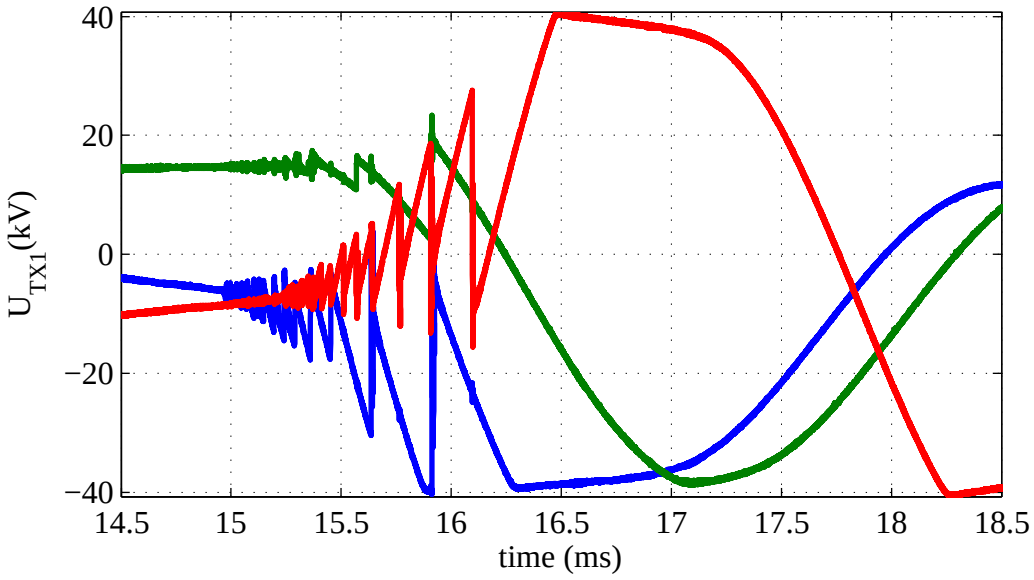

Figure 6.22: Transient voltage at TX1(dry-type) during opening - inductive load ($17mH$) - measurement.

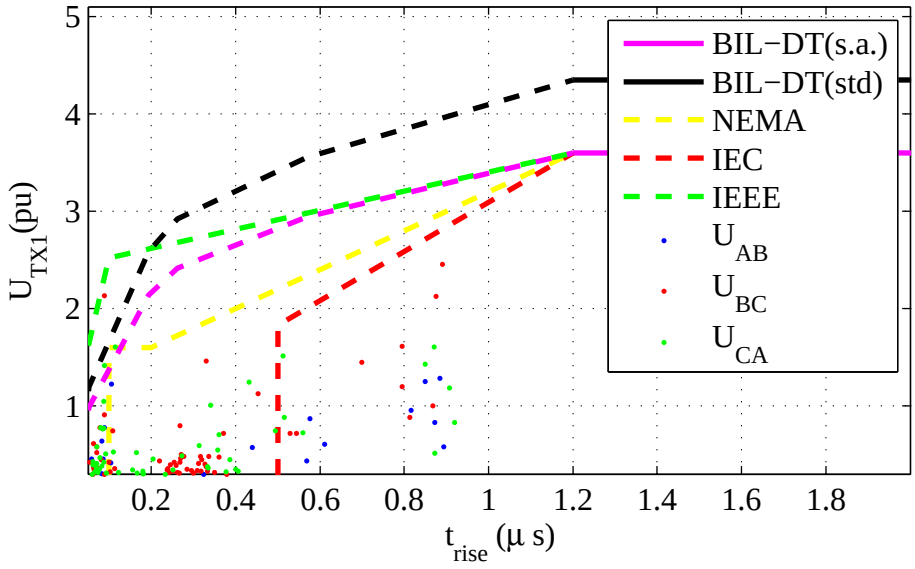

Figure 6.23: Strikes at TX1(dry-type) during opening - inductive load $17mH$ - measurement.

Fig. 6.23 presents the voltage strikes measured line-to-line at the dry-type transformer TX1. The measurement is performed line-to-line since that represents the voltage over the winding for this delta connected transformer. The soild line BIL-DT(std) represents the standard BIL of a $34.5kV$ dry-type transformer given by the standards, while the solid line BIL-DT(s.a.) represents the BIL when surge arresters are used. Due to a very short rise time of voltage strikes, that is about $100ns$ because of the low stray capacitances of the dry-type transformer, a number of restrikes is recorded that exceed the critical voltage level obtained in Section 4.3. This case proves that it is not only the worst case scenario that may lead to critical restrikes.

In order to make a comparison with the oil-insulated transformer test, a simulation with

the dry-type transformer is performed with the same current level as it was with the oil-insulated transformer. This represents the worst case scenario since the current is interrupted close to zero crossing.

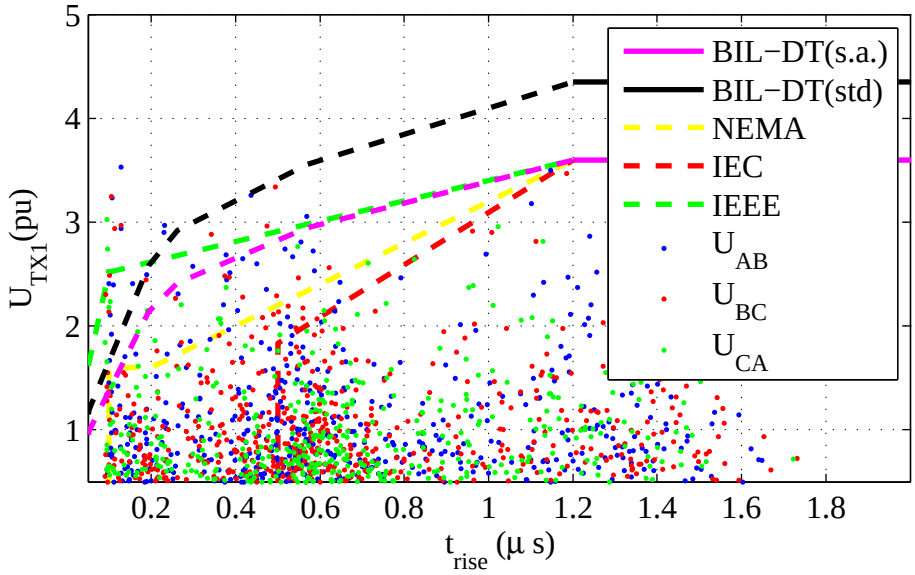

Figure 6.24: Strikes at TX1(dry-type) during opening - inductive load $0.947mH$ - simulation.

Fig. 6.24 shows the voltage strikes during an interruption of the load current drawn by a $0.941mH$ inductor. This represents the worst case switching scenario, where the breaker opens when the load current reaches chopping level at maximum voltage. None of the strikes reach over the BIL when surge arresters are used. However, a large number of recorded strikes with a $100ns$ rise time have a very high magnitude. Many of these voltage strikes are placed above the critical voltage, and the most critical ones are the strikes with a $100ns$ rise time since their magnitude is about three times over the critical level. These strikes exceed the voltage withstand level defined by NEMA, IEC and IEEE standards substantially. This case shows why dry type transformers need additional means of protection that increase the rise time and reduce the magnitude of the voltage strikes such as surge capacitors and RC protection. It is worth mentioning that voltage strikes obtained at some dry-type transformers where a breaker is placed at the transformer reach rise times of about $50ns$ [56]. The turn-to-turn voltage stress in that case is even higher.

6.3.2 Surge Capacitor Protection

Surge capacitors have been commonly used as protection devices to mitigate transients. The combination of surge capacitors and surge arresters has been used to protect medium voltage induction motor windings from steep-fronted voltage surges [73]. The purpose of using the surge capacitor is to reduce the rise time of the surge [74]. In this report, a surge capacitor protection with a $130nF$ capacitance is used. The surge capacitor is installed in front of transformer TX1. The surge arrester is kept at the transformer terminals to limit the maximum overvoltage appearing on the transformer. The scheme showing the full setup is presented in Fig. 6.25.

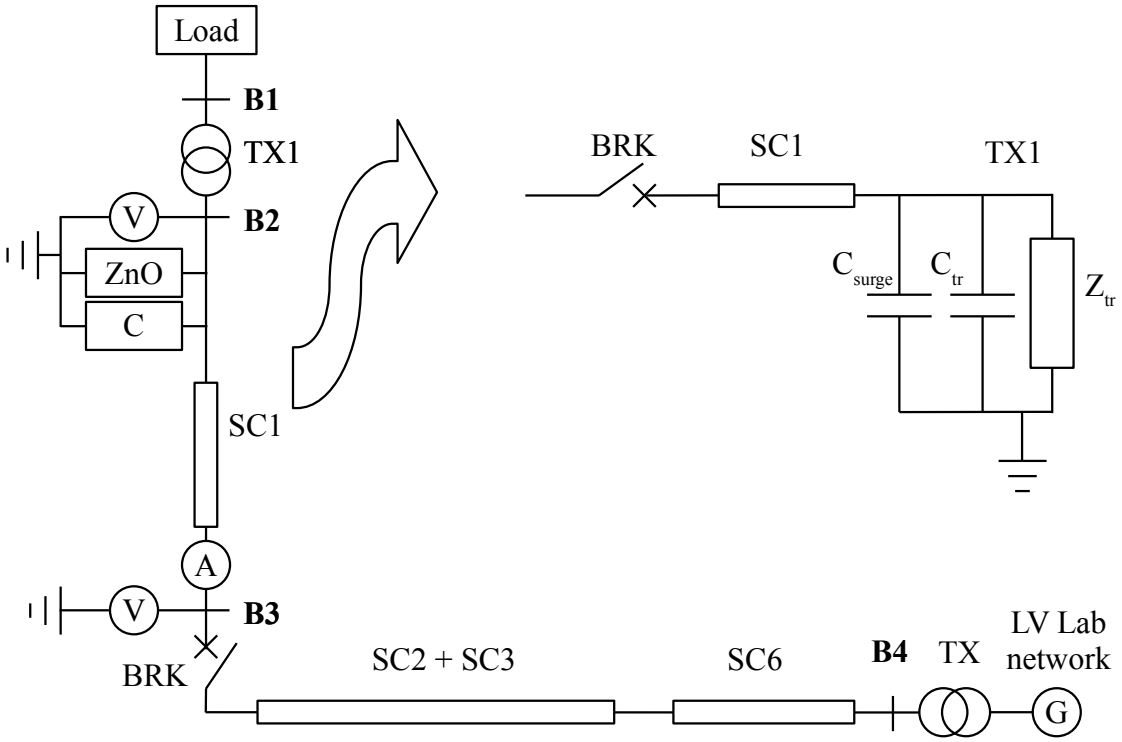

Figure 6.25: Capacitor at TX1.

The purpose of having the surge capacitor is to slow down the surge front and the transient recovery voltage. The consequence of reducing the steepness of the voltage surge is that the rise time of the surge is brought into the limits defined by standards (1.2 μs).

This is achieved by increasing the time constant of the transformer by adding additional capacitance as shown in Fig. 6.26.

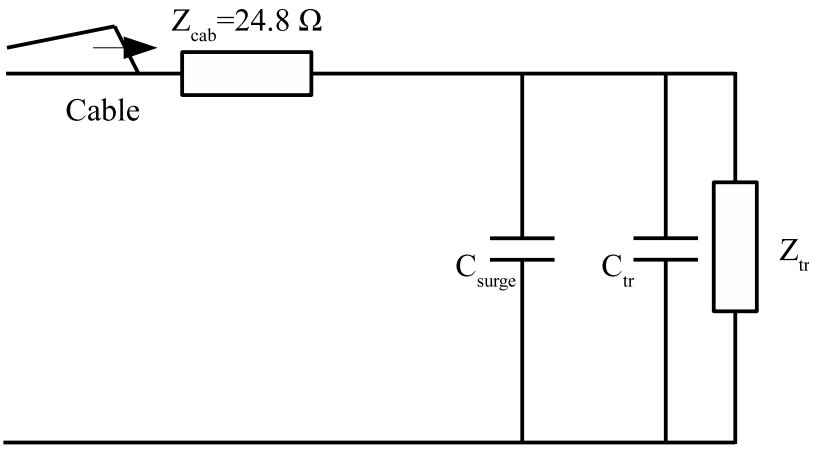

Figure 6.26: Surge capacitor protection - simplified circuit.

The time constant of the surge is given by

$$\tau = Z_{cab}\,(C_{tr} + C_{surge}) \tag{6.3}$$

where C_{surge} is the capacitance of the surge capacitor.

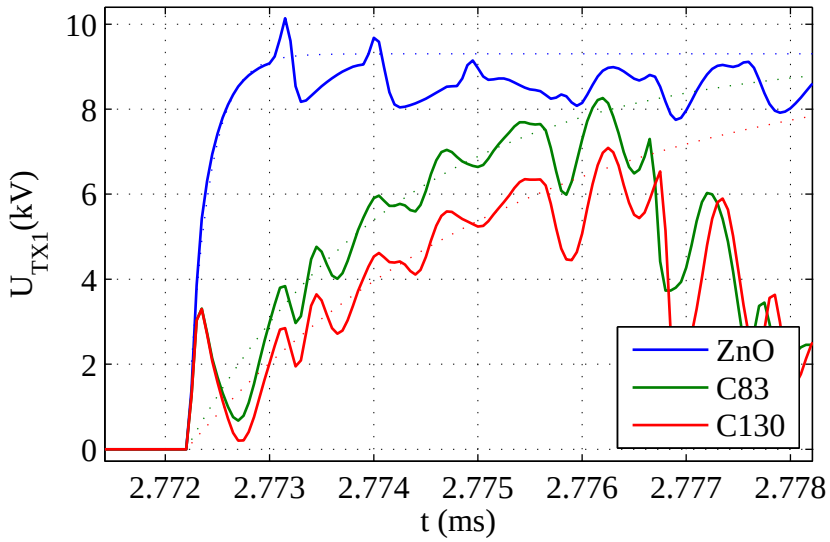

Figure 6.27: Voltage surge rise time without and with surge capacitor protection - simulation.

In Fig. 6.27 the impact of the surge capacitor protection on the surge rise time is observed. The plot marked with $C83$ shows the surge when a $83nF$ capacitor is used, the plot marked with $C130$ shows the surge with a $130nF$ capacitor. The results obtained by the simulation agree with the analytical calculations presented with dotted lines. The oscillations of the voltage that appear in the plot are caused by the stray inductance of the capacitor leads and can be minimized when shorter leads are used. The value of the lead stray inductance is calculated according to the length and the cross section area of the surge capacitor leads.

The transient recovery voltage is also affected by the added capacitance in the system. The rate of rise of the transient recovery voltage is reduced leading to a lower number of reignitions. This can be observed in Fig. 6.28 where the transient recovery voltage is showed both with and without the surge capacitor added.

A stiffer voltage obtained by added capacitance in the system results in a significantly reduced magnitude of the voltage strikes during an opening of the breaker. This behavior is noted in Fig. 6.29.

As it can be noted from Fig. 6.29, the number of reignitions during the breaker opening operation is significantly reduced when the surge capacitors are used. Moreover, the magnitude of the voltage strikes is reduced by a factor of two.

However, the additional capacitance causes voltage oscillations during the energizing transient. The comparison of these voltage oscillations for different values of surge capacitance is shown in Fig. 6.30.

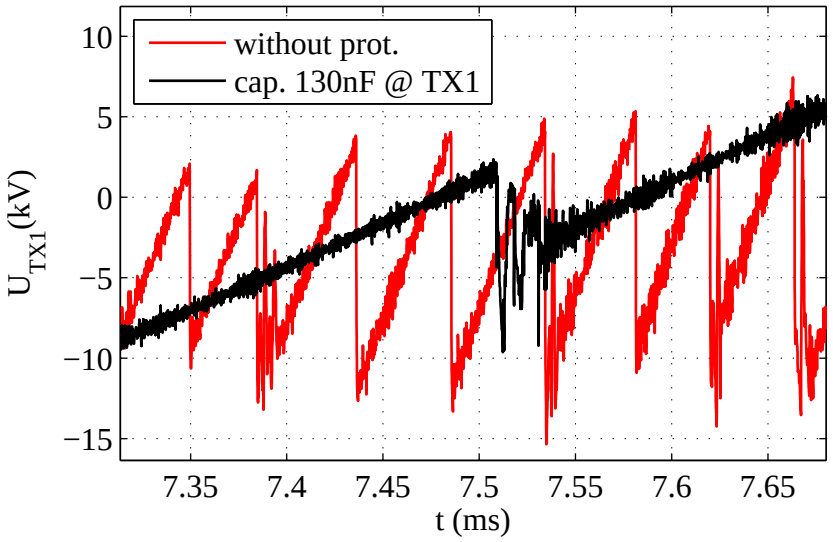

Figure 6.28: Rate of rise of transient recovery voltage - simulation.

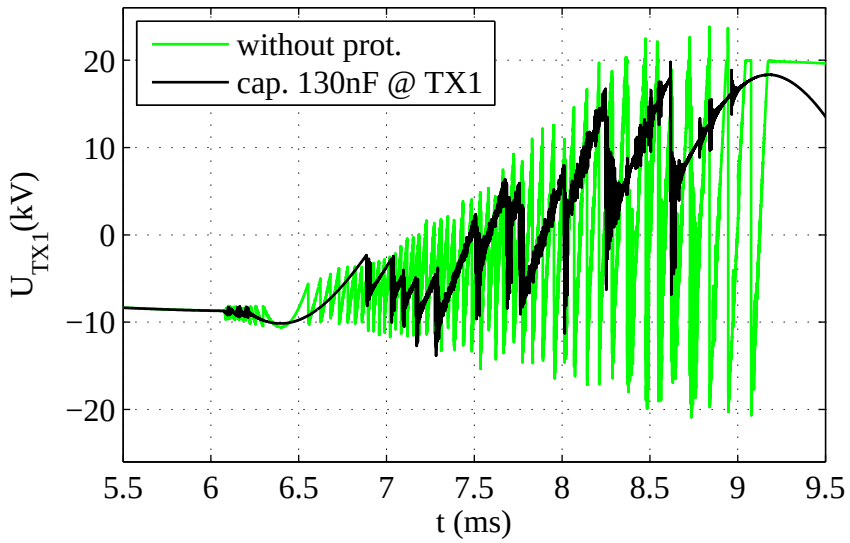

Figure 6.29: Impact of $130nF$ surge capacitor on transient voltage - simulation.

The comparison of the simulation results shows very good agreement to the measurements. In general, the comments made in the analysis of the base case can be confirmed for the case with the surge capacitor protection. The negative impact of the simplified transformer model which does not include the damping added to stray capacitances is even more dominant. The added capacitance produces even more high frequency oscillations with a low damping.

When $130nF$ surge capacitors are installed, the timing of the contact separation in the simulations matches closely the timing recorded in the measurements. Plots that show the transient voltage during the opening operation of the breaker with a $130nF$ surge capacitor, are presented in Figs. 6.31 and 6.32.

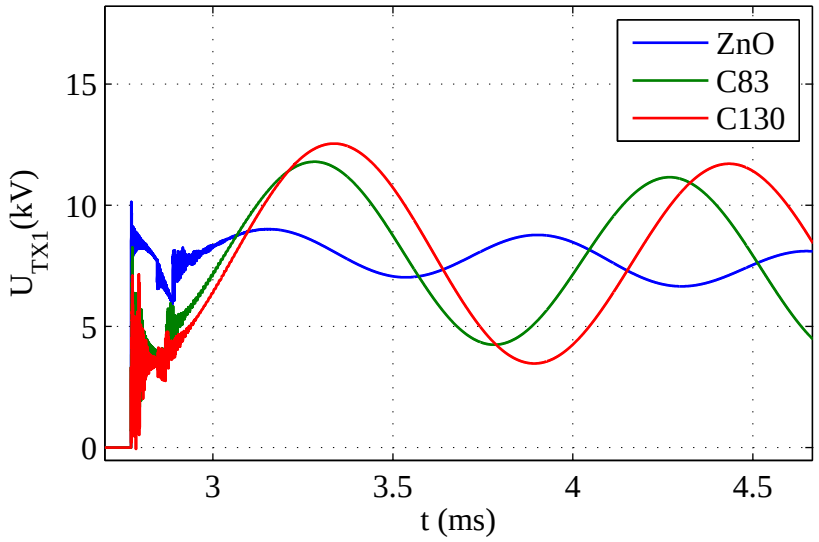

Figure 6.30: Low frequency voltage oscillations - simulation.

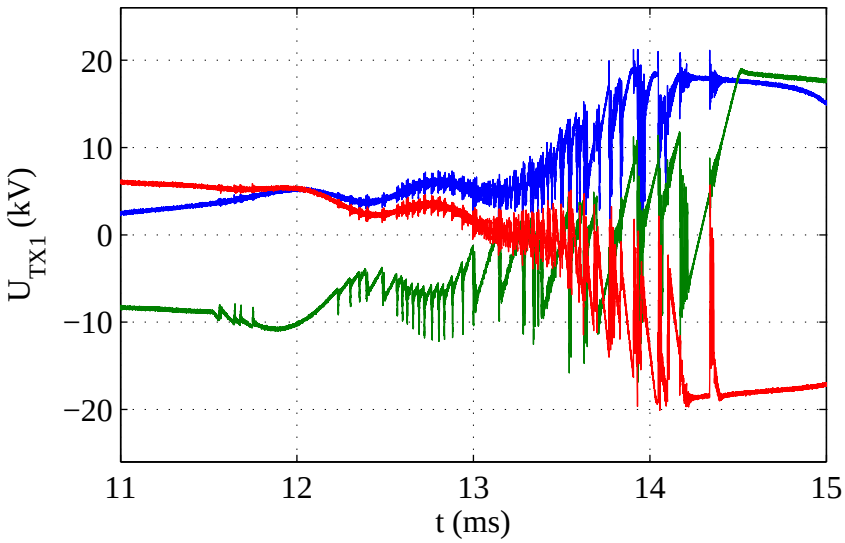

Figure 6.31: Transient voltage during opening - surge capacitor 130nF - measurement.

When the simulation and the measurement results are compared in Figs. 6.31 and 6.32, it is observed that the time instant of the start of the contact separation is in good agreement. Moreover, the magnitude of the strikes and the rate of rise of the recovery voltage are simulated with good accuracy. However, since the damping of the high frequency oscillations at the transformer is very low due to the limitations of the model, the capacitive coupling between phases is more evident in the simulation plot where some very strong high frequency oscillations can be seen after every strike.

The voltage strikes obtained by the characterization of the transient voltages are presented in Figs. 6.33 and 6.34. Although the measurement show the presence of strikes with a rise time of almost 5 μs, in the simulations, the slowest strike has the rise time of 4 μs. A good agreement is observed when the voltage strikes are compared. The error in the mag-

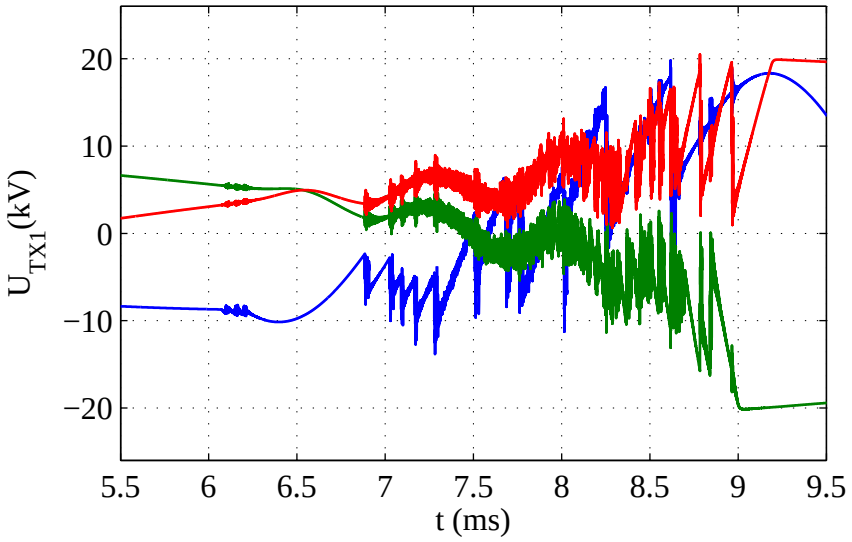

Figure 6.32: Transient voltage during opening - surge capacitor 130nF - simulation.

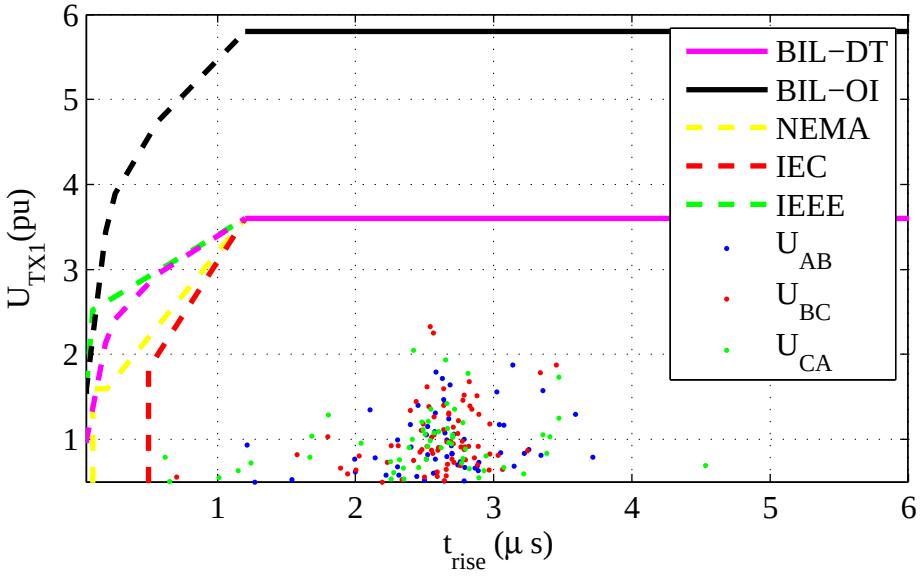

Figure 6.33: Strikes at TX1 during opening - surge capacitor 130nF - measurement.

nitude of the simulated voltage strikes is below 10%, while the comparison of the voltage surge rise times is within a 20% error. The surge magnitudes dropped significantly when compared to the base case and are kept below a $2pu$ limit.

Yet another case with the surge capacitor protection is studied. In this case, the surge capacitor is not placed at the terminals of the protected device but instead at the terminals of the breaker at bus B3. This scheme is presented in Fig. 6.35.

As expected, the impact on the transient voltage in this case is very similar to the case when the same capacitor was placed at transformer TX1. The rate of rise of the transient recovery voltage is significantly reduced when compared to the base case, which can be seen in Fig. 6.36.

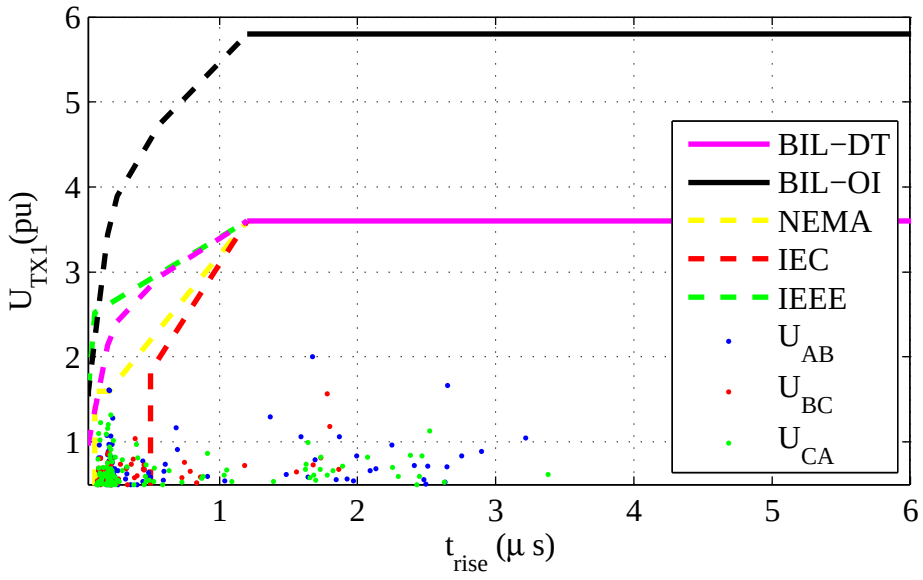

Figure 6.34: Strikes at TX1 during opening - surge capacitor 130nF - simulation.

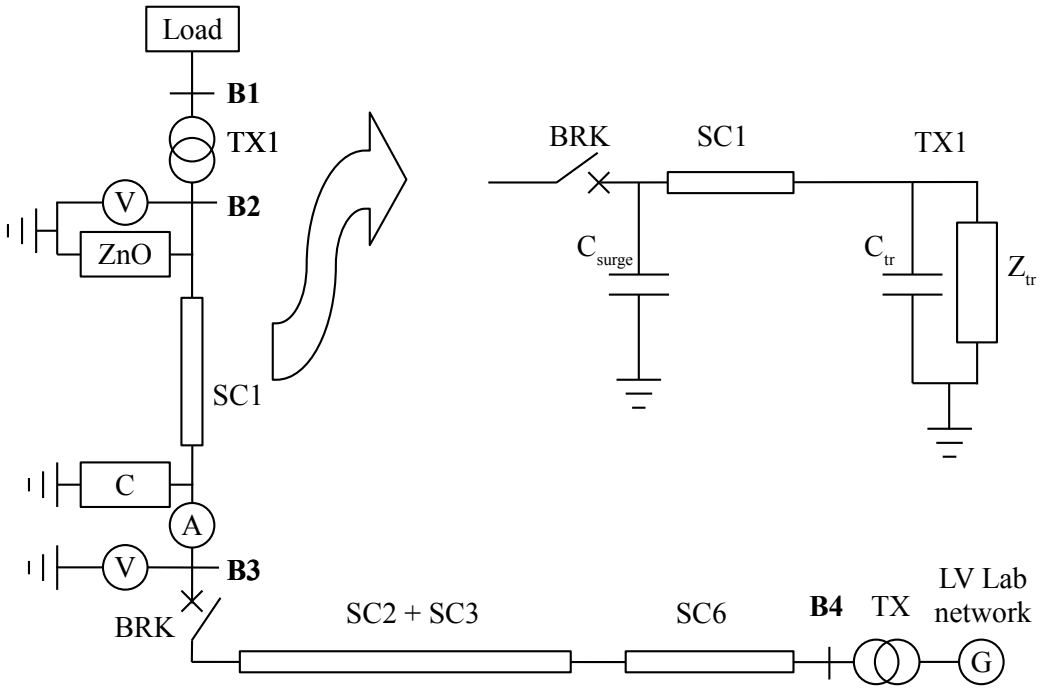

Figure 6.35: Capacitor at breaker.

Moving the surge capacitors to the other side of the cable impacts the behavior of the high frequency oscillations in a way that the capacitive coupling of the phases is more evident in the plots. This is because the current bursts which charge the surge capacitor during the voltage surges, do not travel along the cable any more. Moreover, the wave reflection is also affected by moving the surge capacitor to the breaker since the current waves coming from

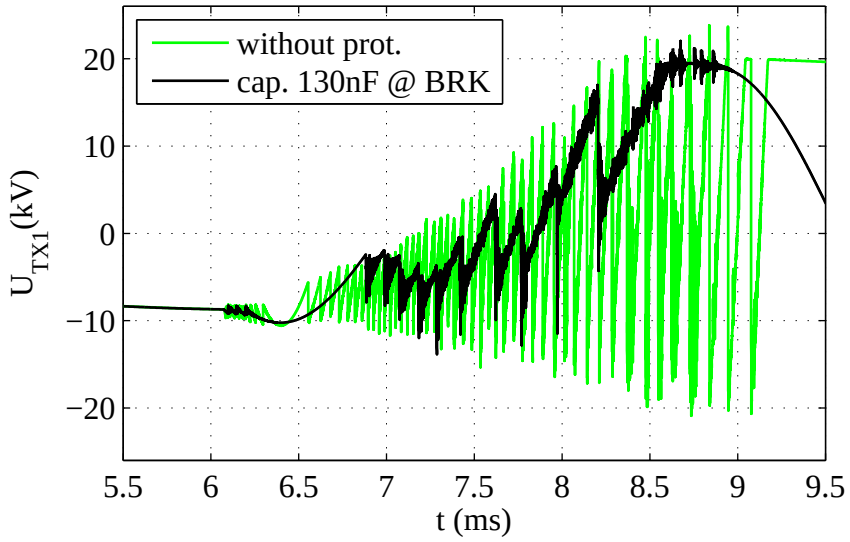

Figure 6.36: Impact of 130nF surge capacitor at breaker on transient voltage - simulation.

TX1 towards the breaker are almost completely reflected back. This leads to an increase of the high frequency oscillations which can be seen in Figs. 6.36-6.38.

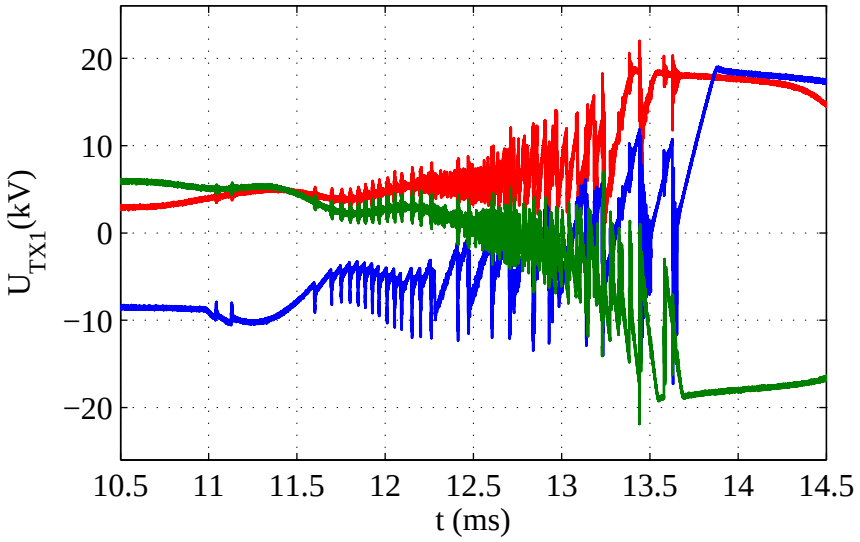

Figure 6.37: Transient voltage during opening - surge cap. 130nF at breaker - measurement.

When the magnitudes and the rise times of the voltage surges recorded at transformer TX1 are compared, a satisfactory agreement between simulations and measurements is observed. Plots showing strikes during the opening of the breaker are shown in Figs. 6.39 and 6.40.

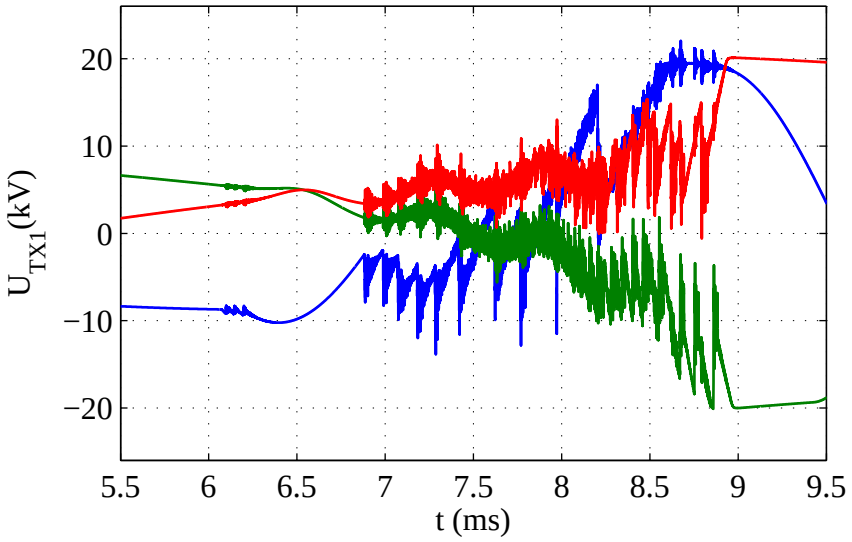

Figure 6.38: Transient voltage during opening - surge cap. 130nF at breaker - simulation.

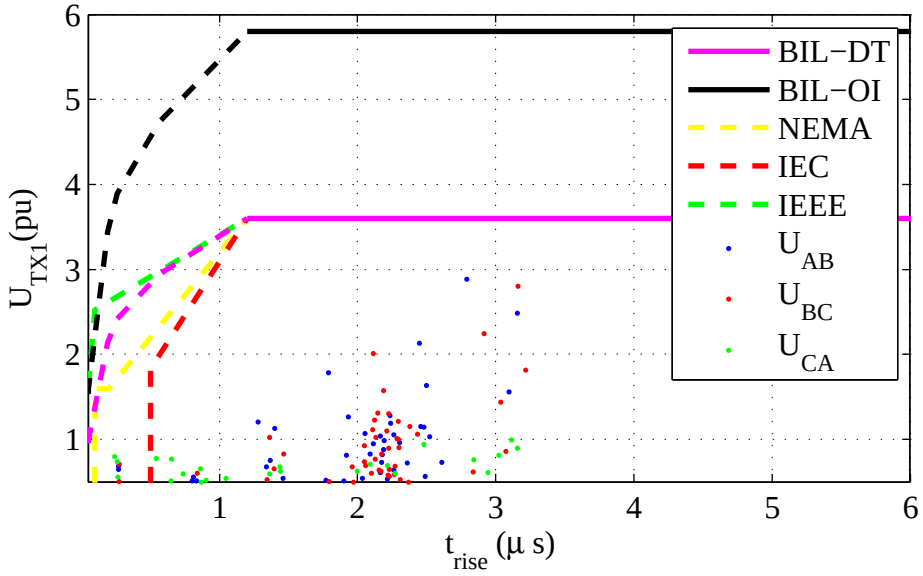

Figure 6.39: Strikes at TX1 during opening - surge cap. 130nF at breaker - measurement.

In Figs. 6.39 and 6.40 it can be seen that results similar to the other $130nF$ surge capacitor case are obtained. The magnitude and the rise times of the highest recorded surges are almost identical. Furthermore, the reignitions are also observed as in other cases when surge capacitors are used, but the number of reignitions is significantly lower when compared to the base case.

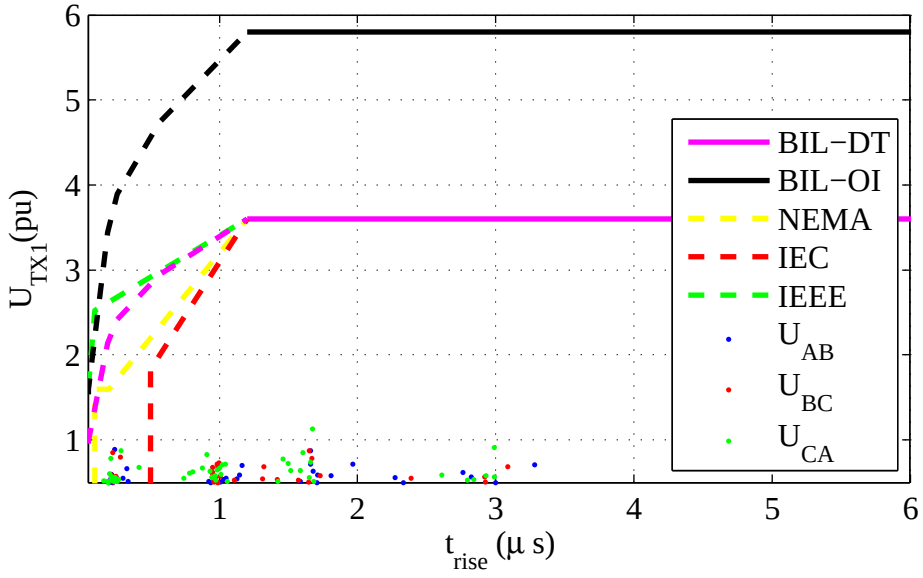

Figure 6.40: Strikes at TX1 during opening - surge cap. 130nF at breaker - simulation.

6.3.3 RC protection

The RC protection is used for mitigation of the high frequency transients and protection of transformers and induction motors [75], [76]. It is very effective and proved to reduce the number of reignitions [75]. The principle of an RC protection is very simple. The wave reflections which give the highest magnitude of transient overvoltages occur in the systems where the surge impedance of the transformer Z_{tr} is much higher than the cable surge impedance Z_{cab}. In order to prevent such reflections, a resistor with a capacitor is connected in parallel to the protected transformer. This is presented in Fig. 6.41.

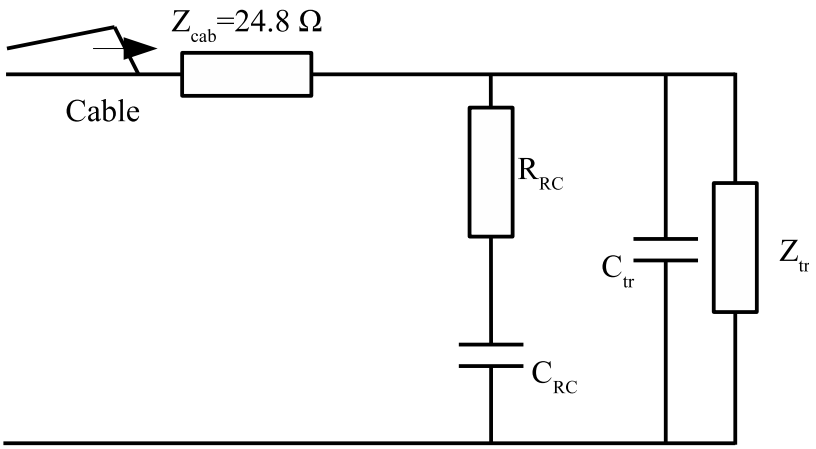

Figure 6.41: RC protection scheme.

The resistance of the resistor is chosen so it matches the surge impedance of the cable Z_{cab}. By doing this, the wave reflections are avoided since the reflection coefficient is equal to zero

$$\alpha = \frac{R - Z_{cab}}{R + Z_{cab}} = 0. \tag{6.4}$$

Another way to explain the principle of the RC protections is to observe it as a special case of the surge capacitor protection. The surge capacitor used in the RC protection will act in the same way as when it is directly connected to the terminals of the protected transformer, which means that the rise time of the surge is increased. The resistor connected in series to it is used to damp the high frequency current which occurs after every strike. By damping the high frequency current superimposed to the power frequency current, the current zero crossing and thus the reignition is avoided if the power frequency current is very high. This method is shown to be very effective during the induction motor starts [75].

However, the generation of the reignition depends on other factors such as the rate of rise of the breakers dielectric strength and the rate of rise of the transient recovery voltage. For this reason, the RC protection may not be sufficient to eliminate reignitions completely, but will definitely reduce the number of reignitions and the magnitude of the voltage strikes.

RC protection - oil-insulated transformer

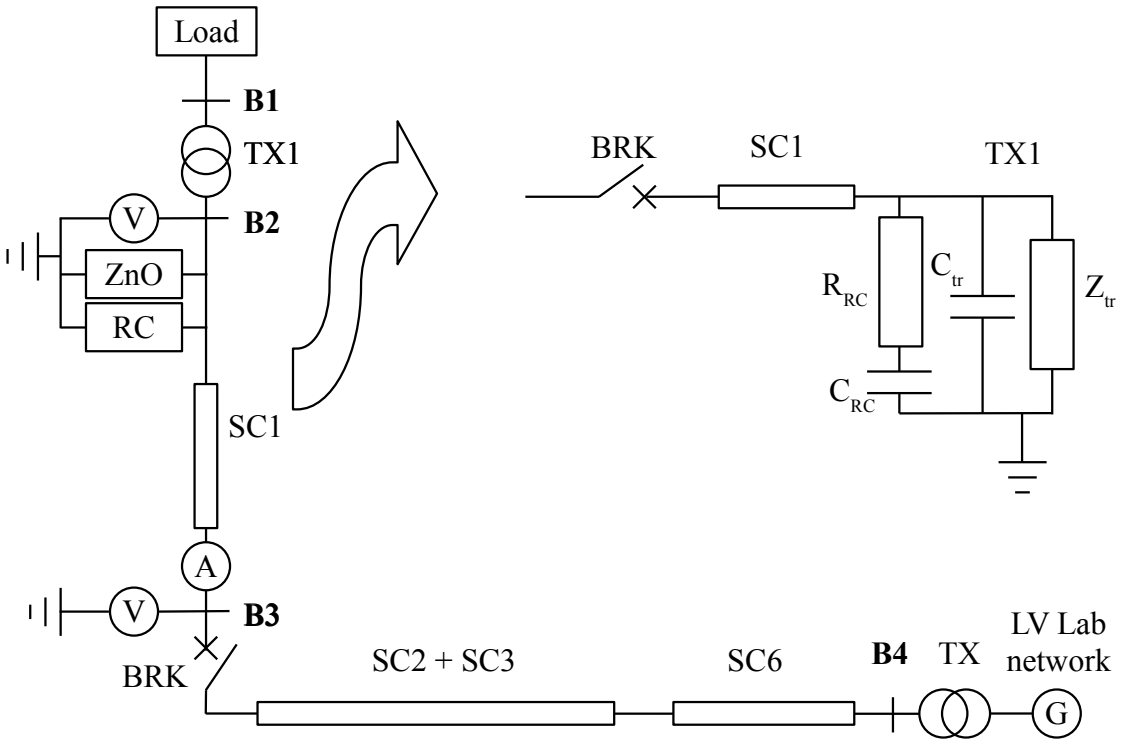

Figure 6.42: RC protection test setup.

Fig. 6.42 present the scheme of the test setup. The RC protection is made using a $R = 20\Omega$ resistor and the capacitor with a capacitance of $C = 130nF$. The surge impedance of

the cable is calculated to be 24.8Ω, and used RC protection does not present a characteristic impedance termination. However, the resistance of the surge resistor is very close to this value and this is acceptable for an RC protection study.

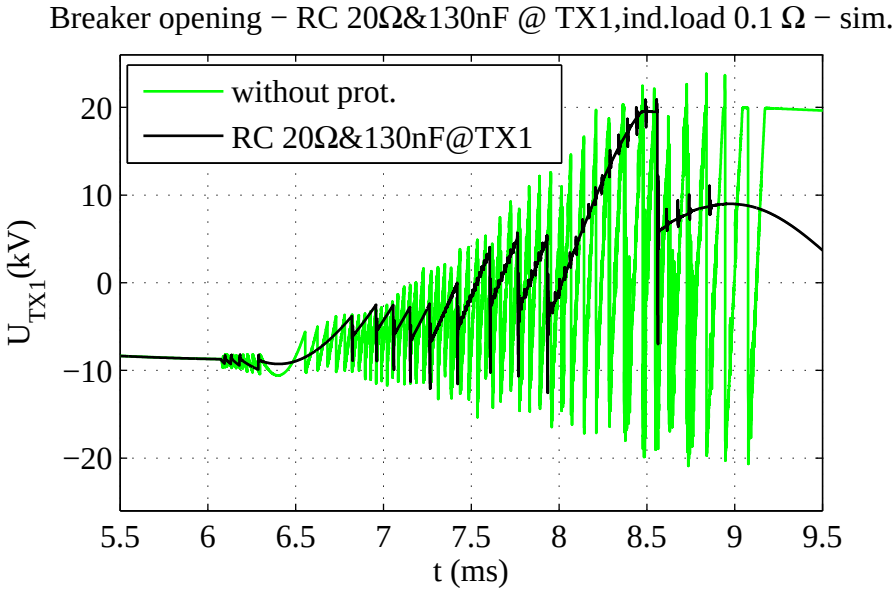

Figure 6.43: Impact of RC protection on transient voltage ($R20\Omega\&C130nF$) - simulation.

The effect of the RC protection on the voltage transient during the opening of the breaker recorded in simulations is shown in Fig. 6.43. In Fig. 6.43 it can be noted that the RC protection did not stop the appearance of the reignitions. Although the transient recovery voltage is slowed down even further by increased capacitance of the system, it was not enough to prevent reignitions. In the very beginning of the transient, the rate of rise of the transient recovery voltage is high due to the current chopping, and the breakers rate of rise of dielectric strength is still very slow with the initial speed of $5.5kV/ms$. The impact is similar to the surge capacitor protection but with improved damping of the high frequency voltage oscillations caused by a high frequency current.

Compared to the measurements, the RC protection case shows a good agreement between the simulation and the measurement results. It can be seen that the voltage strike with the highest magnitude obtained in the simulation matches quite well to the measurements. This can be noted in Fig. 6.44. The high frequency oscillations seen in measurements do not show up in the simulations. These high frequency oscillations are caused by the voltage wave reflections from the bus where the breaker is connected and the transformer TX2.

A graph showing the voltage strikes in a scatter plot is presented in Fig. 6.45. From a transient protection perspective, an RC protection is very good since it keeps the magnitude of the voltage surges within the BIL and below the critical voltage levels obtained in Section 4.3 and defined by standards for large motors.

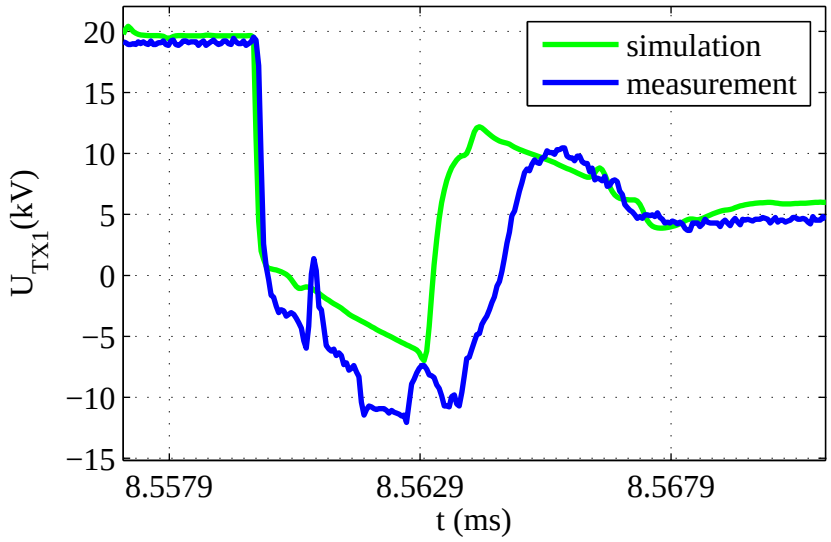

Figure 6.44: Simulation and measurement comparison ($R20\Omega\&C130nF$).

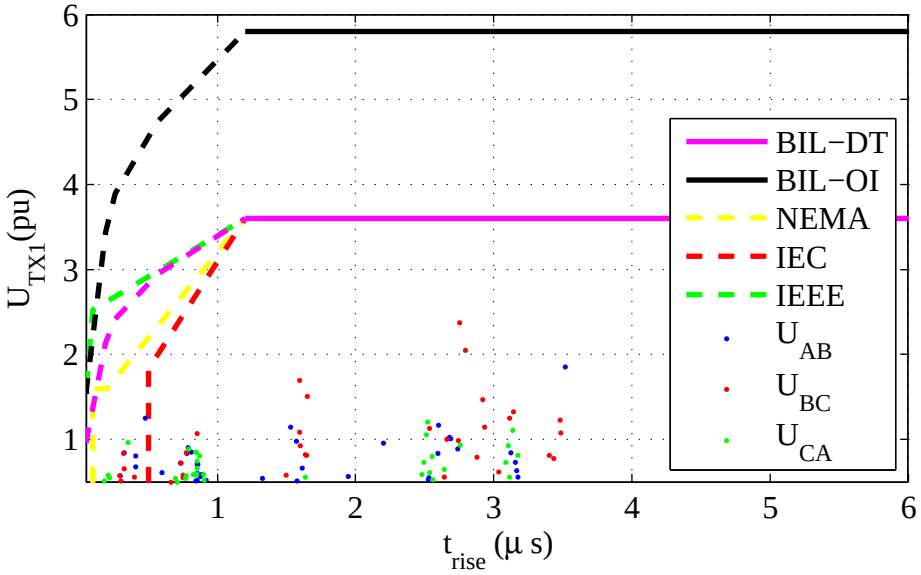

Figure 6.45: Voltage strikes $R20\Omega\&C130nF$ - simulation.

RC protection - dry-type transformer

The test with the RC protection is performed with the dry-type transformer. In this case, the RC protection is again placed in front of the transformer TX2. The RC protection is placed at buses **B2** and **B4** as shown in Fig. 6.2. The RC protection at bus **B2** consists of an $R = 20\Omega$ resistor and a $C = 83nF$ capacitor. At bus **B4**, an $R = 20\Omega$ resistor and a $C = 83nF$ capacitor are used. As mentioned before, a $17mH$ load is used for this test. However, in simulations, a $0.947mH$ is used in order to obtain the same current level as obtained with the oil-insulated transformer test. Furthermore, in this test, three ZnO blocks are used as a surge arresters protection, cutting the voltage at about a $30kV$ level. However,

in order to make the results comparable to oil insulated transformers, four ZnO blocks are used in the simulations.

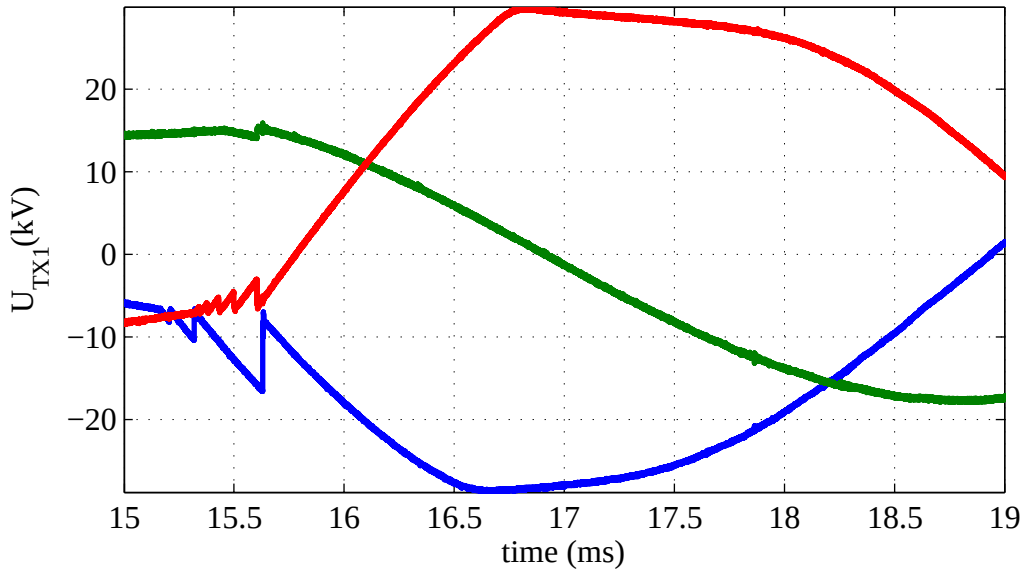

Figure 6.46: Transient voltage at TX1(dry-type) during opening - RC protection - measurement.

Fig. 6.46 shows the transient voltage recorded at dry-type transformer, TX1, when the RC protection is used. It is observed that restrikes have a very small magnitude. The rise time of the restrikes is still about $100ns$, but the magnitude is well below the critical level.

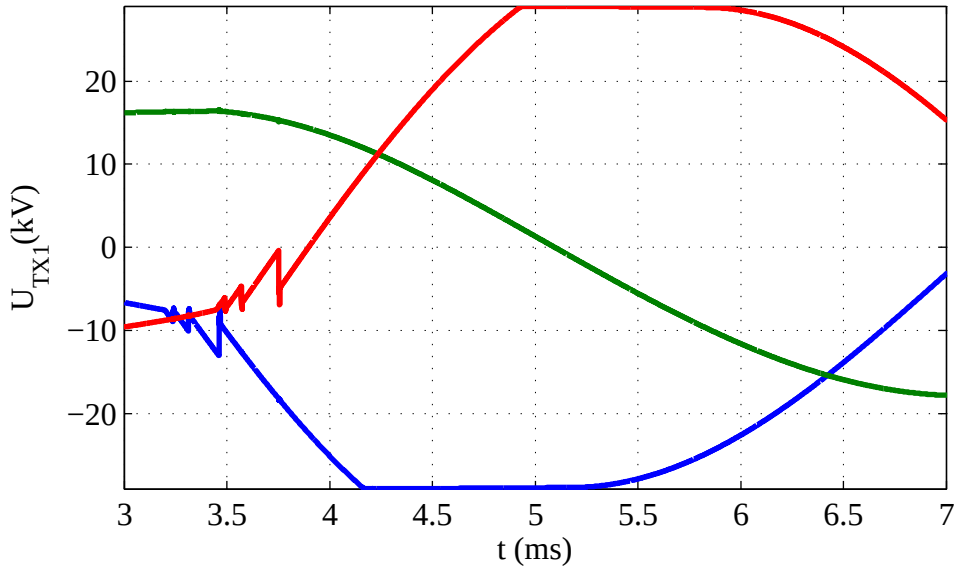

Figure 6.47: Transient voltage at TX1(dry-type) during opening - RC protection - simulation.

Fig. 6.47 shows the same transient recorded in a simulation. It can be seen that very good agreement is obtained with approximately the same level of voltage strike level. Simulations with a higher current level interruption and a higher surge arrester voltage level did not show appearance of critical strikes when the RC protection is used at both transformers.

6.3.4 RC and surge capacitor protection

In order to decrease the magnitude of the voltage strikes even further and to protect transformer TX2, a $130nF$ surge capacitor is connected to the terminals of transformer TX2. Transformer TX1 is protected by an RC protection with a 30Ω resistor and a $83nF$ capacitor. The aim is to even further slow down the transient recovery voltage and to reduce the rise time of the transients reflected from TX2 transformer. The scheme showing this setup is presented in Fig. 6.48

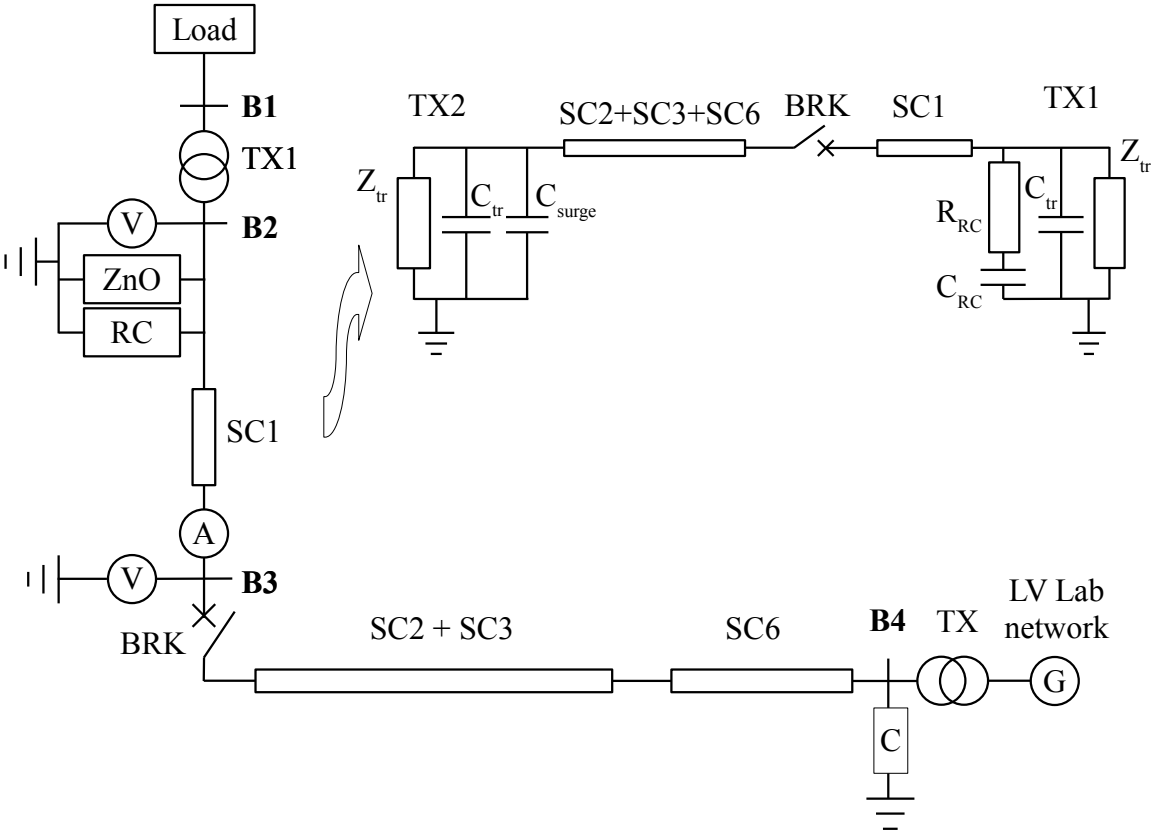

Figure 6.48: RC and surge capacitor protection.

The simulation results showing the impact of the protection installed at two critical points is presented in Fig. 6.49.

Fig. 6.49 reveals that the magnitude of the strikes is increased when compared to the case when only RC protection is used. The explanation can be found when Fig. 6.50 is observed.

The reason for increased magnitude of surges is that at the time instant when the voltage strike is at its minimum, the reflected voltage from the TX2 transformer arrives to TX1 at $t = 8.199ms$ increasing the magnitude of the strike. The reflected voltage is inverted at TX2 due to the presence of the surge capacitor at terminals of transformer TX2. This phenomenon is avoided in the case with only RC protection at TX1 is used. This can be observed in Fig. 6.50.

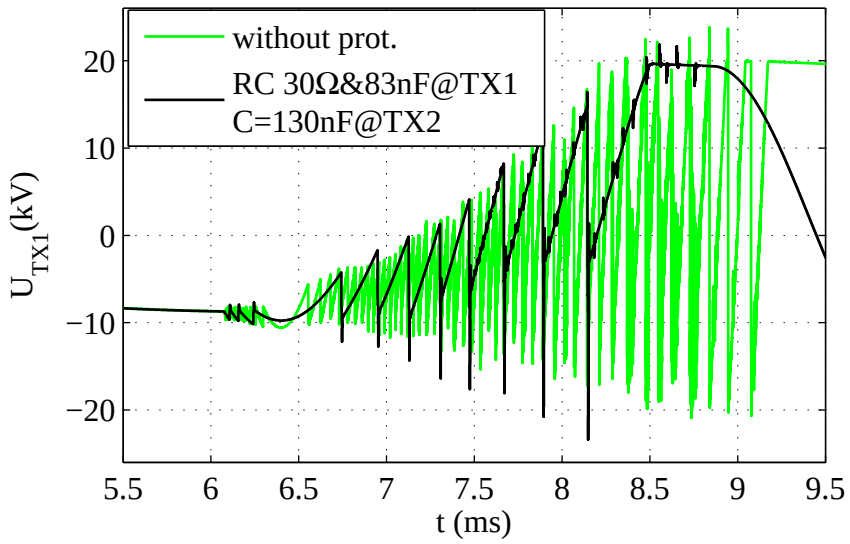

Figure 6.49: Impact of RC and surge capacitor protection ($R30\Omega\&C83nFC130nF$) - simulation.

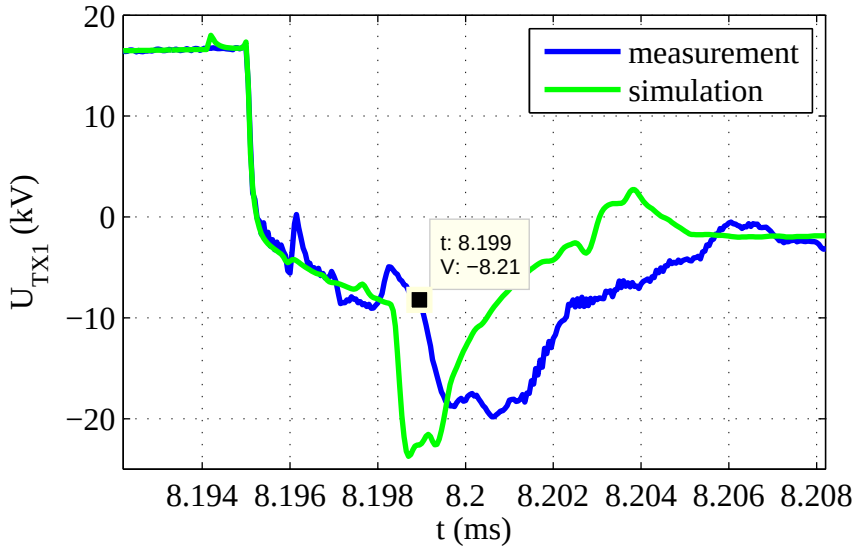

Figure 6.50: Simulation and measurement comparison $R30\Omega\&C83nF$ and $C130nF$.

The scatter plots show clearly the increase of the magnitude of the voltage strikes with slightly increased rise times as seen in Fig. 6.51.

In Fig. 6.51 it can be observed that the magnitudes of the surges almost reach the BIL defined by IEEE standards for the dry-type transformers. This means, that this protection scheme provides marginal protection of transformer TX1 because the wave reflected back from transformer TX2 arrives at TX1 producing high magnitude surges. This means that the length of the cables, and the wave propagation speed should be considered when a surge protection scheme is designed.

This case clearly shows that the high frequency mitigation protection should be carefully calculated and set up. When the additional protection is added to the system in order to

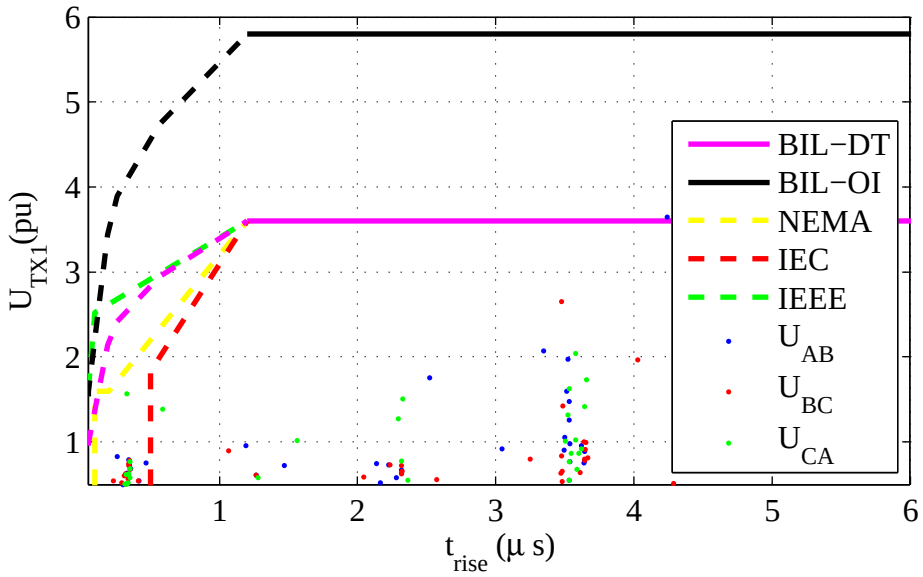

Figure 6.51: Voltage strikes $R30\Omega\&C83nF$ and $C130nF$ - simulation.

improve the high frequency transient mitigation, the final result may be even worse when compared to a simple protection scheme.

Chapter 7

Conclusions and Future Work

In this thesis, the high frequency electromagnetic transient phenomenon was analyzed and studied. Modeling of various components needed for simulations of a wind farm collection grid such as transformers, reactors, cables and breakers for such a study is conducted. Furthermore, measurements of high frequency transients are performed at Chalmers University of Technology and in the cable laboratory at ABB Corporate Research in Västerås, Sweden. The measurements are used for the parameter estimation of the models and for the simulation verification. Cases where surges of the magnitude and/or rise time above the basic lightning impulse voltage level appear are identified. Also, some transient protection schemes are studied and the performance of different transient mitigation devices is analyzed.

7.1 Conclusions

In this study, it is consluded that:

- The frequency dependent cable model available in PSCAD/EMTDC provides a good basis for the high frequency transient phenomenon study if the electrical parameters of the insulation layers are recalculated to compensate for the semi-conducting layers. Since the cable geometry available in PSCAD/EMTDC does not allow for the modeling of the multi-pipe cables, the propagation speed of the surge is somewhat quicker when compared to the measurements. However, the reflection phenomenon is modeled correctly;
- To obtain an accurate transformer model for frequencies up to a couple of kHz, the frequency dependency of resistances in the transformer have to be accounted for. The existing transformer model in PSCAD/EMTDC based on the UMEC algorithm that accounts accurately for the core non-linearities with added Foster network of R and L components to model the frequency dependent resistance can be used for accurate simulations of transients in that frequency range;
- For the high-frequency transient analysis, stray capacitances are dominant in the formation of the transformer response, and an accurate model can be obtained when stray capacitances of the transformer are accurately estimated and added to the existing

PSCAD/EMTDC model. Such a model simulated the voltage surges with accurately calculated magnitudes and rise times. However, it shows a poor damping of the high frequency oscillations caused by the capacitive coupling of the phases and needs to be improved for more accurate simulations;

- A closing of a breaker can generate excessive turn-to-turn overvoltages. The most severe turn-to-turn overvoltages appear in the case of delta connected dry-type transformers. The maximum turn-to-turn voltage exceeds 2.5 times the voltage obtained during the lightning impulse test;

- The rise time of the transient has a strong impact on the magnitude of turn-to-turn voltages. During the breaker switching in cable systems where dry-type transformers or reactors are installed, severe turn-to-turn voltages can appear due to short rise times of the transients. Consequently, the critical voltage as a function of rise time is proposed. The proposed critical voltage is similar to those ones found in standards for the withstand voltages of large motors;

- During the simulations and the measurements, surges which exceed the BIL of dry-type transformers specified by IEEE standards, both in magnitude and rise time are recorded even when surge arresters are used. Furthermore, the obtained voltage strikes exceed the proposed critical voltage level, as well as the standard withstand voltage levels for large motors. The highest overvoltages are recorded with dry-type transformers due to a low stray capacitance of dry-type transformers that contributes to a short rise time of the voltage surges;

- The RC protection used in the tests did not prevent the appearance of repetitive surges and voltage escalations due to a very high rate of rise of the transient recovery voltage which is much faster than the rate of rise of the dielectric strength (RRDS) of the breaker. This was the case even when a breaker with a very fast RRDS is used to interrupt current. Among the mitigation methods tested in this study, it is observed that a surge capacitor protection or an RC protection coupled with surge arresters decreases the voltage stress below the BIL.

7.2 Future Work

The cable modeling for high frequency transients can be improved using a cable model developed in FEM where the frequency dependent impedance and admittance matrices of the cable are obtained. The estimation of the electric and magnetic properties of the insulating materials used in the cable can be obtained by measurements in order to obtain better accuracy. In this work, only the magnitude of turn-to-turn voltages of a particular winding is used to calculate the envelope of the critical voltage. Furthermore, the voltage breakdown in the insulation material is not studied for different rise times of voltage surges. Therefore, it would be of great interest to perform similar research on different types of transformers with different design of transformer windings and different power ratings in order to find the envelope for critical voltages. Furthermore, this research needs to include a research about the influence of the rise time of voltage surges on the voltage breakdown of insulation materials.

Bibliography

[1] Erik Persson, "Transient Effect in Application of PWM Inverters to Induction Motors," *IEEE Trans. Ind. Appl.*, vol. 28, no. 5, pp. 1095-1101, Sep./Oct. 1992.

[2] S.M.Wong, L.A.Snider, E.W.C.Lo, "Overvoltages and reignition behavior of vacuum circuit breaker," *International Conference on Power Systems Transients - IPST 2003 in New Orleans, USA*, 2003.

[3] P.Picot, "Vacuum switching," *Cahier technique Schneider Electric*, no. 198, pp. 4, March 2000.

[4] A. Mazur, I. Kerszenbaum, and J. Frank, "Maximum insulation stresses under transient voltages in the HV barrel type winding of distribution and power transformers," *IEEE Trans. Ind. Applicat.,* Vol. 24, pp. 427-433, May-June 1988.

[5] D. Paul, "Failure Analysis of Dry-Type Power Transformer," *IEEE Transaction on Industry Applications,* Vol. 37 No. 3, May-June 2001

[6] M. Olsen, *"Failure Analysis of Siemens Geafol Cast-resin Transformer,"* Danish Technological Institute, Technical Report No. 1154834-1, May 2003

[7] D.D. Shipp, T.J. Dionise, V. Lorch, B.G. MacFarlane, "Transformer Failure Due to Circuit-Breaker-Induced Switching Transients," *Industry Applications, IEEE Transactions on*, Vol. 47 No. 2 pp. 707-718 March-April 2011.

[8] D.J.Clare, "Failures of encapsulated transformers for converter winders at Oryx Mine," *Electron Magazine*, pp. 24-27, March. 1991.

[9] CIGRE working group A2-A3-B3.21, "Electrical Environment of Transformers; Impact of fast transients," *ELECTRA* 208, February 2005

[10] W. H. Bartley, "An Analysis of Transformer Failures, Part 2 - Causes, Prevention and Maximum Service Life," *The Locomotive, The Full Story,* 1997

[11] B.K. Gupta, B.A.Lloyd, D.K. Sharma "Degradation of Turn Insulation in Motor coils Under Repetitive Surges," *IEEE Trans. on Energi Conv.,* Vol.5 No. 2, June 1990

[12] G.C. Stone, R.G. Van Heeswijk, R. Bartnikas "Investigation of The Effect of Repetitive Voltage Surges on Epoxy Insulation," *IEEE Trans. on Energy Conv.,* Vol. 7 No. 4 December 1992

[13] W. Sweet, "Danish wind turbines take unfortunate turn," *Spectrum, IEEE*, vol. 41, Issue 11, pp. 30-34, Nov. 2004.

[14] J.Larssen, H.Soerensen, E.Christiansen, S. Naef,P.Völund "Experiences from Middelgrunden 40 MW Offshore Wind Farm," *Copenhagen Offshore Wind* , 26-28 Oct. 2005.

[15] B. K. Gupta, N. E. Nilsson, D. K. Sharma "Protection of Motors Against High Voltage Switching Surges," *IEEE Trans. on Energy Conversion,* Vol. 7 No. 1, March 1992

[16] Turn Insulation Capability of Large AC Motors, EPRI Project RP 2307-1, *Final Report, EPRI EL-5862,* Vol. 1 and 2, July 1988

[17] B. K. Gupta, B. A. Loyd, S. R. Campbell, D. K. Sharma, N. E. Nilsson "Turn Insulation Capability of Large AC Motors, Part 1/Surge Monitoring," *IEEE Trans. on Energy Conversion,* EC-2 No. 4, December 1987, pp 658-665.

[18] M.P.Reece, "A review of the development of the vacuum interrupter," *Phil.Trans.R.Soc.Lond.A.* vol.275, no. 1248, pp. 121-129, Aug. 1973.

[19] R. Kirkland Smith, "Vacuum Interrupters Have the Low Environmental Impact Required for Today's Medium Voltage Switching Applications," *IEEE PES Transmission and Distribution Conference and Exposition,* vol.1, pp. 588-592 , 2001

[20] Paul G. Slade, "Growth of Vacuum Interrupter Application in Distribution Switchgear," *Trends in Distribution Switchgear,* Conference Publication no. 459, November 1998

[21] Alexey M. Chaly, Alevtina T. Chalaya, Irina N. Poluyanova, Victor N. Poluyanov "The Features of 0.4 kV motor interruption by a vacuum contactor with different contact materials," *Discharges and Electrical Insulation in Vacuum, Proceedings ISDEIV. XVIIIth International Symposium,* vol. 2, pp. 435-438, Aug. 1998.

[22] Smeets R.P.P., van der Wen W.J., Wartanabe K., "Vacuum Arc Lifetime extension at Small Gaplength: Beneficial for Low-Surge Circuit Interruption," *International Conference on Gas Discharges and Their Applications*, Tokyo, 1995.

[23] Reininghaus U., "Schalverthalten Unterschiedlicher Kontaktwerkstoffe in Vacuum," Ph.D. Thesis, TU Braunschweig, 1983.

[24] Smeets R.P.P., "Low current behavior and Current Chopping of Vacuum Arcs," Ph.D. Thesis, University of Eindhoven, 1987.

[25] J. Helmer, M. Lindmayer "Mathematical Modeling of the High fiequency Behavior of Vacuum Interrupters and Comparison with Measured Transients in Power Systems," *XVIIth International Symposium on Discharges and Electrical Insulation in Vacuum*, pp. 1-9, July. 1996.

[26] M. Glinkowski, "Voltage Escalation and Reignition Behavior of Vacuum Generator Circuit Breakers During Load Shedding", *IEEE Trans. on Power Delivery,* Vol. 12, No. 1, pp.219-226, Jan. 1997.

[27] S.M.Wong, L.A.Snider, and E.W.C.Lo Overvoltages and reignition behavior of vacuum circuit breaker, *6th International Conference on Advances in Power System Control, Operation and Management. Proceedings. APSCOM* Hong-Kong, pp.653-658, Nov. 2003.

[28] Das, J.C. "Surges transferred through transformers," *Pulp and Paper Industry Technical Conference, 2002. Conference Record of the 2002 Annual*, No. pp.139-147, 2002

[29] J. H. Harlow *Electric Power Transformer Engineering*, CRC Press, 2004.

[30] J. A. Martinez, B. Gustavsen, and D. Durbak Parameter Determination for Modeling System Transients - Part I: Overhead Lines, *IEEE Trans. on Power Delivery,* Vol. 20 No. 3, pp. 2038-2044, July 2005.

[31] Marti, L. "Simulation of transients in underground cables with frequency-dependent modal transformation matrices," *IEEE Trans. on Power Delivery,* Vol.3 No.3, pp. 1099-1110, July 1988.

[32] Marti, J. R. "Accurate Modelling of Frequency-Dependent Transmission Lines in Electromagnetic Transient Calculations," *IEEE Transactions on Power Apparatus and Systems,* pp. 147-157, January 1982.

[33] H.V. Nguyen, H.W. Dommel, J.R. Marti "Direct Phase-Domain Modelling of Frequency-Dependent Overhead Transmission lines," *IEEE Trans. on Power Delivery,* Vol. 12 No. 3 July 1997

[34] Semlyen, A. Dabuleanu, A. "Fast and accurate switching transient calculations on transmission lines with ground return using recursive convolutions," *Power Apparatus and Systems, IEEE Transactions on,* Vol. 94 Issue 2 pp. 561- 571 March 1975

[35] Manitoba HVDC Research Centre Inc. *EMTDC User's Guide*, Manitoba HVDC Research Centre Inc. 2005.

[36] Gustavsen, B. Semlyen, A. "Rational approximation of frequency domain responses by vector fitting," *Power Delivery, IEEE Transactions on,* Vol.14 No.3 pp.1052-1061 July 1999

[37] Gustavsen, B. Semlyen, A. "Simulation of transmission line transients using vector fitting and modal decomposition," *Power Delivery, IEEE Transactions on,* Vol.13 No.2 pp.605-614 April 1998

[38] Fergestad, P.I. Henriksen, T. "Transient Oscillations in Multiwinding Transformers," *IEEE Transactions on Power Apparatus and Systems,* Vol.PAS-93 No.2 pp.500-509 March 1974

[39] Guardado, J.L. Carrillo, V. Cornick, K.J. "Calculation of interturn voltages in machine windings during switching transients measured on terminals," *Energy Conversion, IEEE Transaction on,* Vol.10 No.1 pp.87-94 Mar 1995

[40] Shibuya, Y. Fujita, S. Hosokawa, N. "Analysis of very fast transient overvoltage in transformer winding" *Generation, Transmission and Distribution, IEEE Proceedings-,* Vol.144 No.5 pp.461-468 Sep 1997

[41] Soysal, O.A., "Voltage stresses in a distribution transformer under nonideal switching conditions," *Power Engineering Society 1999 Winter Meeting, IEEE,* Vol.2 No. pp. 1031-1035 Feb 1999

[42] Alexander D. Podoltsev, K. G. Nilanga B. Abeywickrama, Yuriy V. Serdyuk, Stanislaw M. Gubanski "Multiscale Computations of Parameters of Power Transformer Windings at High Frequencies. Part I: Small-Scale Level," *IEEE Transactions on magnetics,* Vol. 43, No. 11, November 2007.

[43] Soysal, O. A. "A Method for Wide Frequency Range Modeling of Power Transformers and Rotating Machines," *IEEE Trans. on Power Delivery,* Vol. 8 No. 4 pp. 1802-1810 October 1993.

[44] P. T. M. Vaessen, "Transformer model for high frequencies" *IEEE Trans. Power Delivery*, Vol. 3, pp. 1761-1768, Oct. 1988.

[45] Q. Su, R. E. James, and D. Sutanto "A z-transform model of transformers for the study of electromagnetic transients in power systems," *IEEE Trans Power Systems*, Vol. 5, pp. 27-33, Feb. 1990.

[46] A. Morched, L. Marti, and J. Ottevangers "A high frequency transformer model for the EMTP," IEEE Trans. on Power Delivery, Vol. 8, pp. 1615-1626, July 1993.

[47] Gustavsen, B. "Wide band modeling of power transformers," *IEEE Trans. on Power Delivery* , Vol.19 No.1, pp. 414-422, Jan 2004.

[48] Gustavsen, B. "A Hybrid Measurement Approach for Wideband Characterization and Modeling of Power Transformers," *Power Delivery, IEEE Transactions on* , Vol.25, No.3, pp.1932-1939, Jul 2010.

[49] Gustavsen, B. Semlyen, A. "Application of vector fitting to state equation representation of transformers for simulation of electromagnetic transients," *Power Delivery, IEEE Transactions on*, Vol.13 No.3 pp.834-842, Jul 1998.

[50] Gustavsen, B. "Computer code for rational approximation of frequency dependent admittance matrices," *Power Delivery, IEEE Transactions on*, Vol. 17 No.4 pp. 1093-1098, Oct 2002.

[51] Popov M., "Switching Three-Phase Distributions Transformer With a Vacuum Circuit Breaker - Analysis of Overvoltages and the Protection Equipment," Ph.D. Thesis, Delft University of Technology, 2002.

[52] W. Enright, O.B. Nayak, G.D. Irwin, A. Arrillaga " An Electromagnetic Transients Model of Multi-Limb Transformer Using Normalized Core Concept," *IPST'97 - International Conference on Power System Transients*, pp.93-98 June 1997

[53] W. Enright, N. Waston and O.B. Nayak, "Three Phase five-Limb Unified Magnetic Equivalent Circuit Transformer Models for PSCAD V3," *IPST'99 - International Conference on Power System Transients*, pp.462-467 July, 1999

[54] L. Liljestrand, A. Sannino, H. Breder, S. Thorburn "Transients in collection grids of large offshore wind parks," *Wind Energy*, Vol. 11 No. 1 pp.45-61, 2008

[55] R. B. Lastra, M. Barbieri, "Fast Transients in the Operation of an Induction Motor with Vacuum Switches," *Int. Conf. on Power Systems Transients IPST'2001*, 24-28 June 2001, Rio de Janeiro (Brasil), paper 063

[56] T. Abdulahovic, T. Thiringer "Comparison of switching surges and basic lightning impulse surges at transformer in MV cable grids," *Nordic Wind Power Conference, NWPC 2009,* Bornholm, Denmark, 10-11 October, 2009

[57] T. Abdulahovic, "Analysis of High-Frequency Electrical Transients in Offshore Wind Parks," Licentiate Thesis, Chalmers University of Technology, Gothenburg, Sweden, April, 2009.

[58] P. Chowdhuri, *Electromagnetics Transients in Power Systems*, Research Studies Press, England, 1996.

[59] A. Greenwood, *Electrical Transients in Power Systems*, Wiley, New York, 1991

[60] Gustavsen, B. and Mo O., "Interfacing convolution based linear models to an electromagnetic transients program," *in Proc. Int. Conf. Power Systems Transients,* Lyon, France, Jun. 4-7, 2007, p. 6.

[61] Abdulahovic T., Teleke S., Thiringer T. and Svenson J., "Simulation Accuracy of the built-in PSCAD and an Owner Defined Synchronous Machine Model," *COMPEL: The international journal for computation and mathematics in electrical and electronic engineering,* Vol. 29, No.3, pp.840-855, 2010

[62] Gustavsen, B and Semlyen, A. "Enforcing Passivity for Admittance Matrices Approximated by Rational Functions," *IEEE Trans. Power Systems*, Vol. 16, No. 1, pp. 97-104, Feb. 2001.

[63] B. Gustavsen, "Improving the pole relocating properties of vector fitting," *IEEE Trans. Power Delivery,* Vol. 21, No. 3, pp. 1587-1592, July 2006.

[64] Deschrijver, D., Mrozowski, M., Dhaene, T., and De Zutter, D., "Macromodeling of Multiport Systems Using a Fast Implementation of the Vector Fitting Method," *IEEE Microwave and Wireless Components Letters,* Vol. 18, No. 6, pp. 383-385, June 2008.

[65] N. Abeywickrama, Y.V. VSerdyuk, S.M. Gubanski, "Effect of Core Magnetization on Frequency Response Analysis (FRA) of Power Transformers," *Power Delivery, IEEE Transactions on*, Vol.23, No.3, pp. 1432-1438, July 2008.

[66] P. Gómez, F. de León, "Accurate and Efficient Computation of the Inductance Matrix of Transformer Windings for the Simulation of Very Fast Transients," *Power Delivery, IEEE Transactions on,* Vol.26, No.3, pp.1423-1431, July 2011

[67] "IEEE standard test code for dry-type distribution and power transformers," *IEEE Std C57.12.91-2001*, 2001

[68] "IEEE Standard Requirements for Liquid-Immersed Distribution Substation Transformers," *IEEE Std C57.12.36-2007*, pp.c1-29, March, 2008

[69] "IEEE Guide for Testing Turn Insulation of Form-Wound Stator Coils for Alternating-Current Electric Machines," *IEEE Std 522-2004 (Revision of IEEE Std 522-1992)*, 2004

[70] *National Electrical Motor Association Standards*,NEMA Standard MG1.20-2006.

[71] "Rotating Electric Machines, Part 15: Impulse voltage withstand levels of rotating a.c. machines with form-wound coils," *IEC 34-15*, 1995.

[72] M. Reza, H. Breder, "Cable System Transient Study - Vindforsk V-110. - Experiments with switching transients and their mitigation in a wind power collection grid scale model," Vindforsk Tech. Rep., Sweden, January, 2009.

[73] R. L. Doughty, F. Heredos, "Cost effective motor surge capability," *in Proc. Petroleum and Chemical Industry Conference, 1995. Record of Conference Papers., Industry Applications Society 42nd Annual*, pp.91-103.

[74] D. C. Bacvarov, D. W. Jackson, C. L. Lee, "Effect of Surge Capacitor Lead Length on Protection of Motors from Steep Switching Surges," *IEEE Transactions on Power Apparatus and Systems*, vol.PAS-103, no.7, pp.1879-1882, July 1984.

[75] J.P. Eichenberg, H. Hennenfent, L. Ljiljestrand, "Multiple Re-Strikes Phenomenon when Using Vacuum Circuit Breakers to Start Refiner Motors," *Pulp & Paper Canada* vol. 98, no. 7, pp. 32-36, July 1997.

[76] Popov, M.; van der Sluis, L.; Paap, G.C., "A simplified transformer model for the simulation of fast surges and adequate protection measures," *Power Engineering Society Winter Meeting, 2001. IEEE*, vol.1, no., pp.323-328 vol.1, 28 Jan-1 Feb 2001.